pH Coupled Co-Precipitation of Alkaline-Earth Carbonates and Silica

Complex Materials from Simple Chemistry

DISSERTATION

ZUR ERLANGUNG

DES DOKTORGRADES DER NATURWISSENSCHAFTEN

(DR. RER. NAT.)

DER FAKULTÄT

CHEMIE UND PHARMAZIE

DER UNIVERSITÄT REGENSBURG

vorgelegt von

Josef Eiblmeier

aus Arnstorf

Regensburg 2013

Promotionsgesuch eingereicht am:	04.04.2013
Tag des Promotionskolloquiums:	03.05.2013
Die Arbeit wurde angeleitet von:	Prof. Dr. Werner Kunz
Prüfungsausschuss:	Prof. Dr. Hubert Motschmann (Vorsitzender)
	Prof. Dr. Werner Kunz (1. Gutachter)
	Prof. Dr. Arno Pfitzner (2. Gutachter)
	Prof. Dr. Henri Brunner (3. Gutachter)

"Wenn es überhaupt eine gute Idee gibt, dann die Idee der Skepsis gegenüber allen guten Ideen."

Gerhard Polt

Vorwort

Die vorliegende Dissertation beruht auf Forschungsarbeiten, die im Zeitraum von Oktober 2009 bis März 2013 am Lehrstuhl von Prof. Dr. Werner Kunz (Institut für Physikalische und Theoretische Chemie, Universität Regensburg) durchgeführt wurden. Die Arbeit selbst ist so aufgebaut, dass jedes einzelne Kapitel, in denen die Forschungsergebnisse präsentiert werden, als Manuskriptvorlage für Publikationen in wissenschaftlichen Fachjournalen dienen soll.

Die gewonnen Ergebnisse dieser Doktorarbeit wären sicherlich nicht ohne die Unterstützung von vielen Menschen zustande gekommen, bei denen ich mich an dieser Stelle ganz herzlich bedanken möchte.

Zuallererst möchte ich mich natürlich bei meinem Doktorvater, Herrn Prof. Dr. Werner Kunz, für die Überlassung des interessanten und vielschichtigen Themas bedanken. Vor allem aber auch für die Gewährung großzügiger akademischer und finanzieller Freiräume zur Verwirklichung der eigenen Ideen und natürlich auch für sein stets entgegengebrachtes Vertrauen in mich und meine Arbeit.

Ebenso möchte ich mich bei Dr. Matthias Kellermeier für seine fortwährende Unterstützung bedanken. Wenn man so will war Matthias mein co-Doktorvater, der immer ein offenes Ohr für alle erdenklichen Fragen und Problemstellungen hatte. Sein immenses Wissen, speziell auf dem Gebiet der Silicat-Carbonat Wechselwirkungen, aber auch seine allgemeine Herangehensweise zur Lösung verschiedenster Problemstellungen haben mich persönlich zutiefst beeindruckt. Die gewonnen Erkenntnisse und wesentlichen Konzepte dieser Doktorarbeit wäre ohne die zahlreichen Diskussionen mit ihm sicherlich so nicht zustande gekommen. Weiterhin möchte ich mich bei Ihm noch für seine zahlreichen Korrekturen von verschiedenen Manuskripten bedanken, durch die ich sehr viel lernen konnte. Vor allem aber

möchte ich Ihm für die entgegengebrachte Freundschaft in den vergangenen 3 Jahren herzlich danken.
Weiterer Dank gebührt auch Prof. Dr. Juan Manuel García-Ruiz für sein kontinuierliches Interesse am Fortgang der Arbeit. Durch sein profundes Wissen auf den Gebieten der Silica Biomorphs und der Kristallisation im Allgemeinen, aber auch durch zahlreiche Diskussionen mit Ihm konnte ich sehr viel lernen.
Im Rahmen der Dissertation wurde eine Vielzahl an verschiedenen Messmethoden angewendet, was ohne die Hilfe von externen Kooperationspartnern so nicht möglich gewesen wäre. Deswegen möchte ich mich an dieser Stelle bei verschiedenen Personen bedanken, die mich im Rahmen dieser Kooperationen unterstützt haben:

- Martina Müller für experimentelle Unterstützung zur Gewinnung der Daten für die Abbildungen 5.8, 5.9 und 5.10.

- Prof. Dr. Reinhard Rachel, Prof. Dr. Ralf Witzgall und Cornelia Niemann (Institut für Molekulare und Zelluläre Anatome, Universität Regensburg) für die Bereitstellung der Elektronenmikroskope und Hilfe bei der Benutzung und Interpretation der gewonnen Daten.

- Prof. Dr. Gottfried Schmalz und Gerlinde Ferstl (Poliklinik für Zahnerhaltung und Paradontologie, Uniklinikum Regensburg) für die Bereitstellung des Rasterelektronenmikroskops und diverser Hilfestellungen bei der Benutzung.

- Prof. Dr. Andreas Fery und Melanie Pöhlmann (Physikalische Chemie II, Universität Bayreuth) für die Bereitsstellung des Rasterkraftmikroskops und Hilfe bei der Benutzung und der Dateninterpretation, sowie für die Herstellung der strukturierten PDMS Oberflächen (Kapitel 6).

- Prof. Dr. Lorenz Kienle, Mao Deng und Dr. Ulrich Schürmann für die TEM und micro-EDX Daten aus Kapitel 3 und 4 und für die Hilfestellung bei der Auswertung.

- Prof. Dr. Arno Pfitzner, Dr. Martina Andratschke und Stephan Dankesreiter für die Aufnahme der Pulverdaten und Hilfe bei der Datenauswertung.

- Prof. Dr. Manfred Scheer und Michael Seidl für die Erlaubnis zur Benutzung des FTIR Spektrometers.

- Doris Rengstl (Universität Regensburg) und Dr. Roman Chernikov (HASYLAB/DESY, Hamburg) für verschiedenste Hilfestellungen während der Synchrotronmesszeit am DESY in Hamburg.

- Dr. Matthias Kellermeier, Prof. Dr. Helmut Cölfen und Dr. Denis Gebauer für die Bereitstellung des Titrationsequipments und für Ihre Hilfe bei der Datenauswertung und deren Interpretation.

- Bei Andreas Picker möchte ich mich noch gesondert bedanken, weil ich während meiner Messaufenthalte in Konstanz immer gratis auf seiner kleinen, aber feinen Couch schlafen durfte.

Herrn Prof. Dr. Hubert Motschmann, Herrn Prof. Dr. Arno Pfitzner und Herrn Prof. Dr. Henri Brunner danke ich für ihre Bereitschaft in der Prüfungskommission mitzuwirken.
Den Mitarbeitern der Werkstätten sei für die schnelle und zuverlässige Erledigung der Aufträge gedankt.
Allen aktuellen und ehemaligen Mitarbeitern und Kollegen des Lehrstuhls danke ich recht herzlich für die entspannte und freundschaftliche Arbeitsatmosphäre, stete Hilfsbereitschaft, und natürlich für das ein- oder andere Feierabendbier.
Besonders danke ich Herrn Dr. Fabian Glaab für das Korrekturlesen der Doktorarbeit, für seine Freundschaft in den letzten Jahren und natürlich für seine berühmt berüchtigten Wutausbrüche, die mich immer wieder erheitert haben.
Meiner ehemaligen Bürokollegin Gabi danke ich herzlich für die lockere Arbeitsatmosphäre und insbesonders dafür, dass Sie ständig meine Musik ertragen hat.
Last but no least, möchte ich mich noch aus tiefstem Herzen bei den wichtigsten Personen in meinem Leben bedanken: *meiner Familie*, denen diese Arbeit auch gewidmet sein soll. Ihr seid immer hinter mir gestanden und habt mich unterstützt, wo es nur ging. Ohne Euch wäre ich bestimmt nicht soweit gekommen. Auch meiner Freundin Luisa sei herzlich gedankt, dass Sie mich während meiner Doktorarbeit immer unterstützt hat und dass Sie mich durch die gemeinsam verbrachten Wochenenden den Doktorarbeitsalltag vergessen ließ.

Contents

1 Introduction

1.1 General Background

The principle how nature creates the hard parts in living organism has for long been a fascinating topic and also raised a still growing research field. Such elaborate architectures are often hallmarked by sinuously shaped surfaces which hardly reflect the geometric constraints dictated by the crystallographic phase of the mineral. This is in contrast to classic *abiotic* crystals, where the final crystal shape is defined by the arrangement of atoms within the structure. First pioneering works in the end of the 19^{th} century by Pieter Harting were dedicated to elucidate natures strategy to create such astonishing forms. It soon became clear that the formation of such complex functional structures is linked to the intimate interaction between organic and inorganic matter.[1] His findings were based on the precipitation of so called *"calcospherites"* which resemble certain biominerals and are yielded by combining inorganic salts with biological (organic) matter[2] (see Figure 1.1 right).

On that basis, numerous investigations were dedicated to unravel the design principles of certain biominerals (cf. Figure 1.1 left) and, at the same time, shed light on mechanistic details for the formation of such elaborate organic-inorganic composite materials. Up to now a vast amount of biominerals has been identified, and all of them perform, due to their unique properties, several functions ranging from skeletal support and protection, to gravity, magnetic field perception,[8,9] or serving as specialized photosensitive organs.[10,11] Among identified biominerals, calcium carbonate is by far the most often utilized material and occurs in different polymorphs such as calcite (being the thermodynamic stable form at ambient conditions), aragonite, vaterite as well as the amorphous calcium carbonate (ACC) besides monohydrocalcite.[12]

In this context, nacre (also referred to as "Mother of Pearls") is an interesting biomaterial as

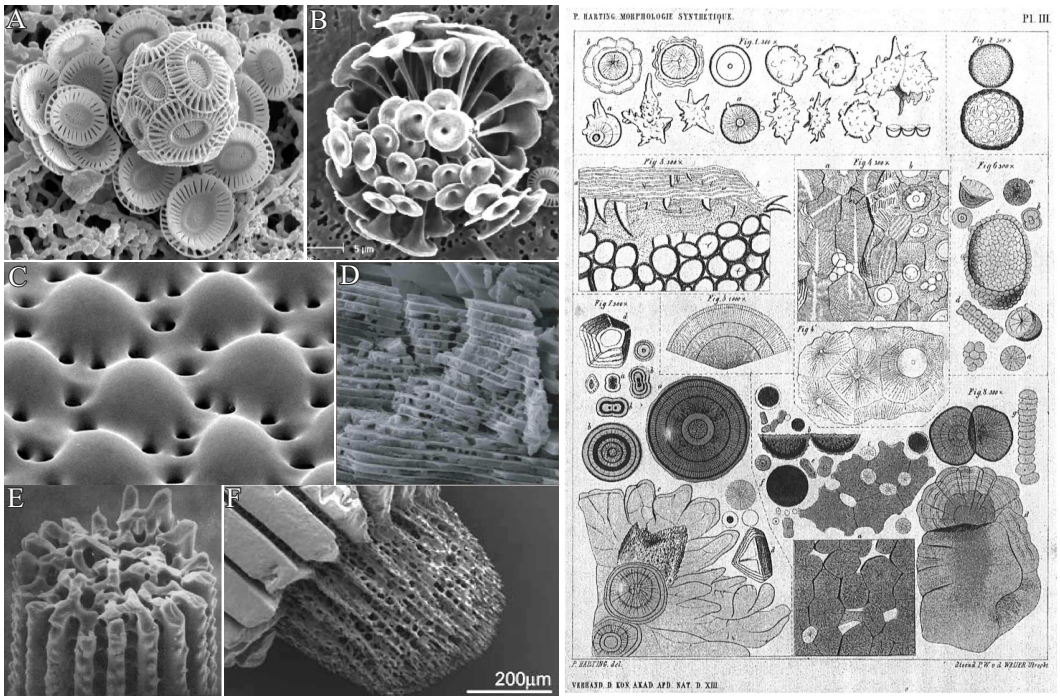

Figure 1.1. Left: SEM images of some exemplary biominerals. (A-B) Calcitic coccoliths of the marine calcareous alga *Discosphaera tubifera* and *Emiliana Huxleyi*[3,4]. (C) Photoreceptors in the light-sensitive brittlestar *Ophiocoma wendtii* comprised of calcite.[4]) (D) SEM close-up view of nacre from the bivalve *A. rigida*.[5]) (E-F) Tips of a sea urchin spine *Paracentrotus lividus*.[6,7] Right: Original drawings of Harting showing the yielded "calcospherites" upon precipitation of inorganic salts in the presence of organic matter.[2]

it attracts the attention of scientists from a wide range of research fields due to its outstanding remarkable mechanical properties (ca. 3000 times tougher than pure aragonite[13]). Such features are explained by the complex ordering of 3-D calcium carbonate plates in a matrix of organic macromolecules, which is also described as a "brick and mortar" arrangement of organic and inorganic components (see Figure 1.1D).

Beneath the structural design further central aspects in the field of biomineralization are the control over nucleation, growth, selection of polymorph and the shape of the resulting composite mineral. These manifold requirements are accomplished in natural crystallization processes via a synergistic interplay between the mineral phase and the surrounding organic matrix. The latter can be treated as an additive which controls the crystallization events over multiple length scales beginning from the Ångström level, (where the arrangement of atoms decides which polymorph of the mineral is preferred) up to the mesoscopic scale in which the manner of integration and alignment of building units defines the final appearance of the

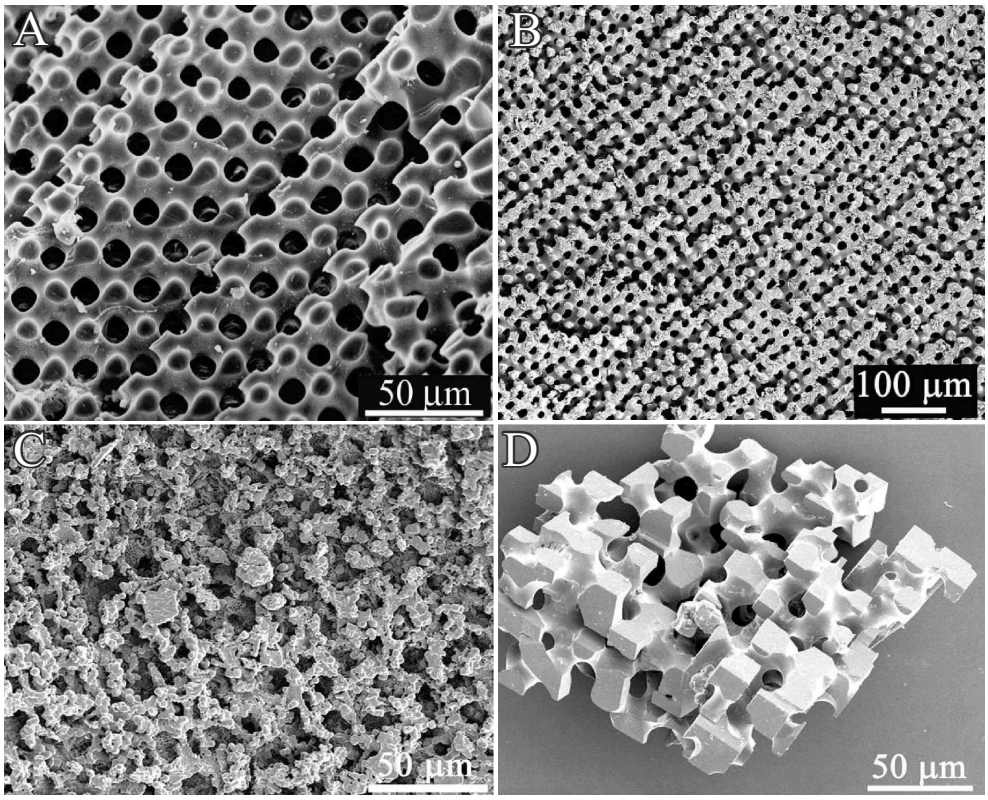

Figure 1.2. (A) SEM cross section of a naturally ocurring skelatal plate of a sea urchin spine and (B) the corresponding polymeric membrane replica.[14] (C) Polycrystalline calcite crystals precipitated in the porous polymer membrane together with a porous calcite single crystal, yield with the same method.[15]

biomineral.

Among the additives which are used for the control in biomineralization processes one can discriminate between two principal types. The first one is comprised of water insoluble biopolymers like chitin or collagen and is utilized by organism for the construction of scaffolds for crystallization.[16] In such templating approaches, mineral deposition occurs in specialised micro-environments like vesicles or even larger compartments separated from the external aqueous neighborhood, by membraneous envelopes, in order to regulate several parameters like flux of ions, saturation state or pH of the inner region.[6,8,13] Additionally, such microreactors are capable to promote crystallization by heterogenous nucleation providing lower activation energy barriers than homogeneous nucleation.[16] Hereby, immobilized organic frameworks act as structured substrates offering preferential sites for oriented nucleation[17] and, beyond that, molding the mature mineral within the walls of the compartmentalized reaction volume providing global control of the morphology.[8]

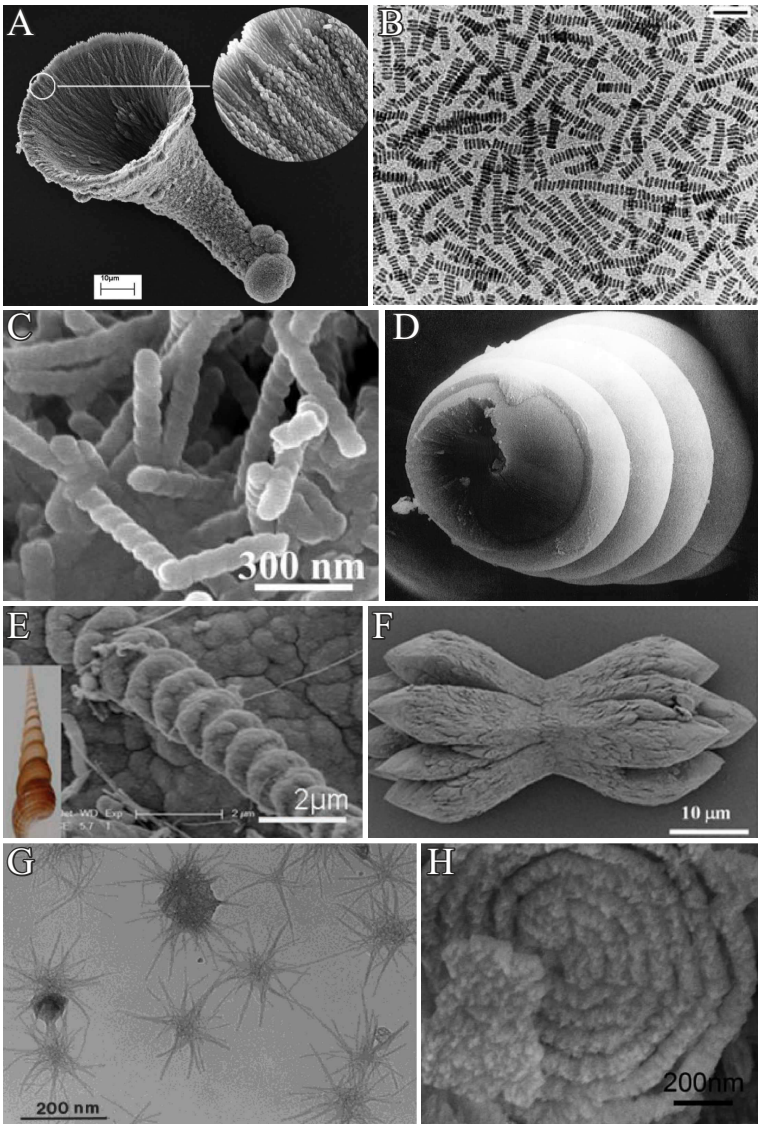

Figure 1.3. Gallery of various minerals, precipitated in the presence of soluble organic (polymeric) molecules. (A) "Microtrumpet" consisting of self-assembled calcite microcrystals formed under the influence of 1,3-diamino-2-hydroxypropane-N,N,N',N'-tetraacetate.[3] (B) Ordered chains of $BaCrO_4$ nanoparticles grown in a surfactant based environment (reproduced from[18]). (C) Silica particles with helical morphologies synthesized with a pyridinium-based cationic surfactant.[19] (D) Polycrystalline $CaCO_3$ (vaterite) helices precipitated in the presence of poly(aspartate).[20] (E) Nanofibres composed of $BaCO_3$ with double-stranded and cylindrical helical morphologies formed in a phosphonated block co-polymer controlled mineralization process.[21] (F) Nanocrystalline $BaCO_3$ superstructures obtained in the presence of poly(ethyleneoxide)-*block*-eicosa aspartate.[22] (G) Neuronlike calcium phosphate/polymer (PEO-*b*-PMAA-C_{12}) mesostructures.[23] (H) Spiral superstructures of $BaCO_3$ crystals prepared in a PNIPAM-b-PLGA polymer micelle solution.[24]

On the other hand, soluble organic (macro)molecules, also referred as so-called soluble or

functional matrix allow for the control over the ongoing crystallization within the micro-environments.[16] This occurs primarily via face-specific adsorption on the growing single crystal or also via stabilization of small building units which self-assemble to polycrystalline architectures later on.

The synergistic interplay between the multiple crystallization modifiers in the course of biomineral formation has inspired scientists from various fields to develop novel synthetic strategies for the creation of novel "biomimetic" materials with desired properties and special morphologies.[16,25] One one of these concepts for the in vitro synthesis of biomimetic material represents a "top down" approach where the organic matrix (or its polymeric replica), is utilized as 3D template in analogy of direct molding strategies in biological systems (see Figure 1.2 A-B). Indeed, macroporous calcite single crystals with the same morphology as skeletal plates of sea urchins were successfully produced via direct precipitation in a sponge-like polymer membrane (Figure 1.2 C-D).[15,26] Alternatively, ACC can also be utilized as precursor material in the same approach for the generation of calcite crystals with extraordinary morphologies. Thereby it is advantageous that the amorphous precipitate can be suitably molded within a preferred geometry to yield crystalline matter with identical shape.[27–29] Further experiments revealed additionally that this strategy is not limited to calcium carbonate, since similar sponge-like structures reminiscent of sea urchin skeletal plates could be yielded with $SrSO_4$, $PbSO_4$, $CuSO_4 \cdot 5\,H_2O$,[30] gold, titanium,[31] and copper,[32] respectively.

Truly, a certain drawback in this "top down" strategy is the complicate and time consuming preparation of suitable templates, making a large scale industrial production impossible. Thus, "bottom up" approaches, where formation of elaborate inorganic matter is based on concerted self-assembly of nanosized building units, are desired, using water soluble organic additives which fulfill the role of the functional matrix in biomineralization processes. Therefore, scientists have screened the influence of a vast amount of additives on the crystallization processes of certain minerals, ranging from simple ions[33–35] or small organic molecules like citric acid[36,37] over ordinary polymers and polyelectrolytes[20,38–40] and surfactants[18,19,41,42] to complex block copolymers (cf. Figure 1.3).[21,22,43–47]

The morphological complexity achieved, by introducing (organic) mineralization additives,

can however not be explained by classical theories[48] which describe a pathway of crystal formation where growth occurs via attachment of single ions or molecules onto crystal faces of already existing nuclei (pathway (a) in Figure 1.5). The latter can either result from heterogeneous nucleation on foreign surfaces such as dispersed impurities (e. g. dust particles), crystal seeds, or tube walls. This process is energetically favored, as the free energy to create a new interface is reduced. On the other side, nuclei can alternatively be formed in the bulk volume via homogeneous nucleation from supersaturated solutions. This is mainly a stochastic event and occurs via association of ion clusters. However, the question whether individual clusters grow or not is dependent on two opposing effects in the overall Gibbs free energy of cluster formation ΔG_{Nucl} (Figure 1.4). The latter is typically related to the positive term of the surface energy ΔG_{Surf} (being proportional to the square of the spherical cluster radius r^2) and to the negative contribution, resulting from a volume term that scales with r^3 which is due to the gain in bulk energy ΔG_{Bulk} since a new crystal lattice is formed. These two effects become balanced when the nucleus reaches a certain, so-called *critical cluster size*, r^*. Enlargement of the nucleus above r^* consequently leads to a gain in the net free energy as the volume term overbalances the surface energy term (cf. Figure 1.4).

According to the classical model, growth occurs via ion attachment and replication of the unit-cell, yielding crystals with defined geometrical outer shapes, smooth surfaces and fixed angles. Such simplistic descriptions for crystal formation might be valid for geological minerals, but classic theories cannot explain the presence of the typical sinuous shapes in biominerals (which can also be single crystalline). Instead, mineralization can also proceed along so called "non-classical crystallization" pathways, starting from pre-formed nanoparticles which serve as building blocks for the final architectures.[50–53] Figure 1.5 (pathway b and c) gives an schematical overview of processes involved. In the absence of additives (pathway b), nanocrystalline building blocks can lock in and fuse to form an iso-oriented single crystal. This phenomenon is also called *oriented attachment*.[54]Alternatively, when suitable additive species are present they can cover the surface of primary building units (being of either crystalline or amorphous nature). In this way, fusion to single crystals (as described in pathway (a) and (b) in Figure 1.5) is at first prevented as the adsorbed polymers dictate the mode of interaction between individual nanoscale units. The stabilized, primary nanoparticles are

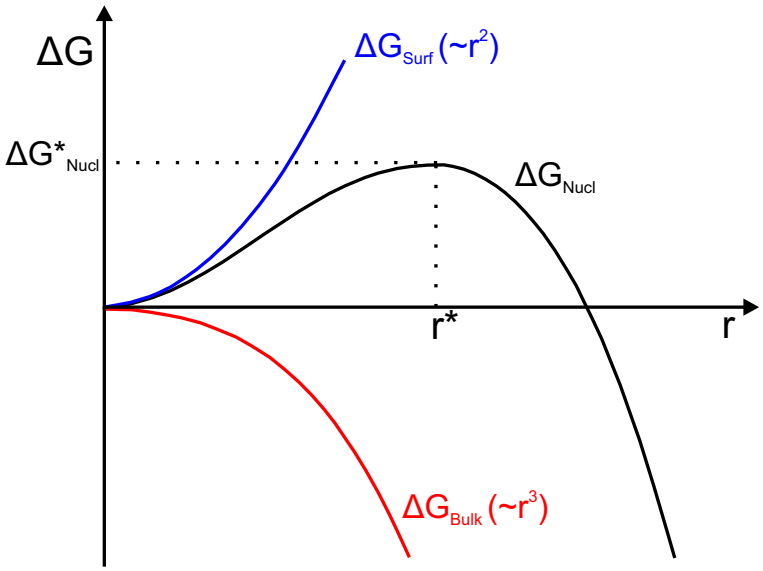

Figure 1.4. Classical nucleation theory: plot of the Gibbs free energy ΔG for the formation of nucleation cluster from supersaturated solutions in dependence of cluster radius. The balance between the cost in energy for creating new surfaces ΔG_{Surf} and the gain due to attractive forces in the emerging lattice (ΔG_{Bulk}) provoke a maximum in the net curve (ΔG_{Nucl}), which defines the critical cluster size r^* and the corresponding activation energy for nucleation $\Delta G_{Nucl}{}^*$.

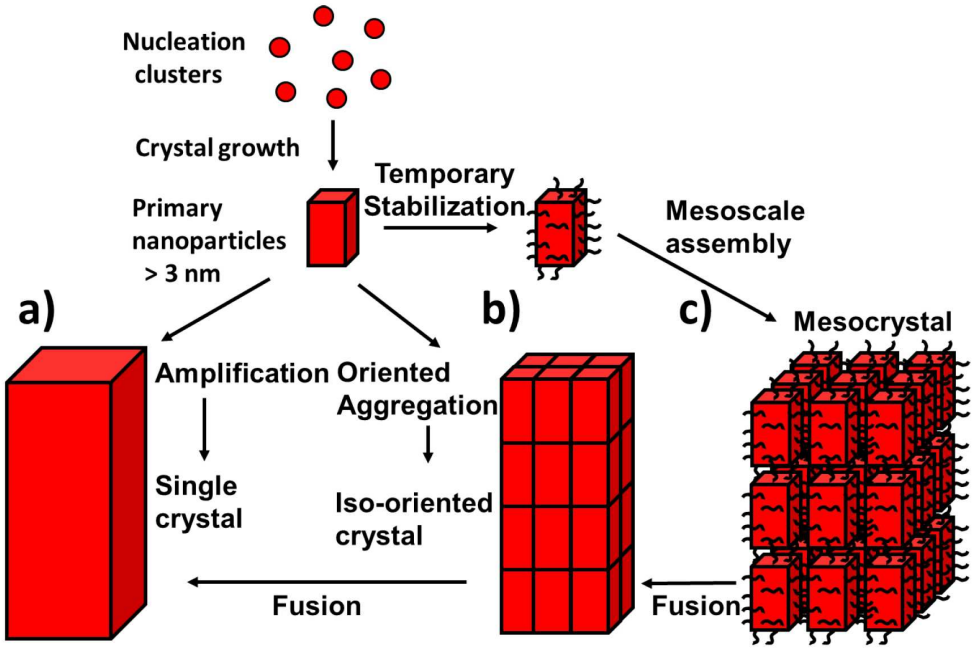

Figure 1.5. Schematic representation of classical (a) and non-classical (b) crystallization. Pathway (c) highlights the stabilization of primary nanoparticles with additives like polymers or surfactants which finally yields mesocrystals via concerted self-assembly of individual nano-units.[49,50]

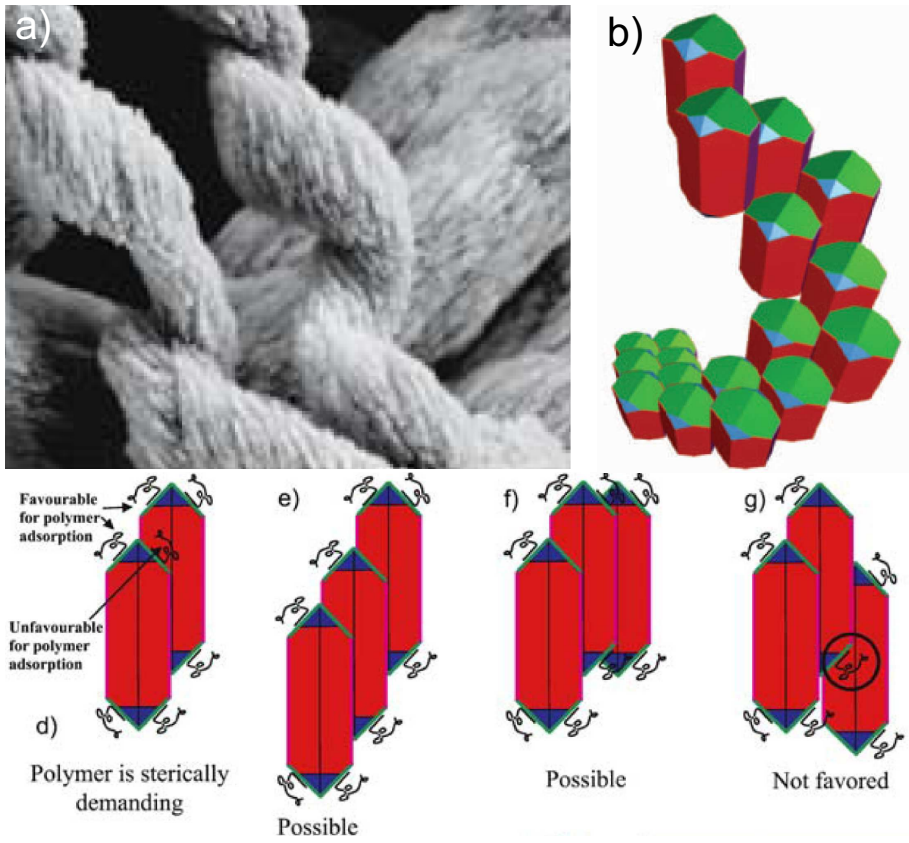

Figure 1.6. (a-c) SEM images of helical $BaCO_3$ fibers formed in solutions containing phosphonated block copolymers.(d-g) Mechanism explaining the helical arrangement. Face selective adsorption of the polymer on (110) planes and sterical hindrance (d) favors particle aggregation in a staggered manner over other, energetically less favorable, arrangements (g). Further growth of individual particles occurs via epitaxial attachment to the uncovered lateral faces (020) and (011). This leads to a situation where incoming building units differentiate between favorable and unfavorable sites for attachment. (b) This eventually induces a helical winding of the whole aggregate, yielding either right-or left-handed superstructures.[55]

subsequently capable to self-assemble to so called *mesocrystals* which is an abbreviation for "mesoscopically structured crystals" (pathway c, Figure 1.5). Similarly additive covered hybrid particles can aggregate in a manner where they are perfectly aligned in a common crystallographic fashion, giving them properties of "ordinary" single crystals in terms of X-ray scattering, despite consisting of multiple individual units (Figure 1.5, pathway b). It seems logical that such additive-mediated crystallization routes enable new synthesis strategies for pseudo-single crystals with remarkable morphologies and unique properties. However, the mesoscale arrangement of previously stabilized precursor units can also produce polycrystalline superstructures, dependent on several parameters like specific interactions between

the adsorbed layers or re-alignment phenomena during aggregation in the presence of spatial constraints.[52] An interesting situation arises when self-aggregation of nanoparticles is provoked by polymeric additives that selectively adsorb on distinct faces of anisotropic (crystalline) particles. This mechanism is nicely exemplified in Figure 1.6, where crystallization of $BaCO_3$ occurred in the presence of sterically demanding racemic block copolymers.[55] In this case, selective adsorption of the stiff polymer onto (110) faces of witherite leads to restricted growth along this direction and to stabilization of the involved face at the same time (Figure 1.6C). This causes staggered arrangement of the carbonate crystals and allows incoming building blocks to discriminate between the lateral faces during aggregation, finally yielding (racemic) helical superstructures (Figure 1.6A).

2 Silica-carbonate biomorphs

2.1 Aims and purpose of the thesis

2.1.1 Introduction

The summarized findings presented above in the field of bio-mimetic material science strongly suggest the presence of elaborate *organic* (macro)molecules and/or supramolecular templates for the synthesis of polycrystalline carbonate structures. In contrast, even simple *purely inorganic* additives like metal ion cations such as Mg^{2+} or Sr^{2+} were found to influence the polymorph selection during $CaCO_3$ crystallization,[36,56,57] but complex shapes, as found in the presence of organic additives, remained absent. This is drastically different when using silica as inorganic additive. Silica itself is a highly abundant material, occurring in Nature as a solid mineral or in dissolved form. In the latter case, the aqueous chemistry is quite complex involving an interplay between dissolution/precipitation, adsorption/desorption and complexation processes. In this context, Juan Manuel García-Ruiz observed during his doctoral thesis in the late 1970t's very spectacular alkaline-earth carbonate-based crystal architectures, when growth was carried out in silica gels at high pH (Figure 2.1).[58–60] Indeed, he observed aggregates in purely *abiotic* crystallization media with similar complex morphologies as those displayed by living organisms in biomineralization processes (cf. Figure 2.1). In order to express their morphological resemblance to certain biological materials, these structures are termed "silica-carbonate biomorphs". Findings were at first unexpected as the formation of curved shapes far away from any crystallographic symmetry was exclusively ascribed to living nature. However, it was demonstrated in later studies that morphology alone can be misleading when discussing about biogenicity in general, i.e. the biological origin of putative precambrian microfossils (Figure 2.2).[62–64]

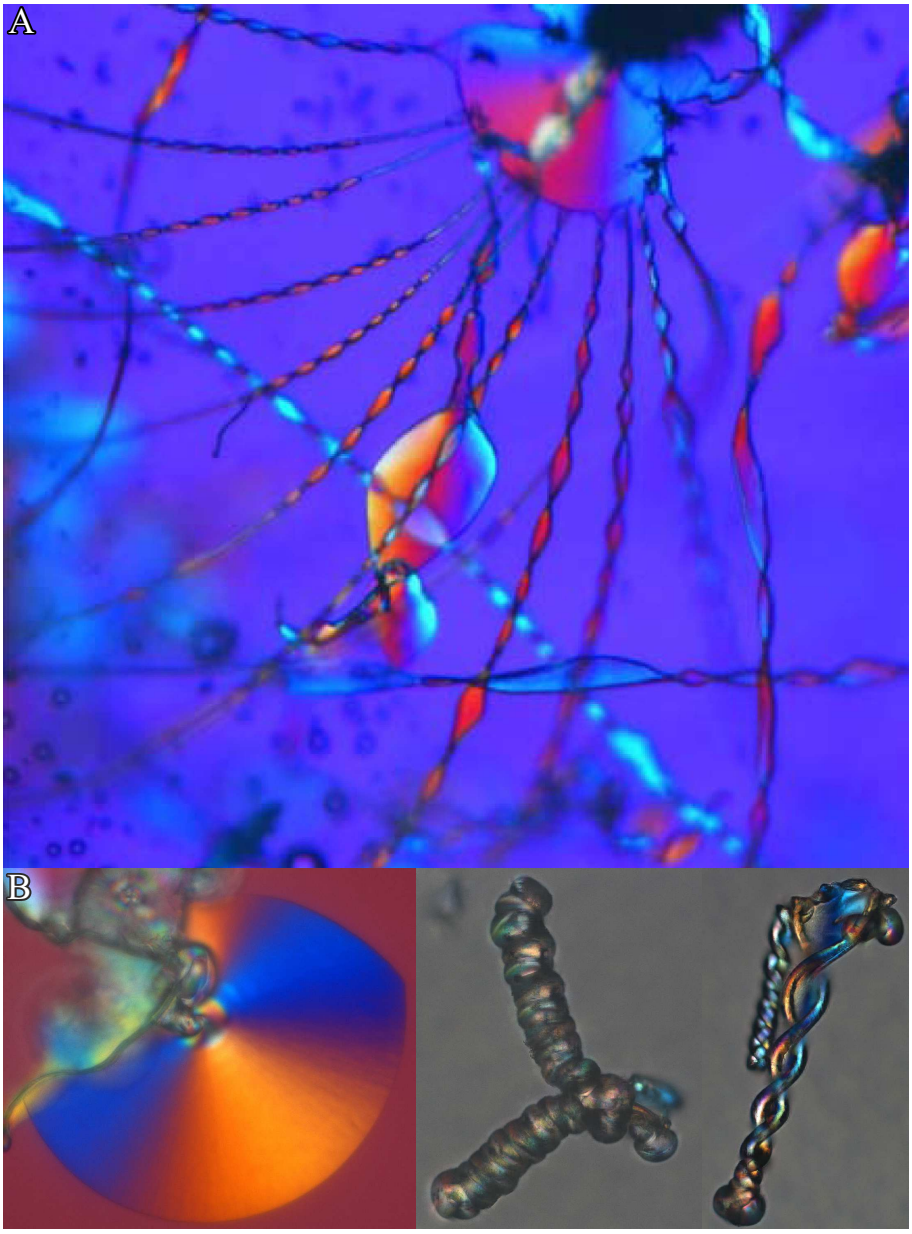

Figure 2.1. Polarized optical micrographs of complex $BaCO_3$ architectures, precipitated in silica containing matrices at elevated pH (panel (A) is reproduced from[61]).

The similarity of silica-carbonate biomorphs to certain biominerals is not only restricted to non-crystallographic shapes. They also show hierarchical ordering of participating building units and continuous intergrowth of components involved (silica and carbonate) over multiple length scales. Inspired by these findings, silica biomorphs are an interesting model system for laboratory scale studies for the design of novel and advanced materials following the bottom-up strategy with simple (and cheap) components.

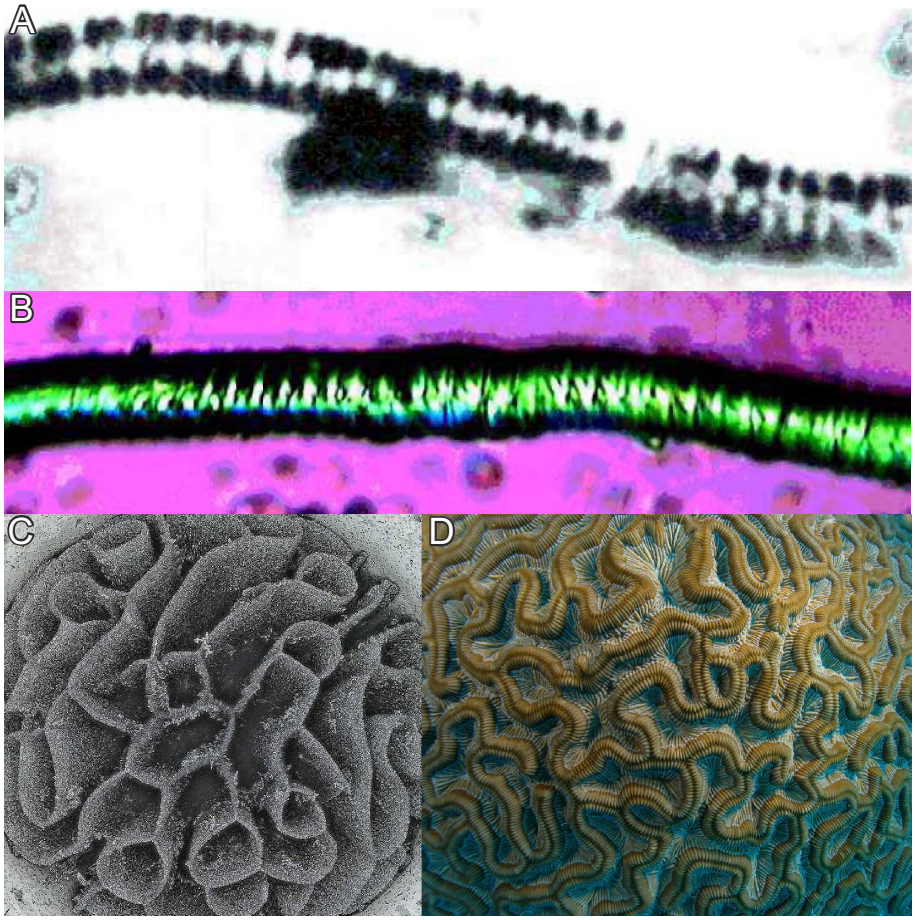

Figure 2.2. Biomimetic but abiotic: Comparison of a Precambrian microfossil (A) and a worm-like "biomorph"[64] (B). (C) A coral-like silica biomorph and its living counterpart[65] (D).

2.1.2 Preparation methods

Another feature of silica biomorph, which is interesting for material scientists in general, is their quite simple preparation. In early works, their synthesis was described utilizing an U-shaped cassette, containing a silica gel body with a pH of about 10 - 10.5. Precipitation of the carbonate architectures was induced via counter-diffusion of separate solutions of alkaline-earth metal salts (typically Ca, Ba, or Sr) and dissolved sodium carbonate.[58–60] Alternatively, an ordinary beaker can be used, half filled with silica gel and containing predissolved atmospheric carbon dioxide or sodium carbonate. In this case, crystallization is induced by covering the gel with concentrated solutions of barium-, strontium-, or calcium chloride (0.5-1 M) which diffuse into the gel.[58–60] During the unidirectional in-diffusion process, the pH is locally decreased and precipitation of biomorphic aggregates occurs at

different locations throughout the gel matrix. The yield (i.e. the size and number) of silica-biomorphs is thereby a function of the respective relative distance from the solution-gel interface. In contrast, biomorphs can also be grown from stagnant alkaline solutions containing equal volumes of dissolved silica and solutions of barium and/or strontium salts.[62,66,67] The reactive volume is in this case exposed to the atmosphere and gradual absorption of CO_2 by the system at the given alkaline conditions (pH ranges roughly from 10.2 - 11.1, see chapter 5) induces crystallization of astonishing carbonate architectures selectively on the solution/air and solution/tube wall interfaces via heterogeneous nucleation.[68] This preparation method was predominatly applied in the respective experiments in the present thesis. As silica source, commercially available water glass can be used or, alternatively, tetraethoxysilane (TEOS), as recently revealed by Voinescu et al.[69] The influence of concentrations of components on the resulting morphologies was extensively studied in recent works,[70,71] but in typical standard experiments the "optimal" concentrations for well developed biomorphs turned out to be 5 mM Ba^{2+} and 8.4 mM SiO_2.

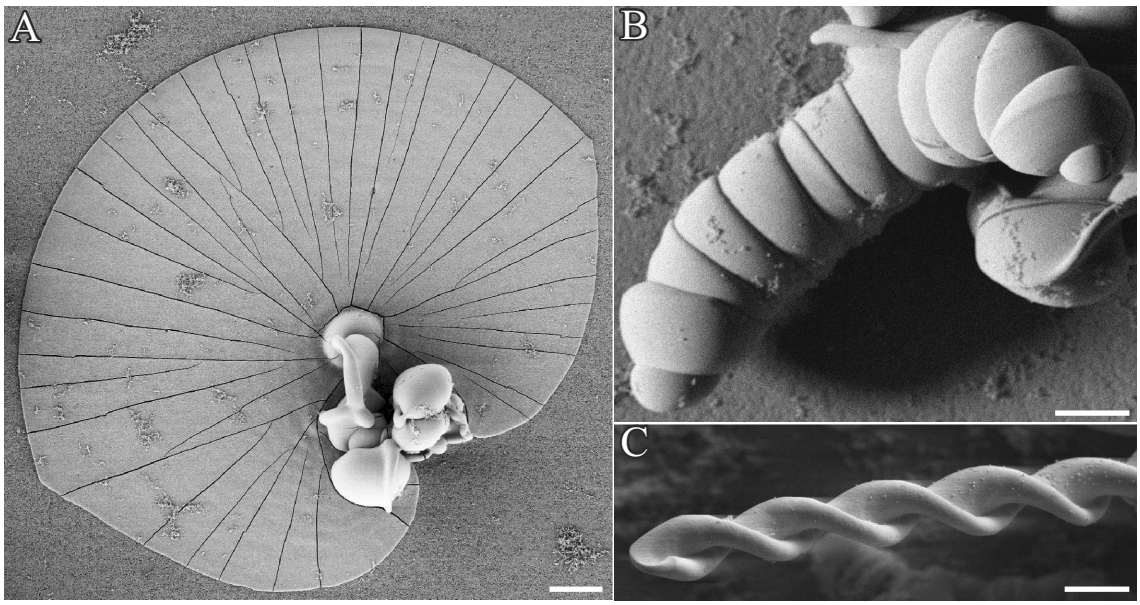

Figure 2.3. Different types of morphologies observed at standard conditions in solution experiments (c(Ba^{2+}) = 5 mM, c (SiO_2) = 8.9 mM, initial pH = 11.0) Scalebars are 20 μm.

A further parameter that has drastic influence on the morphological evolution of aggregates is the particular pH at which crystallization is carried out, as it strongly influences the chemistry and solubility of the silica and carbonate species in solution. In gel experiments the optimal pH window for the production of silica biomorphs ranges, according to Melero-García et

al., roughly from 9.3 and 9.8.[72] For solution experiments this parameter is discussed in detail in chapter 5, but earlier works report that well developed biomorphs only occur above pH values of 10. Instead, at lower pH regimes exclusively cauliflower-like dendrites were observed.[58,66,73] Thus, the pH in a typical standard experiment performed in the context of this thesis was initially adjusted to 11.0.

Those experiments yielded mainly three different types of morphologies, namely nearly flat leaf-like objects (Figure 2.3A), worm-like structures (Figure 2.3B) and twisted helicoids (Figure 2.3C).

2.1.3 Microstructure and composition

A closer inspection of the structural details of the as-formed architectures reveals a textured, polycrystalline core being composed of myriads of nanocrystals (Figure 2.4) with a typical size of 200-400 nm in length and about 50 nm in width.[61,62,67,74–76] Individual rod-like units consist of pseudohexagonal $BaCO_3$ (witherite) crystals. The hexagonal columnar habit is a common phenomenon among the aragonite-type carbonates and is due to the cyclic twinning on the $\{110\}$ planes.[77]

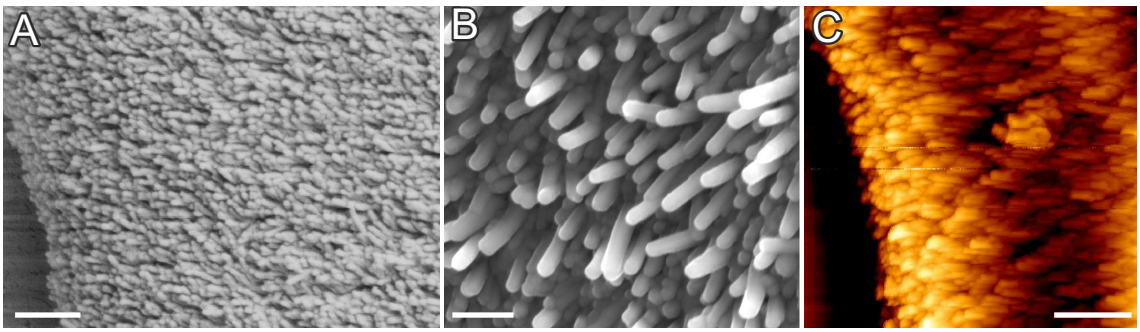

Figure 2.4. (A-B) FESEM and (C) AFM close-up views on the microstructure of silica-carbonate biomorphs, revealing myriads of nanoscale $BaCO_3$-rods.

Further studies concerning the arrangement of building units within the aggregates show that they are not randomly packed, but rather follow a distinct long-range order on the mesoscale.[61–63,67] This is achieved, as individual crystallites are nearly parallel aligned with respect to the long axis of the rods (which is their crystallographic c-axis, Figure 2.5A). However, on the mesoscopic scale, individual building units exhibit a slight, mutual misalignment to one another which is approximately kept constant throughout the whole aggregate such that all the crystalline nano-units describe an orientational field with constantly varying vec-

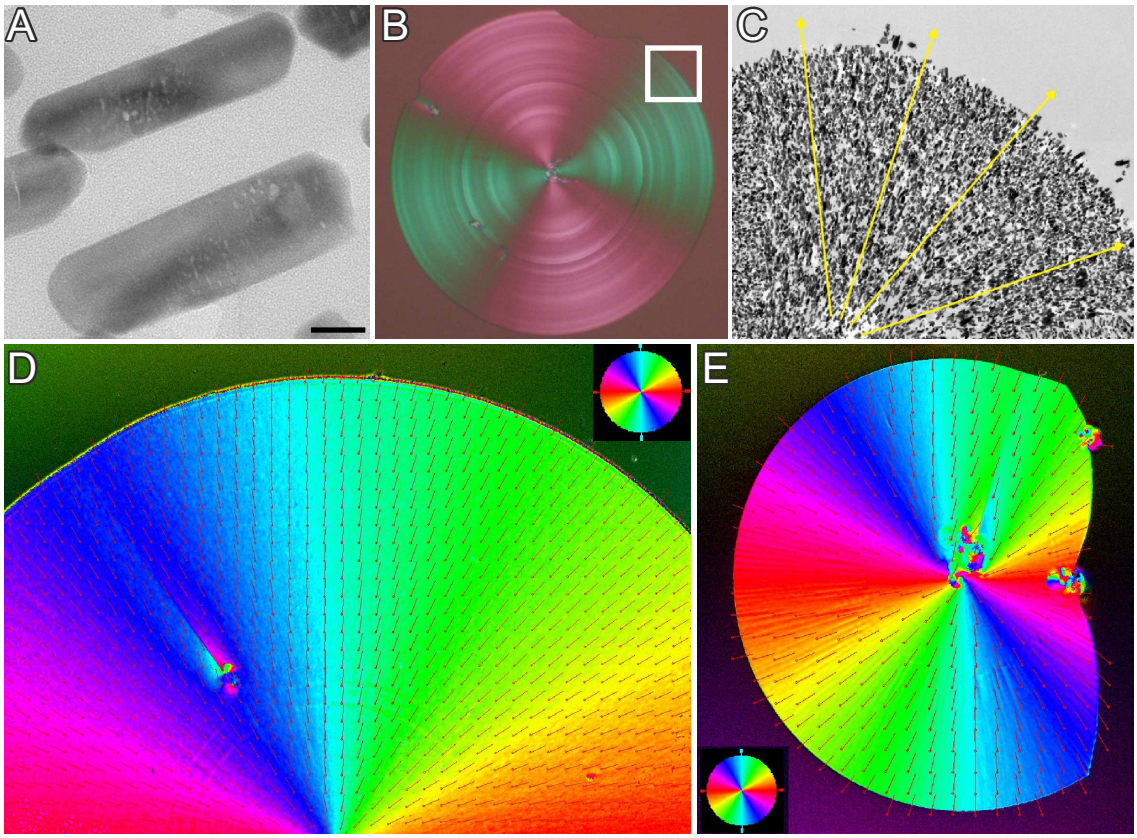

Figure 2.5. (A) TEM micrograph, visualizing the parallel alignment of individual nanocrystallites (adopted from,[61] scalebar is 30 nm). (B) Optical micrograph of a circular sheet between crossed polarizers, showing the typical Maltese-cross extinction pattern, typical objects with anisotropic building units. (C) TEM image of a sample prepared by thin-sectioning biomorphs with leaf-like morphologies. Arrows indicate preferred orientation of the crystallites.[61] (D-E) Quantitative birefringence optical micrographs (Abrio) of sheets. The difference in color in the image means different orientations of the subunits, marked with red arrows.

tor (Figure 2.5C). These trends can be analyzed in polarized optical microscopy images of flat sheet-like architectures between crossed polarizers, where the typical Maltese-cross extinction pattern is visible (Figure 2.5B). These color textures in the optical micrographs indicate the radial orientation of nanocrystallites outwards starting from a common center in the sheet. The inner orientation of the subunits within the sheet-like object can be furthermore analyzed with a quantitative birefringence imaging microscopy technique[78] (Abrio*). In this case, the varying orientation field of the grains can be nicely visualized as different colors

* Abrio imaging system, Cri, Inc. The system measures the retardance magnitude at every pixel of a charge coupled device image.[79] This means that at every pixel with the same color index has the sub-structure the same orientation.

index (Figure 2.5D-E). Consequently, the orientation of subunits (marked with red arrows) can be quantified according to the color wheel (inset in Figure 2.5D-E).

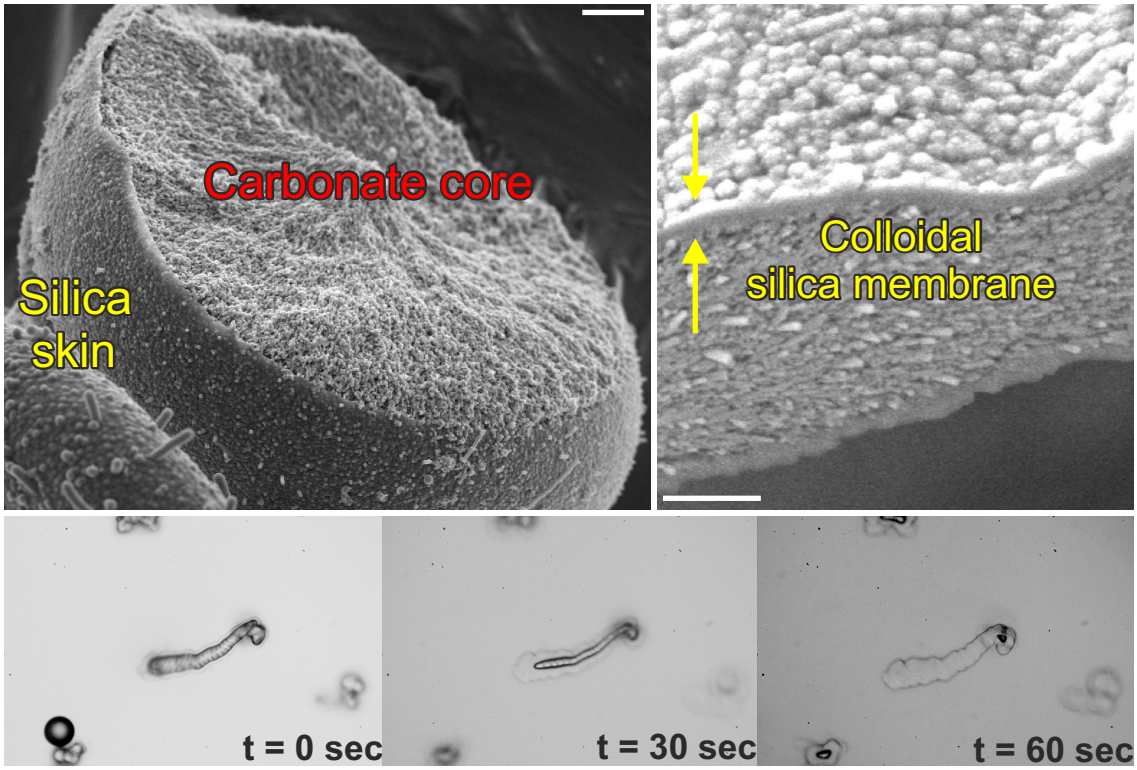

Figure 2.6. Top: FESEM images of fractured silica biomorphs, revealing the dual composite character with an outer silica skin sheathing the inner carbonate texture (images reproduced from[61]). Scalebars are 2 μm (left) and 500 nm (right). Below: Sequence of optical microscopy images showing the gradual dissolution of the inner carbonate phase from a worm-like structure with dilute acid. Such a treatment leaves a hollow silica membrane with the original worm-like morphology.

Apart from the ordering of the nanoparticles, silica biomorphs are also dual composite materials as they are comprised of carbonate and co-precipitated amorphous silica.[58–64,66–69,73,75,76,80,81] In most cases the entire carbonate part of mature architectures is enveloped by a continuous skin of agglomerated colloidal silica spheres which can be nicely visualized in images of fractured aggregates (Figure 2.6). The presence of external silica layers can either be demonstrated by EDX spectroscopy, or by immersion of selected aggregates into dilute acid, leading to selective dissolution of the carbonate core (Figure 2.6). The remaining silica parts (the so-called "ghost") still exhibit the original morphology of the previously intact biomorph architecture. These experiments can be nicely followed *in-situ* with optical microscopy, as

shown in the time-laps sequence in Figure 2.6 (below).[62,63,67,76,82–84] Likewise, the silica part of the biomorphs can also be removed selectivley with dilute NaOH, leaving the intact carbonate ultrastructure.[61,67] It was furthermore reported that the dual composite character of silica biomorphs is not only restricted to the macroscopic length scale. Also single carbonate rods could be surrounded by siliceous skins, stabilizing them against ripening.[74,85] This suggests mutual intergrowth of components over multiple length scales, as observed in many biominerals, and supports furthermore the resemblance of these unique aggregates to products from biological mineralization.

2.1.4 Formation mechanism

Beneath studies concerning the compositional and structural details, recent investigations related to silica biomorphs were focused on morphogenetic scenarios on the nano- and micrometer level, and especially on the physical origin for the formation of these fascinating architectures, since all these aspects remained obscure for long time.[61,62,86,87]

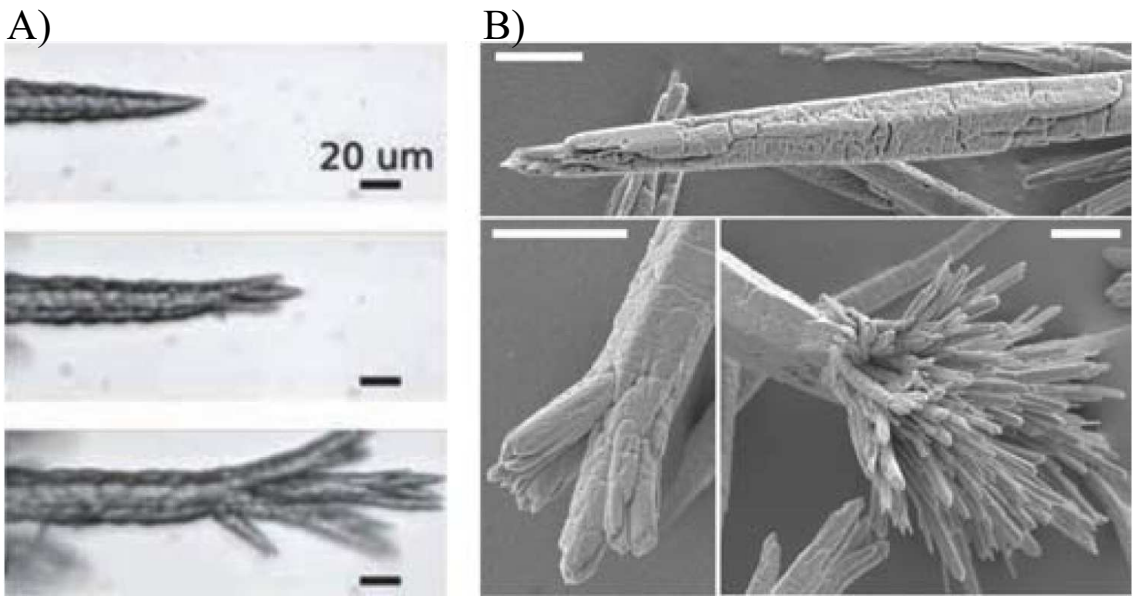

Figure 2.7. A) optical[81] and B) FESEM micrographs[61] showing primary nucleated rod-like barium carbonate crystals that start to split at their tips due to the poisoning influence of silica species. Scale bars in B) are 5 μm.

Stage 1: Fractal Branching

In general, morphogenesis can be subdivided into two fundamental growth modes which are run through successively depending on the temporally changing conditions in the system.

The origin of each individual architecture, presented in Figure 2.1, relies in the nucleation and growth of elongated $BaCO_3$ microcrystals (Figure 2.7) as soon as the bulk volume gets supersaturated, i.e. when enough CO_2 has entered into the system in solution experiments. Further growth of the single-crystalline core leads to self-similar splitting of the rod-like crystal at its tips (Figure 2.7).[66] These observations are caused by the poisoning influence

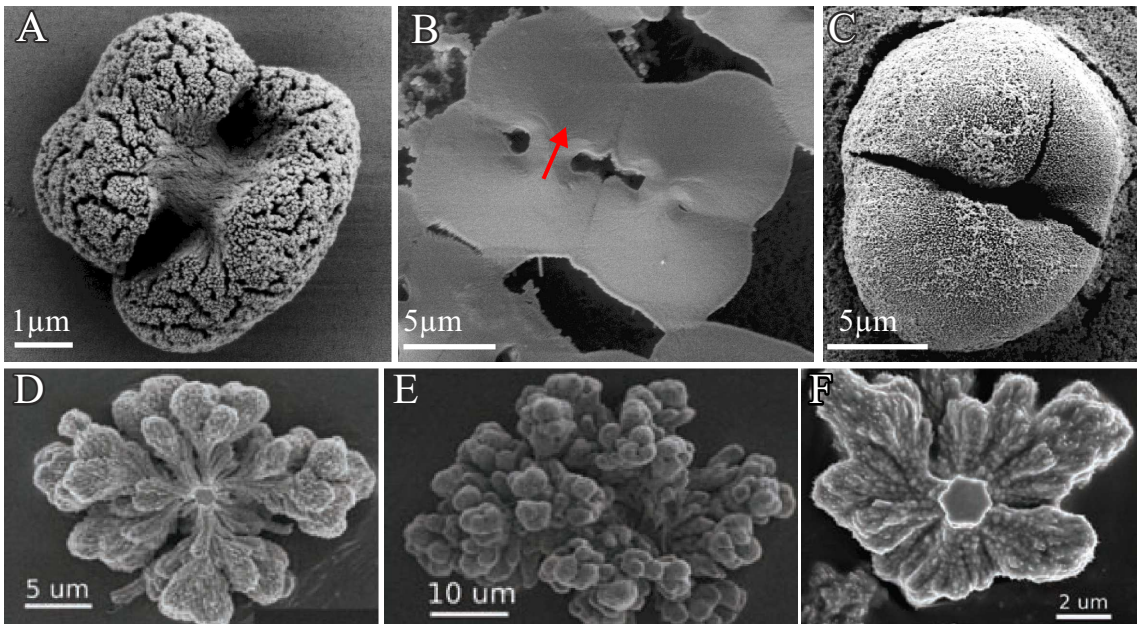

Figure 2.8. Continuous fractal branching in the presence of silica impurities. Initially rod-like witherite crystals successively develop into dumbbell-like aggregates (A-B), yielding closed, spherulithic (C) or even spacious, cauliflower-like architectures (D-F). Scalebars are 1 µm (A) and 2 µm (B-C). (Panels (D-F) adopted from[81])

of partially condensed silica species which act as non-absorbable polymeric impurities, that are pushed ahead of the growth front, generating the formation of misoriented (with respect to the crystalline lattice) two-dimensional "islands".[89] Such a growth mechanism yields at first tilted projections which emanate at non-crystallographic angles, leading to dumbbell-shaped particles which evolve, upon continuous bifurcation, into rather closed spherulithic structures or spacious cauliflower-like architectures (cf. Figure 2.8 E-F), depending on the intensity of branching.[81] The described morphogenetic scenario was observed in all the studies conducted in the context of this thesis (see chapter 5 and 7), but the ultimate experimental evidence that exclusively the silica species is responsible for the ramification of the initial carbonate seed is given in chapter 3. Similar growth mechanisms are also well-documented for fluorapatite crystals, precipitated in gelatin (Figure 2.9).[88,90,91] Here the crystals passed

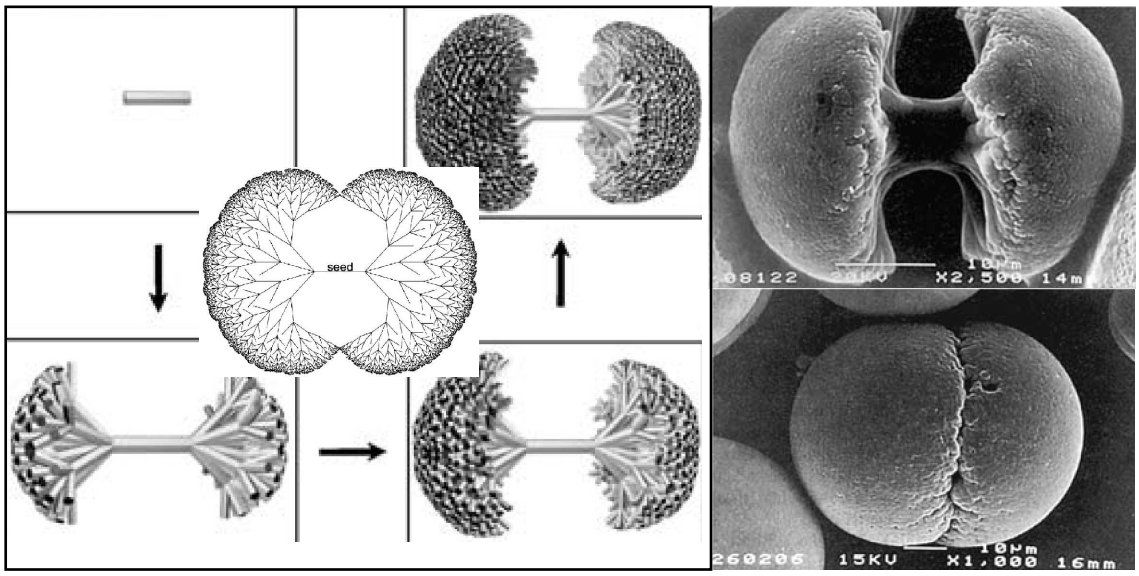

Figure 2.9. Fluorapatite architectures, grown in a gelatin matrix, with dumbbell- and notched-sphere-like morphologies (right), and schematic drawings highlighting their formation mechanism by self-similar branching.[88]

the same morphological transformation from rod-to-dumbbell-to-sphere", due to successive splitting of the parental crystal seed.

Stage 2: Chemically Coupled Co-Precipitation

The presented first stage of biomorph morphogenesis basically occurs roughly within the first 4 h after mixing of reagents.[75] After this period, the silica additive has blocked any active sites for attachment of carbonate units onto the highly branched aggregate, preventing further growth of the fractal architectures. This causes high supersaturation levels of the carbonate species on a local scale, and, as a consequence, myriads of nanocrystals nucleate in a three-dimensional fashion across the whole surface of the locked spherulite. The reason for the spontaneous stabilization and continuous production of nanosized crystallites is principally based on reversed solubility trends of carbonate and silica with pH (silica is soluble at high pH and carbonate at low pH, see Figure 5.14).[81,86] At the given alkaline conditions (pH 9-11) where growth typically occurs, there exist substantially fractions of carbonate and bicarbonate ions in equilibrium. Therefore, nucleation of $BaCO_3$ strongly influences the equilibrium as CO_3^{2-} ions are continuously withdrawn according to: $HCO_3^- \rightleftharpoons CO_3^{2-} + H^+ \xrightarrow{Ba^{2+}} BaCO_3$. Consequently HCO_3^- ions in the near vicinity will dissociate and release a proton in order to balance the short state of local disequilibrium.

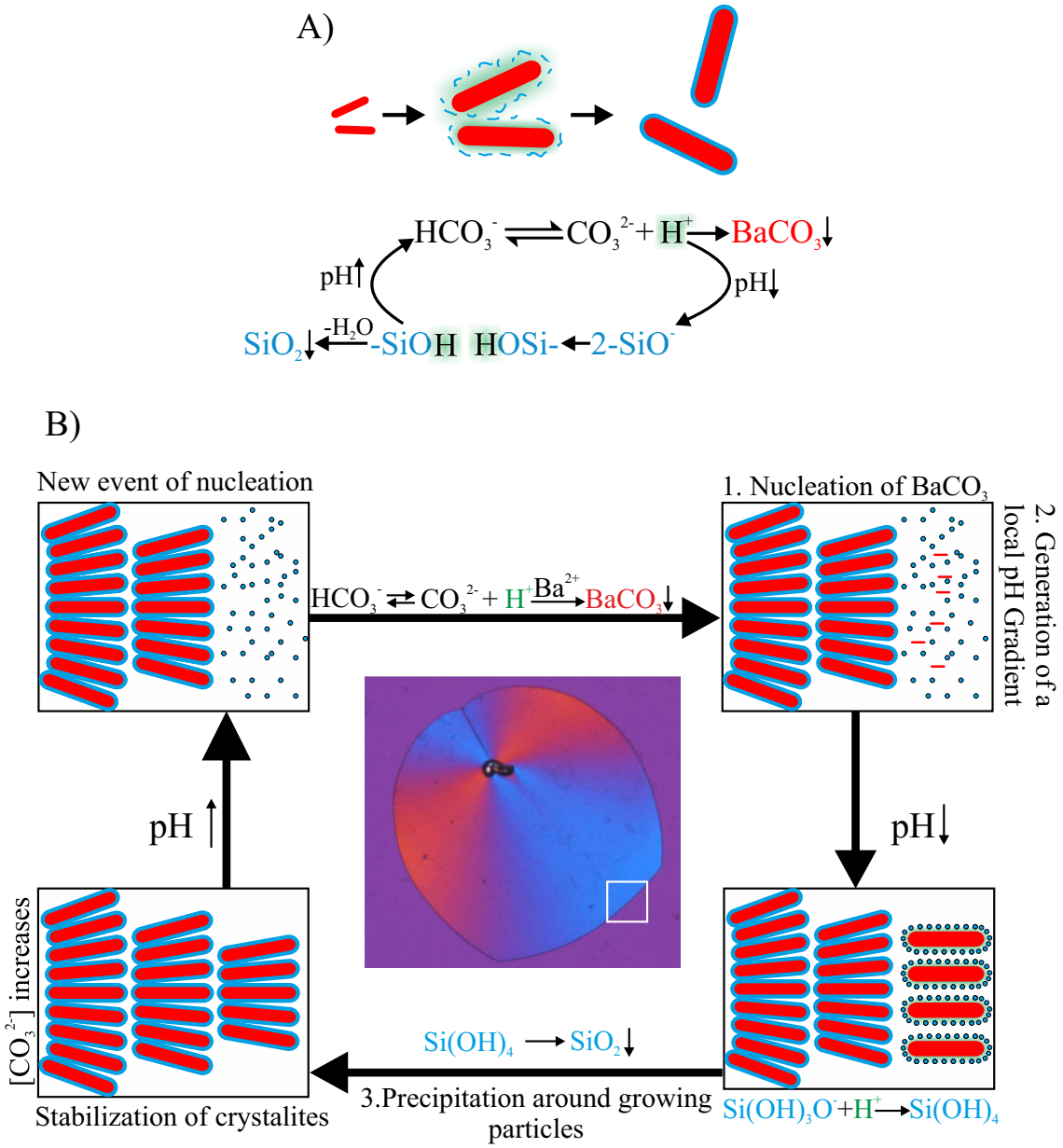

Figure 2.10. The proposed formation model for the continuous production of nanosized crystals, based on the chemically coupled precipitation of carbonate and silicate. (A) During growth of rod-like barium carbonate crystals (red) the pH decreases locally relative to the bulk (gradient highlighted as green shadow) as bicarbonate ions dissociate. This in turn triggers polymerization of silicate which will re-increase the local pH on the growth front, thus raising the supersaturation of $BaCO_3$ in the close vicinity subsequently causing a novel event of carbonate nucleation. (B) Overall, a loop process is generated in which the involved components alternately precipitate. In this way, building units for the construction of silica biomorphs are continuously produced.

However this provokes a local pH gradient relative to the bulk around the as-nucleated carbonate particles, (Figure 2.10A, green shaded area around growing barium carbonate par-

ticles) which in turn has drastic influence on the solubility of the silica species (cf. Figure 5.14) nearby the just nucleated carbonate nanoparticles. As a result, silica polymerizes locally around the surface of the developing crystals, forming coating layers and thus preventing particles from further growth beyond the nanometer scale. Targeted precipitation of SiO_2 in the vicinity of the carbonate units is in principle achieved by protonation of acidic silanol groups (caused by previously dissociated protons) which become subject to condensation reactions, inducing polymerization of silica according to the following sequence: $2-Si-O^- + 2\,H^+ \rightleftharpoons$ -Si-O-Si- $\xrightarrow{-H_2O}$ $SiO_2\downarrow$ (see Figure 2.10). In contrary, these reactions will re-increase the local pH (relative to the bulk) again , thus re-shifting the carbonate/bicarbonate equilibrium towards higher fractions of CO_3^{2-}. This also elevates the carbonate supersaturation in close vicinity of freshly generated carbonate/silicate nanoparticles, therefore triggering a novel event of barium carbonate nucleation (Figure 2.10A). In this way, an autocatalytic loop process is generated where involved components are alternately mineralized, leading to continuous production of uniform building units, which arrange spontaneously, by a still unknown process, to elaborate architectures with sinuously shaped surfaces. The presented mechanism is summarized in Figure 2.10B.

With regard to the envisaged formation model, the particular bulk pH in the growth media plays an essential roles during morphogenesis, as it strongly influences the speciation of involved components. To induce the dynamic interplay between carbonate and silica, certain bulk pH dependent requirements have to be fulfilled, as recently demonstrated for morphogenesis in silica-gel setups.[72] This issue will be furthermore discussed in the framework of the thesis for growth of silica biomorphs from stagnant solutions (chapter 5).

Experimental indications for the theoretical formation model

Despite of the nuerous studies performed up to now the presented scenario for the continuous production of silica stabilized carbonate rods has still mainly a theoretical background. The proposed model implicates however an oscillatory local pH at the growth front, as this parameter is coupled with the alternating mineralization of the two components. Such periodic pH variations are though reduced to the region of active growth which extends only over some microns, as deduced from experiments in stirred solutions.[87] A direct experimental evidence for the proposed model of autocatalytic growth lies in the *in-situ* recording of

the postulated pH oszillations. A promising strategy, followed in the course of the thesis, was to measure the pH in the close vicinity of just-growing biomorphs, utilizing special dyes in combination with a UV-Vis microscope. First experiments using mixtures of UV-active pH indicators did unfortunately not yield the expected results, which was primary based on the insufficient spacial resolution of the instrumental setup.

Apart from that, further attempts to explain the spontaneous stabilization of carbonate nanorods were put forward in terms of crystallographic arguments by Aquilano et al.[85] In this work the miniaturization of carbonate units is ascribed to epitaxially matching of α-quartz on witherite surfaces. Thus adsorption of silicate (which exists in case of biomorphs rather in the amorphous form) onto $BaCO_3$ faces via attachment of single chains or formation of 2D islands is energetically favored. Such interactions are also certainly important for the generation of extended silica sheaths around individual building units.

In the scope of the proposed pH oscillations, recent studies following a different approach, demonstrated that specific, pH induced interactions between carbonate and silicate can in fact trigger local SiO_2 precipitation around growing ACC particles at alkaline conditions, (Figure 2.11a) strongly influencing the crystallization process.[92] In contrast to the preparation methods presented for biomorphs, the experiments were carried out at higher supersaturation via direct mixing of solutions ($CaCl_2$ and dissolved SiO_2 containing carbonate). Corresponding TEM images and micro-EDX spectra (Figure 2.11) of early stage particles clearly evidence that ACC nanograins become coated by extended silica layers upon pH-coupled co-precipitation. The thickness of the skins could be furthermore tuned by varying the silica concentration in the reactive solutions. Results deduced from this investigation can be regarded as fundamental support for the proposed growth mechanism, as local pH gradients provoked by homogenous nucleation of carbonate particles leads to silica polymerization all over their surface. Those results gave additionally the motivation for a study conducted in this thesis following a similar procedure, but replacing calcium by barium in order to investigate if similar tendencies are apparent at the given high (and defined) carbonate supersaturation. Results of these experiments are given in chapter 3.

In view of the still quite hypothetical model for the formation of silica biomorphs, external silica skins, as clearly detected in case of homogeneous nucleated ACC particles from

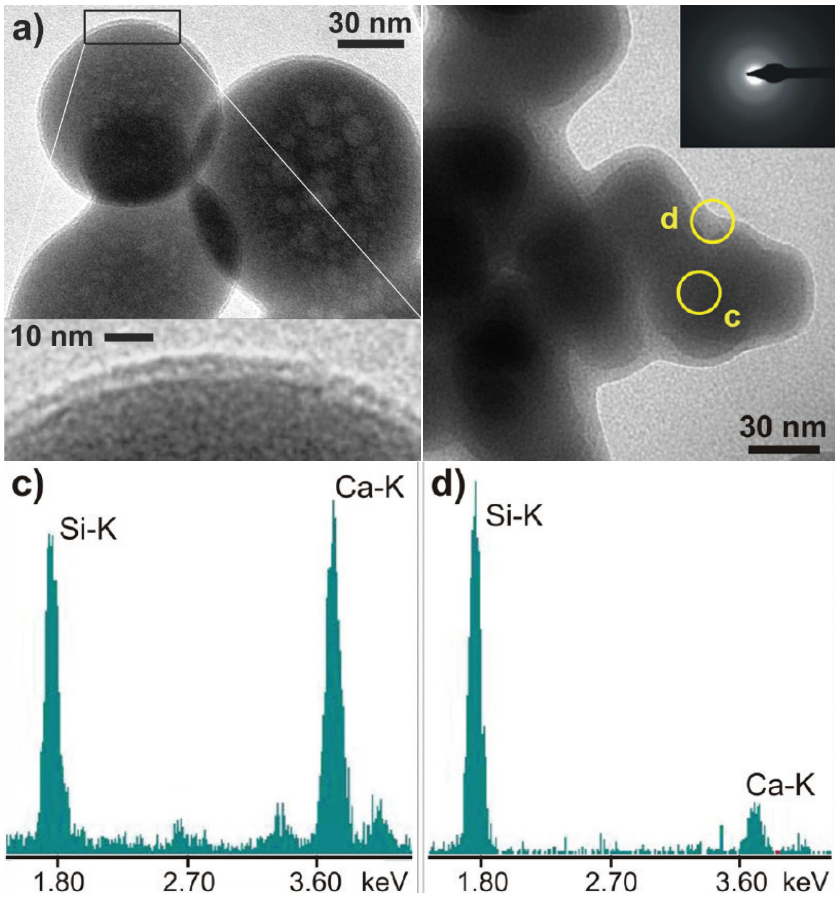

Figure 2.11. Amorphous $CaCO_3$ nanoparticles with silica skins yielded via direct mixing of $CaCl_2$ and SiO_2 containing carbonate solutions at high alkaline pH. EDX-microanalysis of the two different layers reveals that the core of the particles is enriched in $CaCO_3$ while the outer layer mainly consists of silica. (adopted from[92])

silica containing, should also be detectable for nanorods constituting biomorphs. However published data concerning this issue are ambiguous, as silicon counts are present when performing micro-EDX studies on individual building units of biomorphs but pronounced silica skins could not be verified on TEM micrographs (see also Figure 2.5A).[61,75] Further hints were given by Terada et al. in a recent publication where distinct silica coatings around the building units of silica biomorphs grown in gel were postulated. However final evidences supporting this notion were not given.[82]

In order to shed further light on the detailed role of silica during the generation of nanoscale barium carbonate, an experimental procedure was utilized in this thesis which was aimed on the targeted production of $BaCO_3$ nanorods (in the presence of silica), at conditions in

terms of reactant concentrations and pH where biomorphs are usually observed (see chapter 4). This was achieved with the help of a titration based assay in combination with an ion selective electrode (ISE) sensitive for Ba^{2+}. In a recent work by Gebauer et al.,[93] this method was employed to get fundamental insights into the early stages of $CaCO_3$ precipitation using an ion selective electrode (ISE) sensitive for Ca^{2+}. Presented findings lead to novel views on the nucleation of calcium carbonate in general, as so called *prenucleation clusters* were detected, being a thermodynamically stable phase existing in equilibrium with dissolved ions occurring prior to the formation of a solid phase. The applied experimental technique also enables detailed views on the influence of certain additives during different stages of calcium carbonate crystallization.[94–97] In this case, interactions between involved components are discussed on basis of certain characteristics of the temporal development of the free calcium concentration during addition of $CaCl_2$ to a carbonate buffer, containing the respective additive at constant pH. Exemplary curves for the time dependent development of

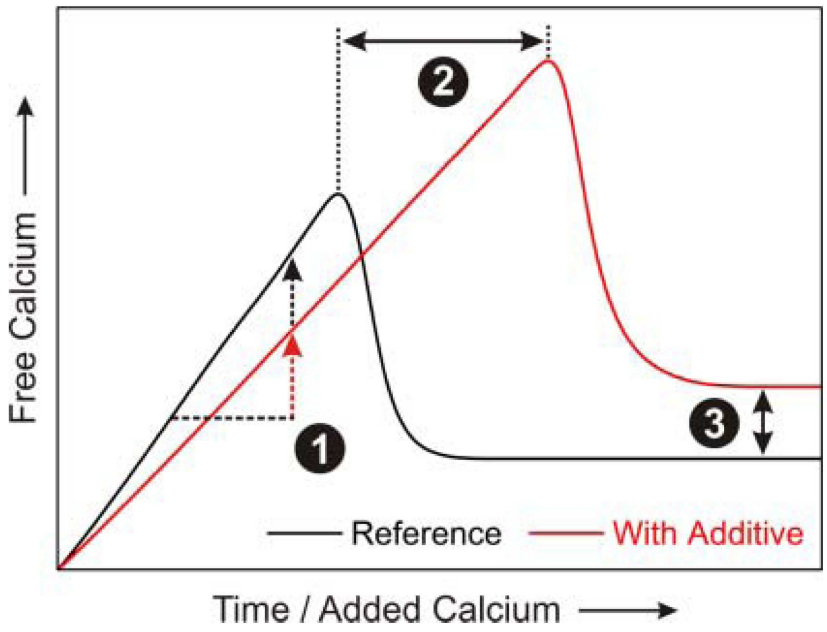

Figure 2.12. Temporal development of the amount of free Ca^{2+} ions, monitored during continuous addition of $CaCl_2$ into a carbonate buffer in the presence and in absence of additives. Typical characteristics of these plots were used to describe the role of the respective additive on the nucleation of calcium carbonate. Stage 1: Slope of the linear increase during the prenucleation stage indicates the fraction of Ca^{2+} bound in clusters and thus the apparent stability of prenucleation clusters. Stage 2: Time of nucleation which is usually retarded in the presence of additives. Stage 3: Level of free calcium in the postnucleation stage, therefore representing the solubility of the initially precipitated phase.[97]

the free calcium potentials in the absence and in the presence of additives (in this case amino acids[97]) are presented in Figure 2.12. At first, a linear increase of free Ca concentration is visible, since calcium chloride is continuously added to the buffer solution. In this regime the concentration of free Ca^{2+}ions was always found to be somewhat lower than the dosed amount, being a result of equimolar binding of Ca^{2+} and CO_3^{2-} ions in stable prenucleation cluster.[93,98] When the curve reaches its maximum, a solid phase nucleates and consequently the amount of free calcium drops to a level that corresponds to the solubility of the precipitated $CaCO_3$ phase. This plateau remains virtually unchanged upon further addition of calcium which is related to the presence of two different phases in equilibrium. As depicted in Figure 2.12, the curve exhibits certain characteristics which allows to interpret the influences of the additive on the nucleation: (1) Slope in the linear part of the titration curve reflecting the stability of prenucleation clusters. (2) Point of nucleation, visible as maximum of the peak and (3) Level of solubility (ion product), in most cases observed immediately after nucleation when the solid phase is in equilibrium with the surrounding solution. All these parameters were found to be strongly influenced by additives in case of calcium carbonate precipitation.[94–97] However, a detailed study on silica-related influences on all of these parameters during precipitation of $BaCO_3$ is given in chapter 4.

2.1.5 Phenomenological description of morphology development

While continuous production of nanoscale building units is explained by a chemically coupled co-precipitation mechanism, morphogenesis of characteristic architectures on macroscopic length scales depends on even more delicate factors, as recently proposed by García-Ruiz et al.[81] Virtually all complex curved architectures displayed by silica biomorphs, initially arise from globular units, yielded during the first stage of morphogenesis via continuous branching of parental crystal seeds. In the second stage, quasi-2D laminar segments with nearly radial symmetry, being composed of myriads of nanosized carbonate crystallites, start to sprout out from the globular units (Figure 2.13A). Recent investigations with time-lapse video microscopy revealed that the radial growth velocities (V_ρ, see Figure 2.13C) are equal in all directions (typically some microns per minute) which is the reason why the growing aggregate adopts the shape of a circular disk (cf. Figure 2.5).[61,75,81,86] Interestingly, the main part of the evolving sheets develop scrolled margins, either pointing down- or upwards

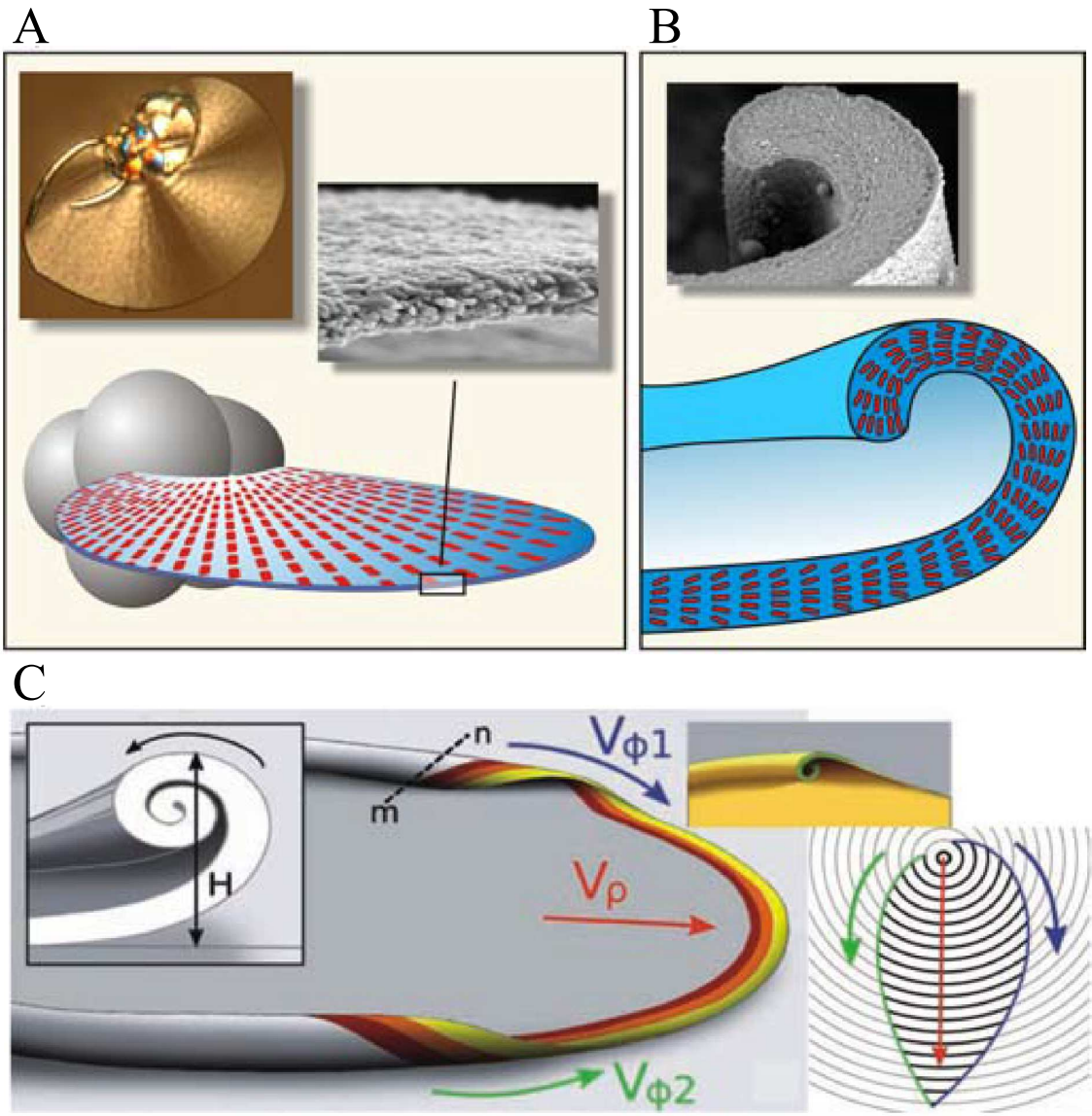

Figure 2.13. Illustration of the macroscopic growth behavior of silica biomorphs. (A) After formation of closed spherulites (indicated as grey globules), thin, polycrystalline leaf-like segments start to sprout out which are composed of myriads of nanorods, generated by chemically coupled co-precipitation. (B) Continuous laminar growth proceeds until curvature is induced, as the sheet becomes scrolled at some point around its perimeter. (C) After formation of scrolled margins, growth in radial direction (V_ρ) arrests, and curls propagate tangentially along the rim of the sheet with azimuthal growth velocities $V_{\varphi 1}$ and $V_{\varphi 2}$ usually yielding cardoid architectures. The relative height H and the relative handedness of two distinct curls thereby determine the occurrence of more twisted morphologies like helicoids or worms.[61,81,86]

at arbitrary positions on the rim (Figure 2.13B). Therefore, these singular curling events introduce curvature to the system and serve as starting points for the morphogenesis of highly twisted shapes.[81] Such curls were proposed to propagate along the perimeter of the leaf-like

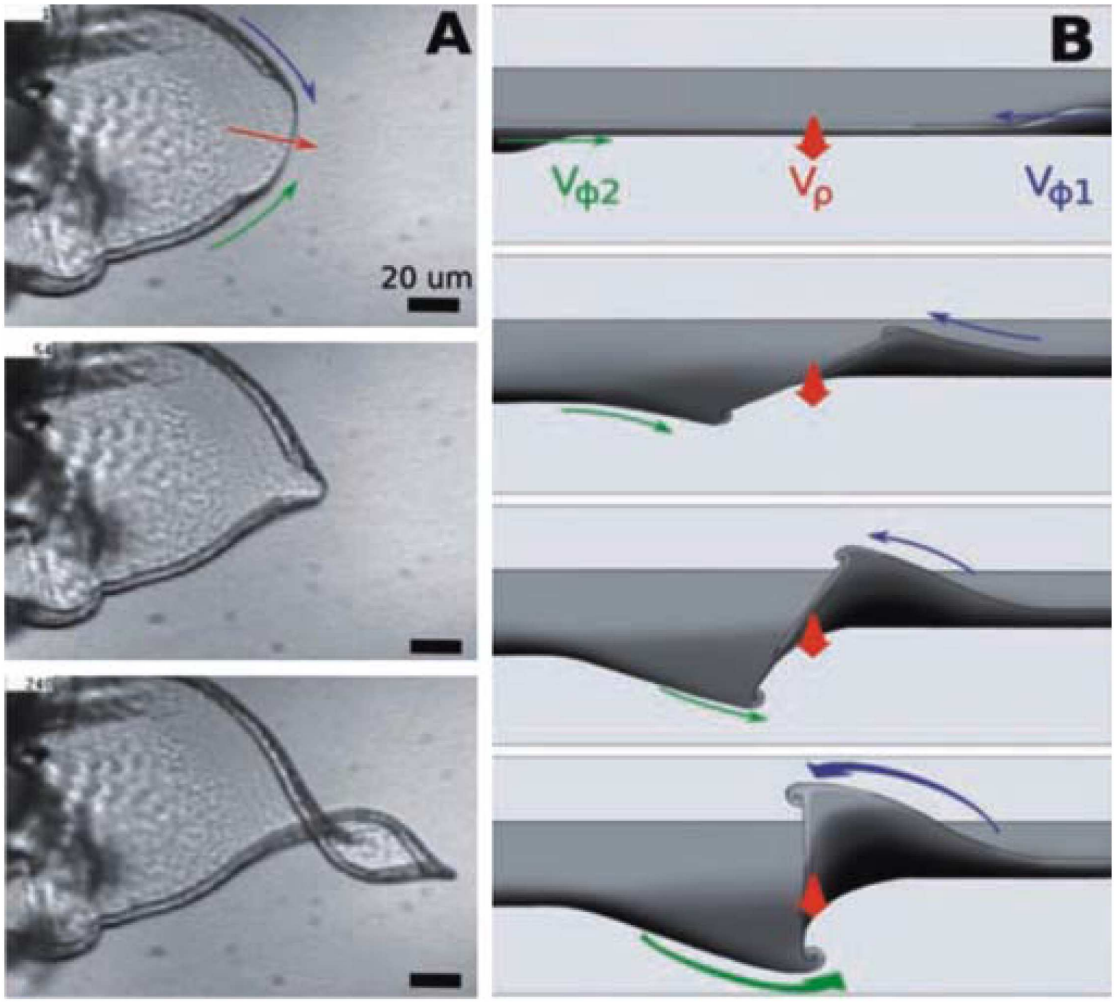

Figure 2.14. Morphogenesis of a helix. (A) Sequence of optical micrographs in which curled segments with equal handedness gradually approach from different directions (the upper curl bent towards the camera, lower curl bent downwards) and meet at the cusp. Both segments intertwine and produce a regular helix upon further growth along the radial direction (indicated by the red arrow). (B) Scheme showing the front-view of the same scenario where two like-handed curls with the same height H and azimuthal growth velocities $V_{\varphi 1}$ and $V_{\varphi 2}$ lock-in to produce a helicoid.[81] (images reproduced from[61])

morphologies in a manner reminiscent of a surfing wave (Figure 2.13C).[61,81] At this point, growth arrests along the radial pathway and a new growth front is generated that propagates orthogonally to the previous circular direction. As in case of the radial growth front, the velocity of tangential propagation ($V_{\varphi 1}$ and $V_{\varphi 2}$, see Figure 2.13C) is also approximately constant, nevertheless the absolute values of $V_{\varphi 2}$ and $V_{\varphi 2}$ were found to be slightly higher than V_{ρ}.[75,81] Therefore the initially circular shape becomes distorted and the leaf-like objects form one or more cusps at positions where two curled segments arrive from opposite direc-

tions. However, this morphogenetical pathway is not only limited to the growth of sheet-like objects with cardioid shapes. The question whether the final aggregate will adopt a twisted shape, as displayed by helicoidal or worm-like architectures is strongly related to the relative velocities of azimuthal and radial growth and to the handedness and height of the curled segments, as described in detail by García-Ruiz et al.[81] A scenario, that exemplarily describes the formation of a helix is presented in Figure 2.14. The sequence shows a case, where two curled segments with equal directionality (one bent downwards the other upwards) and height approach at a cusp from opposite sides of the sheet segment. When the two curls collide, they will intertwine and wind around each other (cf. Figure 2.14B). Upon further growth in radial direction, the induced twist is retained, and due to continuous winding (dictated by the curled rims) a nearly perfect helicoid is formed.[61,81] In contrast, when the height difference between two curls is drastically pronounced and on of them grows faster, a situation arises in which the higher curled segment prefers curling around itself, resulting in a worm-like morphology.[81]. However, a still open question in this context is the origin of curvature, i.e. why do initially flat sheets start to curl at a certain point along the rim? Possible answers to this question are given in chapter 6.

2.1.6 Biomorphs with $SrCO_3$ and $CaCO_3$

The stunning crystal architectures presented in the sections above are, however, not only limited to $BaCO_3$. Replacing this metal ion by strontium yields widely identical biomorphic objects to those observed with barium carbonate (witherite).[59] Indeed, Terada et al.[82] isolated petal-like objects (Figure 2.15A-C) when growth of strontianite biomorphs was performed in silica gels at high pH. Upon further growth, complex wounded helical ribbons formed sporadically at the tips of the petals (Figure 2.15E).[82] Close-up views on the aggregates revealed, in contrast to witherite biomorphs, rather fibrous subunits which are individually sheathed by siliceous skins.[82] As in case of silica-gel setups, crystallization of silica-strontianite biomorphs from solution results in aggregates with morphologies as observed with $BaCO_3$ (see Figure 2.15F, and chapter 7). These findings imply that only carbonate minerals with aragonite-type lattices are able to produce biomorphs when crystallization is carried out in silica gels or sols. This requirement is fulfilled for strontianite and witherite (orthorhombic lattice, space group Pmcn) at room temperature. However, $CaCO_3$, the mineral

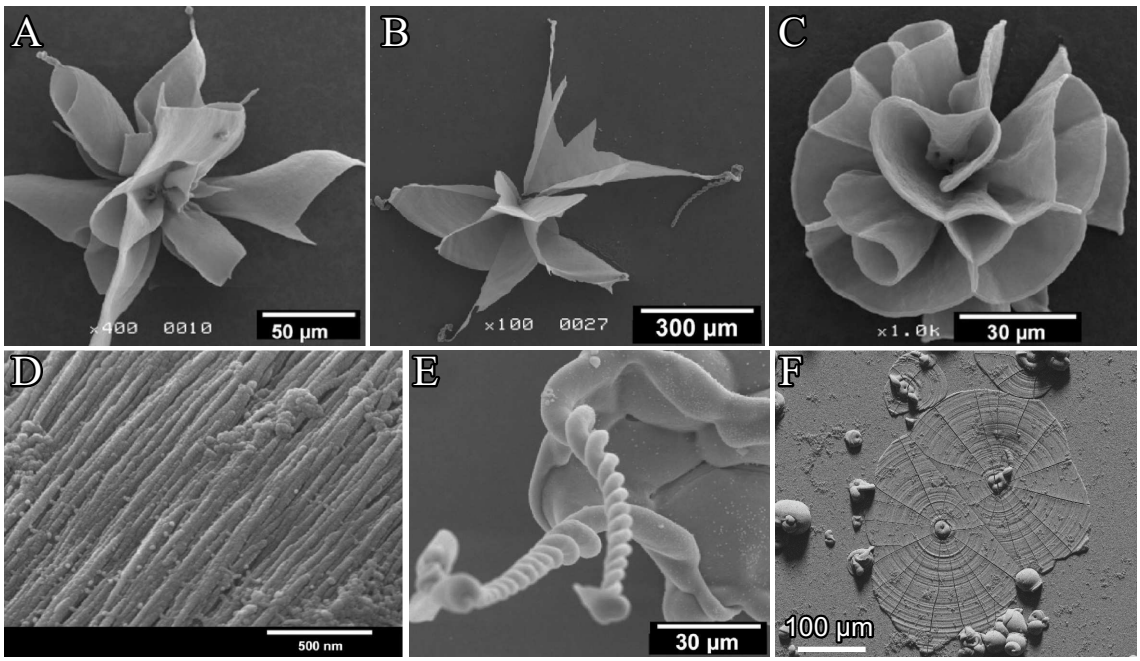

Figure 2.15. Silica biomorphs composed of $SrCO_3$ (strontianite). (A-E) Morphological variety observed in gel setups at pH 10.5. (A-B) Petal-like products from which helicoids (E) emerge upon further growth. (C) Close-up view revealing the texture of observed crystal architectures. (F) Leaf-like objects grown in direct contact with the substrate observed when synthesis is carried out in solutions. (A-E reproduced from[82])

of utmost interest among the alkaline-earth carbonate series, forms predominantly rhombohedral calcite crystals at ambient conditions (due to the smaller size of the cation). Thus, corresponding precipitates in silica rich environments did not yield biomorphs in the true sense, since characteristic morphologies like helicoids or worms remained absent. Instead, biomimetic aggregates with finger-like structures[60] or bundles reminiscent of natural sheaf of wheat[99,100] (Figure 2.16) or even spherulithic single crystals displaying unusual three-fold symmetry were obtained.[101] In contrast to aggregates observed in case of strontianite and witherite, morphogenesis of the calcite architectures is not explained by coupled co-precipitation of silica and carbonate, but rather via selective adsorption of silicate species on specific crystallographic planes causing changes in the relative growth rates of distinct calcite faces.[99–101] In this way, the rhombohedral crystal habit becomes elongated along the c-axis and develops subunits with a three-pointed star-like appearance (three wings arranged at mutual angles of $\sim 120°$, see inset of Figure 2.16C).[61,70,101]

In opposite, $CaCO_3$ biomorphs with mainly coral-like appearance precipitated, when the

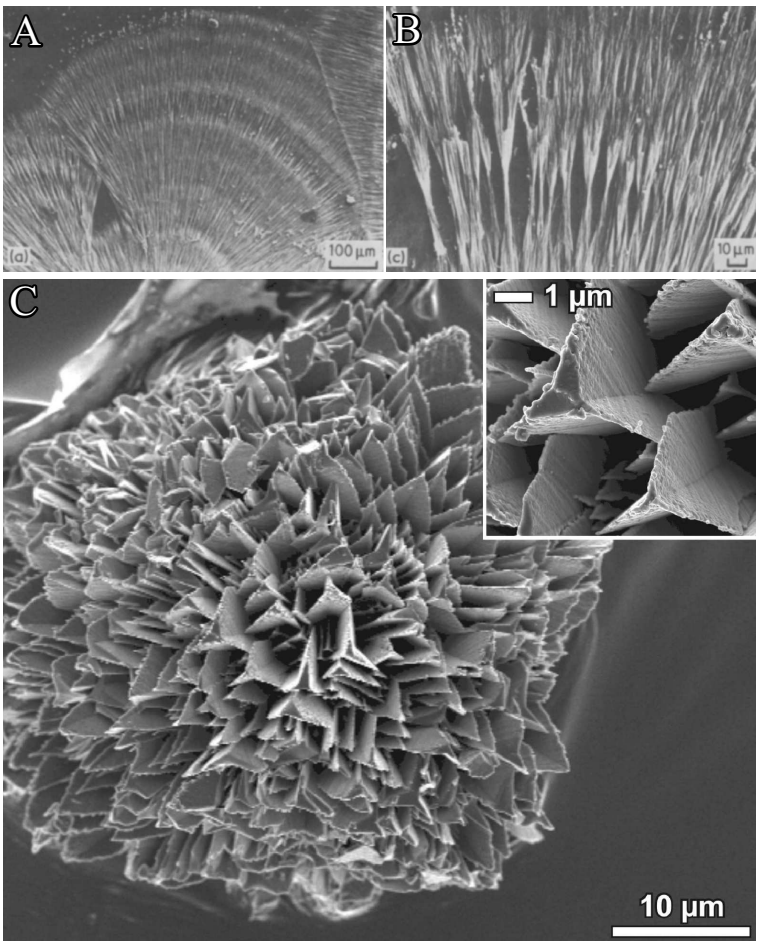

Figure 2.16. (A-B) Radially arranged sheaf of wheat bundles observed when $CaCO_3$ crystallization is carried out in silica gels at alkaline pH (reproduced from[99]. (C) Complex calcite architectures with unusual threefold symmetry observed at high carbonate supersaturation due to selective adsorption of silicate species on certain planes of the calcite lattice.[101]

conditions were adjusted in order to shift the $CaCO_3$ polymorph selection in the direction of aragonite, indicating that the mineralogy (i.e. orthorhombic lattice) is an important parameter for the production of sinuously shaped carbonate architectures in silica matrices.[61] One strategy in this context is to increase the synthesis temperature to $80°C$ since the aragonite modification becomes kinetically favored over the calcite polymorph at these conditions. This was successfully accomplished by Voinescu et al.,[84] and hierarchically structured morphologies reminiscent of natural coralline shapes or architectures with flower-like appearances were isolated from diluted silica sols (Figure 2.17B-D).[84] Similar aggregates (cf. Figure 2.17A) were observed by Imai et al. in silica gels where growth was induced utilizing aragonite seed crystals at ambient conditions.[83] Likewise, preliminary work, perfromed by Bittarello et al., demonstrated the spontaneous presence of aragonite biomorphs in silica gels at specific con-

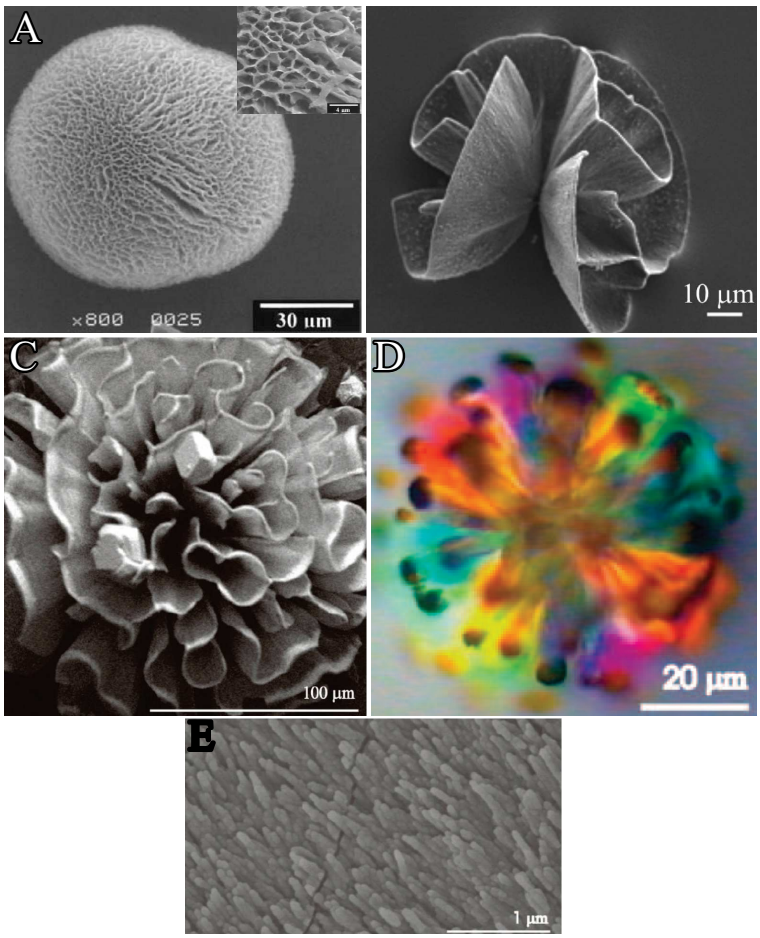

Figure 2.17. $CaCO_3$ biomorphs. (A-D) FESEM and polarized optical micrographs of aragonite aggregates with coral-like morphologies synthesized in (A) silica gel at pH 10.5[83] or (B-D) in diluted silica sols[84] at 80°C. (E) Hierarchical ordering of aragonite subunits of coral-like morphologies.[84]

ditions in terms of pH and reagents concentration and location in the gel.[85] A potential novel strategy to produce $CaCO_3$ biomorphs at room temperature via a simple one-pot route without the need of external aragonite triggers (like seed crystals) was to work with mixtures of calcium and barium or strontium. Findings of this study are given in chapter 7.

3 Bottom-Up Self-Assembly of Amorphous Core-Shell-Shell Nanoparticles and Biomimetic Crystal Forms in Inorganic Silica-Carbonate Systems

3.1 Abstract

Mineralization of alkaline-earth carbonates in silica-rich media at high pH leads to fascinating crystal morphologies that strongly resemble products from biomineralization, despite the absence of any organic matter. Recent work has demonstrated that elaborate $CaCO_3$ structures can be grown in such systems even at high supersaturation, as nanoparticles of amorphous calcium carbonate (ACC) were spontaneously coated by skins of silica, which decelerated their re-dissolution and thus served as storage depots continuously supplying growth units for the formation of crystalline calcite. In this chapter barium carbonate was precipitated under similar conditions and surprisingly different behavior was detected. At low silica concentrations, there was no evidence for an amorphous carbonate precursor phase and crystallization occurred immediately, resulting in elongated crystals that showed progressive self-similar branching and bifurcation due to the poisoning influence of silicate oligomers on the growth process. Above a certain threshold in the silica content, rapid crystallization was in turn prevented and amorphous nanoparticles were stabilized in solution.

However, in contrast to previous observations made for $CaCO_3$, the particles were found to be hybrids consisting of a silica core that was surrounded by a layer of amorphous barium carbonate, which then again was covered by a an outer shell of silica. These self-assembled core-shell-shell nanoparticles were characterized by different techniques, including high-resolution transmission electron microscopy and elemental analyses at the nanoscale. Studies of the time-dependent behavior of the samples further evidence that the carbonate component in the particles can either be permanently trapped in an amorphous state (high silica concentrations, leading to impervious outer silica skins), or be released gradually from the interstitial layers into the surrounding medium (intermediate concentrations, giving porous external shells). In the latter case, enhanced particle aggregation induces segregation of silica hydrogel with embedded amorphous $BaCO_3$ precursors, which later crystallize in the matrix to yield complex ultrastructures consisting of uniform silica-coated nanorods and displaying intricate biomimetic morphologies on the micron-scale. The spontaneous formation of core-shell-shell nanoparticles and their subsequent development in the system is discussed on the basis of local pH gradients and inverse pH-dependent trends in the solubility of carbonate and silica, which link their chemistry in solution and provoke coupled mineralization events. The findings depict a promising strategy for the production of multilayered nanostructures via a facile one-pot route, which is based on self-organization of simple components and may be exploited for the design of novel advanced materials.

3.2 Introduction

One of the key tasks in the world of material science is to investigate new processing routes for the fabrication of advanced materials. A frequently used approach to achieve this is to mimic strategies applied by Nature to produce materials with hierarchical structure and superior, task-specific properties. Living organisms control their crystallization processes by using certain biopolymers as well as functional matrices,[6,8,13,16] which may direct nucleation, regulate the size and polymorphism of crystallites, and trigger concerted aggregation of stabilized particles. In the past years, research on biomimetic mineralization in vitro has demonstrated the existence of alternative crystallization pathways where, unlike the classical picture, crystal growth proceeds via (oriented) attachment of primary nanoparticle units,[54,102,103]

rather than simple ion-by-ion addition, potentially leading to higher-order superstructures of small building blocks.[49,51,104] For example, it was shown that synthetic organic polymers, capable of interacting with the as-formed particles and temporally stabilizing them at colloidal dimensions, can induce self-organization of the building units on the mesoscale and prevent their fusion to a single crystal. This has been realized for a wide variety of minerals,[44] including calcium carbonate[43] and barium carbonate[44,46] with the aid of tailored block copolymers. Among the carbonate minerals, $CaCO_3$ is the most intensively studied one as it represents the major inorganic constituent in many biogenic materials. During biomineralization of $CaCO_3$, its metastable amorphous form (ACC) was often found to serve as a solid precursor for the mature structures in the course of crystallization from solution, as for instance in the case of the spicules, spines, and teeth of sea urchins.[7,105,106] The absence of crystalline order appears advantageous because amorphous matter can be molded into virtually any shape, which ideally will remain after crystallization and thus yield crystal morphologies far beyond euhedral symmetry restraints. While the temporary occurrence of ACC in vivo seems to be regulated by certain proteins (often in combination with magnesium ions)[107–109] or via entrapment in vesicles,[110,111] successful stabilization in synthetic systems was achieved by introducing organic additives like amphiphilic dendrimers,[112] block copolymers,[113] polycarboxylates,[38,114] polyphosph(on)ates,[115–117] and others.[118–122] Recent studies have shown that the transformation of metastable ACC into crystalline polymorphs can also be controlled in purely inorganic systems, namely by using sodium silicate as a soluble additive in alkaline reaction media.[92,101] Under these conditions, ACC is kinetically stabilized as silica precipitates spontaneously on the surface of nucleated carbonate particles, forming a skin that impedes re-dissolution of the amorphous phase. Coating of ACC by silica was thereby ascribed to a local decrease of pH (relative to the alkaline bulk) in the vicinity of evolving ACC, caused by dissociation of bicarbonate ions upon growth of $CaCO_3$ ($Ca^{2+} + HCO_3^- \longrightarrow CaCO_3 + H^+$). This provokes successive condensation, polymerization, and precipitation of silica nearby the ACC surface ($SiO(OH)_3^- + H^+ \longrightarrow Si(OH)_4 \longrightarrow$ "SiO_2" + 2 H_2O), leading to composite particles with a carbonate core and a silica shell. Furthermore, the porosity of the outer silica skin and, with it, the degree of ACC protection was found to depend on the amount of added silica, ranging from temporary stabilization over hours to permanent conservation

in the long term.[92] These findings are consistent with the results of independent studies on the role of the silica content for the stability of the ACC component in biomineralized plant cystoliths.[123,124]

pH-based interactions between growing carbonates and dissolved silicate species as those described above are however not limited to the formation of amorphous core-shell particles, but can also be used to assemble nanosized crystalline units into complex meso- and micron-scale architectures. This is documented in great detail for the higher homologues in the alkaline-earth carbonate series, i.e. $SrCO_3$ and in particular $BaCO_3$.[59–63,67–69,74–76,80–82,85–87,125] Indeed, gradual crystallization of these minerals in silica-rich media (gel or solution) at elevated pH was reported to yield unique non-crystallographic morphologies, including regular helicoidal filaments, which self-assemble spontaneously if the supersaturation is kept at moderately high levels over extended periods of time. These so-called silica biomorphs were further shown to consist of uniform carbonate nanorods, arranged according a specific long-range orientational order on the mesoscale.[61,67,75,80] Crystal aggregates exhibiting a related mode of construction, but different morphologies, were obtained also for calcium carbonate.[84,126]The morphogenetic mechanism underlying the formation of these complex materials has been unraveled recently:[61,81,86,87] it was suggested that, as in the case of the ACC particles, stabilization of nanometric building units is accomplished by pH-induced polymerization of silica all over their surface, preventing further growth and ripening (even though distinct silica skins could not be observed on the crystallites to date).[61] However, in contrast to silica coating of ACC (where all available carbonate is consumed during the initial precipitation step),[92] the interplay between silica and carbonate is not terminated at this point as further material for growth is continuously provided by diffusion processes in the experiments (either CO_2 uptake in silica solutions or Ba^{2+} diffusion into silica gels).[75] Consequently, new carbonate nucleation takes place, and these nucleation events indeed occur preferentially in the vicinity of previously formed crystallites, because ongoing silica polymerization around them now increases the local pH as acidic silanol (-Si-OH) groups vanish in the course of condensation. This leads to an increase in the local supersaturation of carbonate and eventually triggers nucleation of new $BaCO_3$ nanoparticles, which again are covered by silica due to local pH gradients. The whole process is then re-iterated

such that, overall, the pH at the growth front oscillates up and down, causing carbonate and silica to be alternately mineralized due to their reversed solubility trends with pH under alkaline conditions.[81,86,87] In this way, elaborate superstructures of silica-decorated carbonate nanocrystals are generated by dynamic bottom-up self-assembly of simple components.

This chapter demonstrates that by slightly changing the experimental protocol, co-mineralization of barium carbonate and silica can be tuned to afford complex core-shell-shell particles in a straightforward one-pot synthesis. In particular, $BaCO_3$ was precipitated by directly mixing $BaCl_2$ and Na_2CO_3 at nominally high supersaturation and in the presence of varying amounts of sodium silicate. As for calcium carbonate,[92] sufficiently high silica concentrations lead to stabilization of amorphous nanoparticles, which either persist in solution or serve as precursors for the formation of biomorphic ultrastructures. However, unlike the $CaCO_3$ case, these nanoparticles are found to consist of a silica core, which is surrounded by a layer of barium carbonate that in turn is coated by an outer skin of silica.

3.3 Experimental section

3.3.1 Materials

Barium chloride dihydrate (Sigma-Aldrich, $\geq$ 99%) and sodium carbonate (Roth, anhydrous, $\geq$ 99%) was used as received without further purification. The silica source was a commercially available water glass (Sigma-Aldrich, $\sim$13.7 wt% NaOH, $\sim$12.5 wt% Si). All solutions and dilutions were prepared with water of Milli-Q quality, which was bubbled over night with N_2 before use in order to remove dissolved CO_2. The final SiO_2-containing solutions were stored in tightly stoppered plastic bottles to avoid silica contamination from the walls of glass vials and prevent progressive uptake of atmospheric CO_2. All experiments were performed at a temperature of $20 \pm 1°C$.

3.3.2 Precipitation Experiments

Precipitation of barium carbonate was initiated by rapidly mixing equal volumes (usually 5 mL) of 10 mM barium chloride and 10 mM sodium carbonate solutions, with the latter containing different amounts of sodium silicate. The silica/carbonate mixtures were prepared by dissolving Na_2CO_3 in CO_2-free silica sols, obtained by diluting commercial water glass

stock in appropriate ratios with water (dilution factors ranging from 1:100 to 1:1400 (v/v)). The final silica contents in the samples after mixing were 0, 135, 270, 370, 540, 750, 920, and 1870 ppm SiO_2 at a constant concentration of 5 mM for both $BaCl_2$ and Na_2CO_3. This corresponds to molar silica concentrations of 0, 2.2, 4.4, 6.0, 8.8, 12.2, 15.0, and 30.5 mM, or Si/Ba molar ratios of 0, 0.44, 0.88, 1.20, 1.76, 2.44, 3.00, and 6.10. Immediately after combining reagents, the samples were sealed and allowed to age under quiescent conditions at ambient temperature.

3.3.3 Analytical Methods

Visual observations

In a first set of experiments, the time-dependent development of the samples was observed visually. For this purpose, time-lapsed photograph series were taken with a remote-controlled Canon EOS 350D digital camera.

pH measurements

The temporal evolution of the pH in the samples was followed by using a glass microelectrode (Mettler-Toledo, InLab Micro) that was immersed in the solutions straight after mixing of reagents. The electrode was connected to a Schott CG-843 laboratory pH meter and values were read out automatically in an interval of 5 sec for a total period of 30 minutes.

Scanning electron microscopy (SEM) and energy-dispersive X-ray (EDX) spectroscopy.

For SEM studies, the isolated dried precipitates were transferred onto conducting double-sided adhesive carbon tapes, which were fixed on standard aluminum pin stubs. Prior to analysis, specimens were coated with a thin layer of platinum, using a Balzers MED 010 sputter coater. Samples were studied on either a Zeiss LEO Gemini 1530 FESEM or a FEI Quanta 400 T microscope, operated at acceleration voltages ranging from 2-10 kV and a working distance of 4 mm. EDX measurements were carried out at an acceleration voltage of 10 kV with the aid of an installed Oxford INCA microanalysis system. Spectra were recorded from not less than three different positions on the stub, and results were averaged for a given specimen.

Transmission electron microscopy

Nanoparticles formed in the samples were investigated routinely with a Philips CM 12 microscope at an acceleration voltage of 120 kV. Images were taken with a Gatan TV 673 wide-angle camera and a TVIPS slow-scan camera with external control using the EM-MENU 4 software. Selected specimens were further studied at high resolution on a Tecnai F30 STwin electron microscope (300 kV, field-emission gun, spherical aberration constant $\mathrm{C_s}$ = 1.2 mm). STEM Z-contrast images were recorded using a HAADF detector. Elemental compositions of the hybrid particles were characterized by means of EDX spectroscopy, utilizing an EDAX system (Si/Li detector) mounted on the microscope. Spectra were recorded from individual spots (point analysis), over predefined paths (line-scan analysis), and on selected areas (map analysis). Additionally energy filtered TEM (EFTEM) with a post-column Gatan Image Filter was used to obtain elemental maps. In order to derive size distribution for the observed particles, their diameter was determined from the acquired images by fitting circles or ellipses to the borderline, using the DigitalMicrograph software package (Gatan, Version 3.9.0). In case of ellipses, the average of the two diameters was taken to be the corresponding size. At least 100 particles were analyzed so as to gain statistically significant results.

Powder X-ray diffraction (PXRD)

XRD patterns of isolated powder samples were recorded on a STOE STADI P diffractometer using Cu-K_α radiation. Scans were performed over a 2Θ range of 8-90° at a rate of 0.8°/min. Intensities were normalized for the mass of the sample on the holder to obtain comparable results.

Infrared spectroscopy

Fourier-transform infrared spectroscopy (FTIR) was carried out in order to verify the presence of amorphous barium carbonate. For this purpose, powdered samples were mixed at a ratio of 1:6 with anhydrous KBr (Merck, Uvasol) and pressed to a pellet. Data were recorded on a Varian FTS800 spectrometer at a resolution of 4 cm^{-1}.

Dynamic light scattering

DLS experiments were performed at $25^\circ\mathrm{C}$ and a scattering angle of 90°, using a CGS-3 goniometer system from ALV (Langen, Germany), which was equipped with an ALV-

7004/FAST Multiple Tau digital correlator and a He-Ne laser operating at a wavelength of 632.8 nm. Equal volumes of 10 mM $BaCl_2$ and the respective silica/carbonate solution were first passed through syringe filters (VWR, cellulose acetate, 200 nm) and subsequently combined in a vial. 1.5 mL of the resulting mixture were then transferred into a DLS cuvette, and measurements were started 20 s after mixing. The temporal evolution of particle size was traced over the following 30 minutes by performing consecutive runs of 60 s duration each. The used cuvettes were cleaned before the measurements by means of a custom-designed acetone reflux apparatus. The average size of the scattering species was calculated by fitting monomodal equations to the experimental correlation functions.

Titration experiments

In order to probe the interactions between Ba^{2+} and Ca^{2+} cations and the carbonate ions in solution on a comparative basis, dilute metal chloride solutions were added slowly into carbonate buffer, while the pH was held constant at 9.75 and the concentration of free metal ions was determined via corresponding ion-selective electrodes. For this purpose, we used a titration assay (c.f. chapter 4).[93,97] Briefly summarized, the titrations were carried out with the aid of a computer-controlled setup provided by Metrohm, consisting of two dosing units (Dosino 807) that were operated by a titration device (Titrando 809) and custom-designed software (Tiamo 2.2). Carbonate buffers were prepared by mixing 10 mM solutions of $NaHCO_3$ (Riedel de-Haën, ACS reagent) and Na_2CO_3 (Aldrich, anhydrous, ACS grade) in appropriate ratios to achieve a pH of 9.75. Subsequently, 10 mM CaCl2 (obtained by diluting a 1 M standard from Fluka) or 10 mM $BaCl_2$ (Merck, p.a.) were dosed at a rate of 0.01 mL/min into 25 mL of the buffer while stirring. Concentrations of free Ca^{2+} and Ba^{2+} were measured on-line by immersed ion-selective electrodes provided by Metrohm (No. 6.0508.110) and Mettler-Toledo (Model DX337-Ba), respectively. The pH was monitored by a flat-membrane glass electrode (Metrohm, No. 6.0256.100) and kept constant by automatic counter-titration of 10 mM NaOH (Alfa Aesar, standard solution). Free and bound amounts of the cations were calculated from the measured free concentrations and the known dosed volumes, as documented in the literature.[93]

3.4 Results

3.4.1 Fractal branching at low silica concentrations

Under the chosen conditions, direct mixing of barium chloride and sodium carbonate in the absence of silica results in the immediate formation of uniform rod-like crystals (Figure 3.1A), typically several microns in length and showing the pseudo-hexagonal habit characteristic of twinned witherite ($BaCO_3$).[85] Rapid growth of these crystals is evident from an instant clouding of the solutions upon combining reagents (see Figure 3.2), indicating homogeneous nucleation of $BaCO_3$ at the given high supersaturation. The fact that highly crystalline material is developed in the system within seconds is in sharp contrast to the behavior of calcium carbonate which, under the same conditions, precipitated in the form of spherical ACC nanoparticles that persisted in solution up to about one hour.[92] This suggests that amorphous $BaCO_3$ precursors are much more transient than their $CaCO_3$ counterparts.

Addition of silica at concentrations ranging from 135 to 750 ppm does not retard crystallization to a large extent (again unlike observations made for $CaCO_3$),[92] as crystalline precipitates were deposited at the bottom of the vials already after few minutes (Figure 3.2). Solids formed in this range of silica contents were all confirmed to be witherite by means of X-ray diffraction (Figure 3.3). However, the presence of silicate species in the solutions provokes significant morphological changes in the final crystal products (Figure 3.1B-F).

While crystals grown at 135 ppm SiO_2 still exhibit rod-like habits with no marked variation in size or shape (Figure 3.1B), increasing the silica content to 270 ppm induces splitting of the elongated crystal at their tips, where tilted projections emerge at non-crystallographic angles from the parent rod (indicated by red arrows in Figure 3.1C). This effect becomes more and more pronounced as the silica concentration is further increased (Figure 3.1D-F), and it is evident that branching proceeds in a self-similar manner, i.e. the projections split by themselves and produce second-generation outgrowths at non crystallographic angles. This fractal branching pattern leads to the formation of dumbbell-shaped morphologies at 540 ppm SiO_2 (Figure 3.1E) and finally gives rise to spherulitic, cauliflower-like structures with diameters around 20 μm at 750 ppm (Figure 3.1F). Thus, addition of silica at these concentrations induces progressive breaking of crystallographic symmetry, from ini-

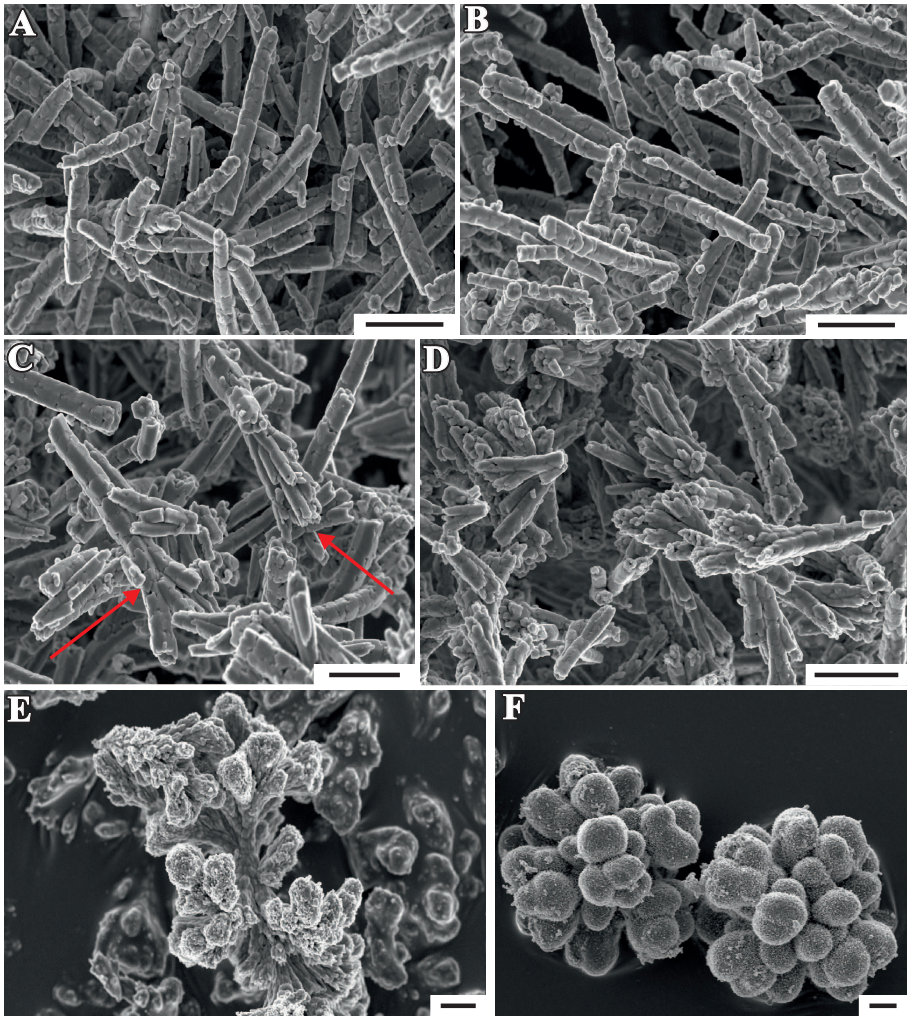

Figure 3.1. FESEM images of $BaCO_3$ crystals formed upon direct mixing of $BaCl_2$ and Na_2CO_3 in A) the absence of silica and the presence of B) 135, C) 270, D) 370, E) 540, and F) 750 ppm SiO_2. Precipitates were isolated after 24 h of ageing. Arrows in (C) mark the onset of crystal splitting at 270 ppm silica. Scalebars are 2 μm

tial pseudo-hexagonal rods towards increasingly bifurcated architectures. Similar growth behavior has been observed in the formation of silica biomorphs, where such fractal entities were found to be precursors of the more complex, curved morphologies (like helicoids).[61,81] The structure evolution seen in the present experiments with increasing silica concentration therefore reflects the morphological development displayed by biomorphs as a function of growth time (over hours). It has been suggested that branching of witherite crystals in silica-containing systems results from growth poisoning by oligomeric silicate species, which act as non-absorbable impurities and generate misoriented 2D islands on the basal {001} faces of the crystal, eventually leading to the formation of tilted outgrowths.[61,81] EDX analyses

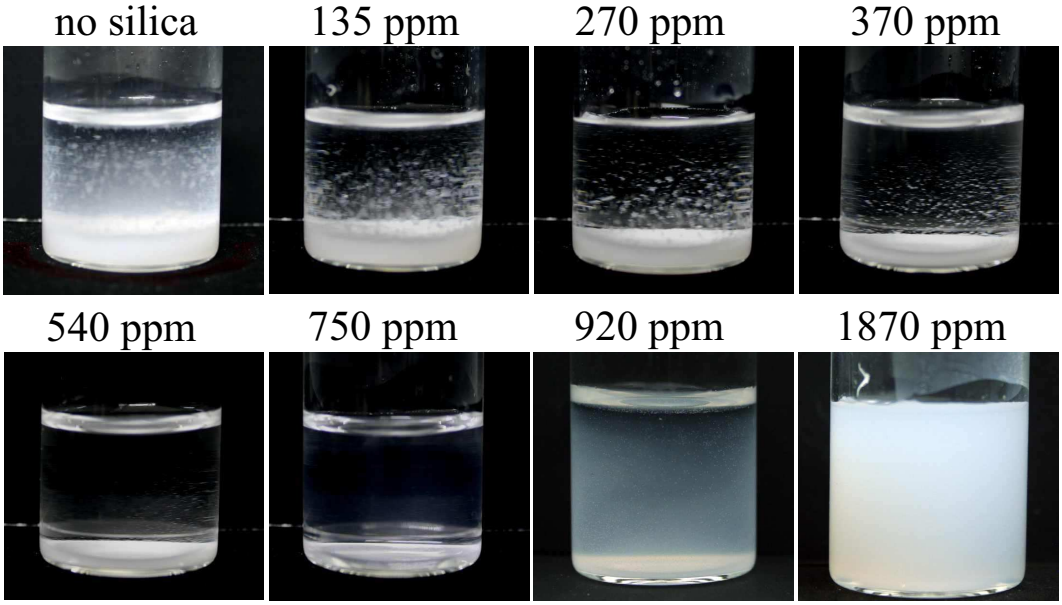

Figure 3.2. Sequence of photographs showing the macroscopic appearance of samples at different silica concentrations. Pictures were taken 10 minutes after mixing. At low silica content (0-370 ppm SiO_2), crystallization of $BaCO_3$ is already completed at this time and sediments of micron-sized crystals (cf. Fig. 3.1 and Fig. 3.3) have accumulated at the bottom of the vial. In the intermediate concentration regime (540 and 750 ppm SiO_2), precipitates found on the walls and the bottom of the vessel are likewise crystalline (Figs. 3.1 and 3.3), but their amount is significantly lower. Simultaneously, the supernatant solution exhibits a slightly bluish cast. This may imply that a certain fraction of the available $BaCO_3$ resides in suspended nanoparticles and thus is prevented from crystallization. At high silica contents (920 and 1870 ppm SiO_2), no crystalline products can be distinguished and all precipitated material consists of amorphous silica/carbonate composite particles. At 920 ppm, these particles are prone to aggregation and become interconnected by superficial silica condensation, such that a layer of silica gel begins to settle. By contrast, the sample at 1870 ppm is a turbid solution that remains cloudy and does not sediment (or segregate a gel phase) over the studied period of time.

show that the amount of silica incorporated into the crystals is fairly low (Si/Ba atomic ratio < 0.05) for solution concentrations of 135-370 ppm (Figure 3.4), which is in line with the notion of crystal growth poisoning by non-absorbable impurity species.[61]

By contrast, the silica content in the precipitates obtained at 540 and 750 ppm SiO_2 is much higher (Si/Ba $\simeq$ 0.3 and 0.4, respectively). Moreover, close-up views of the surface of corresponding cauliflower-like structures reveal that they are composed of numerous elongated nanoparticles, which appear to be largely co-oriented (Figure 3.5). This suggests that growth of these forms proceeds via assembly of small building units (as in the case of silica

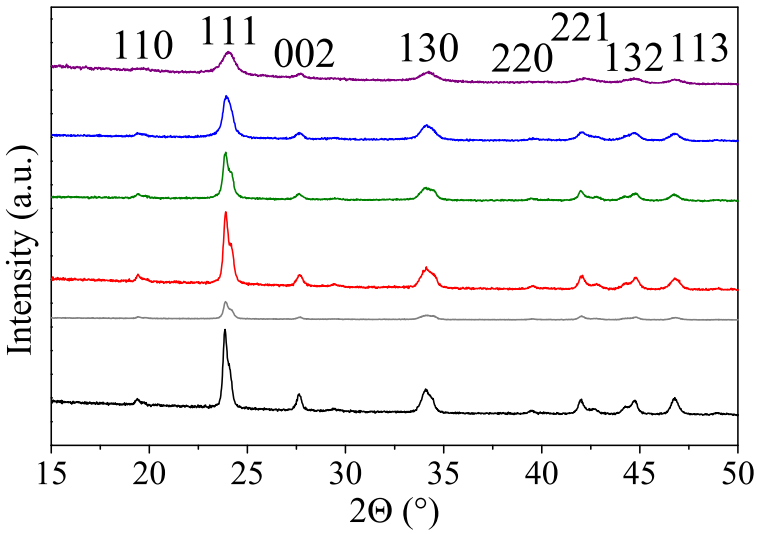

Figure 3.3. Powder X-ray diffraction patterns of precipitates isolated after one day from samples containing 0 (black), 135 (grey), 270 (red), 375 (green), 540 (blue) and 750 ppm SiO2 (purple). In all cases, the occurring reflections can be indexed to witherite-type barium carbonate (orthorhombic structure, space group Pnma).

biomorphs) and, hence, that they are nanocrystalline aggregates rather than bifurcated single crystals (at least during the later stages).

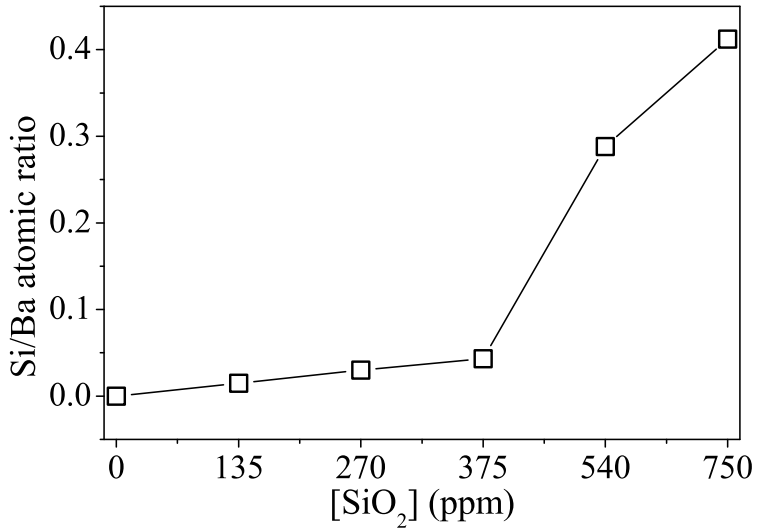

Figure 3.4. Silica content of crystalline structures formed at different analytical silica concentrations in solution, given by the Si/Ba atomic ratio as determined by EDX spectroscopy.

This scenario is supported by XRD patterns of the samples at 540 and 750 ppm SiO_2 (cf. Figure 3.3), where marked broadening of diffraction peaks is observed (as compared to data for lower silica concentrations), indicating the presence of small primary particles. The high Si/Ba ratios detected for the assemblies may originate from coating of individual $BaCO_3$

units in skins of silica, as proposed for the building blocks of silica biomorphs.[61,81,86] Again, it is worth noting that aggregates with such complex structure and composition can obviously be grown in a fast and efficient manner simply by mixing reagents at high supersaturation.

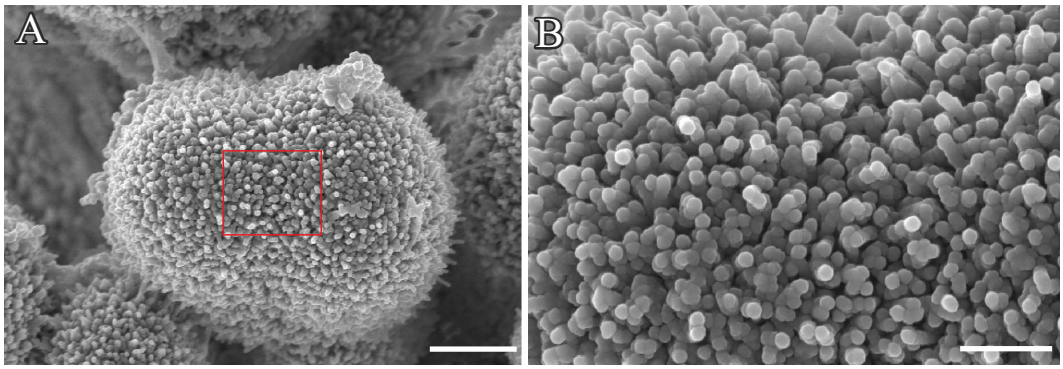

Figure 3.5. A) FESEM image of a cauliflower-like structure formed at a silica content of 750 ppm after a reaction time of one day. B) Close-up view of the area marked by the red box in (A), indicating the presence of nano-sized subunits on the surface of the fractal aggregate. Scale bars are 1 μm in (A) and 200 nm in (B).

3.4.2 Core-shell-shell particles at elevated silica concentrations

When the silica concentration is increased to 920 ppm, an initially clear solution is obtained that turns turbid within several minutes. After about 10 min, macroscopic sedimentation is observed and the precipitates begin to accumulate at the bottom of the vial (Figure 3.2). However, in contrast to the experiments performed at lower silica content, the deposited material is not crystalline, but rather exhibits a gel-like character. At a still higher silica content of 1870 ppm, clouding of the solution sets in again instantaneously. Under these conditions, there is no longer any pronounced settling of the precipitates discernible and the samples stay turbid for the whole period investigated, indicating that generated particles remain dispersed in the solution (Figure 3.2). Particles present in the solutions at elevated silica concentrations were first characterized by means of transmission electron microscopy. Images taken from samples isolated right after mixing disclose fundamental differences between precipitates formed at 920/1870 ppm SiO_2 and the crystals obtained at the same time for lower silica contents (Figure 3.6A-B). Indeed, nanoparticles with more or less distorted spherical shapes are observed, which tend to build interconnected networks owing to agglomeration and merging of primary grains.

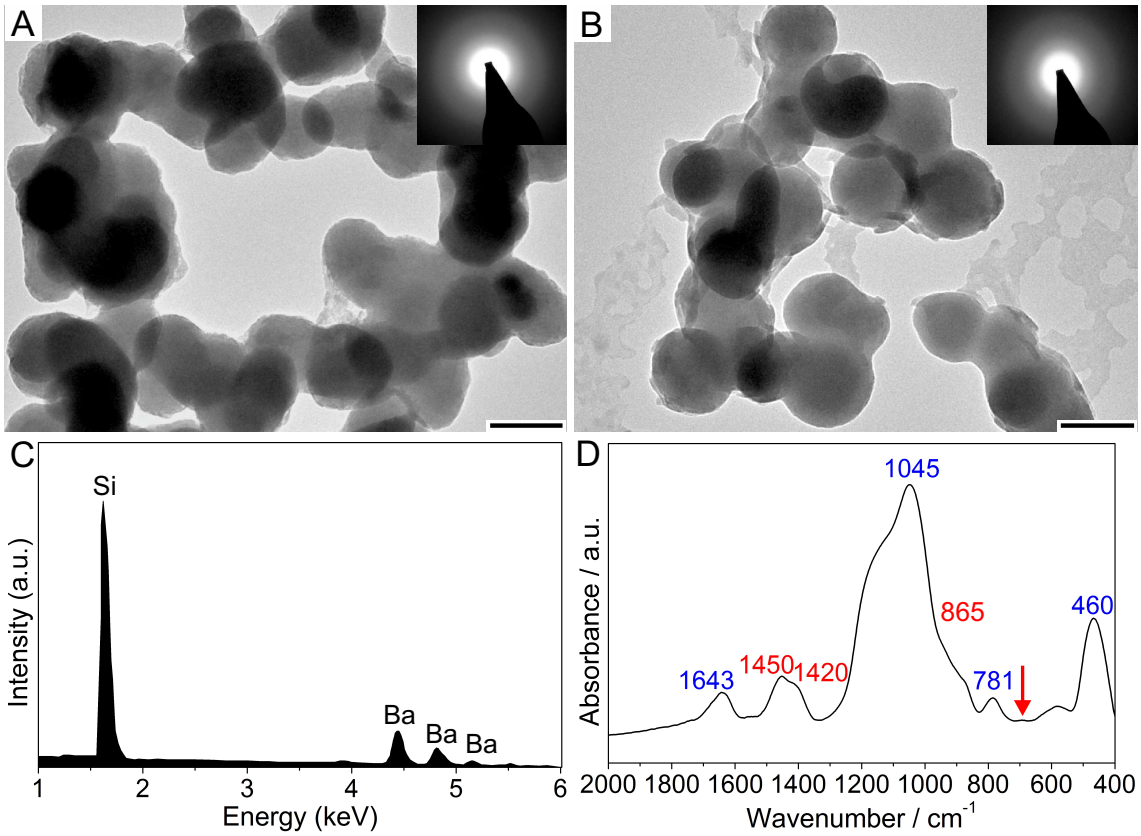

Figure 3.6. A, B) TEM micrographs of nanoparticles isolated 1 min after mixing from samples containing 920 (A) and 1870 (B) ppm SiO_2 (Scale bars: 100 nm). Inserted ED patterns verify that the particles are amorphous. Note that particle aggregation and fusion is more pronounced at the lower silica concentration. C) EDX spectrum recorded from powder samples containing 1870 ppm SiO_2, obtained by quenching the reaction after 1 min via filtration. Signals for Si and Ba confirm the presence of silica and barium carbonate in the precipitated material (Si/Ba atomic ratio: 2.20 at 1870 ppm and 1.35 at 920 ppm). D) IR pattern of the powder, showing characteristic bands of amorphous $BaCO_3$ and silica.

The degree of aggregation seems to be higher at 920 ppm SiO_2 (Figure 3.6A) than at 1870 ppm (Figure 3.6B), as is confirmed quantitatively by dynamic light scattering measurements (see below). The average diameter of the particles determined by measuring more than 100 individuals was found to be 100 ± 15 nm, independent of the silica concentration. Electron diffraction (ED) patterns collected from the nanoparticles further demonstrate that they are amorphous (insets in Figure 3.6A-B), although crystalline reflections corresponding to witherite could be discerned in some cases (Figure 3.7) however, the presence of crystalline barium carbonate might well result from transformation of amorphous domains under the influence of the electron beam at high resolution.

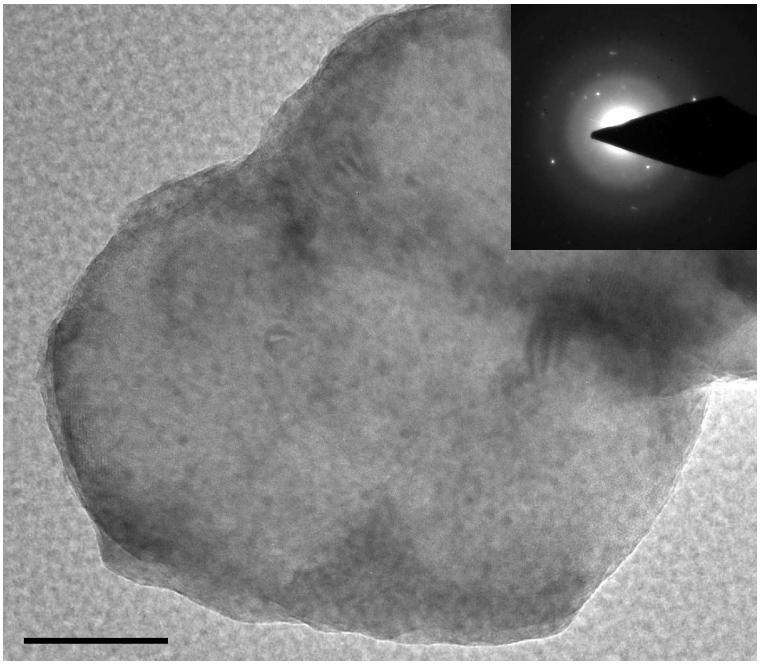

Figure 3.7. Hybrid nanoparticle isolated after 1 min from samples containing 1870 ppm SiO_2. In rare cases as here, the carbonate component of the particles was found to be crystalline, as demonstrated by selected-area electron diffraction (SAED) (inset, reflections corresponding to witherite). This transformation is possibly due to the exposure of the particles to the high voltage electron beam. Scale bar: 50 nm.

The composition of these early-stage particles was further analyzed using EDX and infrared spectroscopy. While EDX profiles show that the precipitates contain both Ba and Si (Figure 3.6C), IR spectra evidence the co-existence of silica and barium carbonate (Figure 3.6D). Bands at 1045, 781, and 460 cm^{-1} can be assigned to amorphous silica (corresponding to stretching, bending, and rocking vibrations of the SiO_2 network, respectively), whereas the peak at 1643 cm^{-1} originates from water molecules entrapped in the siliceous matrix.[127] For crystalline witherite, sharp IR bands at 694 (ν_4-mode), 857 (ν_2), 1065 (ν_1), and 1449 cm^{-1} (ν_3) would in principle be expected.[128] However, the collected spectra display a split ν_3-peak (1420/1450 cm^{-1}), and the ν_4-band at about 700 cm^{-1} is entirely absent (arrow in Figure 3.6D; the ν_2-band is seen as a shoulder at 865 cm^{-1}, whereas the ν_1-band is hidden by the strong silica vibration in this range). These two criteria identify the carbonate component in the material as amorphous,[107,121] in agreement with electron diffraction data (Figure 3.6A-B).

The above results suggest that addition of silica at concentrations exceeding a certain thresh-

old (between 750 and 920 ppm) leads to stabilization of amorphous barium carbonate precursors and prevents immediate witherite crystallization. Similar effects have been observed for calcium carbonate, where a silica shell was formed around ACC nanoparticles (already at lower silica content) and thus impeded their transformation.[92] Interestingly, fundamentally

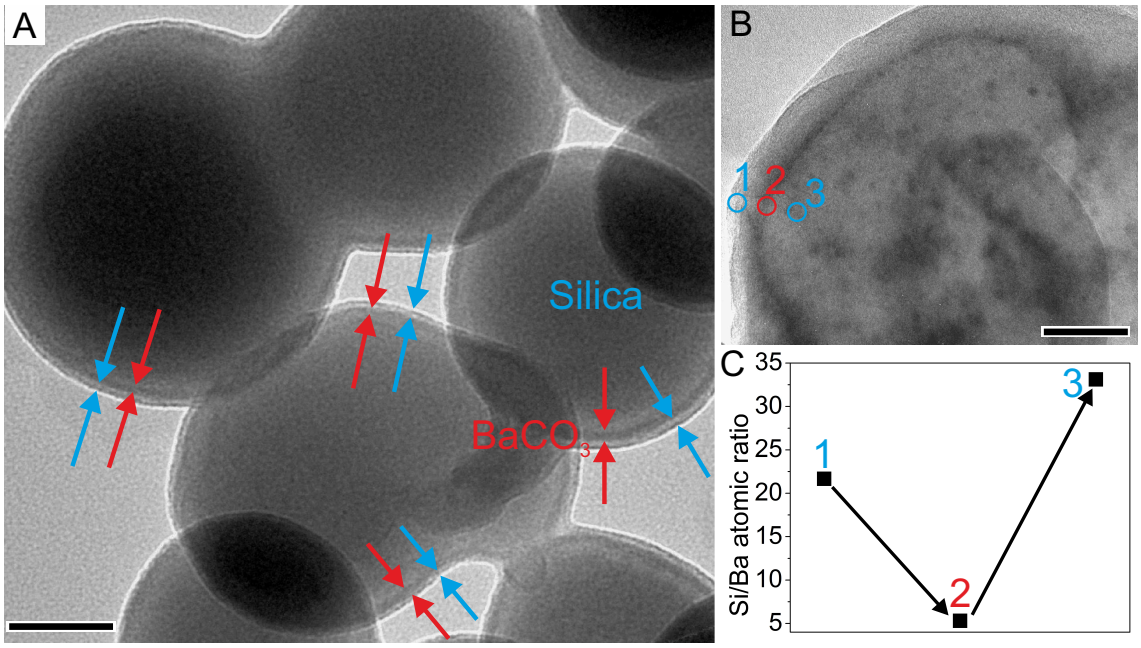

Figure 3.8. A-B) TEM images of core-shell-shell nanoparticles formed in the presence of A) 920 and B) 1870 ppm silica after 1 min. Red and blue arrows in (A) mark the interstitial $BaCO_3$ layer and the outer silica skin, respectively. Scale bars are 40 nm in (A) and (B). C) Si/Ba atomic ratios calculated from three selected points (as defined by circles in B) along the EDX line scan path on the rim of the composite particles. The line shall be a guide for the eye.

distinct behavior is encountered in the case of $BaCO_3$, as demonstrated by high-resolution TEM and micro-EDX studies (Figure 3.8 and Figures 3.9-3.11). In fact, a closer look at the generated nanoparticles reveals that their inner core is surrounded by a first layer with enhanced electron contrast (delimited by red arrows in Figure 3.8A), which then again is covered by an outer shell of lighter contrast (highlighted by blue arrows). Si/Ba atomic ratios calculated from EDX spectra of the core as well as from the two coating layers (as defined in Figure 3.8B) show that while the core and the outer shell are composed of silica, the interstitial layer with dark is clearly enriched in Ba (as indicated by a minimum in the measured Si/Ba ratio, cf. Figure 3.8C 3.8), and thus most likely consists of (amorphous) barium carbonate. This is further supported by EDX line scans over the rim of the particles

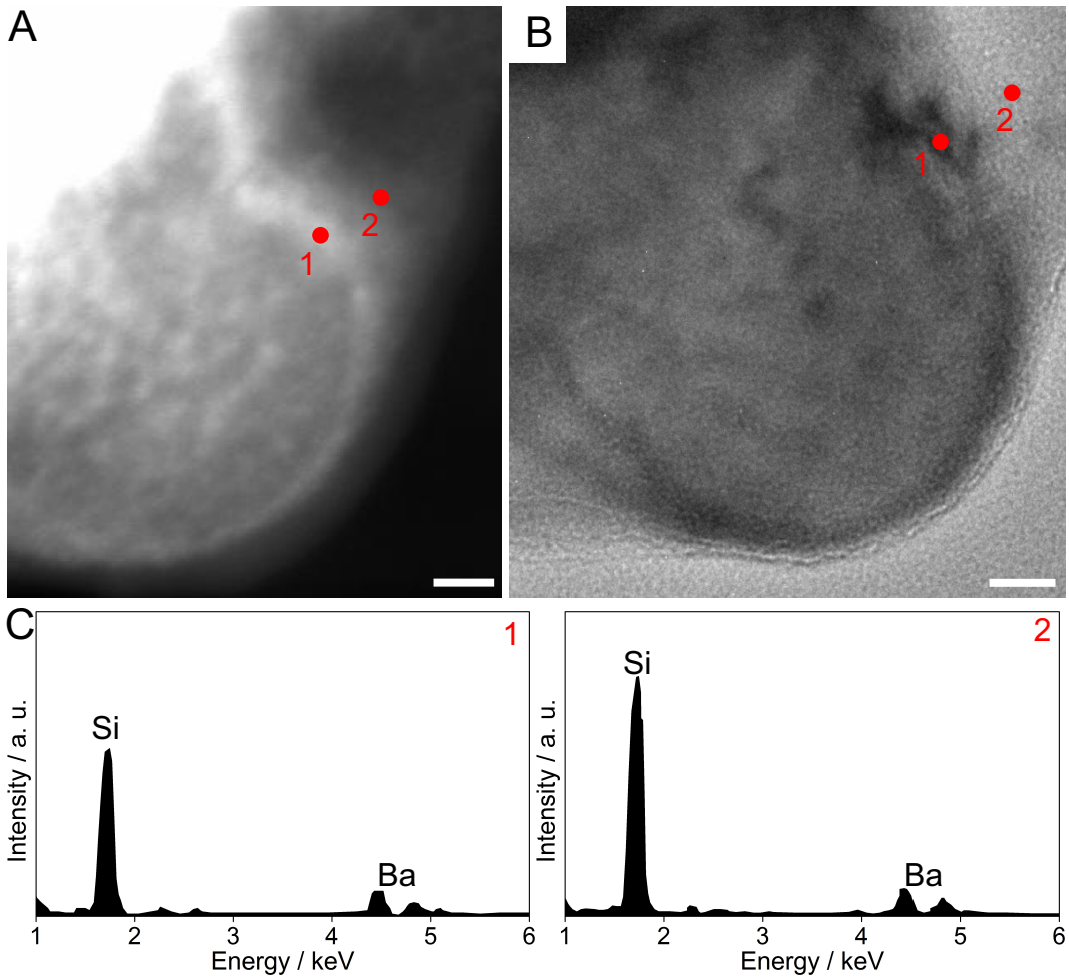

Figure 3.9. A-B) STEM and TEM images of core-shell-shell particles formed in solutions at 1870 ppm SiO_2 after 1 min. Regions of higher contrast in (B) evidence the presence of an interstitial $BaCO_3$ layer. C-D) EDX spectra acquired by point analyses of the two marked positions as indicated. The resulting Si/Ba atomic ratios are 9.24 for position 1 and 22.33 for 2, thus confirming that the outer shell is composed of silica while the inner layer consists of $BaCO_3$. Scale bar: 20 nm.

(Figure 3.10), demonstrating that Ba and C counts run through a maximum when passing the supposed $BaCO_3$ layer along the scanning path, as well as by EFTEM elemental maps (Figure 3.11). Additional evidence for the core being made up of silica and the first shell consisting of barium carbonate (thus an inverse scenario as compared to the CaCO3 case[92]) is finally provided by EDX mappings on particles generated at higher silica concentrations (3740 ppm), as shown in Figure 3.12. The thickness of the occluded carbonate layers was found to be only a few nanometers in most cases (4 ± 1 nm), whereas the outer silica shells often extended over 10 nm or more. The width of the two layers was confirmed to be largely

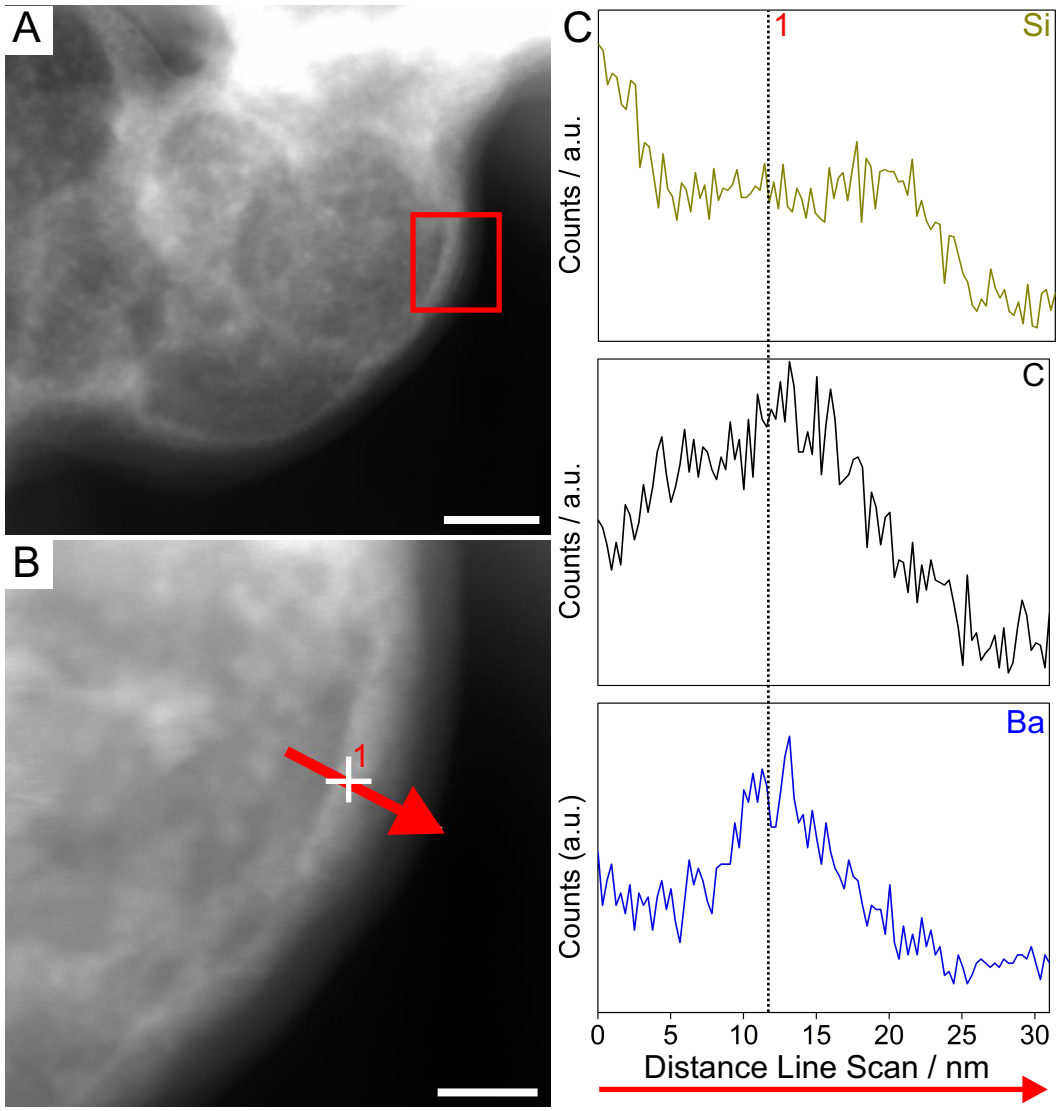

Figure 3.10. EDX line-scan analysis of core-shell-shell nanoparticles grown at a silica concentration of 1870 ppm (cf. Figure 3.6B-C in the main text). A) STEM image granting an overview of the investigated particle aggregate. B) Close-up view of the area marked by the red box in (A). The line scan was performed along the path indicated by the red arrow. C) Results of the EDX line scan, showing the distribution of relevant elements (Si, Ba and C) across the different layers. The vertical dashed line corresponds to position 1 in (B), where the counts of barium and carbon run through a maximum. Scale bars are 50 nm in (A) and 20 nm in (B).

independent of the silica concentration (cf. Figure 3.8A-B). In turn, the overall composition of the particles varied with the silica content of the mother solutions, that is, higher Si/Ba ratios were usually found for particles formed at 1870 ppm SiO_2 (2.20) as compared to mean values determined for the samples at 920 ppm (1.35). The core-shell-shell character of the nanoparticles was further investigated by means of leaching experiments. For this purpose,

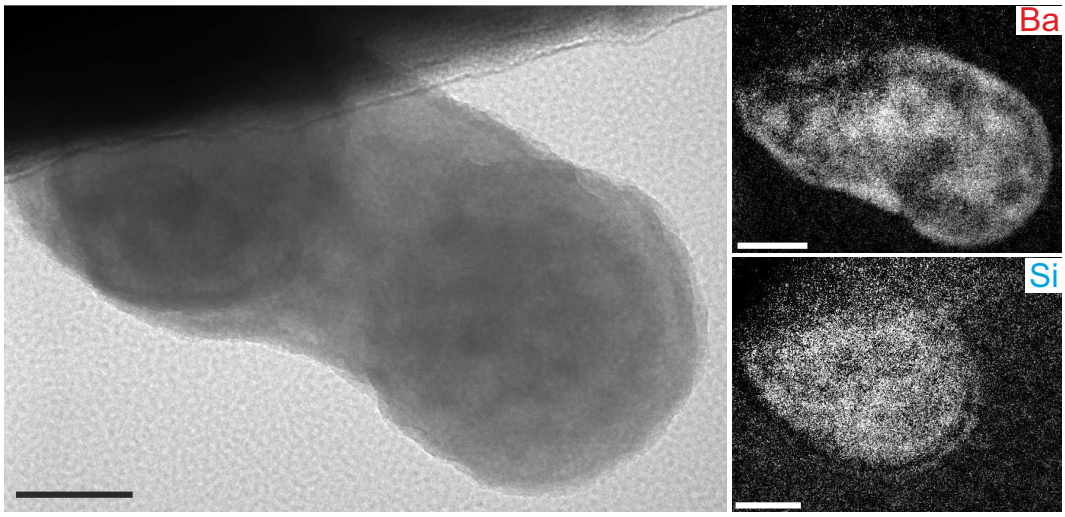

Figure 3.11. Left: Bright field TEM (left) image of hybrid nanoparticles formed in samples containing 1870 ppm SiO_2. Right: Corresponding EFTEM maps of barium (top) and silicon (bottom), showing that Ba is preferentially located at the border of the particles, whereas Si is found predominantly in their core. Note that the particles shrink slightly after longer exposure to the electron beam without losing their composite character. Scale bars are 50 nm.

the precipitates were immersed in dilute acid for several days, subsequently washed with water and dried. Such a treatment ought to dissolve the carbonate part of the nanostructures and leave the siliceous component, which is scarcely soluble at low pH values. For $CaCO_3$, this procedure gave frameworks of hollow silica particles, as the inner ACC core was selectively removed.[92] In the present studies, leaching in acid did not affect the core part of the nanoparticles, as expected in view of the above discussion. Indeed, particles generated at 1870 ppm SiO_2 remained largely unchanged upon immersion in acid, whereas their counterparts produced at 920 ppm were heavily eroded at the surface (Figure 3.13), presumably due to removal of the interstitial carbonate layer. Complete dissolution of the $BaCO_3$ component is clearly evidenced by EDX spectra recorded before and after acid treatment: while Si and Ba are present in high amounts prior to leaching, any peaks belonging to Ba are absent afterwards (Figure 3.13). This was true for both studied silica concentrations. However, while the mean diameter of the nanoparticles formed at 1870 ppm remained nearly constant upon acidification, those precipitated at 920 ppm shrank in size (to 80 $\pm$ 11 nm). This suggests certain differences in the stability of the external silica skins as a function of the additive concentration in solution. In other words, silica shells deposited at 920 ppm are likely to be

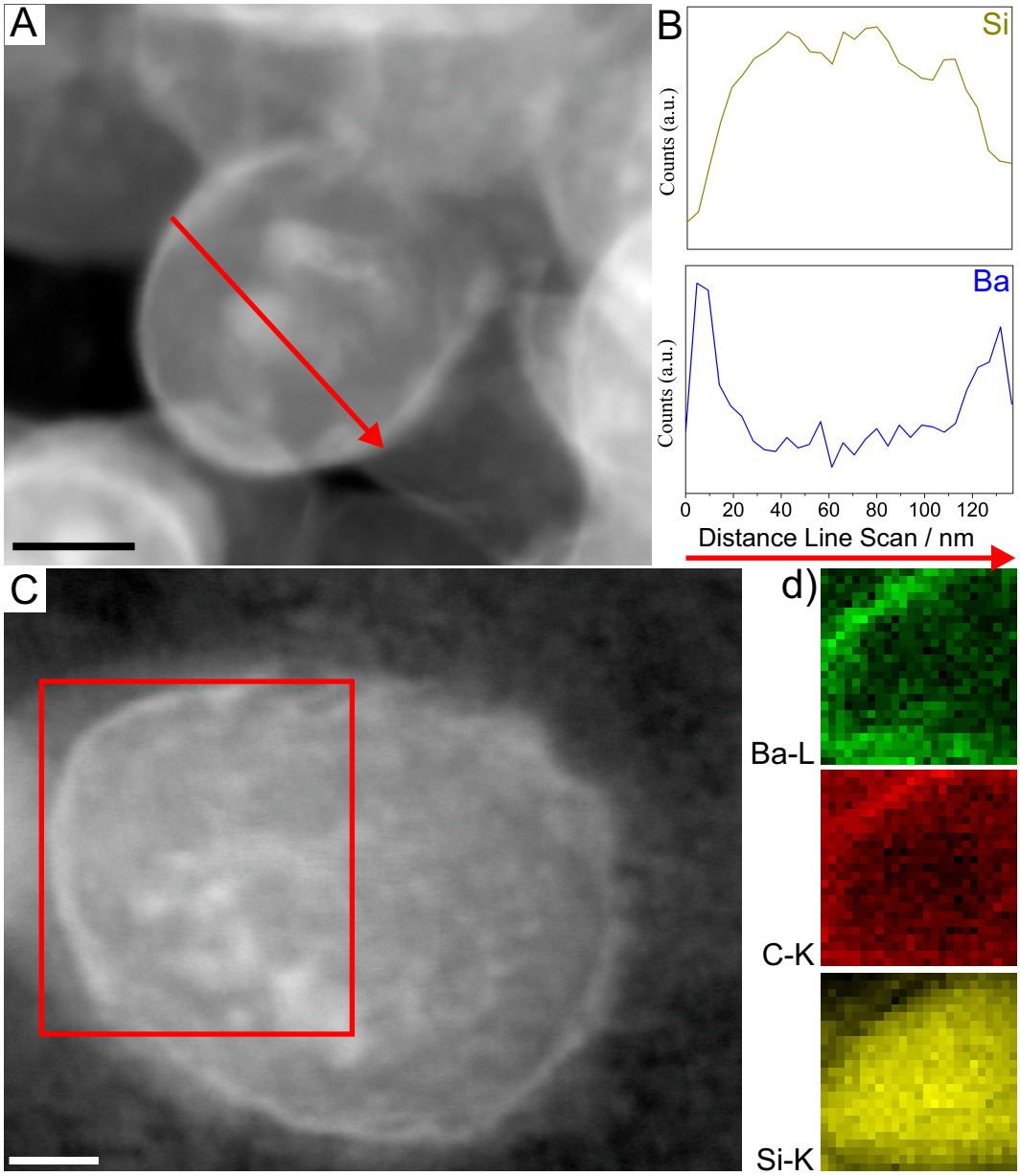

Figure 3.12. EDX line-scan and mapping studies of $BaCO_3$-coated silica particles bearing no external silica shell, as found occasionally in samples at 3740 ppm SiO_2. A) STEM micrograph of a corresponding core-shell particle, which was analyzed concerning its composition via a line scan along the path delineated by the red arrow. B) Development of Si and Ba counts over the scanned track, demonstrating that the core and shell consist of silica and barium carbonate, respectively. C) STEM images of the particle used for elemental mapping. D) Distribution of barium (green), carbon (red), and silicon (yellow) across the area marked by the red box in (C). The maps clearly show that the outer skin is rich in Ba and C, whereas the core contains high amounts of Si. Scale bars are 50 nm in (A) and 20 nm in (C).

less dense (and continuous) than those generated at 1870 ppm, in line with previous work.[92] Thus, removal of the enclosed carbonate layer may well result in a collapse of the external

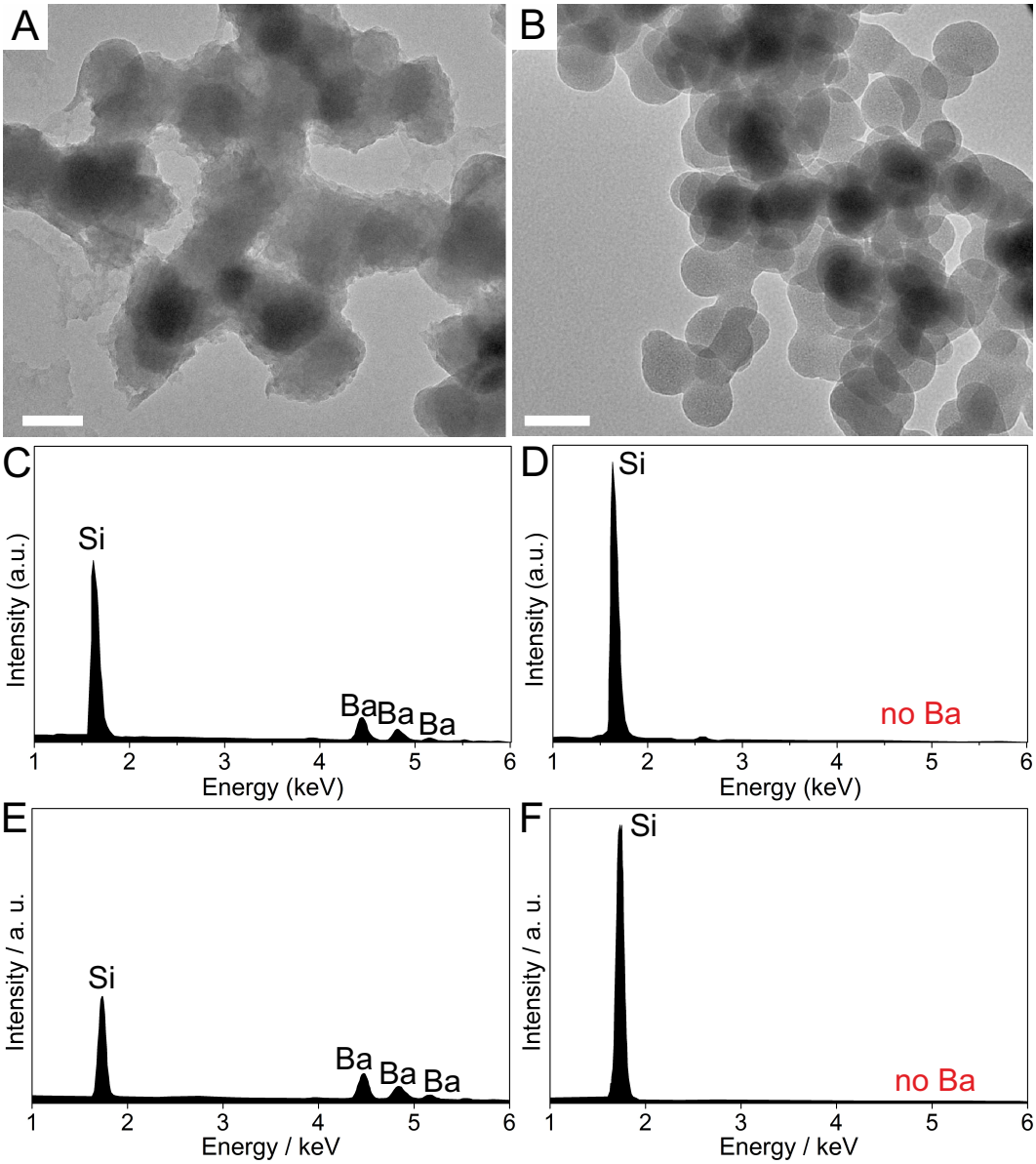

Figure 3.13. A-B) TEM micrographs of nanostructures remaining after acid treatment of the silica-$BaCO_3$ composite particles formed in samples containing 920 (A) and 1870 (B) ppm SiO_2. C-F) EDX spectra acquired from the nanoparticles produced at 1870 (C-D) and 920 ppm (E-F) before (C and E) and after (D and F) the leaching procedure. It is evident that acidification leads to selective dissolution of the carbonate part and leaves a precipitate consisting purely of silica, as no significant counts for Ba could be detected after acid treatment at both concentrations. Scale bars are 100 nm.

silica skin at the lower concentration, leading to a substantial decrease in size. This might be further enhanced by contraction of the exposed core part, given that protonation of the silica lattice under acidic conditions can induce additional condensation and densification of the structure.[129] At 1870 ppm SiO_2, the outer shell in turn appears to be quite stable and does not

break down upon acid treatment, indicating that dissolution of the carbonate part proceeds slowly in this case and is accompanied by merely a minor change in volume.

3.4.3 Temporal stability and transformation of the composite nanoparticles

In a further suite of experiments, we have studied the behavior of the silica-$BaCO_3$-silica particles when left to age in contact with the mother solution for extended periods of time. First, any occurring aggregation processes were investigated in situ by means of dynamic light scattering. At 920 ppm SiO_2, the resulting time-dependent development of the size of scattering species reveals a continuous increase of the average hydrodynamic radius (Figure 3.14), which soon exceeds values measured for single grains in TEM micrographs (cf. Figure 3.6A-B) and reaches dimensions in the micron-scale after about 15 min. This shows that the suspended nanoparticles do not grow, but agglomerate into fairly large assemblies, which finally coalesce and segregate from solution in the form of a gel-like sediment (as observed macroscopically). With respect to the composition of the particles, aggregation is most probably driven by condensation reactions in-between free silanol groups at the surface of the outer silica shells, connecting the nanoparticles as reported for silica-coated ACC.[92] Thus, co-precipitation at 920 ppm SiO_2 leads to the formation of a silica hydrogel containing amorphous barium carbonate domains, which are incorporated within the nanoparticles constituting the gel matrix. By contrast, DLS analyses of samples at 1870 ppm SiO_2 evidence that the mean hydrodynamic radius increases only slightly within the first 5 min in this case and subsequently levels off at 300-320 nm, indicating that aggregation has ceased. This is again in line with visual observations, as the samples were found to be fairly stable suspensions that did not sediment to a large extent over days. We suspect that particle agglomeration is suppressed under these conditions due to the higher pH of the solution at 1870 ppm SiO2 (pH $\sim$ 10.9) as compared to 920 ppm (pH $\sim$ 10.7; see Figure 3.15). It is well known that the number of negative charges at silica colloids increases with pH[129] and hence, as the surface of the core-shell-shell particles was shown to be rich in silica, their aggregation should become less favored as the pH is raised.[92]

When samples at 920 ppm SiO_2 are allowed to age for 24 h, crystals can typically be ob-

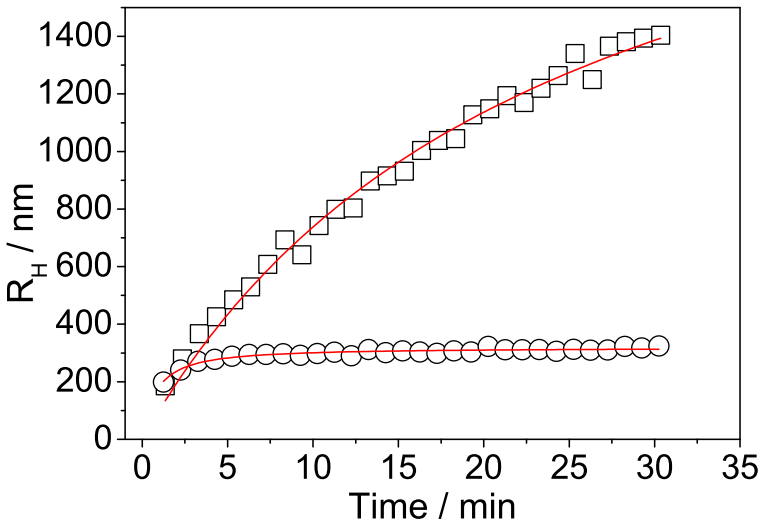

Figure 3.14. Time-dependent hydrodynamic radii of scattering species (open symbols) measured by DLS for $BaCl_2/Na_2CO_3$ solutions containing 920 ppm (@) and 1870 ppm (E) SiO_2. Data were fitted to a modified Hill-type function (red lines), given as:

$$\mathrm{R_H} = \mathrm{R_{H,max}} \cdot \frac{\mathrm{t}}{k + \mathrm{t}}$$

where $\mathrm{R_{H,max}}$ is the maximum particle radius at infinite time and k the rate constant. Fits yielded $\mathrm{R_{H,max}}$ values of 274 nm and 322 nm at silica concentrations of 920 ppm and 1870 ppm, respectively, with correlation coefficients greater than 0.99. These values are substantially larger than the sizes of individual particles observed by TEM (cf. Figure 3.6), indicating that the increase of $\mathrm{R_H}$ is due to particle aggregation (rather than growth). It is furthermore evident that agglomeration is much more pronounced at 920 ppm SiO_2, where the forming particle networks eventually segregate from the solution as a gel phase (cf. Figure 3.2). By contrast, particle aggregation at 1870 ppm SiO_2 leads to smaller assemblies of about 320 nm in diameter, most probably owing to the higher pH of the sample (cf. Figure 3.15) and correspondingly increased numbers of negative charges on the silica-coated nanoparticles.

served as isolated spots within the gel sediment (or on the walls of the vessel). The presence of crystalline barium carbonate was confirmed by isolating the gel bodies via filtration and performing XRD analyses on the dried specimens. Corresponding patterns show reflections characteristic of witherite, along with strong background scattering at low angles, likely originating from the silica matrix and/or remaining amorphous $BaCO_3$ (Figure 3.16). This is further supported by IR spectra which, in addition to bands of amorphous silica, display well-defined peaks at 856 and 690 $\mathrm{cm^{-1}}$ as well as a single (now non-split) band at 1440 $\mathrm{cm^{-1}}$ (Figure 3.17), all being indicative of a crystalline witherite phase.[128] SEM

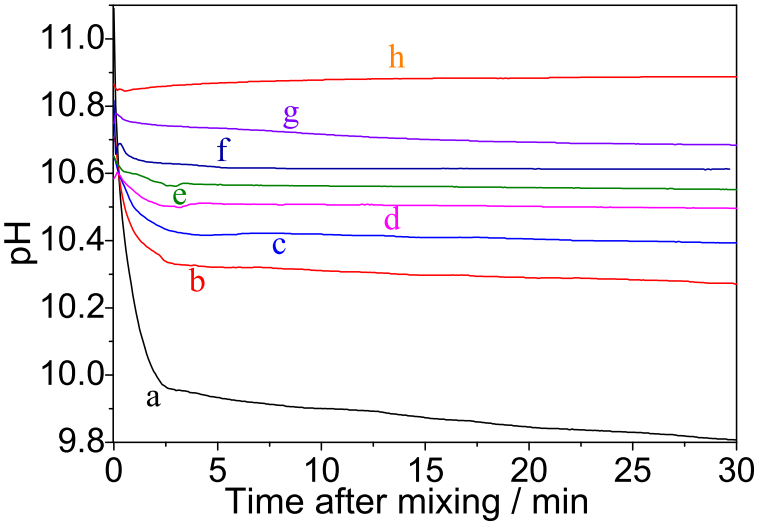

Figure 3.15. Temporal evolution of the bulk pH in samples containing (A) 0, (B) 135, (C) 270, (D) 375, (E) 540, (F) 750, (G) 920, and (H) 1870 ppm SiO_2, monitored over the first 30 minutes after mixing of reagents. The initial pH of the solutions was found to range from about 10.6 to 10.9 (± 0.1) and increase with the amount of silica present. With time, a decrease of pH was observed for samples with low silica content (0-750 ppm), as a result of carbonate precipitation ($Ba^{2+} + HCO_3^- \longrightarrow BaCO_3 + H^+$). Thereby, the overall drop of pH and the period required to achieve stable values are reduced as the silica concentration is raised. This can be ascribed to the buffering ability of silica in solution. In turn, the final pH increases with the silica content (from 10.3 at 135 ppm SiO_2 to 10.9 at 1870 ppm), due to the alkaline character of sodium silicate sols. At 920 and 1870 ppm SiO_2, the buffering capacity of silica is high enough to compensate any changes due to carbonate precipitation, such that the pH remains virtually constant over the entire period of time investigated.

and optical microscopy studies (Figure 3.18) on the dried gel sediments reveal helicoidal (Figure 3.18A) and worm-like structures (Figure 3.18B) with a thickness of 10-20 μm and lengths up to the millimeter scale (Figure 3.18C). These morphologies are typical for silica biomorphs and have previously been obtained by $BaCO_3$ crystallization in silica gels or sols at low supersaturation.[59–63,67–69,74–76,80,81,85,87,125] In addition to these complex forms, cauliflower-like aggregates closely resembling those found at 750 ppm SiO_2 (cf. Figure 3.1F) were also observed (Figure 3.18D). As already mentioned, such fractal architectures are generated during the first stage of the morphogenesis of silica biomorphs[61,75,81,86,87] and, hence, they frequently occur as byproducts next to the curved ultrastructures. Interestingly, both the biomimetic morphologies and the fractal aggregates usually develop in the vicinity of coagulated nanoparticles and are often embedded in networks thereof (i.e. they clearly grew

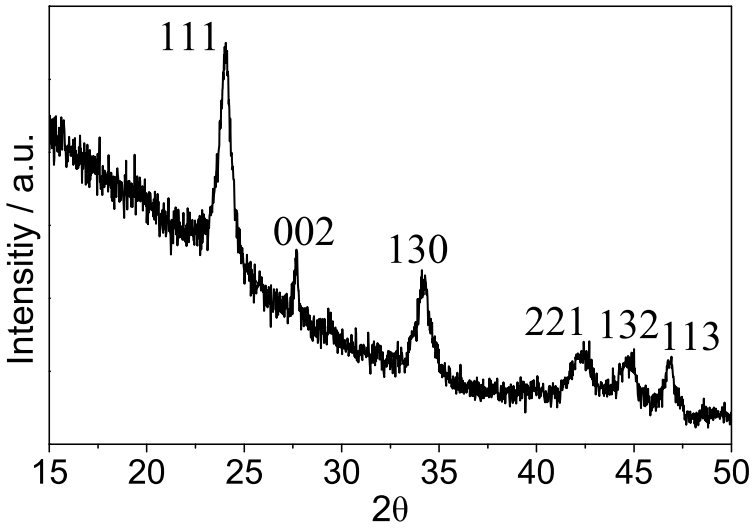

Figure 3.16. XRD pattern of a powder sample obtained by filtration of a sample containing 920 ppm SiO_2 after ageing for 24 h (i.e. the segregated gel phase with embedded crystals). Diffraction peaks characteristic of witherite are observed, along with strong background scattering at low angles, likely caused by amorphous contents in the material (silica and possibly remnants of amorphous barium carbonate).

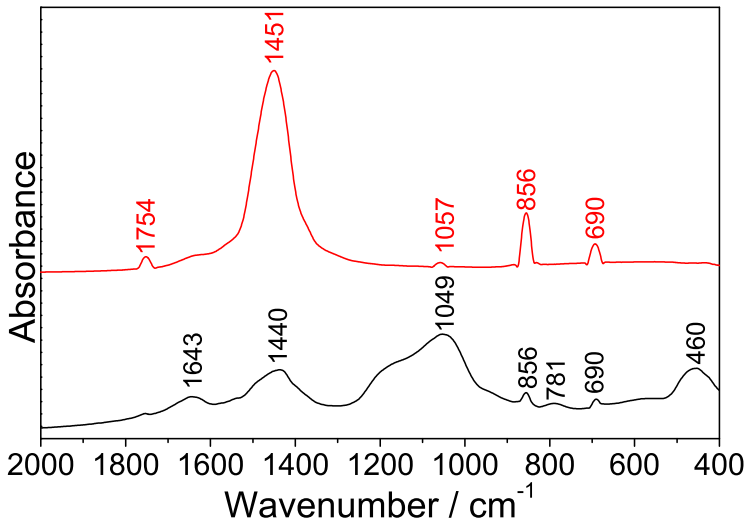

Figure 3.17. Infrared spectrum of the gel phase formed at 920 ppm SiO_2, isolated by filtration and drying after one day (black curve), together with a reference pattern of crystalline barium carbonate (red curve). Bands centered at 460, 781, and 1049 cm^{-1} can be attributed to amorphous silica, whereas the peak at 1643 cm^{-1} originates from water bound in the matrix.[127] The occurrence of defined peaks at 690 and 856 cm^{-1}, as well as the non-split band at 1440 cm^{-1}, corroborate the presence of an orthorhombic $BaCO_3$ phase.[128]

within the gel matrix). Moreover, high-magnification SEM images disclose that barium carbonate crystals evolved directly from the spherical composite particles formed during the

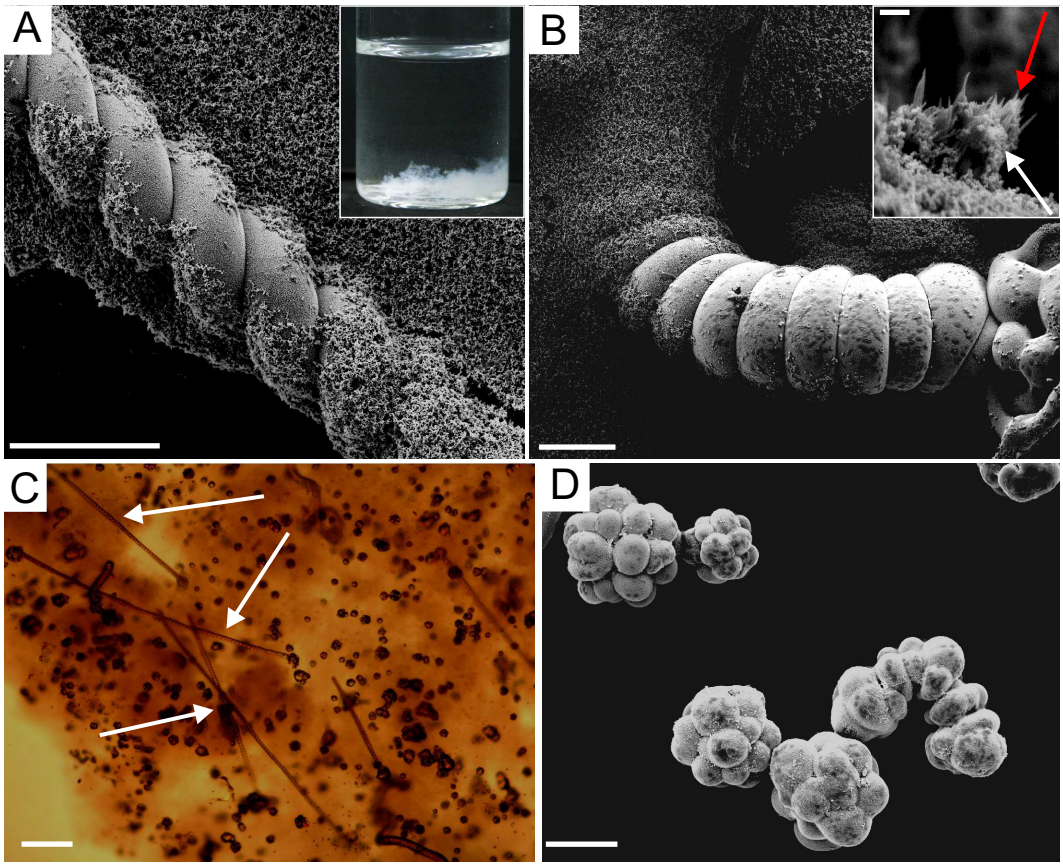

Figure 3.18. FESEM and optical micrographs of biomorphic $BaCO_3$ structures grown in samples containing 920 ppm SiO_2 after ageing for 1 day. A) Helicoidal filament formed within the gel sediment that settled from solution after about 10 min (as shown by the picture in the inset). The particle networks covering and surrounding the crystal aggregate are remnants of the gel matrix upon drying. B) Worm-like morphology, again grown within the gel body. Inset: close-up view of the nanoparticle networks, showing the onset of $BaCO_3$ crystallization (red arrows point to witherite needles) from temporarily stabilized amorphous domains (adjacent core-shell-shell particles marked by white arrow). C) Overview of crystal aggregates produced in the silica gel after 24 h. Note that helical filaments (indicated by the arrow) reach lengths up several millimeters. D) Cauliflower-like spherulites, similar to those obtained at a silica concentration of 750 ppm (cf. Figure 3.1F). Scale bars are 20 μm in (A), (B) and (D), 1 μm in the inset of (A), and 200 μm in (C).

early stages of the experiment (inset in Figure 3.18B). This suggests strongly that crystallization takes place via dissolution of the interstitial amorphous $BaCO_3$ layer and subsequent re-precipitation. Thereby, the carbonate fraction in the core-shell-shell particles is likely to act as a storage depot, which gradually releases Ba^{2+} and CO_3^{2-} ions for growth in its vicinity. The role of the outer silica skin would thus be to temporarily stabilize the inner carbonate layer (presumably by decelerating its re-dissolution) and, in doing so, keep the

actual solution supersaturation relatively low. In turn, the silica shell must be porous enough to permit exchange with the surrounding medium, as the occluded amorphous $BaCO_3$ would otherwise not dissolve.[92] Under these circumstances, the carbonate-containing gel matrix provides ideal conditions for the self-assembly of silica biomorphs, despite the nominally high initial supersaturation of the system. Finally, it can only be speculated about the fate of the external silica skin upon release of the enclosed $BaCO_3$ layer. With regard to the results of the leaching experiments, it seems most reasonable that the outer shell collapses onto the inner core and/or dissolves in the mother solution. In any case, partially hollow silica nanoparticles in the samples after crystallization was completed could not be trace.

At 1870 ppm SiO_2, distinct crystalline objects could not be observed at any stage (Figure 3.19), even if the samples were left in contact with the mother solution for weeks. Accordingly, SEM images of the suspended precipitates (isolated after 24 h) show distorted and more or less agglomerated spherical nanoparticles with no sign of crystallinity being discernible (Figure 3.19A), whereas TEM micrographs and ED data confirm the amorphous character of the particles and their core-shell-shell structure (Figure 3.19B). The absence of crystalline witherite is moreover verified by powder diffraction patterns, where no discrete reflections are observed (Figure 3.19C). Measurements of the mean particle diameter after distinct periods of ageing indicate that individual grains grow slightly during the first 5 minutes, from initially 100 ± 15 nm to 130 ± 15 nm. Subsequently, no further change in size could be distinguished. Tracing the Si/Ba atomic ratio as a function of ageing time further reveals a continuous increase of the Si content over an interval of 5 h after mixing. The highest jump in Si/Ba occurs between 1 and 5 minutes, that is, in parallel to the slight increase in the average particle size. This suggests that silica precipitation proceeds over longer frames of time on the surface of the nanoparticles. In a first step, this does obviously lead to widening of the outer silica shells (thus explaining why the external silica skins are often much thicker than the interstitial $BaCO_3$ layers), which effectively increases the apparent particle diameter. However, in a second stage (i.e. at times greater than 5 min), ongoing condensation does no longer cause the particles to grow larger, such that the observed further increase in the silica content must be due to densification of the outer shells, as found also in the case of $CaCO_3$.[92] In this manner, the external silica skins become more compact and less porous, so

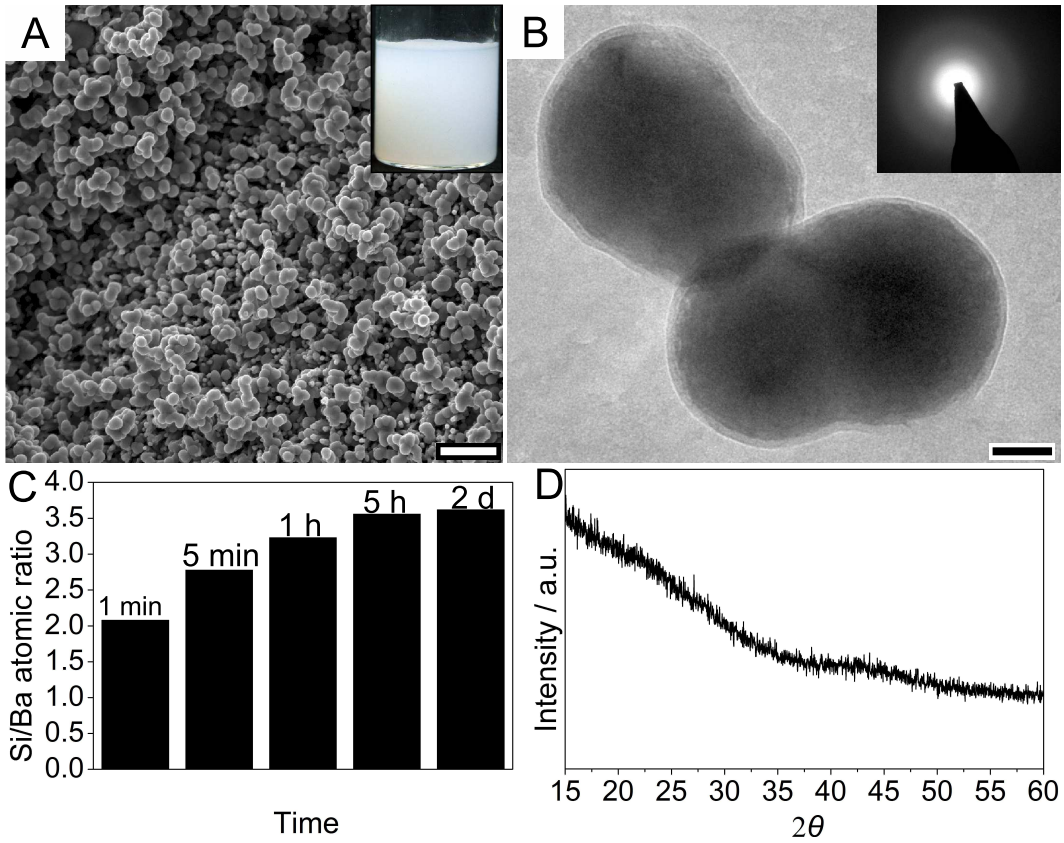

Figure 3.19. Long-term stabilization of amorphous barium carbonate in core-shell-shell particles at 1870 ppm SiO_2. A) FESEM image of precipitates isolated by filtration after ageing for 24 h (scale bar: 1 μm). Inset: photograph of the sample before filtration, demonstrating that the formed nanoparticles remain suspended in solution. B) Corresponding TEM micrograph, showing the layered structure of the particles (scale bar: 50 nm). The inserted ED pattern proves that the grains (and in particular their barium carbonate component) are still amorphous. C) Si/Ba atomic ratio determined for the amorphous nanoparticles after different ageing times by means of EDX spectroscopy. D) X-ray diffractogram of the isolated powder, confirming the absence of crystalline material.

that transport of reagents across this layer is impeded and dissolution of the enclosed amorphous $BaCO_3$ - as well as its transformation to crystalline witherite - cannot take place. We note that this holds essentially true for the alkaline conditions prevailing in the precipitation experiments, whereas stabilization of the amorphous phase can evidently not be maintained in acidic media (cf. Figure 3.13). This indicates that protonation of the outer silica layer during leaching results in structural changes, which render the shell pervious for ions and thus enable removal of the $BaCO_3$ component upon ageing.

3.5 Discussion

The collected data clearly demonstrate that added silica can have a dramatic influence on the mineralization of barium carbonate under precipitation conditions. At low silica contents (135-750 ppm), crystallization occurred immediately and the resulting elongated crystals were found to be branched to an extent that depends on the concentration of the additive. Similar growth behavior has been reported previously, however only at low supersaturation and as a function of time rather than silica concentration.[61,75,81,86] It was proposed that the obtained shapes originate from self-similar branching at non-crystallographic angles, induced by crystal growth poisoning of silica oligomers; this causes successive ramification of the initially pseudo-hexagonal core, eventually yielding spherulitic cauliflower-like architectures. The present results confirm this mechanism and suggest that crystal splitting is dramatically enhanced when the amount of added silica is increased (cf. Figure 3.1). Moreover, it is evident that fractal structures with extended dimensionality can be grown within minutes by a simple precipitation technique, and do not necessarily require slow crystallization rates in diffusion-based assays.

Our experiments have furthermore shown that direct mixing of $BaCl_2$ and Na_2CO_3 at sufficiently high silica concentrations leads to spontaneous self-assembly of composite nanoparticles consisting of a silica core, an intermediate layer of amorphous barium carbonate, and an outer shell of silica. These particles are either stable in solution for extended periods (1870 ppm SiO_2), or gradually release $BaCO_3$ units for the formation of crystalline biomimetic ultrastructures (920 ppm). A mechanism rationalizing the observed processes is depicted schematically in Figure 3.20. Regarding the detected composition of the nanoparticles (cf. Figure 3.8), it seems clear that silica is nucleated first to give amorphous spheres, which later make up the core volume of the hybrid particles. Condensation of silicate monomers and dimers (which are the dominant species in solution at pH 10.7-10.9[129–131] is likely to be triggered by divalent barium cations, which are capable of screening negative charges and thus aid in connecting individual units (Step 1 in Figure 3.20). Continued oligomerization then results in silicate polymers that, upon further cross-linking, will ultimately coagulate (again assisted by screening Ba^{2+} ions) into colloidal particles of amorphous silica (Step 2 in Figure 3.20, where blue spheres correspond to silica colloids).[129] It is worth noting that

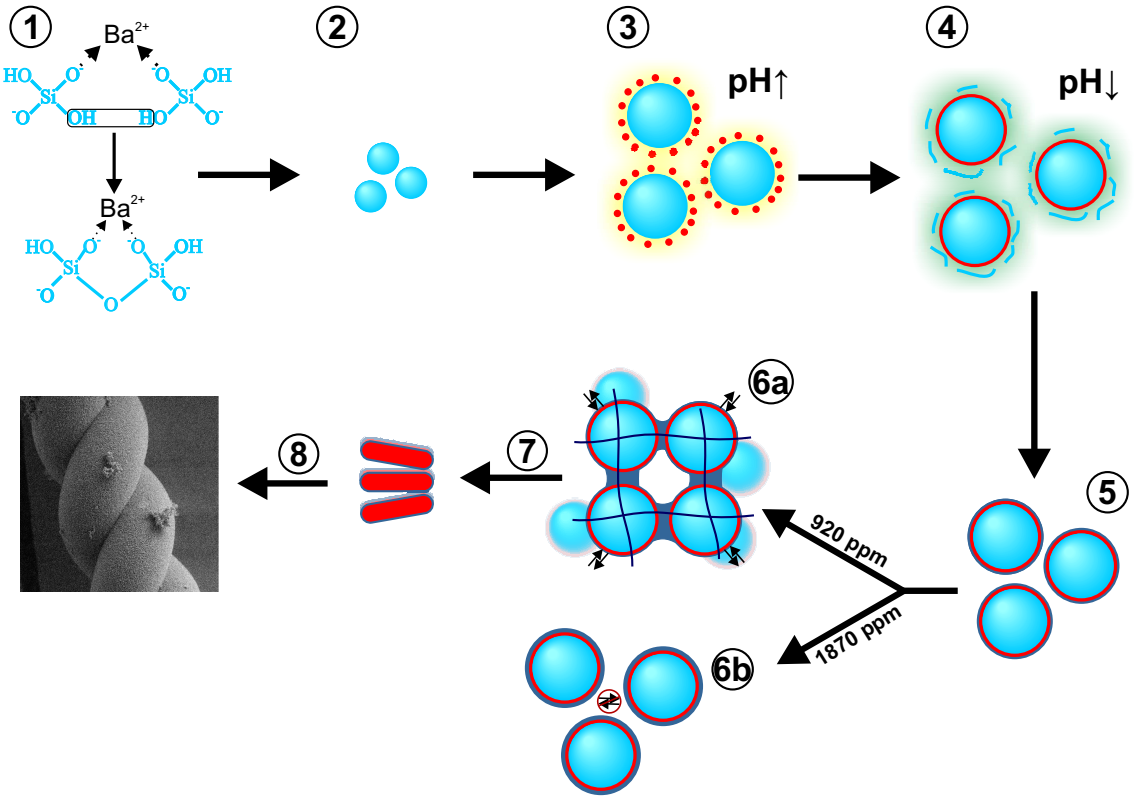

Figure 3.20. Schematic model for silica-mediated stabilization of amorphous barium carbonate and controlled self-assembly of biomimetic crystal ultrastructures. See the text for explanations. Note that structures are not drawn to relative scale.

the Ba^{2+} cations only catalyze condensation processes and are not actively incorporated to the forming siliceous phase to a large degree, as confirmed by reference experiments in the absence of carbonate (data not shown) and reported also in other studies.[129,132] As growth of the silica particles proceeds, the local pH at their surface is expected to increase relative to the bulk, because acidic silanol groups are consumed in the course of condensation ($(Si(OH)_3O^- + H^+ \longrightarrow Si(OH)_4 \longrightarrow$ "SiO_2" + 2 H_2O).[61,81,86] This, in turn, will provoke a shift in the bicarbonate-carbonate equilibrium towards the side of CO_3^{2-} and thus generate locally elevated supersaturation levels of $BaCO_3$ in the vicinity of the evolving silica colloids. Consequently, nucleation of barium carbonate takes place preferentially near the surface of the nanoparticles (Step 3 in Figure 3.20, where the $BaCO_3$ nuclei are drawn as red dots and the envisaged pH gradient is indicated in yellow). Subsequent growth of the nuclei inevitably results in coating of the silica particles by a layer of barium carbonate, which apparently is amorphous in first instance. However, ongoing $BaCO_3$ precipitation now decreases the local pH ($Ba^{2+} + HCO_3^- \longrightarrow BaCO_3 + H^+$), since bicarbonate ions (which coexist in significant

fractions with CO_3^{2-} at the given pH values[92]) will dissociate in order to restore equilibrium speciation at the particle surface (Step 4 in Figure 3.20, where the opposite pH gradient is shaded in green). This affects the solubility of silica in the local environment, as protonation of silicate species will be enhanced at lower pH, facilitating condensation into higher oligomers (blue chains in Figure 3.20) and eventually leading to the deposition of a continuous silica skin around the $BaCO_3$ layer (Step 5 in Figure 3.20).[61,81,86,92]

Depending on the silica concentration, the as-formed core-shell-shell nanoparticles display different aggregation behavior and temporal stability. At 920 ppm SiO_2, agglomeration is quite pronounced and the particles soon build networks, which ultimately segregate from solution as a silica hydrogel hosting embedded amorphous carbonate precursors (Step 6a in Figure 3.20). Moreover, the silica shells around the $BaCO_3$ layers appear to be porous under these conditions and therefore allow the amorphous phase to be gradually dissolved, inducing carbonate crystallization in the surrounding gel medium. This yields silica-stabilized $BaCO_3$ nanorods (Step 7 in Figure 3.20), which self-assemble into biomimetic aggregates displaying complex morphologies like helicoids (Step 8), as observed previously for $BaCO_3$ crystallization in silica gels at low supersaturation.[61,68,75,81,86,125] At 1870 ppm SiO_2, aggregation of primary grains is largely suppressed due to their higher surface charge, and the particles hence remain suspended in solution rather than coagulate (Step 6b in Figure 3.20). In addition, the outer silica shells are dense enough to block active transport of reagents, such that dissolution of the enclosed $BaCO_3$ layer is prevented in the long term. This provides further evidence for the ability of silica to freeze crystallization processes at an early stage and stabilize even highly transient precursor phases, in line with results reported for $CaCO_3$ in earlier work.[92,132]

A most surprising observation is that silica precipitation precedes nucleation of carbonate in the present experiments, whereas an inverse scenario (i.e. a carbonate core sheathed by a layer of silica) was found when Ca^{2+} was used instead of Ba^{2+}.[92] In view of the proposed mechanism (Figure 3.20), this means that interactions between the barium cations and silicate species (Step 1) are initially favored over those of Ba^{2+} and CO_3^{2-}. Such behavior is counter-intuitive at first glance, since Ca^{2+} ions are known to be more powerful coagulants for silica than Ba^{2+} (due to their higher polarity).[133,134] Consequently, cation-induced silica

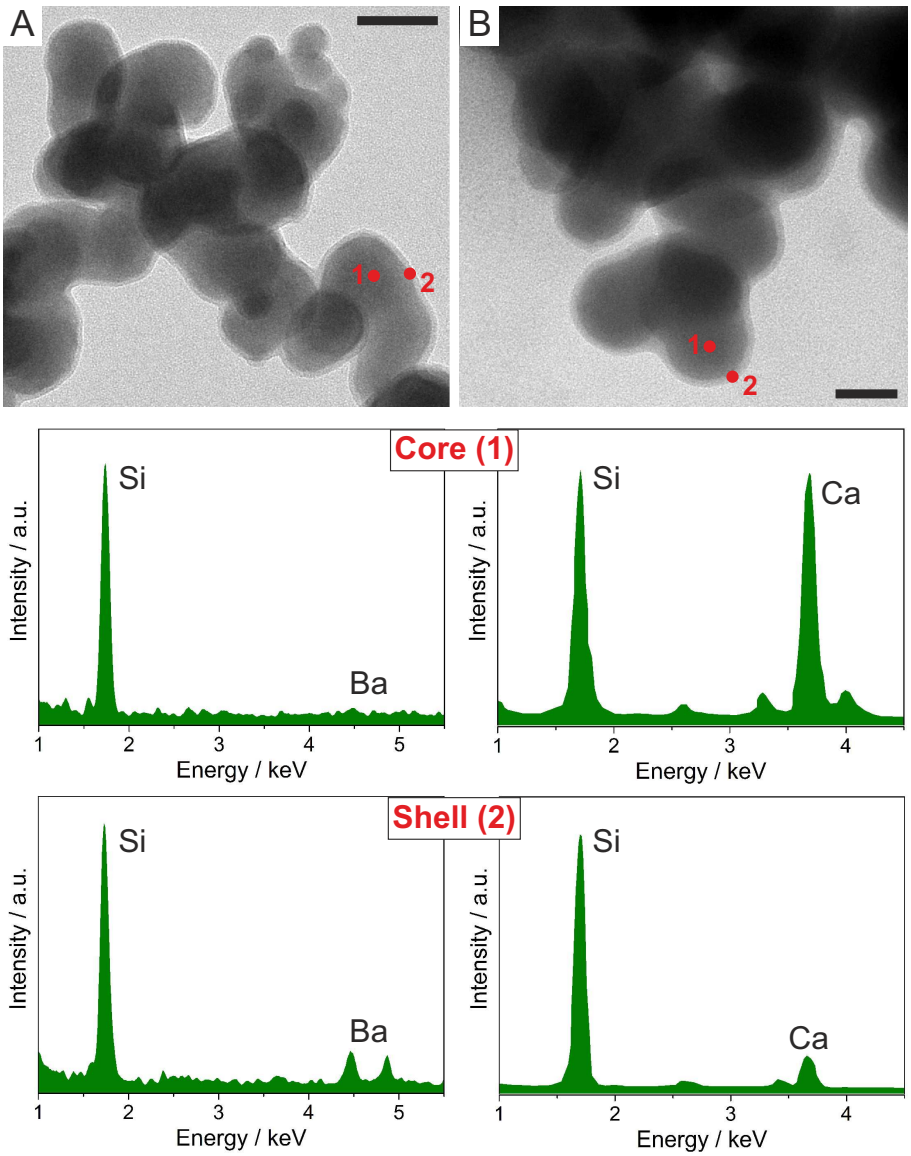

Figure 3.21. TEM studies of nanoparticles formed upon precipitation of (A) $BaCO_3$ and (B) $CaCO_3$ in alkaline solutions containing 750 ppm silica. In both cases, electron micrographs disclose a core-shell structure (upper panels). However, EDX point analyses performed on the core part (middle panels) and the outer shell (lower panels) demonstrate that the composition of the particles is substantially different: while the nanostructures obtained with Ba^{2+} consist of a silica-rich core that is surrounded by a layer of $BaCO_3$, those grown with Ca^{2+} exhibit an inverse constitution, i.e. a $CaCO_3$ core sheathed by a skin of silica. Scale bars are 50 nm.

precipitation should be more pronounced in the case of Ca^{2+}. As this is not observed, the interactions between barium and carbonate must be significantly weaker than with calcium, so that more free Ba^{2+} ions are available for silica coagulation in the beginning. This notion is supported by titration experiments, in which $CaCl_2/BaCl_2$ was slowly added to dilute car-

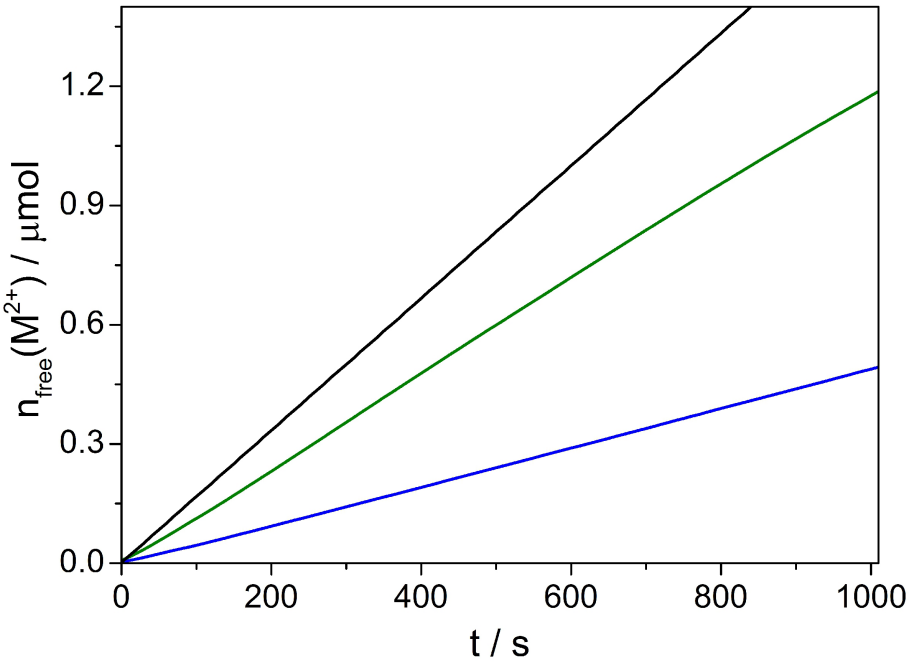

Figure 3.22. Time-dependent development of the amount of free Ba^{2+} (green) or respectively Ca^{2+} (blue) detected upon addition of 10 mM $BaCl_2$/$CaCl_2$ into 10 mM carbonate buffer at pH 9.75, as compared to the dosed amount (black). It is evident that binding of Ba^{2+} by CO_3^{2-} is much less pronounced than for Ca^{2+} (on average, about 70% of the added cations are bound in the case of calcium and only around 28% for barium).

bonate solutions and the amount of free cations was simultaneously measured by means of ion-selective electrodes. Corresponding data evidence that binding of Ba^{2+} and CO_3^{2-} prior to nucleation is much less distinct than for Ca^{2+} and CO_3^{2-} (Figure 3.22), thus rationalizing the observed different precipitation behavior. Another possible explanation is that the solubility product of amorphous barium carbonate is noticeably higher than that of ACC, again leading to a higher free concentration of screening Ba^{2+} cations. In any case, it is obvious that a straightforward replacement of Ca^{2+} by Ba^{2+} yields hybrid nanoparticles with substantially dissimilar composition. This becomes most evident when comparing particles produced with the two cations under otherwise exact same conditions. For example, nanoparticles isolated during the very early stages of precipitation at 750 ppm SiO_2 exhibit a core-shell structure in both cases. Their chemical constitution, however, is inverted as described above and demonstrated in the Supporting Information (Figure 3.21). For $CaCO_3$, this results in stabilization of ACC because the carbonate core is protected against transformation by its outer silica skin already at low SiO_2 contents.[92] By contrast, no such stabilization is observed under

these conditions for $BaCO_3$, since the carbonate component is located in the shell of the particles and thus directly exposed to the surrounding medium. This applies for the given silica concentration of 750 ppm, where no external silica skin is formed around the carbonate layer (cf. Figure 3.21); therefore, crystallization of $BaCO_3$ takes place rapidly (cf. Figure 3.1 and 3.2). In turn, at higher silica contents, sheathing of the carbonate-rich regions by another layer of silica enables stabilization of the amorphous phase also for $BaCO_3$ and inhibits (or prevents) its conversion into the stable crystalline polymorph. Finally, it is worth mentioning that a change in the composition of the nanoparticles, as observed here with different cations, could also be induced simply by an increase of the silica concentration. That is, nanostructures consisting of a silica core and a carbonate shell might be formed with $CaCO_3$ as well, if the silica content exceeds a certain threshold. Although there were no indications for any such transition in our earlier work,[92] further experiments will have to be carried out in order to study the precipitation behavior at high silica concentrations in more detail.

3.6 Conclusions

Mineralization of barium carbonate in silica-containing media can lead to a broad variety of shapes and structures, which happen to be much more complex than one may assume for such a simple inorganic system. The present work performed in this chapter has extended the applicability of this concept from the formation of fractal aggregates and biomorphs to the synthesis of elaborate core-shell-shell nanoparticles, comprising a layer of amorphous $BaCO_3$ that is sandwiched between two domains of silica. This was achieved by direct mixing of the components at nominally high carbonate supersaturation levels, instead of using controlled crystallization conditions in diffusion-based setups as commonly applied in previous studies[59,60,62,63,67–69,74–76,80–82,84–87,125,126] and in chapter 5-7. Spontaneous growth of the hybrid nanoparticles was explained in the framework of local pH gradients, which are expected to exist near silica and carbonate surfaces evolving in alkaline solutions.[61,81,86,92] In particular, precipitation of carbonate causes a decrease of pH in its vicinity, whereas polycondensation of silica has an opposite effect. Since the two components show inverse trends with pH regarding their solubility, local pH variations during growth of one of the minerals causes precipitation of the other.

In this way, the solution speciations of silica and carbonate are coupled and, depending on specific parameters like supersaturation or the nature of the cation, this interplay can result in different structure evolution. For example, co-precipitating calcium carbonate and silica yields nanoparticles of ACC that are coated with a single layer of silica (i.e. there is one coupled mineralization event).[92] In turn, if crystallization is carried out at low supersaturation, the components self-assemble into biomorphic materials, which consist of numerous silica-coated nanocrystals as a result of continuous alternating precipitation (thus there are an infinite number of coupled mineralization events).[61,81,86] The core-shell-shell particles obtained in this chapter represent a state that is intermediate to the previous ones, as their formation involves two such coupled precipitation events and the local pH undergoes at least oscillation period (whereas countless successive oscillations are envisaged in the case of silica biomorphs).[61] Finally, it can be noted that intermediate storage of mineral in stabilized amorphous domains and their subsequent use as depots supplying growth units for structured crystallization - as observed for silica-embedded barium carbonate in this work - bears analogy to concepts applied by Nature in biomineralization,[135] and thus supports the biomimetic character of these inorganic systems.

4 New Insights into the Early Stages of Silica-Controlled Barium Carbonate Crystallization

4.1 Abstract

Recent work has demonstrated that the dynamic interplay between silica and carbonate during co-precipitation can result in the self-assembly of unusual, highly complex crystal architectures with morphologies and textures resembling those typically displayed by biogenic minerals. These so-called biomorphs were shown to be composed of uniform elongated carbonate nanoparticles that are arranged according to a specific order over mesoscopic scales. In this chapter, the circumstances leading to the continuous formation and stabilization of such well-defined nanometric building units in these inorganic systems are investigated. For this purpose, in-situ potentiometric titration measurements were carried out in order to monitor and quantify the influence of silica on both the nucleation and early growth stages of barium carbonate crystallisation in alkaline media at constant pH. Complementarily, the nature and composition of particles occurring at different times in samples under various conditions were characterized ex-situ by means of high-resolution electron microscopy and elemental analysis. The collected data clearly evidence that added silica affects carbonate crystallization from the very beginning on (i.e. already prior to, during, and shortly after nucleation), eventually arresting growth at the nanoscale by cementation of $BaCO_3$ particles within a siliceous matrix. The findings thus shed novel light on the fundamental processes driving bottom-up self-organisation in silica-carbonate materials and, for the first time, pro-

vide a direct experimental proof that silicate species are responsible for the miniaturization of carbonate crystals during growth of biomorphs, hence confirming previously discussed theoretical models of their formation mechanism.

4.2 Introduction

Modern approaches for the design of advanced materials with specific properties often follow bottom-up synthesis strategies starting from simple, molecular-scale components.[136,137] Based on this concept, it has for instance been possible to induce concerted self-assembly of carbonate minerals into elaborate, higher-order architectures by using custom-designed block copolymers as structure-directing agents.[44,46,55] Such studies are typically inspired by natural biomineralization, where an organic matrix controls the crystallization of inorganic matter to produce superior hybrid structures.[25,138] However, there are also other examples for complex mineralization phenomena, which do not require organic species but may readily occur in purely inorganic environments. Among these, the processes observed during precipitation of alkaline-earth carbonates into alkaline, silica-containing media are probably the most prominent and well-studied case.[59–62,67,68,74,75,81,84–87,125] Under the influence of dissolved silicate as a crystallization modifier, metal carbonates (usually $BaCO_3$) can indeed assemble spontaneously into a range of sinuously shaped non-crystallographic aggregates (such as regular helicoids), which mimic products from biomineralization closely in terms of morphology and internal hierarchy, and therefore were termed "silica-carbonate biomorphs".[62,63,66] The structural complexity of these peculiar materials relies on the fact that they are constituted by a multitude of uniform carbonate nanocrystals, which are largely co-oriented and thus generate mesoscopic order in the mature aggregates (as a third level of hierarchy in addition to molecular ordering at the nanometer- and morphological control at the micron-scale).[61,67]

After a recent surge of interest in this field,[61,67,68,74,75,81,84–87,125] it has been proposed that the formation of biomorphs is driven by an autocatalytic co-precipitation cycle, in which the components are alternately mineralized due to their opposite trends of solubility with pH.[81,86,87] In essence, it is assumed that growth of carbonate particles in alkaline solutions is accompanied by a reduction of the local pH (with respect to the bulk), due to reinforced

dissociation of bicarbonate nearby active surfaces ($Ba^{2+} + HCO_3^- \longrightarrow BaCO_3 + H^+$). This pH gradient leads to enhanced protonation of silicate species in the vicinity of the carbonate particles, triggering condensation reactions and finally resulting in precipitation of a layer of amorphous silica around the nanocrystals soon after nucleation ($SiO(OH)_3^- + H^+ \longrightarrow Si(OH)_4 \longrightarrow SiO_2 + 2\ H_2O$).[61,81,86,87,92] As polymerization of silica proceeds at the surface, the local pH is in turn re-increased (due to continuous consumption of acidic silanol groups during condensation), thus raising the local carbonate supersaturation ($HCO_3^- + OH^- \longrightarrow CO_3^{2-} + H_2O$) and ultimately facilitating nucleation of novel $BaCO_3$ crystallites, which by themselves will be cemented by silica in the following. This feedback loop is thought to ensure constant supply of the growing aggregates with nanometric building blocks, and hence represents the driving force for ordered polycrystalline mineralization.[61,81,86,87]

In view of the model outlined above, one would expect that each of the nanorods constituting the final crystal aggregates is coated by an individual skin of silica. Indeed, corresponding core-shell structures could be experimentally verified for hybrid nanoparticles of amorphous calcium carbonate (ACC)[75] or barium carbonate and silica produced at high supersaturation (cf. chapter 3).[92] However, direct analyses on thin sections of mature biomorphs only confirmed the presence of small amounts of silica on the nanocrystals, whereas distinct outer layers could not be observed. Consequently, the detailed role of the silica species in the stabilization of $BaCO_3$ nanoparticle units during growth of biomorphs has not yet been clarified. Therefore, a titration-based technique was used in order to gain deeper insight into the pre- and early post-nucleation stages of barium carbonate crystallization under the influence of dissolved silica, which are considered to be crucial steps in the progress of bottom-up self-assembly. In particular, precipitation assays were employed in which the supersaturation of $BaCO_3$ was gradually increased up to the point of nucleation and beyond, while the solution chemistry (and the effect of silica thereon) was continually monitored. Similar experiments have recently been employed to investigate the nucleation of calcium carbonate in general,[93,139] as well as to study the impact of various soluble additives on $CaCO_3$ crystallization pathways.[94–97] In line with earlier work, precipitation was induced by slowly adding dilute barium chloride solution into an excess of sodium carbonate/bicarbonate buffer containing different amounts of dissolved silica, at concentrations and pH levels simulating the

conditions where growth of silica biomorphs is typically observed.[61,67,69,75,76,80,125] During addition, the Ba^{2+} potential was recorded in situ with the aid of an ion-selective electrode, while the pH was kept constant by back-titration with sodium hydroxide. Based on the measured values, actual concentrations of free and bound barium and carbonate ions were calculated, and used to compare time-dependent progressions obtained for different silica contents to reference scenarios traced in the absence of the additive. The resulting data are then combined with ex-situ analyses of nucleated particles, carried out by means of high-resolution electron microscopy and energy-dispersive X-ray (EDX) spectroscopy. Taken together, the findings in this chapter paint a consistent picture for the effect of silica on the nucleation and growth of barium carbonate, which can be extrapolated to explain the role of the additive in the formation of biomorphs at the nanometer level.

4.3 Experimentals

4.3.1 pH-constant titration measurements

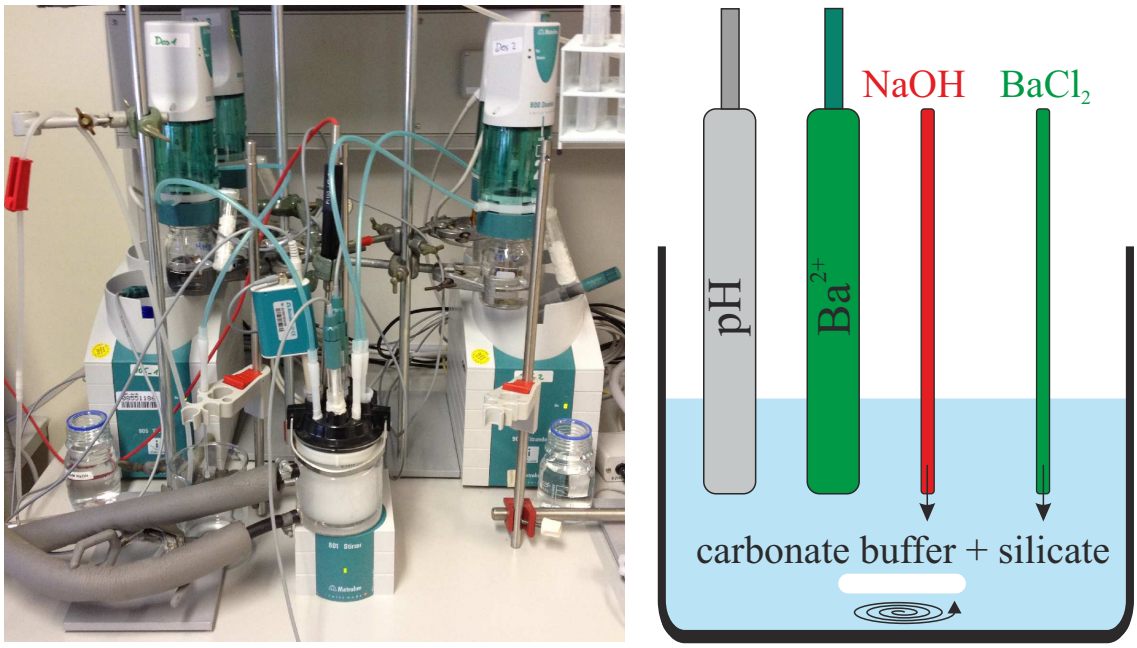

Figure 4.1. (left) Photograph and schematical drawing (right) of the titration setup.

Titration measurements were performed on a commercially available setup manufactured by Metrohm (Filderstadt, Germany). A photograph of the device and a scheme depicting the setup is presented in Figure 4.1. It consists of a Titrando 809 device that controls two

attached Dosino 807 dosing units, capable of dispensing liquids at volume steps of down to 0.2 μL. Experiments were carried out in an oil-jacketed vessel held at $25.0 \pm 0.2°C$, into which initially 50 mL of 5 mM carbonate buffer solution were given. Buffers were prepared by mixing appropriate volumes of 5 mM Na_2CO_3 (Aldrich, anhydrous, $\geq$ 99.8%) and 5 mM $NaHCO_3$ (Riedel de-Haën, $\geq$ 99.7%), in order to achieve final pH values of 10, 10.5 and 11, respectively (the latter being the pH of a neat 5 mM Na_2CO_3 solution). The three distinct pH levels were chosen because the formation of biomorphs is most efficient in this range as presented in detail in chapter 5. The concentration of the carbonate buffers used for crystallization had to be reduced from 10 to 5 mM as compared to previous studies,[93,97] as it turned out that $BaCO_3$ precipitated preferentially at the outlet of the $BaCl_2$ solution in 10 mM Na_2CO_3/$NaHCO_3$ at all studied pH values. Silica was introduced by dissolving 5 mM Na_2CO_3 in different dilutions of commercial water glass (concentrated sodium silicate solution, Aldrich, reagent grade), leading to final SiO_2 concentrations of 300, 600, and 1200 ppm (500-600 ppm being the usual silica content of mother solutions in a typical synthesis of biomorphs).[61,67,69,75,76,80,125] The pH of the silica/carbonate mixtures was subsequently adjusted to the particular target value by using aliquots of either 1 M NaOH or 1 M HCl (both Merck, p.a.), whereby the concomitant dilution was negligible.

In the actual measurements, 10 mM barium chloride solution (prepared from $BaCl_2 \cdot 2\,H_2O$, Riedel de-Haën, $\geq$ 99%) was continuously added to the buffer at a rate of 0.01 mL min^{-1} (with or without silica and at different pH levels). The pH of the buffer was kept constant at its set value through automatic counter-titration with 10 mM sodium hydroxide (Riedel de-Haën, standard solution). During titration, the Ba^{2+} potential and the pH of the sample were monitored on-line by means of an ion-selective electrode (ISE; Mettler-Toledo, DX337-Ba) and a flat-membrane glass electrode (Metrohm, No. 6.0508.110), which simultaneously served as reference for the Ba^{2+}-selective half-cell. Calibration of the ISE was achieved by titrating $BaCl_2$ into water (brought to the same pH as the respective buffer by NaOH addition) and measuring the Ba^{2+} potential as a function of the known solution concentration, using identical settings as in the precipitation assay. The glass electrode was calibrated weekly with buffers of pH 4.0, 7.0 and 9.0 (purchased from Metrohm). After every experiment, beaker, burette tips and electrodes were washed with acetic acid (10%) to

remove crystallized carbonate, and subsequently rinsed with water.

4.3.2 Data treatment

The recorded Ba^{2+} potentials were first corrected for the interfering influence of sodium ions (using the Nikolsky-Eisenman equation[140] and the electrode selectivity coefficient for Na^+ given by the manufacturer, $\log K_{Na}$ = -0.9) and then translated into apparent free concentrations via the calibration data obtained in water. Since the volumes added to the reaction vessel are known at all times, free and bound amounts of barium ions can readily be computed from these concentrations and, when assuming 1:1 association of Ba^{2+} and CO_3^{2-} (as demonstrated explicitly for $CaCO_3$),[93,139] used to derive corresponding values for the carbonate species in the system. Based thereon, time-dependent profiles for the free ion concentration products (IP = $[Ba_2^+]_{free} \cdot [CO_3^{2-}]_{free}$) were calculated and are discussed in the following.

4.3.3 TEM and EDX analyses

Precipitates formed in the titration experiments were isolated at distinct times by filtering the samples through 200 nm membranes (Whatman, mixed cellulose esters) and washing the retained particles with ethanol (Baker, p.a.). The dried powder was then re-dispersed in ethanol, and aliquots of the resulting suspension were placed on carbon-filmed copper grids (Plano GmbH, 200 mesh). Excess liquid was carefully removed with a small piece of filter paper, before allowing the remaining precipitates to dry in air.

The as-obtained particles were investigated routinely with a Philips CM 12 microscope at an acceleration voltage of 120 kV. Images were taken using a Gatan TV 673 wide-angle camera and a TVIPS slow scan camera with external control utilising the EM-MENU 4 software. Selected specimens were further analysed at high resolution with a Tecnai F30 STwin electron microscope (300 kV, field-emission gun, spherical aberration constant Cs = 1.2 mm). STEM Z-contrast images were taken with a HAADF detector. In order to reveal the composition of the particles, elemental mapping was performed on selected areas by means of an EDAX system (Si/Li detector) mounted on the microscope.

For SEM-EDX analysis, the filtered and dried powders were directly transferred onto conducted double-adhesive carbon tapes which were fixed on standard aluminum pin tubs. Sam-

ples were studied using a Hitachi TM 3000 table top SEM operated at an acceleration voltage of 15 kV and a working distance of 10 mm. EDX measurements were performed with the aid of an installed Quantax 70 EDX detector (Bruker). Spectra were recorded from not less than three different positions on the stub, and results were averaged for a given specimen.

4.4 Results

4.4.1 In-situ potentiometric titration

Figure 4.2 shows the temporal evolution of the free ion products detected upon titration of barium chloride into carbonate buffers at different pH and silica contents. Regarding at first the reference experiments with no added silica (black curves), it is evident that the free ion product increases more or less linearly with time, until a critical point is reached and nucleation of $BaCO_3$ occurs (maximum of the curve). Subsequently, the concentration of free Ba^{2+} and CO_3^{2-} ions in solution drops sharply and then gradually approaches a constant level that corresponds to the solubility of the initially precipitated phase. Comparison of measured solubilities (IP $\approx$ 1-2 $\cdot 10^{-8}$ M^2)[141] suggests that under the given conditions, barium carbonate nucleates in an amorphous state, which exhibits a solubility similar to that of ACC nanoparticles produced in analogous experiments with $CaCO_3$[93,97] and soon transforms into a crystalline phase when left in contact with the mother solution (see below). Alternatively, one may speculate that the higher solubility observed in the titrations reflects differences in the thermodynamic stability between bulk and nanosized witherite, as reported previously for other minerals.[142]

Apart from that, the amount of free Ba^{2+}detected in solution prior to nucleation is significantly lower than the dosed amount (see Figure 4.3), indicating the formation of $BaCO_3$ ion pairs and/or clusters as in the case of $CaCO_3$.[93] In fact, about 32, 52 and 65 % of the added cations are bound in the prenucleation regime at pH 10, 10.5 and 11, respectively. Thus, the fraction of Ba^{2+} residing in ion associates is by trend smaller than what has been observed for Ca^{2+} under similar conditions (about 75 % bound at pH 10[93]), suggesting that $BaCO_3$ ion pairs/clusters are somewhat less stable than their $CaCO_3$ counterparts. Finally, it is worth mentioning that the time of nucleation does not vary significantly with pH (3140, 2810 and 3470 s at pH 10, 10.5 and 11) while the critical supersaturation required for nucleation to

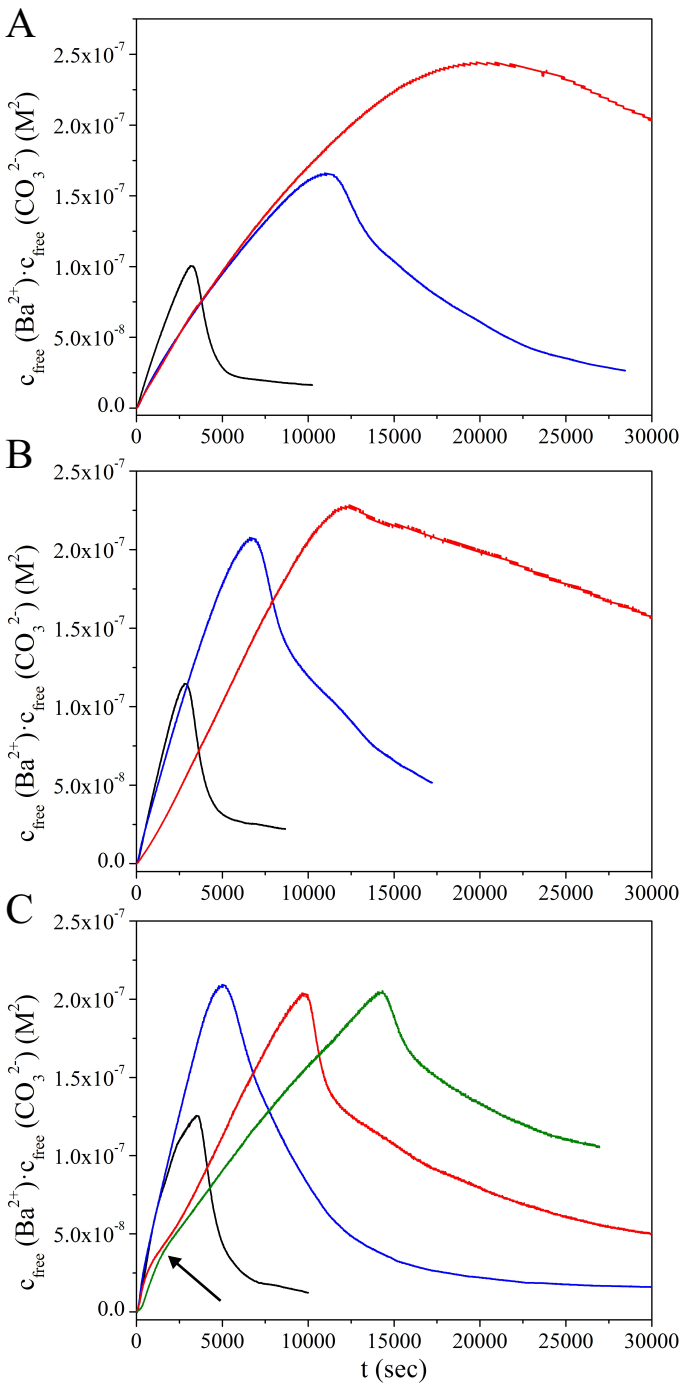

Figure 4.2. Time-dependent profiles for the free $BaCO_3$ ion products traced during continuous addition of 10 mM $BaCl_2$ to 5 mM Na_2CO_3/$NaHCO_3$ buffers at (A) pH 10, (B) pH 10.5, and (C) pH 11. Experiments were performed in the absence of silica (black curves) and in the presence of 300 ppm (blue curves), 600 ppm (red curves) and 1200 ppm SiO_2 (green curve, only measured for pH 11).

occur increases slightly as the pH is raised (IP $\approx 1 \cdot 10^{-7}$, $1.15 \cdot 10^{-7}$, and $1.26 \cdot 10^{-7}$ M^2 at the point of nucleation at pH 10, 10.5 and 11, respectively). This, as well as the larger fraction of bound Ba^{2+} at higher pH , can be ascribed to changes in the carbonate/bicarbonate

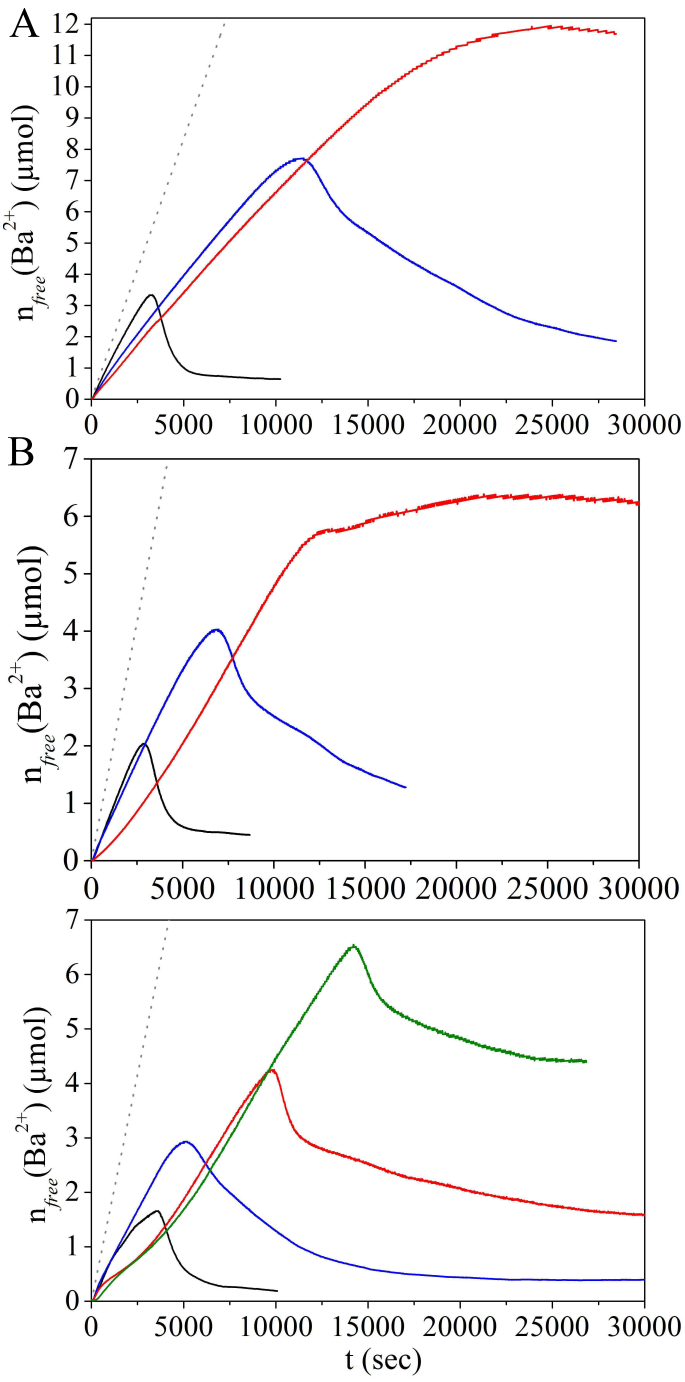

Figure 4.3. Time-dependent progressions of the amount of free Ba^{2+} detected upon titration of 10 mM $BaCl_2$ into 5 mM carbonate buffer at pH (A) 10.0, (B) 10.5, and (C) 11.0 in the absence of silica (black curves) and in the presence of 300 (blue curves), 600 (red curves) and 1200 ppm SiO_2 (green curve, only for pH 11). The dotted grey lines represent the dosed amount of Ba^{2+}.

buffer equilibrium (≈ 30% CO_3^{2-} co-existing with HCO_3^- in solution at pH 10, vs. ≈ 80 % at pH 11).

The effect of silica as an additive in $BaCO_3$ precipitation can now be evaluated by compar-

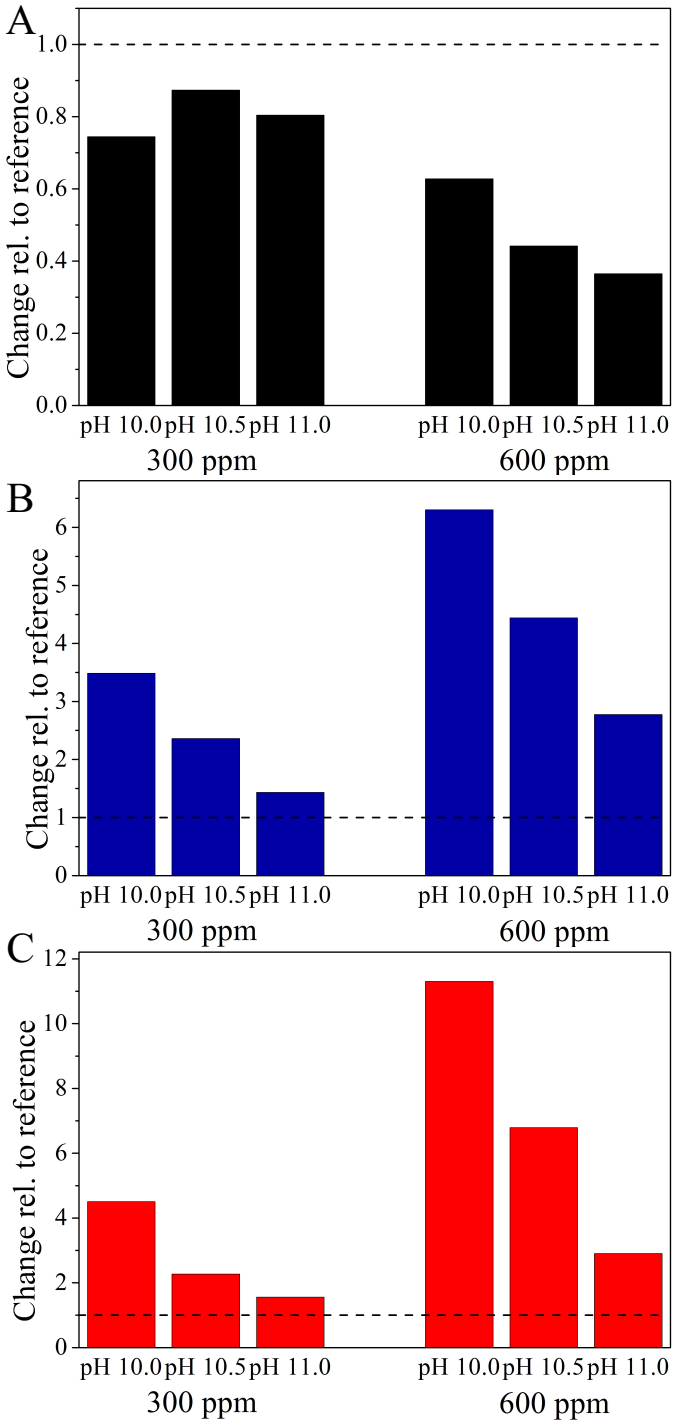

Figure 4.4. Bar plots illustrating the effect of added silica on (A) the slope of the titration curves in the prenucleation stage, (B) the nucleation time, and (C) the solubility of the initially precipitated phase for different buffer pH levels and analytical silica concentrations (as indicated). Results are given as relative changes to the silicate-free reference experiments at each pH, that is, as quotients of the respective values determined in the presence and in the absence of silica.

ing titration profiles obtained in its presence to those seen in the reference experiments. In line with previous work on $CaCO_3$,[94,97] three distinct aspects in the curves are discussed: i) the slope of the temporal increase in free Ba^{2+} prior to nucleation (reflecting the stability of ion associates in solution), ii) the time of nucleation and any occurring delay of nucleation, and iii) the level of the free ion product after nucleation (indicating the solubility/stability of the precipitated phase as well as possible interactions with formed particles, e.g. growth inhibition). Changes in these three parameters relative to the reference scenario are outlined as a function of pH and silica concentration in Figure 4.4.

Looking first at the prenucleation slopes (Figure 4.4A), one can observe that added silica leads to a flattening of the curves, the extent of which depends on both the pH and the SiO_2 content. Linear fits to the experimental $n_{free}(Ba^{2+})$-time data (cf. Figure 4.3) show that while the slopes are reduced to 40-60% of the reference value under the influence of 600 ppm silica at all studied pH levels, there is a clear variation with pH at 300 ppm: at both pH 10.5 and 11, the slope remains virtually unchanged with respect to the reference, whereas a significant decrease (to ca. 75%) is seen at pH 10 (cf. Figure 4.4A). Generally, flatter slopes mean an enhanced binding tendency for the barium ions and thus indicate that prenucleation species are stabilized by the investigated additive.[97] Obviously, this effect is more pronounced at lower pH (as is also evident from the data at 600 ppm SiO_2), where the speciation of silica in solution is shifted towards higher oligomers.[129,131] This suggests that oligomeric and/or polymeric silicate species are more efficient in stabilization than the mono- and dimers prevailing at higher pH.[130] An interesting feature occurring at pH 11 is that the curves recorded for 600 and 1200 ppm SiO_2 follow the reference in the beginning, before they bend down after about 1000-2000 s (see arrow in Figure 4.2C) to subsequently increase at a smaller slope. This might hint at the formation of larger silicate oligomers during an initial induction period (likely due to Ba^{2+}-induced silica condensation[129]), which then - above some critical concentration - influence $BaCO_3$ prenucleation complexes in a way related to what is found for lower pH values.

Similar trends can be distinguished concerning the nucleation time (Figure 4.4B). Here, it is evident that the presence of silica causes a noticeable delay of nucleation, and that the degree of retardation depends on both the pH and the silica concentration (see also Figure

4.2). Corresponding inhibition factors (IF, defined as the ratio of the nucleation time in the presence of silica to that in the additive-free reference experiment) evidence that the influence of silica becomes much more distinct when its concentration is raised (IF = 3.5 and 6.3 respectively for 300 and 600 ppm at pH 10). On the other hand, for a given silica content, the data show a clear and consistent decrease in the inhibition ability with increasing pH so that, at 300 ppm SiO_2 and pH 11, there is merely a minor extent of retardation discernible (IF = 1.4). Consequently, oligomeric silicates seem to be much more suitable for impeding nucleation than monomers and dimers, in analogy to what has been observed with regard to the stabilization of prenucleation species (Figure 4.4A).

Nevertheless, the most drastic impact of silica on the early stages of $BaCO_3$ crystallization can be seen in the apparent solubility of the initially precipitated phase (Figure 4.4C), which is higher in all silica-containing samples than in the references without silica. In fact, the free ion product measured at the end of the experiment at pH 10 and 600 ppm SiO_2 exceeds that of the corresponding reference by a factor of more than 10. Another striking aspect of the precipitation behavior in the presence of silica is that the level of free ions in solution does not fall to a constant solubility within the duration of the measurements (see Figure 4.2). Rather, the free ion product decreases continuously and at a rate that is markedly slower than in the reference experiment. In some cases (300 ppm SiO_2 at pH 10 and 10.5, and 600/1200 ppm at pH 11), we observed an initially steep decline which, at a more or less pronounced breakpoint, turns into a much flatter decay in the following. These findings suggest that the precipitated phase is not in equilibrium with the surrounding solution, so that its actual solubility product cannot be established (at least not during the studied period, except for the sample at pH 11 and 300 ppm SiO_2). In other words, the nucleated particles cannot grow freely, likely because added silica inhibits also growth of $BaCO_3$ (as will be further discussed below). Again, the effects become dramatically stronger when the concentration of silica is increased and/or the pH of the buffer is decreased (cf. Figure 4.4C), indicating that growth inhibition is likewise performed in a more effective manner by oligomeric silicate species, which are more abundant at lower pH.

4.4.2 Characterization of nucleated particles

The precipitates formed at the end of each titration experiment were further analysed by means of transmission electron microscopy (Figure 4.5). In the absence of silica (Figure 4.5A-C), crystals with rod- or needle-like shapes and sizes in the micron-range (typically about 5 μm in length and 1 μm in width) were obtained, with no distinct variations being discernible between the samples produced at different pH values. Electron diffraction pat-

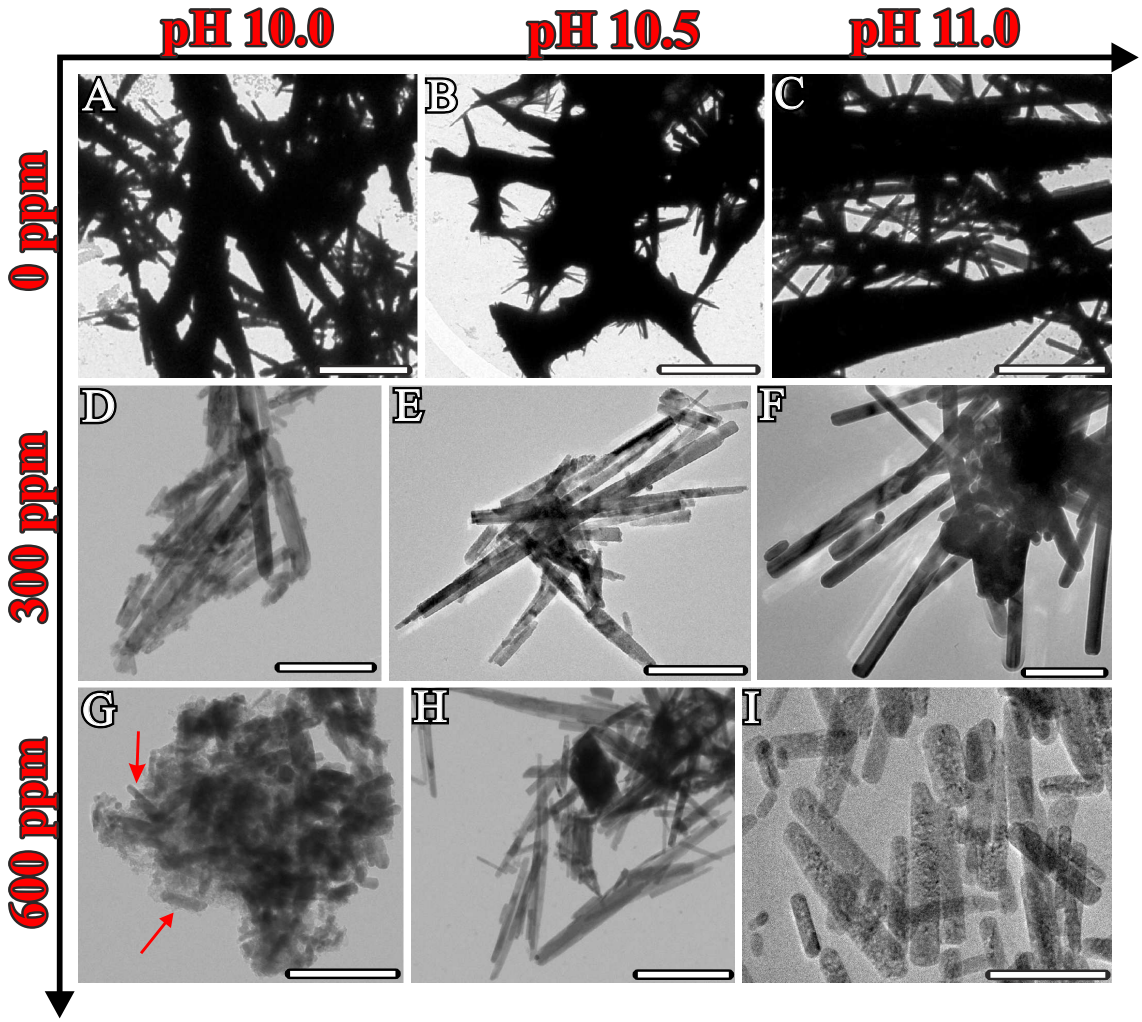

Figure 4.5. TEM images of crystals isolated at the end of titration experiments carried out at pH 10 (A, D, G), pH 10.5 (B, E, H), and pH 11 (C, F, I), in the presence of 0 (A-C), 300 (D-F), and 600 ppm silica (G-I). Note that addition of silica leads to a progressive miniaturization of the formed carbonate crystals, from blocky micron-sized needles in the reference samples (A-C) to quite well-defined nanoparticles (highlighted by arrows in (G)) embedded in a matrix of amorphous silica at pH 10 and 600 ppm SiO_2. Scale bars are 3 μm (A-C, and F), and 300 nm (D-E, and G-I).

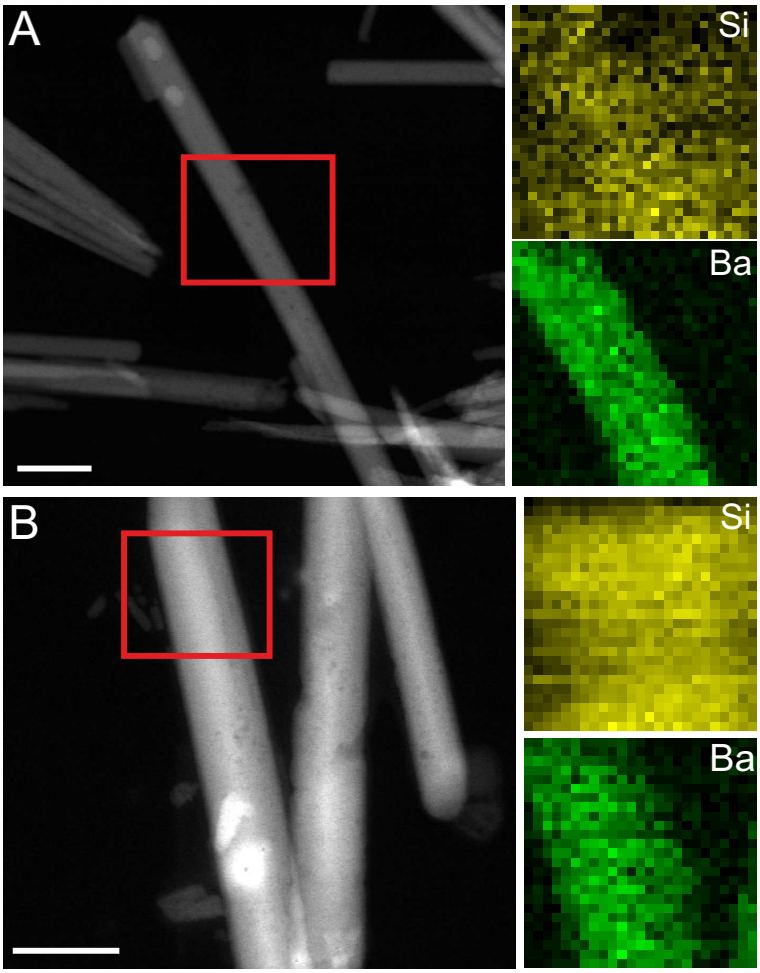

Figure 4.6. STEM images and corresponding Si and Ba elemental maps for carbonate nanorods formed during titration of $BaCl_2$ into carbonate buffer at pH 10, containing (A) 300 and (B) 600 ppm silica. The red rectangle marks the region analyzed by EDX. The data show that increased counts of silicon are detected around the carbonate particles. Scale bars are 100 nm.

terns confirmed these particles as well as those generated under the influence of silica to be orthorhombic, witherite-type barium carbonate (see Figures 9.3 - 9.5 in the Appendix). Addition of silica proved to have a drastic size-reducing effect on the resulting crystals, which thus became scaled down to dimensions in the nanometre regime (with characteristic lengths of 200-700 nm and widths of 1-50 nm, cf. Figure 4.5D, E, and G-I). This is true for all silica-containing samples except for 300 ppm SiO_2 at pH 11, where micron-sized crystals only slightly smaller than in the reference case were produced (Figure 4.5F). These observations comply well with the results of the titration measurements, in which silica also showed only a minor influence on the precipitation behavior under these conditions (cf. Figures 4.2 and

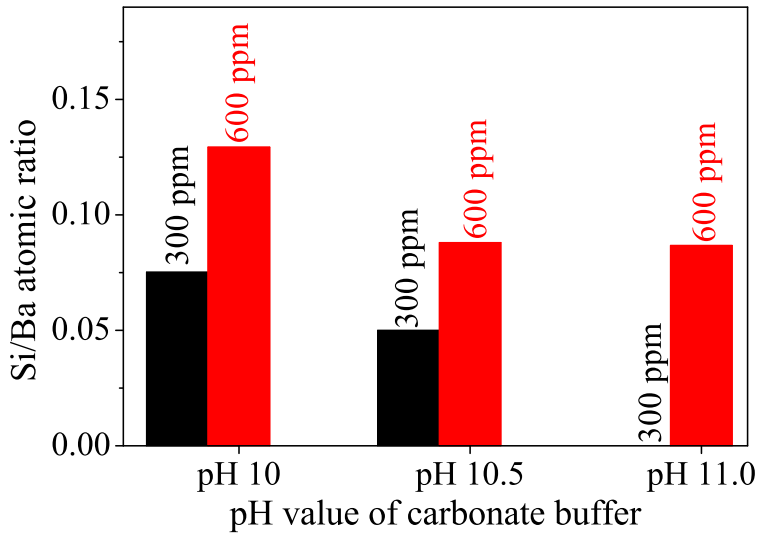

Figure 4.7. Si/Ba atomic ratios obtained by EDX spectroscopy from powder samples of particles formed in titration assays under different conditions (as indicated). Generally, the relative Si content in the precipitates increases with the silica concentration in solution, whereas it decreases with growing pH (both correlating inversely with the bulk solubility of silica). Note that at pH 11.0 and 300 ppm SiO_2, there is no silica associated to the $BaCO_3$ crystals. In all other cases, the determined silica content is in the same range as reported for the building units of silica-witherite biomorphs.[75]

4.4). Beyond that, also trends in the size of the nanoparticles can be distinguished that are consistent with (though not as clear as) those reflected in the titrations, that is, the crystals become smaller as the silica content is raised or the pH is lowered. This is most evident in the sample at pH 10 and 600 ppm SiO_2, where fairly uniform nanorods, about 100 nm long and 20 nm wide, were generated (Figure 4.5G).

In a further suite of experiments, the composition of the precipitates formed under the distinct conditions was investigated using micro-EDX analysis (Figure 4.6 and Figures 9.1 and 9.2 in the Appendix). Corresponding elemental maps of crystals grown at different silica contents demonstrate the presence of a continuous matrix of silica (visible as increased Si counts) around individual $BaCO_3$ nanorods. The amount of silica associated to the carbonate crystals was determined independently by EDX spectroscopy of bulk powder samples (see Figure 4.7). It was found that the overall Si content in the precipitates depends on the silica concentration in solution as well as on the pH of the buffer, with general tendencies that, again, very well match those identified in the titrations and the particle size. While the highest silica content is obtained at 600 ppm SiO_2 and pH 10 (Si/Ba $\approx$ 0.13), lower amounts

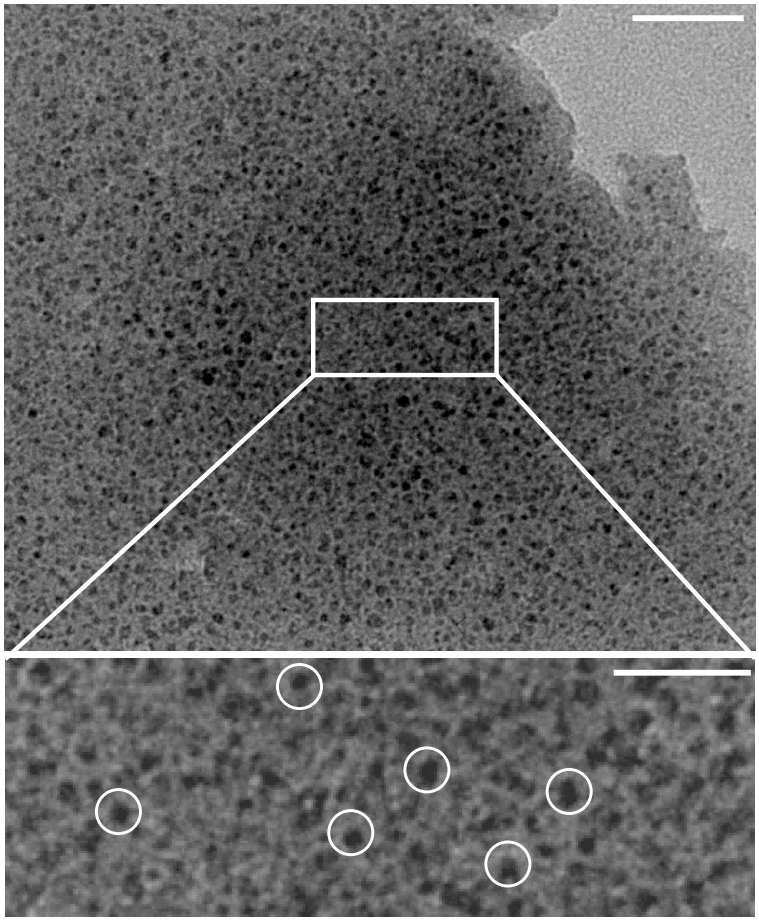

Figure 4.8. TEM micrographs of $BaCO_3$ nanoclusters (black spots) that are distributed throughout a matrix of lower electron contrast, presumably consisting of amorphous silica. These structures were isolated immediately after the maximum in free Ba^{2+} had been reached in titrations at pH 10.5 and 600 ppm SiO_2. Scale bars are 40 nm.

are detected when the pH is increased (Si/Ba $\approx$ 0.09 for 600 ppm at pH 10.5 and 11) or less silica is added to the mother solution (Si/Ba $\approx$ 0.08 for 300 ppm at pH 10). Remarkably, we could not detect any significant counts for Si in the crystals formed at 300 ppm and pH 11, i.e. exactly under those conditions where no considerable downsizing was observed either (Figure 4.5G). This suggests strongly that the silica content of the crystals and their size are interrelated, with higher Si levels being linked to smaller particles. On that basis, one can conclude that addition of silica provokes miniaturization of $BaCO_3$ particles formed during precipitation from solution.

To gain additional insight into the actual nucleation process of barium carbonate in the presence of silica, we have studied further samples that were drawn directly after the maximum in the titration curve ($\sim$10500 s for the system at pH 10.5 and 600 ppm SiO_2). HR-TEM micro-

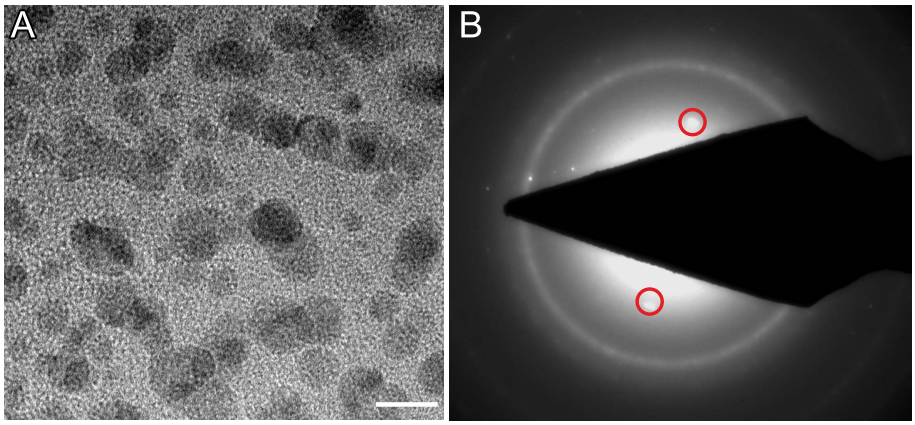

Figure 4.9. (A) TEM image of barium carbonate nanocluster (black spots) which grow from about 1 nm to dimensions of about 10 nm upon exposure to the electron beam. (B) Electron diffraction image revealing spots along a discrete ring. The measured distance in-between the reflection pair marked in red corresponds to a lattice spacing of 3.32 Å. This spacing can be indexed, within common limits of error in electron diffraction, to the (002) plane of witherite.[143] Scale bar is 10 nm.

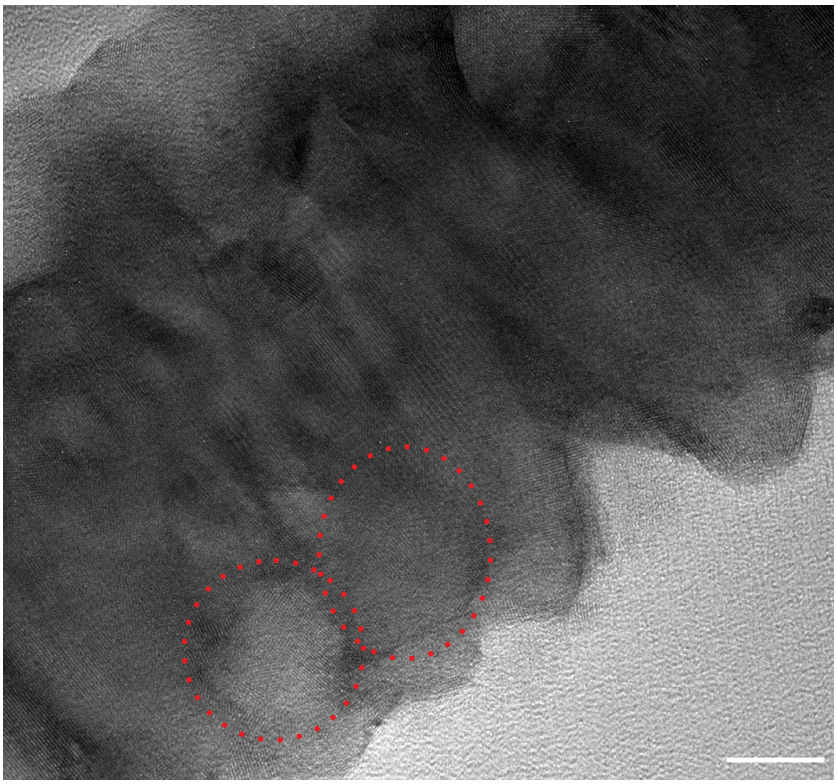

Figure 4.10. HR-TEM image of a mature $BaCO_3$ rod obtained from a sample at pH 11.0 and 600 ppm SiO_2. Close examination suggests that the crystal was formed via fusion of spherical primary particles, the contour of which can still be distinguished (highlighted by dotted red circles). Scale bar: 100 nm.

graphs of corresponding specimens reveal a continuous solid matrix with relatively low electron contrast, which hosts numerous individual spots that exhibit higher contrast and measure only a few nanometers (3-5 nm) in diameter (Figure 4.8). Interestingly, these nanoclusters increase in size (to about 10 nm) and become crystalline when exposed to the electron beam, with diffraction patterns that are indicative of witherite (see Figure 4.9). Therefore, these units are possibly $BaCO_3$ clusters dispersed in a matrix of amorphous silica. In this regard, one may speculate that nucleation of $BaCO_3$ proceeds via these clusters and involves their aggregation and final coalescence, as reported in detail for calcium carbonate.[93,132,144] The role of the silica would thus be to keep the clusters apart and hinder their agglomeration,[132] hereby delaying nucleation under otherwise identical conditions (as observed in the titrations). Growth of witherite crystals (and/or any possible amorphous precursors) might moreover occur through attachment (or fusion) of these primary units. This notion is supported by HR-TEM images of mature crystals, in which domains with contours reminiscent of the spherical precursor particles are still visible (see Figure 4.10).

4.5 Discussion

In this chapter a titration-based setup was employed to get novel insights into the nucleation of barium carbonate under the influence of dissolved silica at constant pH. The obtained results were correlated with particle sizes and compositions determined for the crystals isolated at the end of the experiments. From the Ba^{2+} potentials monitored in situ during titration, it was possible to assess the multiple effects of added silica on distinct stages of nucleation and early growth in a quantitative manner, i.e. changes in the equilibria of ion associates existing in solution before nucleation, the ability of the additive to retard nucleation, and also its impact on the solubility (and thus nature) of the initially formed solid phase. All these parameters were noticeably affected in the presence of dissolved SiO_2, to an extent that depended on both the silica concentration and the pH of the system.

Concerning the prenucleation regime, our data show that Ba^{2+} and CO_3^{2-} undergo association into ion pairs and/or larger clusters (as reported previously for $CaCO_3$[93,139]), and that silica is obviously capable of stabilizing these species. The degree of stabilization seems to be a function of the chemistry of silica in solution (apart from the silica-additive con-

centration alone), with higher oligomers (as prevailing at lower pH) being more efficient than simple monomers or dimers. Alternatively, the reduced number of charges at siliceous species under less alkaline conditions[129] could also contribute to the comparably high stabilization efficiency seen at pH 10. This, however, would be in conflict with observations made for $CaCO_3$ in a recent work,[132] where the interactions between silica and prenucleation clusters were found to become weaker with decreasing pH. At this point, we can only speculate about possible mechanisms for silica-mediated stabilization of $BaCO_3$ ion associates. It may be argued that oligomeric silicates encapsulate ion pairs or clusters and thereby effectively remove them from the equilibrium with the free ions, hence increasing the fraction of bound ions and rationalizing the traced trends with pH. In any case, this stabilizing effect is accompanied by a delay of nucleation relative to the reference without added silica. With regard to the TEM analyses performed on precipitates isolated shortly after nucleation (Figure 4.8), it seems as if embedding of small clusters in a siliceous matrix is the basis for this inhibition. Again, lower pH and/or higher silica contents promote retardation, suggesting that the ability of silica to condense and polymerize under the given conditions plays an important role in this context. Similar behavior was encountered in mixtures of calcium carbonate and silica, for which it was proposed that silicate species bind onto the periphery of ion clusters and thus generate a negative charge around them that leads to mutual electrostatic repulsion in-between individual clusters.[132] Consequently, the tendency of the clusters to aggregate and finally merge is restricted, so that nucleation becomes inhibited if it proceeds via cluster agglomeration. Such colloidal stabilization of prenucleation species against aggregation and nucleation has been observed also for other polymeric additives,[94,96] whereas changes in the structure of the clusters (possibly due to additive incorporation) were invoked as a reason for enhanced association in the presence of simple molecules like aspartic or citric acid.[97,145]

In view of the formation of silica biomorphs, the most important effect identified in the titrations occurs in the early postnucleation stage, where the measured free ion products are dramatically higher in silica-containing solutions than in the reference experiment. In addition, the concentration of free ions does not reach a plateau over the studied period of time in most cases (except for 300 ppm SiO_2 at pH 11), but rather decreases monotonously (cf. Figure 4.2). This shows that the high ion products observed after nucleation do not reflect the

formation of a less stable and hence more soluble intermediate phase (stabilized by silica), for which a constant level of free ions in solution (dictated by the solubility product of the most soluble phase present) would be expected.[93,139] Nevertheless, the behavior of the system under the influence of silica can readily be understood when considering the structure and composition of the formed particles (cf. Figures 4.5 and 4.6). In additive-free experiments, the $BaCO_3$ crystals can grow freely and soon reach dimensions in the micron-range (cf. Figure 4.5A-C); thus, the solid phase is in equilibrium with the surrounding solution (no growth inhibition), as is reflected in constant ion products after nucleation. In the presence of silica, the situation is drastically different: according to TEM and EDX analyses, the additive precipitates around the carbonate rods, thereby stabilizing them at small particle sizes. Coating by silica consequently impedes growth of $BaCO_3$ and probably also delimits exchange of Ba^{2+} ions between the solid carbonate and the solution, both being essential for a constant solubility to be established. Further, as growth cannot be simply continued, novel nucleation events will occur as the system is still far beyond saturation, leading to the formation of new nanoparticles that again will be embedded in silica. Therefore, supersaturation (i.e. the level of free Ba^{2+} and CO_3^{2-} in solution) can only gradually be diminished in a cascade of successive nucleation and - short - growth periods, which is fully in line with the slow decrease of the free ion product seen under these conditions.

Over time, this results in a multitude of uniform, silica-covered $BaCO_3$ nanorods with sizes that are very similar to those of the building blocks constituting silica biomorphs (typically 200-400 nm in length and up to 50 nm in width).[61,62,67,75,76,80] Interestingly, even the composition of the nanoparticles formed in the titration assays (Si/Ba atomic ratio: 0.05-0.13) is nearly identical to what has been reported for the units in the carbonate core of biomorphs (0.05-0.10).[75] This suggests that the effects identified in the present experiments should be directly relevant for the self-assembly of silica biomorphs, too. In this regard, the data demonstrate that the limitation of particle sizes to the nanoscale, as well as the concomitant high nucleation frequency, is due to the silicate species in solution. Most likely, growth inhibition and miniaturization are caused by the deposition of a continuous skin of amorphous silica around individual rods, owing to local pH gradients nearby growing carbonate surfaces as proposed theoretically in recent studies[61,81,86,87] and supported experimentally by the results

of the present work. Based on this model of coupled co-precipitation, it is furthermore possible to explain the distinct efficiency of silica to downsize the $BaCO_3$ crystals at different pH values. If this effect would rely on a coating of the carbonate particles in a skin or matrix of silica, then the propensity of silica to condense and polymerize under the respective conditions should be a decisive factor. Correspondingly, the smallest crystallites (Figure 4.5) and highest silica contents (Figure 4.7) were obtained at pH 10 and 600 ppm SiO_2, where the oligomerization tendency is clearly strongest.[129,131] While particles with somewhat larger sizes (yet still in the nano-range) and lower Si counts were produced when increasing the pH to 10.5 and/or decreasing the silica concentration to 300 ppm, there is a marked and abrupt change in the behavior at pH 11. Here, the silica does not affect the crystal size to a large extent at 300 ppm, nor is it co-precipitated with the carbonate particles in any detectable amounts. This indicates that the mechanism of stabilization cannot take place under these circumstances, which is reasonable in light of the concept of pH-based chemical coupling: on the one hand, the fraction of bicarbonate ions in equilibrium at pH 11 is rather low ($\sim$17%), so that the generation and maintenance of a pH gradient due to local HCO_3^- dissociation during $BaCO_3$ growth should be more difficult than at lower pH (at least any such gradient would be less pronounced). On the other hand, the solubility of silica is relatively high at pH 11,[129] and hence, the fewer protons released at the carbonate surface may not be sufficient to reach a critical level of supersaturation and trigger local silica precipitation. In turn, this seems to be possible when the silica concentration is raised to 600 ppm at pH 11, where - again - nanosized particles with considerable amounts of associated silica were formed. These considerations further corroborate the idea of pH-induced co-mineralization of silica and carbonate at local scales.

4.6 Conclusions

In summary, the experiments in this chapter have revealed detailed aspects of the nucleation and early growth stages of barium carbonate crystallisation in the presence of silica and under conditions that reflect those typically applied for the preparation of self-assembled biomorphic materials. By using a pH-constant titration methodology, it was observed that $BaCO_3$ precipitation is preceded by the formation of ion associates in solutions (ion pairs and/or clusters), and that nucleation occurs - in all likelihood - through aggregation and fusion of these precursors into spherical primary particles that then merge to yield rod-like nanocrystals (at least under the influence of silica).

The impact of silica as an additive during this process proved to be manifold and concerned virtually any of the investigated stages. First, a stabilizing influence on $BaCO_3$ prenucleation species could be identified, presumably originating from binding of oligomeric silicates on solute clusters. Second, the initial nucleation step was progressively delayed, supposedly due to embedding and mutual shielding of small carbonate nuclei within a matrix of amorphous silica. Both of these effects were found to depend on pH and the additive concentration in the samples, and could be correlated with the speciation of silica in solution under the respective conditions. Finally and most importantly, the data give clear evidence that the presence of silica leads to a substantial miniaturization of the resulting carbonate crystals, from rather ill-defined micron-sized rods to uniform elongated nanoparticles. This change can be ascribed to the deposition of extended silica skins around the evolving crystallites (as demonstrated by elemental analyses), which impedes further growth and ripening.

The latter feature is also apparent in silica biomorphs, which are composed of exactly such sub-micron $BaCO_3$ crystallites as building blocks. While it has previously been argued that silica facilitates stabilization of these nanometric units,[61,81,86,87] the present work provides a direct proof for this claim and, moreover, confirms the notion that spontaneous precipitation of silica around the carbonate crystals results from local variations in pH (or, in other words, from a decrease in pH nearby the surface of growing $BaCO_3$ particles). Further, it can be noted that the observed stabilization of prenucleation species and the simultaneous delay of nucleation may allow for high levels of supersaturation nearby the front of evolving biomorphs, which is an essential prerequisite for the envisaged autocatalytic mechanism

of growth and would explain the large number of small crystallites produced in each of the consecutive nucleation events occurring during the development of these biomimetic crystal aggregates.[61,87]

All in all, the measurements performed in this study shed novel light on the nucleation of barium carbonate in general and, particularly, enable a much more profound understanding of the processes leading to the formation of well-defined building units in silica biomorphs, which may be translated to explore the physical origin of other self-assembled hybrid materials as well.

5 Effect of bulk pH and supersaturation on the growth behavior of silica biomorphs in alkaline solutions

5.1 Abstract

In this chapter, the influence of the bulk pH on the morphogenesis of silica biomorphs in alkaline solutions is studied in detail. To that end, crystallization experiments were carried out at initial pH values between about 9.8 and 11.9, using atmospheric CO_2 as carbonate source. Formed aggregates were characterized quantitatively by statistical analyses of their morphology, number and size. Corresponding data evidence that well-developed polycrystalline architectures with elaborate shapes occur only when the starting pH is adjusted to values within a rather narrow corridor, ranging roughly from 10.2 to 11.1. Otherwise, merely ill-defined, globular or dumbbell-shaped particles were obtained. In addition, the pH of the mother solutions was monitored continuously during growth and correlated with time-dependent Ba^{2+} concentration profiles determined by in-situ X-ray fluorescence spectroscopy. By combining the collected data, temporal progressions of the bulk supersaturation were estimated for different conditions and used to re-evaluate the role of pH in the formation of silica biomorphs, particularly with regard to the model of the growth mechanism, presented in section 2.1.4. It is shown that a suitable starting pH is required not only to allow for dynamically coupled co-precipitation of the components, but also to maintain continuous CO_2 uptake and hence adequate levels of supersaturation over extended periods of time during growth. The experiments rationalize previous observations concerning the effect of pH on the formation

of silica biomorphs, and disclose fundamental differences between growth in solutions and gels.

5.2 Introduction

In the past years, the study of biomineral formation has been a central scope of research in the fields of colloidal chemistry and material science, since the strategies learned from nature may lead to novel potential routes for the synthesis of inorganic frameworks with remarkable shapes and structure, typically featured by outstanding properties. One such concept is to stabilize nanometric crystal building blocks and arrange them in a specific manner, thus constructing higher-order mesoscale patterns.[25,52,53] Concerted self-organization can for example be stimulated by the influence of certain organic polymers, which control the crystallization process in terms of nucleation, growth, as well as the stabilization and coherent alignment of nanocrystal units.[18,20,23,40,45,50,55,88,146–153] A natural archetype for such materials is the nacreous layer of seashells, which consists of numerous aragonite platelets surrounded by a thin film of biopolymers, resulting in a brick-and-mortar structure of superior hardness.[5,154,155] However, the presence of biomolecules or synthetic organic substances is not a mandatory requirement for the production of polycrystalline textures as described above. Indeed, ultrastructures of similar complexity can also be formed from purely inorganic precursors via delicate interactions between the components, as exemplified by the existence of so-called "silica biomorphs".[60] These peculiar materials occur when alkaline-earth carbonates and silica are co-precipitated at elevated pH, and self-assemble spontaneously into complex crystal aggregates with non-crystallographic shapes closely resembling certain biogenic forms.[59,60,62–64,66] The resulting morphologies are quite diverse and include curved forms such as helicoids as well as coral- and worm-like structures, but also
flat sheets.[61,67,69,73–75,80,82–85] Detailed analyses of the precipitates revealed that they are composed of a core of uniform rod-like crystallites, which exhibit a slight mutual misalignment and hence describe a long-range orientational field on the mesoscale.[67,75] Furthermore, the crystal assembly as a whole happens to be sheathed by a skin of amorphous silica,[62,67,69,75,76,84] and there is also some evidence that individual carbonate crystallites in the core are coated by silica[75,80,82], or adsorb silicate species in their lattice.[85]

The morphogenetic mechanism underlying the formation of silica biomorphs has for long been an enigma. However, recent work revealed crucial aspects of the process and identified both the driving force for co-precipitation on the nano-level and parameters determining the morphological evolution on the micron-scale.[61,81,86] In essence, a scenario based on two principal stages was proposed. It was shown that morphogenesis is initiated by growth of regular elongated microcrystals, which then undergo self-similar splitting at both ends induced by the poisoning influence of polymeric silicates, to eventually yield heavily branched and more or less closed fractal structures.[81] Subsequently, in a second stage, myriads of nanocrystals are nucleated on the surface of these fractal particles, which serve as building blocks for the curved morphologies characteristic of silica biomorphs. The reason for the stabilization of nanosized crystallites and their continuous production at the growing front of an aggregate was proposed to be based on a coupling between the precipitation of silica and carbonate, which relies on their reversed solubility trends with pH[61,81,86]: during growth of carbonate particles in alkaline solutions, CO_3^{2-} ions are consumed and, as a consequence, nearby CO_3^{-} ions must dissociate to re-establish equilibrium, causing a release of protons and hence a local drop in pH.[92] This results in a decrease of the solubility of silica around the just generated crystallites, which therefore become coated by siliceous skins and thus are prevented from further growth. As silica polymerization proceeds in the vicinity of the carbonate particles, ongoing condensation reactions will re-increase the local pH and, ultimately, trigger novel carbonate nucleation. Overall, a feedback cycle is initiated during which the components are alternately mineralized and sinuous polycrystalline aggregates emerge.[61,75,81,86]

While their preparation is utterly simple, growth of silica biomorphs premises certain conditions and the resulting morphologies were shown to depend on various experimental parameters such as species concentrations[67,85] or the presence of additives.[69,76] However, the most important factor was repeatedly confirmed to be the pH of the medium, from the early works on.[59,66,74,82,83] In particular, it was found that when growth is carried out in dilute solutions, typical forms are obtained only when the initial pH was adjusted to values higher than $\sim$10, while below only cauliflower-like fractal particles occur.[66,73] A strong influence of the pH on the growth process appears reasonable when considering that the speciation of both carbonate and silicate varies sensibly with the pH, and that the proposed model assumes

pH-dependent changes in their solubility to be responsible for self-organized mineralization. Therefore, the role of the pH during the formation of silica biomorphs based on the meanwhile existing knowledge about the growth mechanism was re-evaluated in this chapter. Indeed, a similar study has recently been carried out by Melero-García et al.,[72] but their work was focused exclusively on growth in silica gels. It was found that the formation of complex shapes with continuous curvature takes place at a pH of less than 9.8, which is significantly lower than what has been argued previously.[66,73] In the present chapter, the effect of the bulk pH for the case of growth from solution was examined. To that end, dilute silica sols of different pH were prepared and combined with barium chloride solution, covering initial pH values of about 10 to 12. Crystallization occurred upon prolonged exposure of the mixtures to the atmosphere, due to gradual ingestion of CO_2. To quantify the influence of the pH, formed precipitates were analyzed statistically with respect to the frequency and size of distinct types of morphologies. In addition, the bulk pH as well as the concentration of Ba^{2+} in the solutions was monitored in a time-resolved manner, and the acquired data were used to calculate temporal progressions of supersaturation for samples with distinct starting pH. The results demonstrate that growth of silica biomorphs from solutions occurs at a pH well above 10 and that their morphogenesis is restricted to a certain window of initial pH values.

5.3 Experimental section

5.3.1 Crystallization experiments

Growth of silica-witherite biomorphs was performed in stagnant solutions following a procedure described previously.[61,70,71,75,76] As silica source, commercially available water glass (Sigma-Aldrich, sodium silicate solution containing $\sim$ 13.7 wt% NaOH and 26.8 wt% SiO_2) was used and diluted with water by a factor of 1:350 (v/v). The resulting silica solution (pH $\sim$ 10.6) was then mixed at a ratio of 20:1 (v/v) with either sodium hydroxide or hydrochloric acid solutions at different concentrations (0.05-0.3 M NaOH and 0-0.1 M HCl), in order to achieve distinct initial pH levels. Eventually, crystallization of barium carbonate was initiated by combining 5 mL of the pH-adjusted silica sol with the same volume of 0.01 M $BaCl_2$ (prepared with $BaCl_2 \cdot 2\,H_2O$, Sigma-Aldrich, $\geq$ 99%). The final concentrations in the reaction mixture thus were 5 mM Ba^{2+} and 8.4 mM SiO_2, with initial pH values ranging from

9.90 to 11.90. Experiments were carried out at $20 \pm 1°\mathrm{C}$ in sterile 6-well microplates (Nunclon, polystyrene, 10 mL total volume, 9.6 cm^2 bottom area, 1.7 cm in depth), into which glass coverslips (22 x 22 mm) were placed as growth substrates before filling with solution. After exposure of the samples to the atmosphere over a predefined growth period of 10 h, the substrates were removed with a pair of tweezers and subsequently washed with water and ethanol (Baker, p.a.), followed by drying in air. All solutions were prepared with water taken from a Millipore system and stored in tightly stoppered plastic bottles, to prevent previous uptake of atmospheric CO_2 and possible silica contamination from glass walls.

5.3.2 Characterization methods

Statistical analysis

Dried precipitates were investigated routinely by means of polarized optical microscopy. Images were taken with a Nikon Eclipse E400 transmission microscope, onto which a Canon EOS 350D camera was mounted. For statistical analyses, a plastic slide with a 4-mm square grid was fixed on the bottom side of the coverslips carrying the aggregates, so as to facilitate counting of the distinct morphologies. The counting itself was performed using a Wild macroscope (model M420). For each initial pH level, samples from two independent experiments were examined. Under typical growth conditions, the observed polycrystalline morphologies can be divided into three classes, namely flat sheets, helical filaments and worm-like braids.[67] Each of these forms usually emerges from globular particles or clusters thereof, which correspond to the fractal architectures generated during the first stage of growth.[75,81] However, many of these fractal globules do not give rise to any of the polycrystalline morphologies (i.e. growth ceased after the first stage was terminated). This population of particles is referred to in the following as "globules", in line with previous work.[75] To gain reliable statistics, at least several hundreds of aggregates were counted for each sample. The size of the aggregates was measured using the DigitalMicrograph software package (Gatan, Version 3.9.0). Thereby, diameters of fractal globules and sheets were determined by fitting circles or ellipses to their borderline. In case of ellipses, the average of the two diameters was taken to be the corresponding size. Straight lines were used to measure the length of worms and helicoids. For each pH level, more than 100 aggregates of each of the occurring

types of morphology were analyzed.

Electron and atomic force microscopy

For scanning electron microscopy (SEM), biomorphs were grown directly on circular glass substrates (Mica, 10 mm in diameter) placed on the bottom of the well. After rinsing with water and ethanol, the dried substrate was mounted on a SEM stub and coated with gold. Specimens were studied with a Zeiss LEO Gemini 1530 microscope at working voltages between 3 and 5 kV. Atomic force microscopy (AFM) analyses were performed using a commercial device (NanoWizard, JPK Instruments, Germany) and Si cantilevers with a force constant of 40 N/m (NSC 15, MicroMash, Estonia, resonant frequency: 325 kHz).

pH measurements

The temporal evolution of the bulk pH in the different samples was monitored by immersing a microelectrode (Metrohm, Biotrode) into the mother solution and acquiring data continuously during growth for 10 h. Values were read automatically in intervals of 10 seconds via an attached Metrohm Titrando 809 controlling unit, which was operated by corresponding software (Tiamo 2.0). Before each long-term measurement, the electrode was calibrated using buffers of pH 4, 7 and 9 obtained from Metrohm. Afterwards, the probe was regenerated by successive treatment with 1 M solutions of HCl and NaOH, followed by equilibration in 3 M KCl

Barium concentration measurements

Changes in the concentration of free Ba^{2+}ions during growth in solution were traced by means of X-ray fluorescence spectroscopy (XFS). Experiments were performed at Beamline C of the storage ring DORIS III at the synchrotron radiation facility HASYLAB (DESY, Hamburg, Germany). Measurements were carried out in the region of the Ba-K edge (37441 eV) using the Si(311) monochromator setup. Sample fluorescence was monitored with a detector positioned at 90° relative to the incident light path. Data acquisition was started as soon as possible after a single well filled with $BaCl_2$/silica-mixtures of the desired initial pH (9.90, 10.05, 11.00, 11.15, 11.75, 11.90) had been placed in the center of the beam. Scans from 37191 to 37710 eV were performed continuously for up to 6 h, using a step width of 5 eV in the pre- and post-edge region and 1 eV at the edge jump. The integration time per

step was 0.5 s, thus resulting in an overall time resolution of about 7 min. After normalizing the recorded spectra for the incoming beam intensity, the height of the edge jumps was determined by fitting linear equations to the post- and pre-edge region and calculating the step at the inflection point of the curve, as described previously[75] (see Figure 5.1). In order

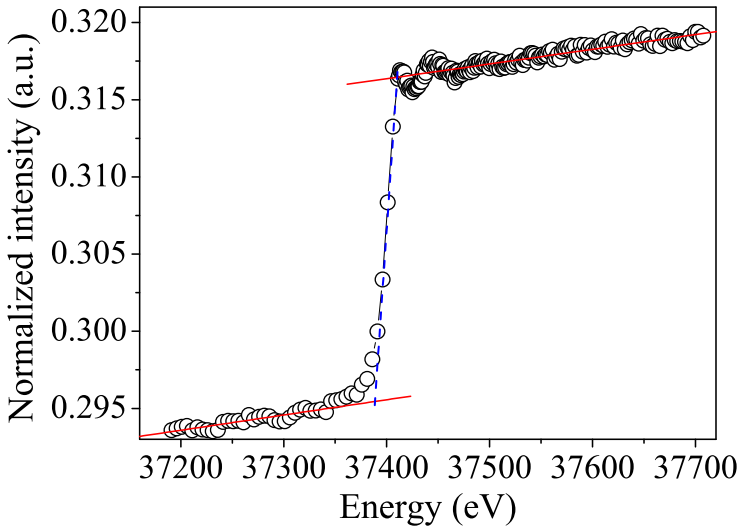

Figure 5.1. Exemplary x-ray fluorescence spectrum recorded in the region of the Ba-K-edge from a mother solution of silica carbonate biomorphs. The red lines represent linear fits to both, the pre-and post edge region. The dashed blue line highlights the edge jump.

to convert the obtained edge jump values to actual Ba^{2+} concentrations, pure $BaCl_2$ solutions (1-5 mM) without silica were measured with the same routine, giving a straight calibration line with good correlation (cf. Figure 5.2).

Calculation of supersaturation values

Based on the acquired time-dependent data for the pH and the Ba^{2+} concentration, it is possible to estimate the supersaturation of the system, using a method introduced recently.[70,75] To that end, biomorph mother solutions were titrated with hydrochloric acid in the absence of any carbonate (CO_2-free solutions, N_2 atmosphere). By fitting polynomial equations to the resulting pH-n_{added} H^+ data, pH values from the in-situ measurements can be directly converted to apparent quantities of protons generated in the solutions during growth (due to continuous acidification by in-diffusion of CO_2). The number of generated protons depends on the amount of dissolved bicarbonate and carbonate ions as well as on the fraction

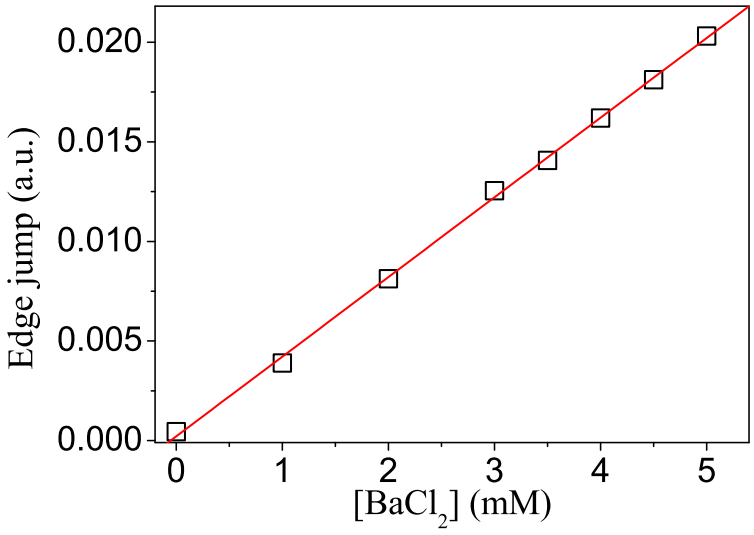

Figure 5.2. Edge jump values from aliquots of $BaCl_2$ solutions, determined in the absence of silica. A linear fit to the data (R^2=0.9989) was used for calibration, to determine the concentration of Ba^{2+} in the actual sample.

of carbonate precipitated at a certain time t, and can be written as follows:

$$n_{H^+generated}(t) = n_{HCO_3^-}(t) + 2n_{CO_3^{2-}}(t) + 2n_{BaCO_3}(t) \tag{5.1}$$

The amount of precipitated barium carbonate can readily be calculated as the difference between the analytical Ba^{2+} concentration (5 mM in all cases) and the actual value determined at time t by means of XFS measurements, according to:

$$n_{BaCO_3}(t) = \left[\left(5mM - [Ba^{2+}](t)\right) \cdot 0.002\ L\right] \tag{5.2}$$

The mole numbers of dissolved carbonate and bicarbonate ions are in turn accessible considering the law of mass balance and the distribution of carbonate species in solution as a function of pH.[75,92] Rearranging Equation 5.1 in this respect and introducing $x_{CO_3^{2-}}$ as the fraction of carbonate ions in equilibrium with bicarbonate at a given pH yields the following expression for the amount of dissolved bicarbonate:

$$n_{HCO_3^-} = \frac{1 - x_{CO_3^{2-}}}{1 + x_{CO_3^{2-}}} \cdot \left(n_{H^+generated}(t) - 2n_{BaCO_3}(t)\right) \tag{5.3}$$

Combining Equations 5.1-5.3 eventually allows calculating time-dependent variations of the actual carbonate concentration in the mixtures which, together with the XFS data, gives the relative supersaturation S defined as:

$$S = \frac{[Ba^{2+}] \cdot [CO_3^{2-}]}{K_{SP}(BaCO_3)} \tag{5.4}$$

where $K_{SP}(BaCO_3)$ is the solubility product of barium carbonate($5.01 \cdot 10^{-9}\ mol^2L^2$).[141] However, calculations according to the above-described methodology frequently yielded negative values for S during the first 30 min of growth. These unexpected results likely originate from the fact that a certain amount of carbonate was pre-dissolved in the alkaline silica sol prior to the start of the growth experiments, such that fractional precipitation of $BaCO_3$ occurred immediately after $BaCl_2$ had been added.[75] This is evident from the y-axis intercepts of linear fits to the data of the temporal $[Ba^{2+}]$ progression, which were in all cases lower than the analytical barium concentration of 5 mM. Thus, the number of protons generated in the system at t=0 ($n^0_{H^+generated}$) will not be zero (as assumed in the above calculations), but adopt a positive value that depends on the amount of $BaCO_3$ initially precipitated ($n^0_{BaCO_3}$) as well as the quantities of carbonate and bicarbonate ions co-existing with the solid phase at this time ($n^0_{CO_3^{2-}}$ and $n^0_{HCO_3^-}$):

$$n^0_{H^+generated} = 2n^0_{BaCO_3} + n^0_{HCO_3^-} + 2n^0_{CO_3^{2-}} \tag{5.5}$$

While $n^0_{BaCO_3}$ is known from the y-intercept of the $[Ba^{2+}]$ (t) curve, $n^0_{CO_3^{2-}}$ and $n^0_{HCO_3^-}$ can be derived from the solubility product of $BaCO_3$, when assuming that the solid phase is in equilibrium with the solution right after mixing of reagents. Finally, the measured amount of generated protons is corrected for initial precipitation according to:

$$n^{corr}_{H^+generated} = n_{H^+generated}(t) + n^0_{H^+generated} \tag{5.6}$$

5.4 Results

5.4.1 Morphological analysis

Standard growth conditions

When crystallization was carried out under typical conditions (i.e. at 5 mM Ba, 5-10 mM SiO_2, and a pH of ~11), silica biomorphs with morphologies, textures and sizes similar to previously reported aggregates were obtained.[62,66,67,69,73,76,80] Figures 5.3 and Figure 5.5 give an overview of the formed structures. Precipitates isolated after 2-3 h exhibit dumbbell-like or closed spherulitic morphologies, with diameters in the range of 10 μm (Figure 5.3A-B). These architectures result from silica-induced poisoning of a growing micron-sized carbonate crystal, causing the initially rod-like crystal to split at both of its ends[66,81]. In the following, branching at non-crystallographic angles is continued according to a self-similar motif[89], such that the crystal undergoes a rod-to-dumbbell-to-sphere morphological evolution, quite akin to what has been observed for fluorapatite aggregates grown in gelatin matrices[88,90,91]. These fractal structures may eventually develop into cauliflower- or raspberry-like forms (Figure 5.3C), depending on the particular degree of branching and time of active growth.

Occasionally, polycrystalline assemblies composed of uniform nanosized rods (cf. Figure 5.3D and 5.5) sprout from such fractal precursors. This transition, called fibrillation, is accompanied by 3D nucleation of numerous nanoparticles all over the surface of the fractal architecture.[81] In accordance with what is usually found in gels,[72] extrusion of nanocrystalline aggregates in solution proceeds at first in the form of quasi-2D laminar segments, which may grow in a flat manner to yield extended sheets with dimensions of up to several hundreds of micrometers (Figure 5.5C).

However, growing sheets also have a certain tendency to curl at some point along their rim and fold back to develop scrolled margins. This singular event, which occurs quite often in solutions, triggers a morphogenetic mechanism that is governed by radial and tangential growth velocities as well as the height and handedness of individual curls,[61,81] resulting in delicate filamentous structures that may loosely be classified into regular helicoids (Figure 5.5B) and thicker, more tightly wound worm-like forms (Figure 5.5A).

Here, we have quantified the occurrence and size of the three main morphologies displayed

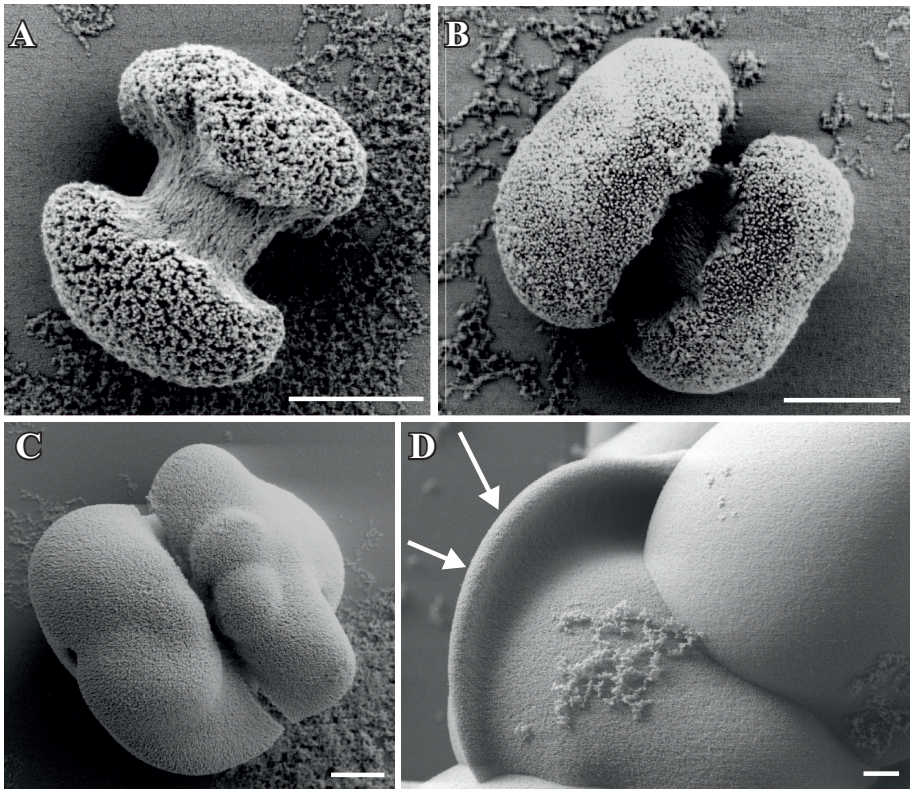

Figure 5.3. (A-C): Early fractal architectures of silica-witherite biomorphs, collected 2.5 h after mixing reagents.(D) Globular cluster from which a laminar "tongue" (indicated by the arrows) emerges after 4 h of growth. Scale bars are 2 μm (A-C).

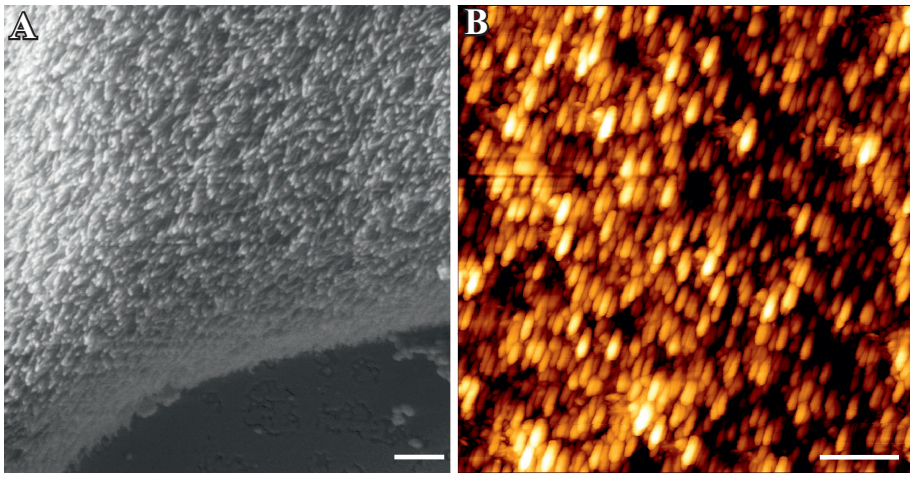

Figure 5.4. (A) HR-FESEM image of the growth front of a sheet, demonstrating that the building units consist of elongated $BaCO_3$ nanocrystals with a large degree of co-orientation, depicted by the AFM image (B). Scalebar 500 nm.

by silica biomorphs (i.e. sheets, helicoids, and worms) by means of statistical analysis, and additionally determined the number of fractal precursors formed in the experiments (c.f Figure 5.8). For conditions as outlined above, about 55% of the counted fractal globules gave

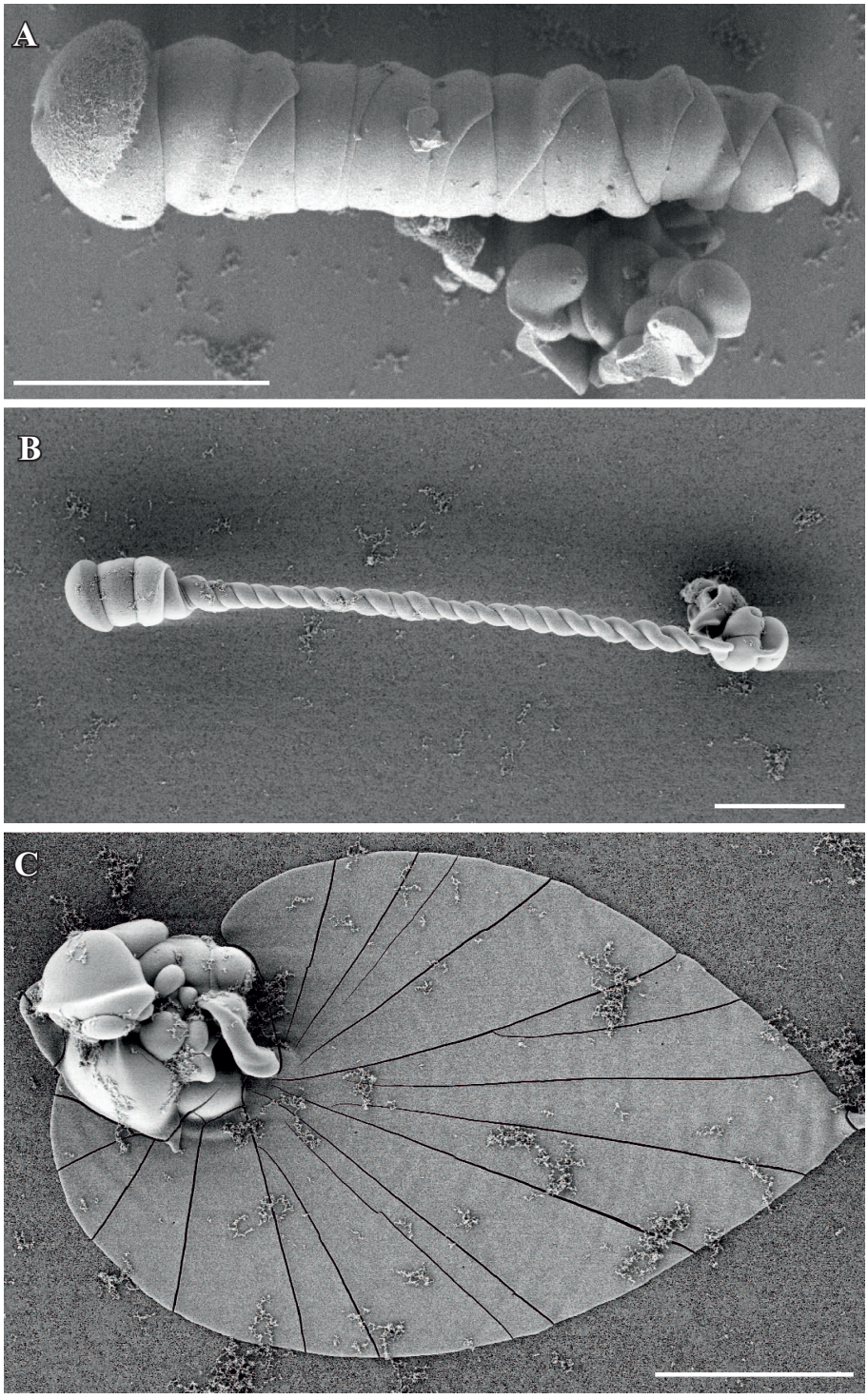

Figure 5.5. FESEM images of commonly observed mature crystal aggregates of silica-witherite biomorphs grown under "standard" conditions after 10 h. (A) Worm-like braids, (B) helical filaments and (C) extended flat sheets. Scalebar is 100 μm.

rise to characteristic polycrystalline forms. Among these, worms were found to be the most frequent morphology (ca. 30%), while the percentages of sheets and helicoids are considerably lower and amount to slightly above and below 10%, respectively. These values are in

good agreement with the results of a recent study carried out under similar conditions.[68,70]

Effect of the initial bulk pH

Varying the starting pH of the mother solution proved to have a strong influence on the morphological distribution of the aggregates - as soon as a certain deviation from "standard" conditions (as defined above) is provided, towards both higher and lower pH. In turn, there is a corridor of initial pH levels around the "standard" value, for which crystallization yields widely identical results.

Figure 5.6 shows a gallery of optical micrographs granting an overview on precipitates grown from solutions with different initial pH values. It is obvious at first glance that extended flat sheets, easily distinguished by their Maltese-cross extinction pattern between crossed polarizers, are observed predominantly at starting pH values between 10.65 and 11.15 (Figure 5.6C). In the same range, fairly large filamentous structures, both worm-like and helicoidal, were obtained at these pH levels (cf. Figure 5.9). The longest helical aggregates (up to 250 μm) were identified under standard conditions at an initial pH of 11.00. Twisted forms looked quite alike in terms of morphological aspects in this range of starting pH values. They grew straight with a constant width in most cases and occurred in roughly equal numbers of right-and left-handed individuals. Worm-like morphologies turned out to vary slightly in their specific appearance between pH 10.65 and 11.15 (cf. Figure 9.6). For instance, some of the worms observed at pH 10.65 have, in addition to the fractal architecture from which they emerged, further globules attached to them, which seemingly extrude from their sides. At higher pH, worms were often seen to grow in conjunction with helicoids. Helicoidal and worm-like crystal aggregates with the largest dimensions (mean length of 100 μm) were again found at pH 11.00. The fractal particles formed in this pH regime typically display mainly single-spherical shapes and often agglomerated into rather undefined clusters. The latter feature complicated measurements of the size of individual particles and presumably led to higher apparent mean diameters in the analyses (about 50 μm, cf. Figure 5.9).

When the initial pH of the mother solution was decreased to 10.20, no more worms and helicoids were observed, and the only characteristic morphology of silica biomorphs left were sheets, however their average diameter (ca. 50 μm) was significantly smaller than at starting pH levels of 10.65-11.15 (100-200 μm). Simultaneously, the fraction of fractal particles

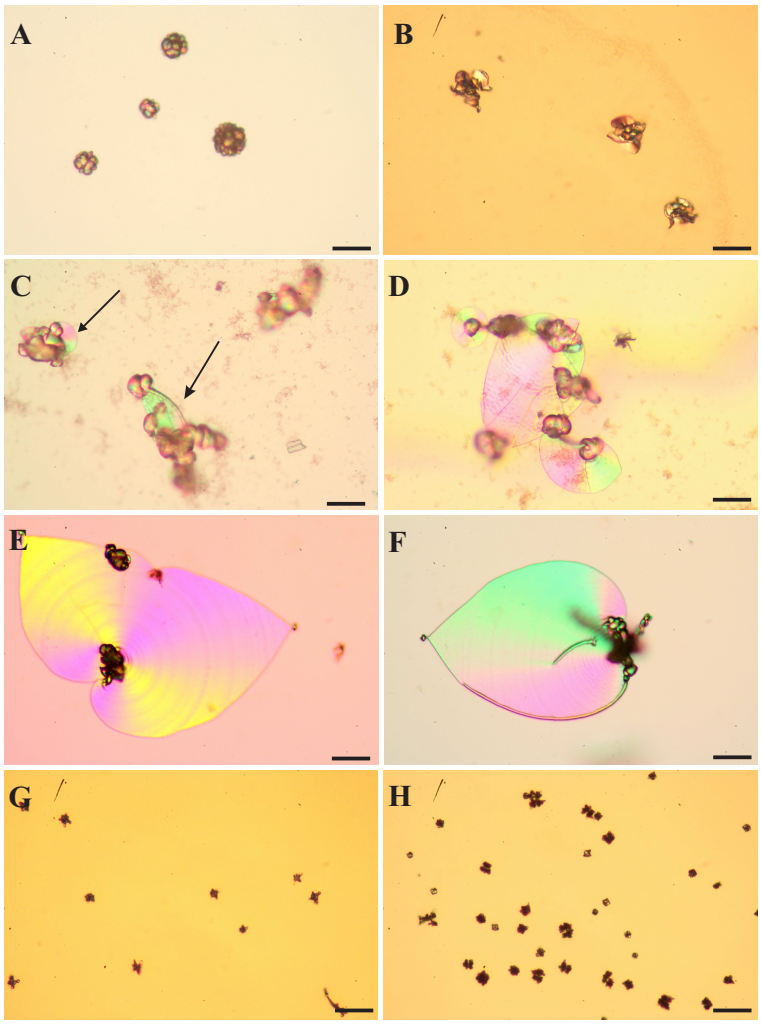

Figure 5.6. Polarized optical micrographs showing typical morphologies of precipitates isolated after 10 h from solutions at an initial pH value of (A) 9.90, (B) 10.05, (C) 10.20, (D) 10.65, (E) 11.00, (F) 11.15, (G) 11.75, and (H) 11.90. (A-B): At lower pH, globular particles and conglomerates thereof are observed, while characteristic biomorphic forms are absent. (C): At pH 10.20, small sheet-like domains are occasionally seen to emerge from the globular particles (indicated by the arrows). (D-F): Between pH 10.65 and 11.15,the formation of non-crystallographic ultrastructures is most pronounced, with spacious sheets and large filaments being typical kinds of morphology. (G-H): At pH values equal to or higher than 11.75, again only fractal particles are found, which now show predominantly dumbbell-like shapes. However, their number is higher and their mean size smaller as compared to counterparts grown at low pH. Scale bars are 50 μm.

not associated to any polycrystalline form increased significantly, and their morphology partially changed from closed spherulites to more open, dendritic structures (cf. Figures 5.6B and 5.7B for a close-up view), this indicates that the branching motif is to some degree different at lower pH, in particular with respect to the density of bifurcations in the fractal

architectures. These and the above observations are confirmed in a quantitative manner by

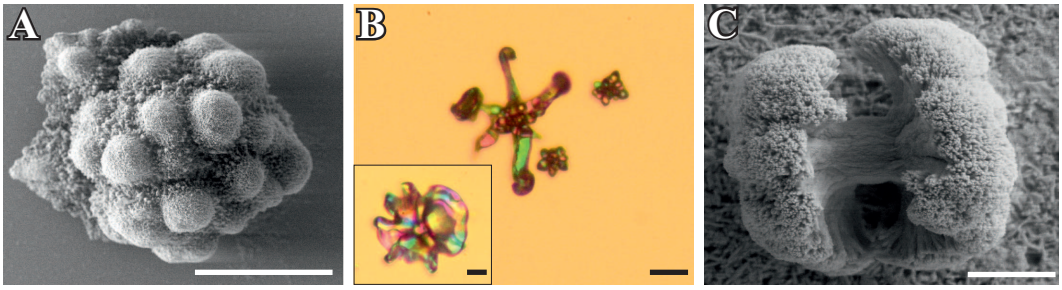

Figure 5.7. FESEM and optical images of fractal architectures grown at an initial pH of 9.90 (A), 10.05 (B) and 11.90 (C). Note that particles at low pH are significantly larger and display closed raspberry-like (pH 9.90) or open dendritic (pH 10.05) shapes, whereas those formed at high pH usually show dumbbell-like morphologies. Scale bars are 20 μm (A and B), and 2 μm (C).

statistical analyses, as illustrated by Figures 5.8 and Figure 5.9. At initial pH values of $\leq$ 10.05 (Figure 5.6A), polycrystalline aggregates were fully absent and merely fractal entities were isolated, which mostly had a raspberry-like appearance (see Figures 5.6A and 5.7A). These morphologies presumably result upon further growth (and closure) of the dendritic forms shown in Figure 5.7B, and are similar in shape to structures reported previously for growth in solutions at relatively low pH.[66] In some cases but very rarely, minute sheets could be distinguished at the border of these fractal particles however, they did hardly grow larger than a few microns under these conditions (Figure 5.7B inset).

When the starting pH was increased to 11.75, morphogenesis of typical polycrystalline forms was largely prevented. Indeed, we observed almost exclusively fractal particles and could not find a single worm or helicoid (cf. Figure 5.8). Again, some of the fractal precursors developed laminar domains around their rim, which however rarely grew to sizes beyond a few microns (as at low pH). Interestingly, the fractal architectures obtained at high pH differ from those formed in the intermediate range (pH 10.65-11.15) in that the majority of the particles had a dumbbell-like rather than a closed spherulitic morphology (cf. Figure 5.7C). This suggests that self-similar branching proceeded to a minor degree at elevated pH (rather than there was a change in the mode of branching, as at low pH). In other words, growth of individual particles ended sooner (given that dumbbells are precursors of closed spherulites). This notion is supported by the mean size of these particles, which is markedly smaller than

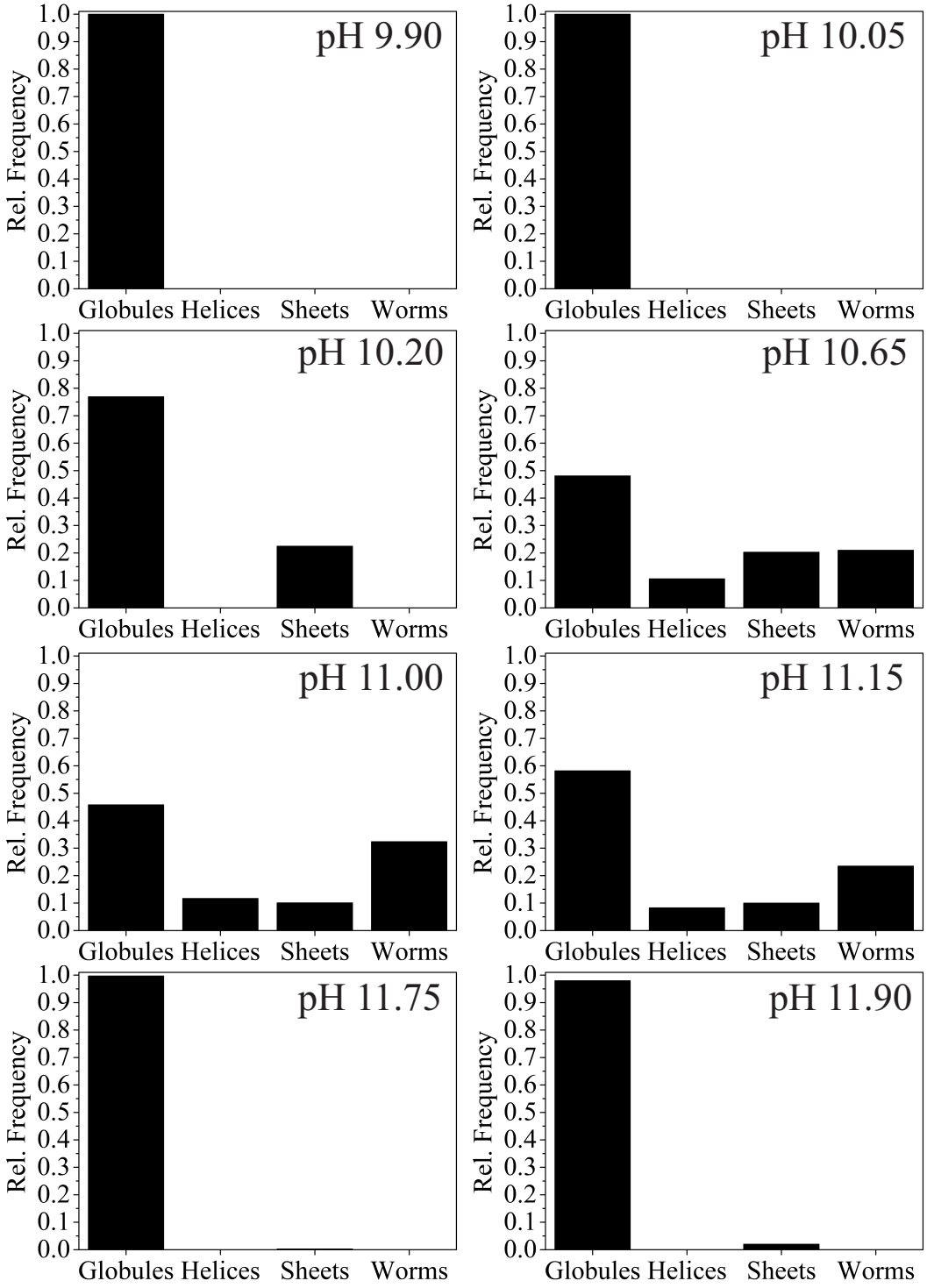

Figure 5.8. Normalized relative frequencies of globules, helices, sheets, and worms observed in experiments performed at different initial pH levels (as indicated). Values were obtained by counting particles on a defined area of the glass substrate. It is evident that significant amounts of characteristic polycrystalline morphologies are only present if the starting pH is adjusted to values between 10.30 and 11.15.

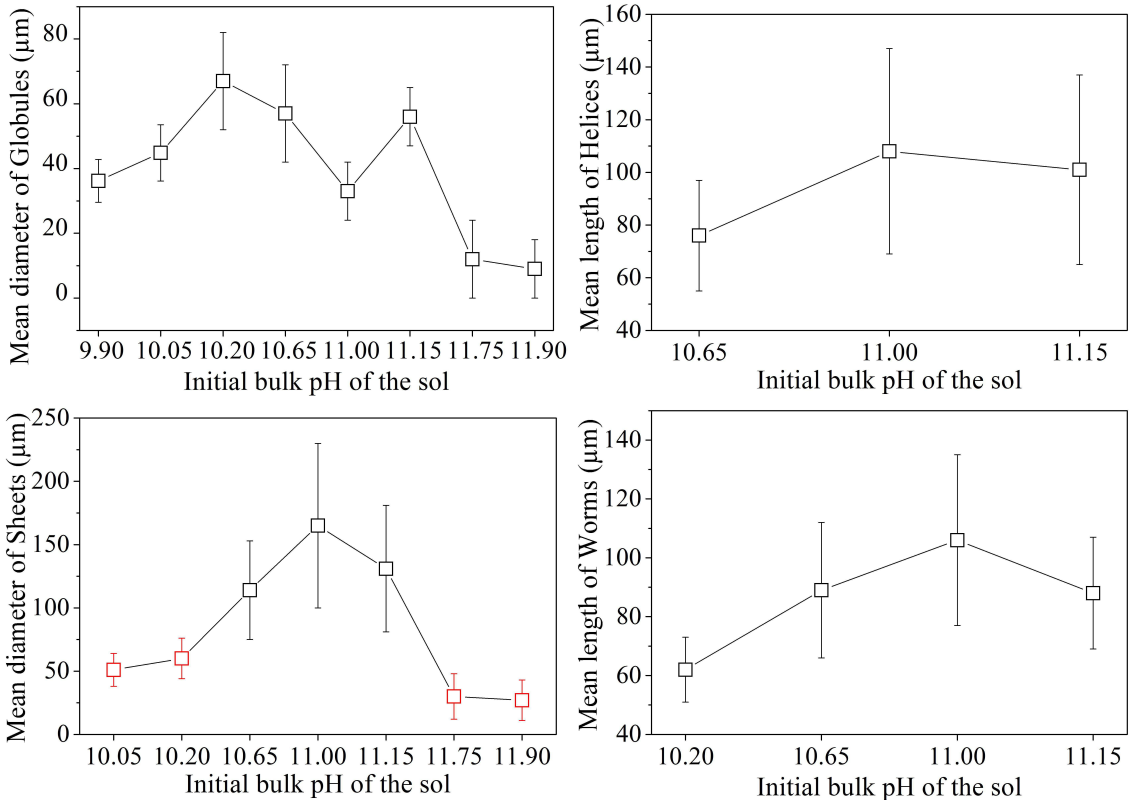

Figure 5.9. Average size and corresponding standard deviations determined for the distinct morphologies displayed by silica-witherite biomorphs, outlined as a function of the chosen starting pH. Data were obtained by measuring at least 100 individuals for each type of morphology where possible. For initial pH values of 10.05, 10.20, 11.75, and 11.90, the number of sheets observed was rather low and did not permit size analyses with statistical significance; therefore, corresponding data points are drawn in red and put in brackets. Note further that the mean size determined for fractal globules in the intermediate pH range (10.65-11.15) overestimates the true value, due to clustering of individual particles.

at lower pH (cf. Figure 5.7C and Figure 5.9). When comparing the morphology of leaf-like aggregates formed at the various initial pH levels investigated, certain differences can be noted apart from the fact that they reach merely a few microns in size at both low and high pH. For example, at a starting pH of 10.20, multiple sheets frequently developed in distinct directions from a single central globular particle, partly growing on top of each other. On occasion, the laminae became linked to one another or happened to wind around neighboring globules. In turn, for initial pH values ranging from 10.65 to 11.15, the observed sheets were largest and most uniform, growing in a defined manner and widely separate from each other (cf. Figure 9.7).

The above findings can be summarized in a morphology distribution diagram as given in Fig-

ure 5.10. It is evident that on both, the upper and lower end of the studied pH range (i.e. at initial values of 9.90/10.05 and 11.75/11.90), no characteristic biomorphic forms have been generated after 10 hours of growth and merely fractal architectures (referred to as "globules") occurred. At intermediate pH levels, the percentage of globules not giving rise to any polycrystalline morphology is in turn decreased and sheets, helicoids and worms are observed.

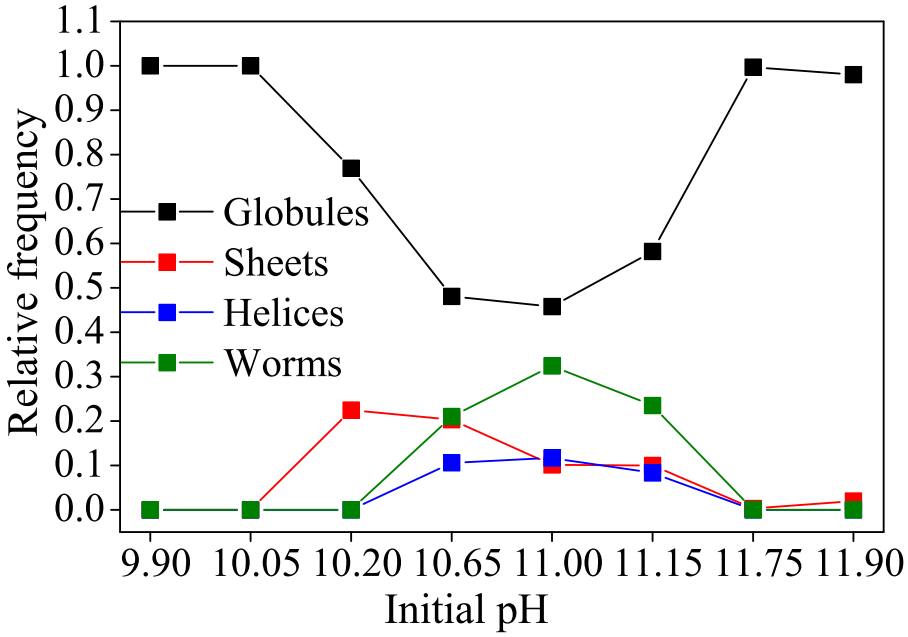

Figure 5.10. The relative occurrence of the distinct types of morphology displayed by solution-grown silica biomorphs, as depending on the initial pH of the system. Note that the term "globules" signifies those fractal architectures from which none of the characteristic polycrystalline forms developed.

It is worth noting that at the lower limit of pH for which pronounced biomorph formation was verified (i.e. at a starting pH of 10.20), only sheet-like aggregates were obtained, while all three typical morphologies were present in roughly similar ratios between pH 10.65 and 11.15. This indicates that the pH plays a certain role in determining which of the polycrystalline forms is generated. According to the recently proposed formation mechanism of silica biomorphs,[81] helicoids and worms can only emerge when an evolving sheet starts to curl and twist. However, in light of the present data, growth of sheets at lower pH is apparently abandoned soon after being initiated, such that curling cannot take place and twisted morphologies are not observed.

To understand the traced growth behavior, it is furthermore interesting to consider the absolute amount of aggregates formed in experiments at a given pH. Corresponding data show

that the number of particles on the investigated substrate area is approximately equal for starting pH values of 10.65, 11.00, and 11.15, apart from minor variations (see Figure 5.11). A slight decrease in the number density can be noted at pH 10.20, whereas drastically less

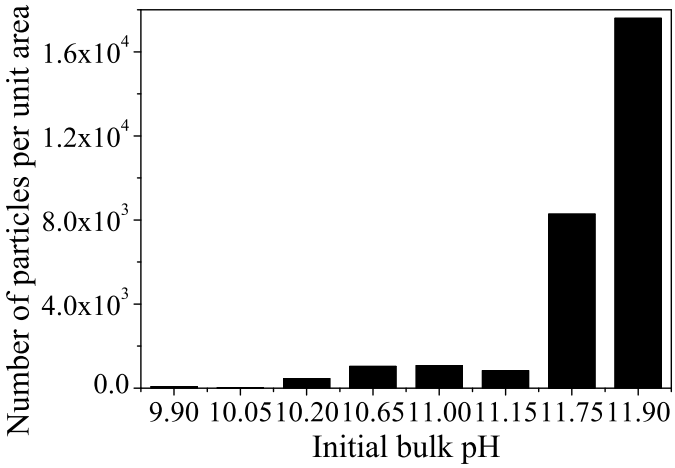

Figure 5.11. Absolute number of aggregates formed after 10 h of growth from solutions at different initial pH. Data were obtained by counting all particles precipitated on a predefined area of the used glass substrate.

particles were counted for initial values of 10.05 and 9.90. In turn, towards higher pH, the total number of precipitates escalates when going from pH 11.10 to 11.75 and is clearly highest at pH 11.90. This implies that, with increasing bulk pH, a growing number of $BaCO_3$ seeds are nucleated in the samples and subsequently undergo fractal branching. This enhanced nucleation frequency at elevated pH is related to the high supersaturation of the system caused by rapid ingestion of atmospheric CO_2, and vice versa. This leads to the formation of a larger number of fractal particles which - since the amount of available Ba^{2+} is constant - on average grow to smaller dimensions, as reflected by measurements of their size at pH $\leq$ 11.75 (cf. Figure 5.9). In turn, at low pH (9.90-10.20), less seed crystals are generated in the solutions and the resulting raspberry-like architectures eventually become larger, again in line with the collected data.

5.4.2 Evolution of the bulk pH and barium concentration during growth from solution

In order to quantify the above considerations, the time-dependent changes in the concentrations of species relevant for $BaCO_3$ crystallization were traced in situ during growth. For

this purpose, two different starting pH values were selected from both the low and high pH regime (where only fractal particles were observed) as well as from the intermediate range, in which well-developed biomorphs formed. While the concentration of dissolved Ba^{2+} could be directly determined by monitoring its fluorescence upon irradiation with X-rays, information on the amount of carbonate ions present in the system at a given time had to be derived in an indirect manner, that is, by measuring the pH. This was achieved by immersing a microelectrode into the mother solutions during growth. Time-dependent profiles acquired for samples with varying initial pH are displayed in Figure 5.12. In general, the pH was found

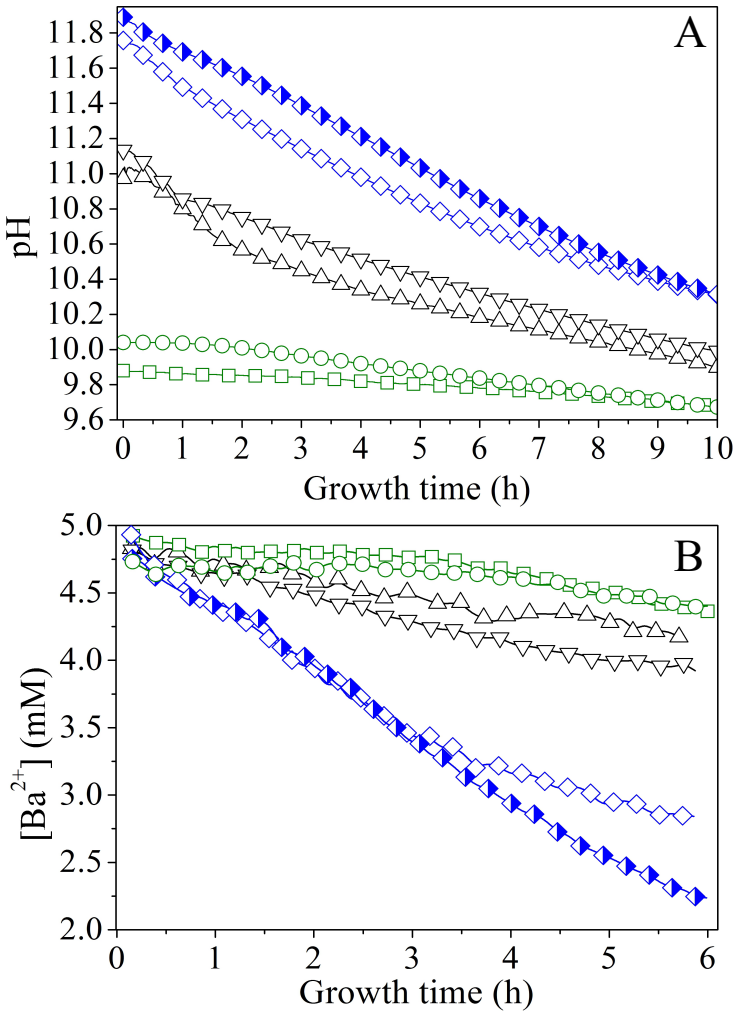

Figure 5.12. Profiles during growth of silica biomorphs from solutions at different initial pH values. -◆- pH 11.90, -◇- pH 11.75, -▽- 11.15, -△- 11.00, -○- pH 10.05, and -□- pH 9.90. Note that the decrease in the Ba^{2+} concentration is linear in time over a period of at least 4 h.

to decrease with time, reflecting diffusion of atmospheric CO_2 into the alkaline mixtures and

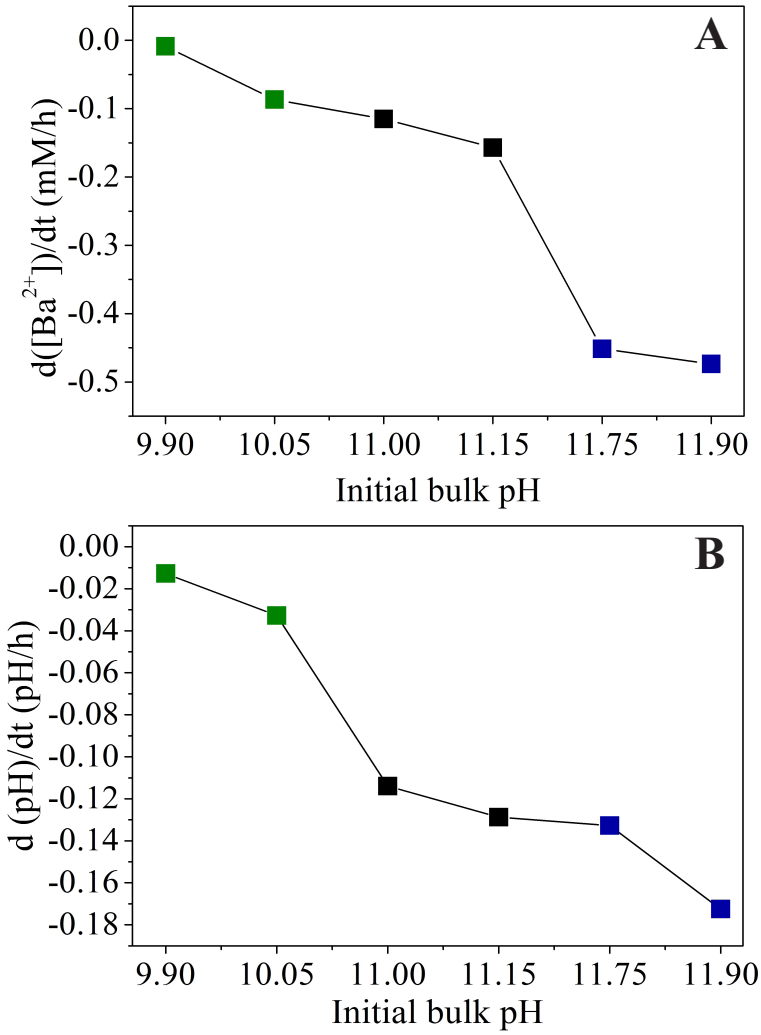

Figure 5.13. Apparent slopes of (A) the time-dependent pH profiles and (B) the temporal progression of the Ba^{2+} concentration, both outlined as a function of the initial pH. Values were obtained by approximating the experimental data with linear fits.

its conversion to bicarbonate and carbonate ions. The actual ratio of the latter is thereby an intimate function of the actually prevailing pH.[72,75,80,86,92] Once initiated, precipitation of $BaCO_3$ further fuels the absorption of CO_2, as carbonate ions are removed from the solution equilibrium.

We note that the traced progressions of pH with time do not show any distinct oscillations, which one might expect in view of the mechanism proposed to underlie the formation of silica biomorphs (i.e. alternating precipitation of carbonate and silica, associated with a slight decrease and subsequent re-increase in pH), at least for those starting pH values where growth of well-developed biomorphs was found to occur (black curves in Figure 5.12). However, recent work in stirred systems has suggested that growth takes place only at a local scale

within an active region nearby the front of the evolving aggregates, which was estimated to extend merely over some microns into the solution.[75] Therefore, subtle variations in pH caused by the growth process of individual aggregates are not reflected in measurements of the bulk pH and should be sensible only in the close vicinity of growing fronts.

Apart from that, the data shown in Figure 5.12A evidence that the rate of CO_2 uptake is notably affected by the particular starting pH. The higher the value of the starting pH, the steeper the pH declines with time, as is evident from a plot of approximate slopes obtained by linear fits of the experimental data (Figure 5.13A). This confirms that ingestion of CO_2 proceeds faster at higher bulk pH values, likely due to corresponding shifts in the carbonate equilibrium to the side of CO_3^{2-}. Thus, it can be expected that the concentration of carbonate ions present at a given time will increase with the starting pH and that, during the early stages of growth, the actual supersaturation of barium carbonate should reach higher levels in a shorter period of time under these conditions (as will be discussed in section 5.5). The temporal development of the Ba^{2+} ion concentration is outlined in Figure 5.12B for different initial pH values. The data show a nearly linear decrease of the amount of dissolved Ba^{2+} during the first hours in all cases. This indicates that precipitation of $BaCO_3$ occurs at a constant rate during the formation of silica biomorphs, in good agreement with previous work.[75] Moreover, as the initial pH of the sol is increased, the decay in the Ba^{2+} concentration becomes steeper, as illustrated by trends in the slopes of linear equations fitted to the data (Figure 5.13B). This implies that more barium is consumed at higher pH within the studied period, which is consistent with the results from statistical analyses concerning the absolute number of aggregates produced under the different conditions, and corroborates the notion of an increase in supersaturation towards more alkaline bulk pH. It is worth noting that the slopes of the concentration-time profiles acquired from solutions in the low-pH region (pH 9.90 and 10.05) differ only slightly from those obtained for samples in the intermediate range (pH 11.00 and 11.15), while there is a much more distinct change in the high-pH regime (cf. Figure 5.13B). Interestingly, an opposite trend can be discerned in the slopes of the pH-time curves, where the difference between the low- and intermediate-pH region is significantly larger (Figure 5.13A). This indicates that insufficient CO_2 flux into the solution prevents biomorph formation at low pH, whereas the lack of characteristic morphologies at

high pH is due to a too fast decline of the Ba^{2+} concentration.

5.5 Discussion

The results clearly show that when syntheses are carried out in solutions, morphologies characteristic of silica biomorphs can only be obtained when the initial pH is adjusted to values within a rather narrow corridor which, in view of the statistical analyses carried out in this work, extends roughly from pH 10.2 to 11.1. Outside this range, predominantly fractal architectures were isolated after 10 h, in the form of either large raspberries (low pH) or smaller dumbbells (high pH). Since these fractal particles result as a consequence of the first stage of the proposed formation mechanism,[81] it seems reasonable to assume that at the end of this process, the conditions prevailing in systems at either low or high pH were not appropriate to initiate the second stage of growth, i.e. chemically coupled co-precipitation and the self-assembly of nanoscale crystallites.

A crucial prerequisite for chemical coupling to occur is that an appreciable fraction of bicarbonate ions exists in equilibrium with carbonate ions in the solution (given that the envisaged local changes in pH rely on HCO_3^--dissociation), and that silica is sufficiently, but not too soluble in the bulk medium. In principle, these criteria are met for a pH range of about 9-11, as is evident from Figure 5.14, which shows the distribution of carbonate species in solution and the solubility of silica as a function of pH. Above pH 11, the percentage of bicarbonate ions in equilibrium obviously becomes quite small and the solubility of silica very high. Below pH 9, the fraction of carbonate ions is in turn too low to facilitate $BaCO_3$ precipitation. Accordingly, Melero-García et al. found that growth of biomorphs in gels occurs at pH values between 9.3 and 9.8.[72] By contrast, the present data prove that the formation of well-developed biomorphs in solutions takes place at significantly higher pH. This is corroborated by time-dependent analyses of the evolving precipitates, which showed that growth of characteristic polycrystalline morphologies starts around 3-4 h after mixing and is essentially terminated after another 6-8 h (cf. Figure 5.3 and 5.5). In view of the recorded pH profiles (Figure 5.12A), this means that sheets, helicoids and worms form at bulk pH levels well above 10.

A possible reasoning for these apparent discrepancies is the following. Aside from the prin-

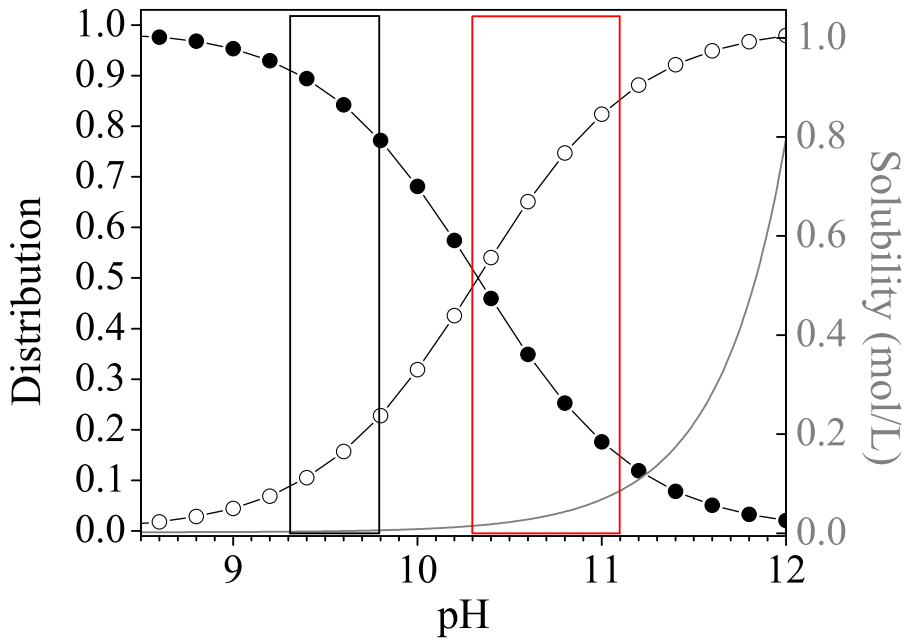

Figure 5.14. Plot of the relative fractions of carbonate species (-●- HCO_3^- and -○- CO_3^{2-}) present in equilibrium as a function of pH, together with the pH-dependent progression of the solubility of silica (grey curve). The red box marks the range of starting pH values for which morphogenesis of silica biomorphs was observed in solutions, whereas conditions reported to be suitable for growth in gels are highlighted by the black box[72].Curves were calculated on the basis of the corresponding acid/base equilibria assuming ideal conditions and considering only monomeric silicate species, as described elsewhere[70,92].

cipal feasibility of chemical coupling (i.e. that precipitations influence each other via the local pH), another important factor for self-assembly is the actual supersaturation of the system and its temporal variations. In gels, this parameter is largely governed by the diffusion of Ba^{2+} ions from a concentrated solution into the silica matrix already containing a given amount of pre-dissolved CO_2.[72] To trigger morphogenesis, enough Ba^{2+} must be transported to the growth site to establish proper conditions, which is inevitably accompanied by a decrease in pH due to the acidity of the divalent cations. Nevertheless, as long as the pH does thereby not fall below a certain threshold, the second stage of growth can still be initiated. In solutions, supersaturation is in turn regulated by diffusion of CO_2 into media with evenly distributed Ba^{2+} ions. Unlike the situation encountered in gels, this process is not only driven by a concentration gradient, but also depends intimately on the bulk pH, which dictates the rate of CO_2 uptake by affecting the $H_2CO_3/HCO_3^-/CO_3^{2-}$ equilibrium. For the emergence of typical biomorphic forms, the pH must still be high after the fractal stage in this case, in

order to maintain sufficient CO_2 flow into the solution and hence provide adequate levels of supersaturation.

In that sense, as already stated in the earlier work[72], there is no universal correlation between the bulk pH and the expected morphologies. Instead, within a distinct window allowing for coupled precipitation (ca. 9-11), particular pH values found to produce regular silica biomorphs mainly reflect the conditions necessary to reach and sustain suitable supersaturation in a given setup. In order to assess these conditions for stagnant solutions as those investigated in the present study, we have used the collected time-dependent data of the pH and Ba^{2+} concentration to estimate the evolution of the bulk supersaturation during growth. Figure 5.15 shows corresponding results for two initial pH values each of the low-, intermediate-, and high-pH regime. On that basis, the growth behavior traced in the present

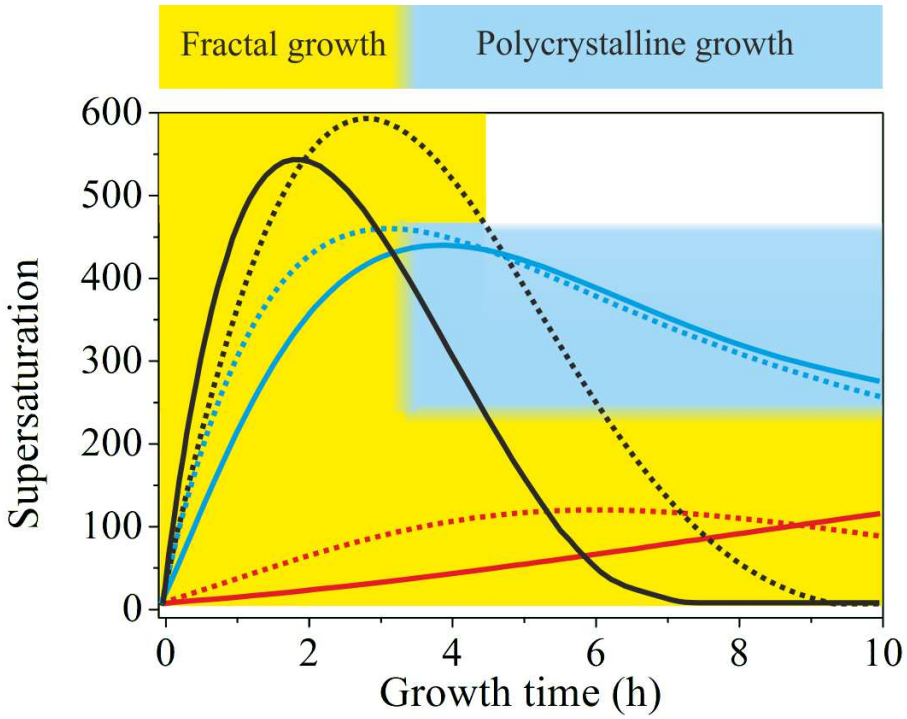

Figure 5.15. Temporal development of the relative supersaturation of $BaCO_3$ during growth from solutions at different starting pH values. Dashed black line pH 11.90, black line pH 11.75, dashed blue line pH 11.15, blue line pH 11.00, dashed red line pH 10.05, red line pH 9.90. The blue-shaded area signifies the interval of bulk supersaturation levels at which the formation of well-developed silica biomorphs is possible. Fractal growth (yellow-shaded area) in turn occurs over a much broader range of conditions and proceeds as long as the system remains supersaturated.

study for different starting pH levels can be explained. At medium pH values of 11.00 and

11.15 (blue curves in Figure 5.15), the bulk supersaturation increases gradually over the first 3-4 h, as CO_2 is progressively ingested while the Ba^{2+} concentration is still high. During this period, fractal structures are generated owing to non-crystallographic branching. Subsequently, the curves arrive at a maximum that is followed by a continuous decrease. At this point, the system passes into the second stage of morphogenesis, during which complex crystal aggregates are formed. Importantly, the decay in supersaturation is rather slow up to 10 h, and S remains relatively high until growth of biomorphs is terminated. This suggests that the conditions encountered in this period are those which allow chemical coupling to be excited and, hence, that precipitation of silica biomorphs in solution can occur at bulk supersaturation levels of about 250-450.

When growth is carried out at lower starting pH (9.90 and 10.05, red curves in Figure 5.15), characteristic crystal aggregates can in turn not be obtained because the bulk supersaturation does not reach values in this range over the entire period investigated. This is most likely due to the depressed flow of CO_2 into the system under less alkaline conditions, as evidenced by corresponding pH-time profiles (Figure 5.12A). Consequently, the requirements for fibrillation and successive polycrystalline growth to occur are not met (although the bulk pH would as such be suitable for chemical coupling). Therefore, precipitation ceases at the end of the first stage, and any further precipitation of $BaCO_3$ barely leads to an enlargement of fractal structures, which therefore become bigger than at higher pH and adopt their typical raspberry like appearance.

In turn, when the initial pH is increased to 11.75 and 11.90 (black curves in Figure 5.15), the uptake of CO_2 is accelerated and significantly higher levels of supersaturation are achieved in a shorter frame of time. As a result, nucleation rates are enhanced and a much larger number of $BaCO_3$ crystals are formed in the system (cf. Figure 5.11), which subsequently undergo fractal branching. This becomes clearly manifest in the steep decline of the Ba^{2+} concentration (cf. Figure 5.12B), which causes the supersaturation to run through a maximum after rather short times (2-3 h), despite the relatively high amounts of carbonate ions generated in parallel. Subsequently, S decreases quite rapidly to values that are too low to allow for dynamically coupled co-precipitation, that is, the window of suitable conditions is passed too quickly (< 2 h) under these circumstances. In fact, most of the crystals cannot even complete

the fractal route and therefore exhibit small dumbbell-like morphologies rather than closed spherulitic shapes at the end of the experiments. This is mainly due to the low amount of Ba^{2+} available after the fractal stage, owing to previous ample precipitation (as reflected by the slope of the [Ba^{2+}]-time curve, cf. Figure 5.12B). Further, even if the Ba^{2+} concentration would be sufficient to enable polycrystalline growth, the minor fraction of bicarbonate ions existing in equilibrium at pH values close to 12 (cf. Figure 5.14) may as such prevent any noticeable interplay between the precipitation of carbonate and silica.

On the other hand, it is evident from Figure 5.14 that the solubility of silica increases steeply with pH starting from about 11.5. Thus, at pH 11.75 and 11.90, the silica supersaturation is more sensitive to any release of protons around growing carbonate crystals due to bicarbonate dissociation and, as a consequence, more silica will be incorporated. However growth ceases then after the fractal stage at these pH levels, since the remaining silica supersaturation is not sufficient, rendering stabilization of nanocrystals and coupled growth impossible and hence generally avoiding the formation of biomorphs. In turn, at lower starting pH values, the solubility of silica is reduced and the bulk solution gradually becomes supersaturated as the pH is further decreased over time until, eventually, amorphous silica precipitates independently of the biomorphs. Obviously, this removes reactive silicate species from solution and may be another reason why well-developed crystal aggregates are not observed at low pH. These considerations suggest that, in principle, the supersaturation of both carbonate and silica must be moderate for co-precipitation and the formation of biomorphs to occur.

5.6 Conclusion

In this chapter the crystallization of barium carbonate from alkaline, silica-containing solutions upon diffusion of atmospheric carbon dioxide at various initial pH levels was studied. The data show that co-precipitation of witherite and silica affords crystal aggregates with complex curved morphologies only if the starting pH of the mother solution is adjusted to values within a certain corridor, which was found to range roughly from 10.2 to 11.1. At both lower and higher initial pH, only fractal architectures, resulting from self-similar branching of carbonate crystal core, were obtained. This finding is ascribed to inadequate supersaturation levels prevailing in the system at the stage when chemically coupled co-precipitation

would actually be initiated (rapid depletion of Ba^{2+} at high pH, insufficient CO_2 flow at low pH). The observed pH-dependent growth behavior highlights the peculiarity of silica biomorphs as self-assembled materials which result from coupled mineralization processes operating far from equilibrium. It is typical for such systems that proper starting conditions have to be provided in order to achieve an optimum structuring effect. For growth from solutions, the initial bulk pH is a crucial parameter in terms of the speciation of the components, but in particular also with respect to the rate of CO_2 uptake and, thus, the temporal evolution of the carbonate concentration. This is a fundamental difference to syntheses conducted in silica gels, where diffusion of Ba^{2+} ions is the key factor for supersaturation. In both cases, morphogenesis of well-developed biomorphs occurs if, during active growth, the pH of the medium surrounding the aggregates is within a window of approximately between 9 and 11. However, to achieve this and maintain sufficient supersaturation during crystallization, the initial pH of a corresponding solution has to be significantly higher than that of a gel. In the present work, these circumstances have been elucidated in a quantitative manner by in-situ measurements of the bulk pH and Ba^{2+} concentration, yielding time-dependent absolute values for the actual supersaturation of the system at distinct growth stages. Taken together, our experiments have shed novel light on the role of the bulk pH in the formation of silica biomorphs from solutions. The quantification of the traced morphological changes with pH, accomplished by statistical analyses of formed precipitates, paints a picture that is widely consistent with previous observations and allows for understanding the effect of the pH on the basis of the recently proposed growth mechanism.

6 Evolution and Control of Complex Curved Form in Simple Inorganic Precipitation System

6.1 Abstract

This chapter focuses on the influencing role of foreign surfaces during the growth of silica biomorphs, as it was proposed that this external parameter is responsible for the expression of curvature. To that end, surfaces with a defined topology on the micrometerlevel were used instead of flat substrate surfaces. The conducted experiments demonstrate that morphological selection is strongly linked to the geometries of topology, as the distribution of yielded architectures becomes shifted towards higher fractions of helices and worms. This finding therefore corroborates the common hypothesis that curvature is induced due to the absence of foreign surfaces which provokes emanating sheets to curl around themselves in order to use their own intrinsic surface as a templating substrate. Finally, results indicate that, upon increasing the geometric dimensions of the patterned topology, growth of silica biomorphs can be directly tuned in that way that the resulting polycrystalline architectures completely adopt the given geometries of the underlying structured substrate.

6.2 Introduction

In literature, silica carbonate biomorphs have frequently been presented as an archetypus of biomimetic crystallization in totally inorganic environments, clearly demonstrating that the formation of mineral architectures with sinuous shapes is not restricted to biological systems or the presence of organic substances.[62–64] Such unique ultrastructures can be ob-

served, when alkaline-earth carbonates crystallize in silica-containing solutions at alkaline conditions upon gradual in-diffusion of atmospheric CO_2.[61,62,66,67,74,75] Typically, growth of mature silica biomorphs is finished within a timescale of 8- 10 h,[75] and aggregates like helicoids, fractal spheroids, worm like braids, and leaf-like objects are found floating on the surface of the mother liquid or adhering on the surfaces of the reaction vessels. Thereby, dimensions of such biomorphs reach values up to several hundreds of micrometers.[59,60,67] (see Figure 2.3 and 5.5)

In order to analyze the morphogenesis of biomorphs on a phenomenological point of view, the crystallization can be quenched after certain timepoints of growth. After mixing the necessary reagents the first particles can be isolated a few hours later, showing deformed globular particles or partially open dumbbell-like shapes with dimensions $\leq$ 10 μm.[61–63,67,75,81] Detailed analysis of such particles reveal a core consisting of an elongated pseudohexagonal carbonate seed, about 1 μm in size. During ongoing growth, transition to dumbbell-like objects and nearly closed spherical architectures subsequently occurs via continuous non-crystallographic branching at both ends of the seed crystal due to specific adsorption of oligomeric silica species onto preferred crystallographic faces of the pseudohexagonal seed crystal.[61,66,75,81]

After about 3-4 h, polycrystalline laminar segments with dimensions of a few microns start to sprout out from the previously observed fractal precursor particles in a nearly radial manner (see Figure 5.3D), being composed of a multitude of carbonate nano-units stabilized by silica. Formation of the observed nanoscaled carbonate particles is thereby primary caused by increased carbonate supersaturation which reaches its maximum after 4 h from beginning, afterwards decreasing continuously but slowly as presented in chapter 5. On nanoscale, the production of building units is reported to be based on reversed solubility trends of carbonate and silicate species with pH at alkaline conditions present in the system.[61,81,86,87] Consequently, nucleating barium carbonate particles become enveloped by a thin skin of silica right after mineralization, as the pH is lowered in the vicinity of nucleating nanoparticles therefore triggering local polymerization of silica and thus preventing further growth of carbonate nanorods. On the other hand condensation reactions of single silica units re-increase the local pH on the growth front, provoking the beginning of a new cycle of carbonate crystallization.

In summa, these coupled processes induce a continuous circle of alternating precipitation of nanoscaled and isolated crystallites.[61,87]

Furthermore, emanating quasi-2D sheet-like segments accidentally start to develop curled segments around their rim. As a consequence of both, scrolled margins and different rates of tangential and radial growth the formation of one or more cusps is observed.[81] When two approaching curls with the same handedness converge and intertwine at one cusp, helicoidal structures emerge and grow to dimensions of about 200-400 μm due to continuous mutual winding. In contrast, worm-like morphologies originate when a complete sheet curls in one direction and keeps on coiling around itself during the overall period.[81] In general, the observed phenomenological scenarios occur during biomorph growth conducted in aqueous solution as well as in gels. However, emergence of laminar segments, i.e. the transition from fractal- to polycrystalline growth, is predominantly a statistical event, since only about 50% of all isolated aggregates typically exhibit complex curved shapes (see Figure 5.8, pH 11.0). In addition, growth of flat sheets usually proceeds in direct contact with the prevailing substrate (bottom or wall of wells, and solution-air interface), whereas worms and helices generally protruded to arbitrary angles into the solution.[70] These observations are confirmed by the fact that twisted filaments sprout out from sheets with a dimension not larger than a few microns with a noticeable distance from a foreign surface. Similar arguments can be put forward for the morphogenesis of worm-like structures, where sheets start bending immediately after their generation and continuously wind around themselves during ongoing growth with a direction that points away from the substrate. Logically, growth of planar sheets far off the surface is generally unfavored and obviously pronounced curling of large leaf-like objects seems impossible since their morphogenesis occurs in direct contact with the surface. In addition the transitions from initially flat grown sheets to helical filaments was only rarely observed in solution experiments, as rims can only fold upwards (in contrast to experiments conducted in silica gels) consequently resulting in scrolled margins with unequal handedness.[70]

In view of these observations, it can be considered that growth and also the statistical distribution of distinct morphologies of silica-carbonate biomorphs are strongly linked to the presence of both extrinsic and intrinsic surfaces. This means that sheets grow in direct con-

tact with interfaces like vessel walls or solution surfaces, therefore forming a 2-D replica of the topology due to the beneficial influence of reduced nucleation barriers at interfaces. In opposite, when sheets propagate in the absence of a substrate they will develop a curved growth mode in order to fold back on themselves as the own surface is then preferred to reduce the energy barrier to facilitate further nucleation. In this case, depending on the degree of curling and the prevailing conditions, growth of worm-like braids or extended helicoids is preferred over flat sheets. These assumptions taken here lead to the hypothesis that morphogenesis of silica biomorphs should be sensitive to the geometrical parameters of the substrate surface. In order to verify these considerations, experiments are performed in this chapter using substrates with a defined and non-planar topology.

6.3 Experimentals

6.3.1 Fabrication of Micropatterned Substrates

Surfaces with defined periodic topology were obtained by manufacturing a polymeric replica of lithographically processed molds. For this purpose, silicon masters exhibiting different micrometer-scale structural motifs were purchased from GeSiM (Grosserkmannsdorf, Germany) and used to prepare stamps consisting of poly(dimethylsiloxane) (PDMS) following a procedure reported in the literature.[156] First, masters were hydrophobized by treatment with (heptadecafluoro-1,1,2,2- tetrahydrodecyl)-dimethylchlorosilane (ABCR Specialty Chemicals) to ensure removability of the PDMS stamp after completed preparation. Then, polymer precursor solution made by mixing Sylgard 184 (prepolymer received from Dow Corning) and a curing agent in a mass ratio of 10:1 was cast onto the masters. After degassing in a vacuum, samples were cured for 12 h at $60°C$. Eventually, the templated polymeric matrix was detached from the mold and hydrophilized in oxygen plasma for 45 s at 0.2 mbar and an intensity of 80 W, using a Flecto10 instrument from Plasma Technology.

In case of stamps with a wrinkled surface, the cross-linked PDMS was cut into 30 mm x 6 mm stripes and stretched uniaxially with the help of a customer made apparatus to a strain of 50 % of their length. Subsequently the streched substrates were oxidized for 60 min in oxygen plasma at 0.2 bar using plasma etcher operating at 0.1 kW (flecto10, Plasma Technology, Germany). The geometrical surface dimensions of the fabricated silicon substrate were fur-

thermore analyzed with atomic force microscopy (AFM) and revealed a wrinkle wavelength of λ = 43 μm and a wrinkle amplitude of A = 6 μm.

6.3.2 Crystallization and Characterization of Silica-Carbonate Biomorphs

Synthesis of silica-carbonate biomorphs was carried out in stagnant solutions according to a standard procedure applied in chapter 5. In short, a silica containing solution, prepared by diluting commercially available water glass (Sigma-Aldrich, reagent grade, containing 13.8 wt% Na and 12.5 wt% Si) with water. Subsequently, the pH of the silica sol was adjusted to values of about 11.3 by mixing with 0.1 M NaOH (Merck, p.a.) in a ratio of 20:1. In order to initiate crystallization 5 mL of the sol were rapidly combined with the same volume of 0.01 M solution of barium chloride dihydrate (Sigma-Aldrich $\geq$ 99%) in Nunc polystyrene multidish wells plates, which have a total volume of 10 mL (9.6 cm^2 bottom area, 1.7 cm depth). Prior to mixing of reagents, the as-prepared PDMS stamps were placed on the bottom of the wells to realize growth of silica biomorphs on micropatterned surfaces. The final reaction mixtures had a starting pH of 11.0 ± 0.1 and species concentrations of 5 mM Ba^{2+}, 8.4 mM "SiO_2" and 8.9 mM Na^+. After a chosen growth time of 8 h, the PDMS stamps were removed with a pair of tweezers and formed aggregates could readily be cleaned by careful rinsing with water and ethanol. All experiments were performed at ambient standard conditions ($20 \pm 1°\mathrm{C}$). All solutions were prepared using water of Milli-Q quality and stored in tightly stoppered plastic bottles so as to avoid undesired ingestion of both additional silica from glass walls and acidic carbon dioxide from the atmosphere prior to growth start.

Formed precipitates were at first inspected by means of polarized light microscopy using Nikon AZ100 and Eclipse E400 microscopes. For scanning electron microscopy (SEM) the dried PDMS substrates with the formed precipitates on the surface were directly mounted on a SEM stub. After coating with gold, specimen were inspected with a Zeiss LEO Gemini 1530 microscope working at acceleration voltages ranging between 3 and 5 kV. Suitable samples for AFM were obtained in a similar manner, but using glass cover slips as growth substrate. Analysis were performed on a commercial AFM (NanoWizard, JPK Instruments, Germany), equipped with Si cantilevers having a force constant of 40 N/m (NSC 15, Micro-

Mash, Estonia, resonant frequency: 325 Hz).

6.4 Results and Discussion

In a first set of experiments surfaces with a line-pattern structure on the microscale, exhibiting rectangular division bars which were periodically arranged were utilized. In all setups the height of the bars was kept constant at 5 µm, which is evidently a larger dimension than the approximate mean thickness of one representative sheet-like aggregate of 0.65 µm, demonstrated by the corresponding AFM height profile (cf. Figure 6.1).

The parameters which were varied in the different experiments were the mutual distance (d)

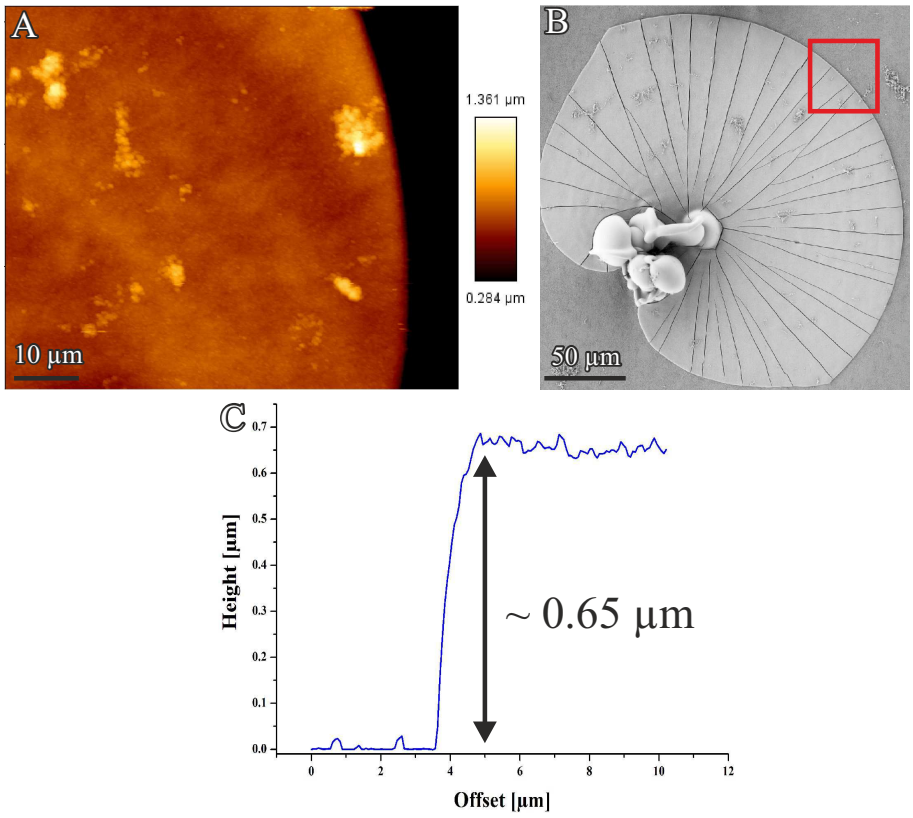

Figure 6.1. Determination of the thickness of a typical biomorph sheet. (A) AFM image of a leaf-like aggregate close on the border. (B) FESEM image of the sheet investigated with AFM. The position where AFM analysis were carried out is indicated with the red rectangle. (C) Corresponding height profile obtained by a line scan, starting at a certain point on the plain substrate (Offset=0) over the rim of the sheet, yields an approximate thickness of 0.65 µm.

and the width (w) of the division bars and detailed studies of resulting samples demonstrated that the dimension of the indents between individual bars had the most pronounced effect

on the morphological evolution of the architectures formed. When both parameters had the same dimension of 5 μm, aggregates developed exclusively on top of the bars, most probably due to the limited space in the gaps and the poor accessibility of the enclosed volume. Architectures resulting from fractal branching were found to be arranged to clusters which

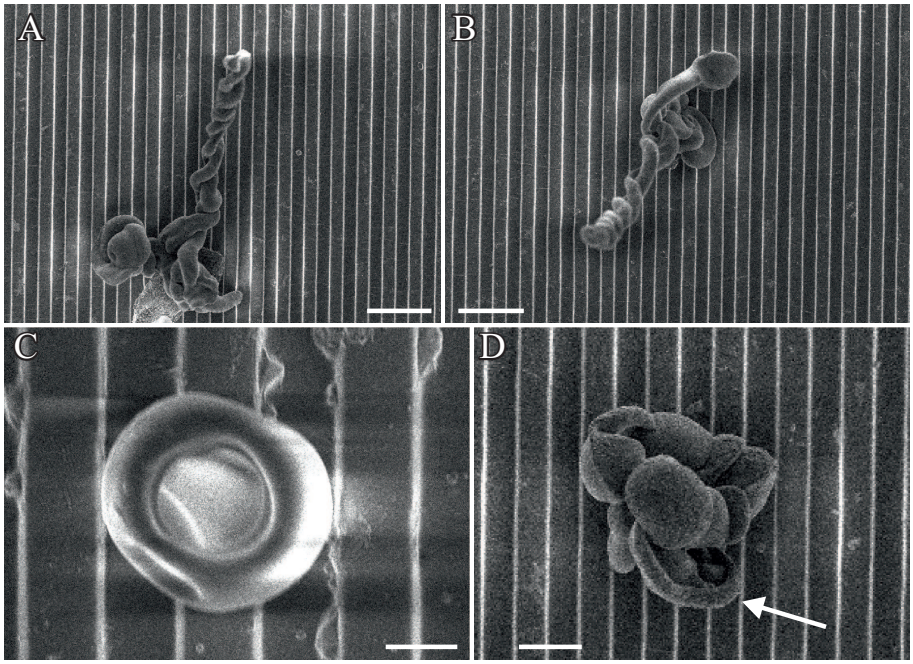

Figure 6.2. FESEM images of silica biomorphs grown on a silicon substrate which has a regular line-pattern topology with w = d = 5 μm. As a result of the uneven relief on the micrometer-scale emerging laminar segments are forced to curl imediately (indicated by the arrow in (D)) and extended flat sheets remain absent on the substrate. Helicoids and worms which protrude from the surface represent therefore the major fraction of aggregates observed in the experiments. Scalebars are 25 μm (A-B), 5 μm (C), and 10 μm (D).

often extended over several bars bridging the indents (see Figure 6.2 C-D). Remarkably the morphological distribution of polycrystalline aggregates formed on the patterned substrate differed drastically from those experiments conducted at standard conditions in the absence of structured surfaces. No single sheet was found to grow planar over distances exceeding 10 μm. Instead, observed morphologies were mainly of worm-like or helicoidal nature, and most aggregates were emanating in a direction away from the substrate (Figure 6.2A-B). Apart from this, the low fraction of laminar segments that was found were also heavily rolled around their rim (indicated by the white arrows in Figure 6.2D)

Observed differences in the growth behavior are obviously not influenced by the the chemical composition of the surface, as spacious sheets were also found in close vicinity of un-

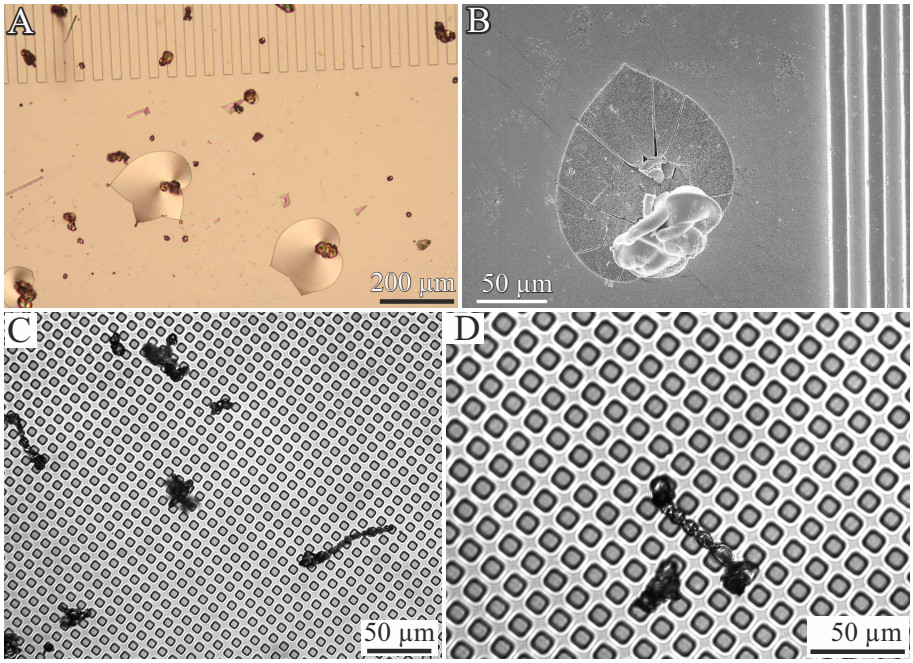

Figure 6.3. (A-B) SEM and polarized optical microscopy micrograph showing the borderline of structured and unpatterned areas of PDMS stamp with division bars in the dimension of 5 µm. It is clearly evident that extended flat sheets can developed in unstructrured regions of the silicon substrate. (C-D) Optical images of silica biomorphs grown on a substrate with square like meshes of islands (area of one mesh 10 x 10 μm^2 and a height of about 5 µm). Also here exclusively globular particles, worms and twisted morphologies were yielded, while extended flat leaf-like objects remained absent.

structured regions of the polymeric substrate (cf. Figure 6.3 A-B). Results of further experiments performed with different substrate materials such as glasses, metals or other polymeric material confirmed the assumption that the chemical nature of the substrate surface has no influencing effect on the growth behaviour of biomorphs. From these observations it can be concluded that the only reason for the observed alterations in the morphological distributions can be found in the topological conditions of the substrate surfaces. Beyond that, similar results were achieved using PDMS substrates having a mesh of quadrate islands with comparable structural dimensions as described above (see Figure 6.3 C-D).

In some cases, the typical growth mode on line patterns with d = 5 µm (cf. Figure 6.4 was different, and sheets extruded from globular clusters on top of a bar covered its surface over distances of up to several hundreds of micrometers and thus adopting intricate rectangular shapes (see Figure 6.4 A-C). A close-up view at one such aggregate reveals that also the side faces of the bar were covered with the crystal assembly (Figure 6.4A). This observation

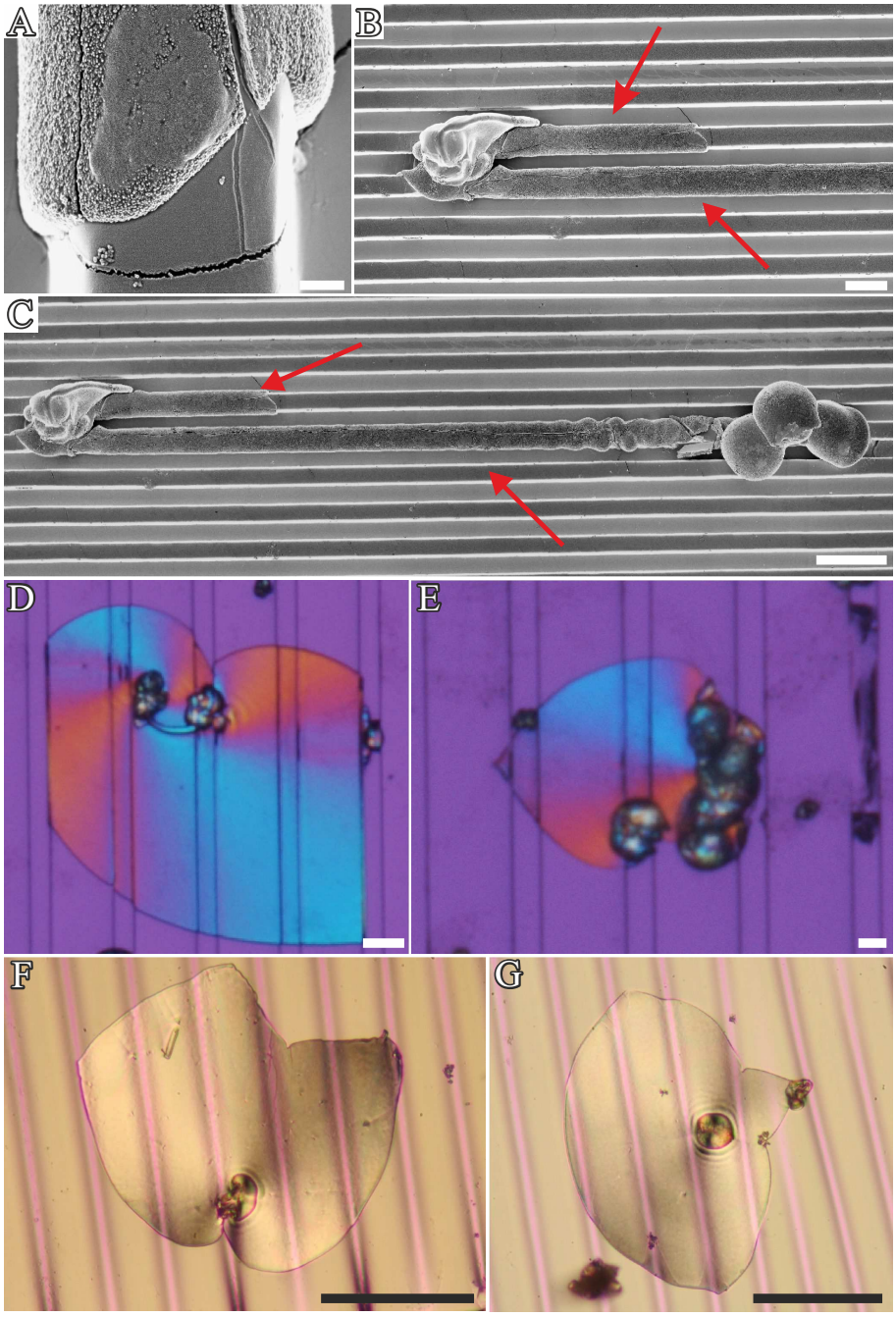

Figure 6.4. Novel forms of silica biomorphs, yielded upon growth on micropatterned substrates. (A-C) FESEM images showing crystal aggregates which are wrapped around the top face of a division bar over fairly large distances (w = d = 5 μm). (D-E) Polarized optical micrographs of sheets which extend over several bars in close contact to the underlying surface, forming a replica of the substrate topology (w = 30 μm, d = 10 μm). (F-G) Also on wrinkled substrates (wrinkle wavelength λ of 43 μm and a wrinkle amplitude A of 6 μm) flat polycrystalline aggregates are able to grow in contact with the substrate and adopting its topology. Scalebars are 1 μm (A), 10μm (B, D-E), 20 μm (C), and 100 μm (E-F).

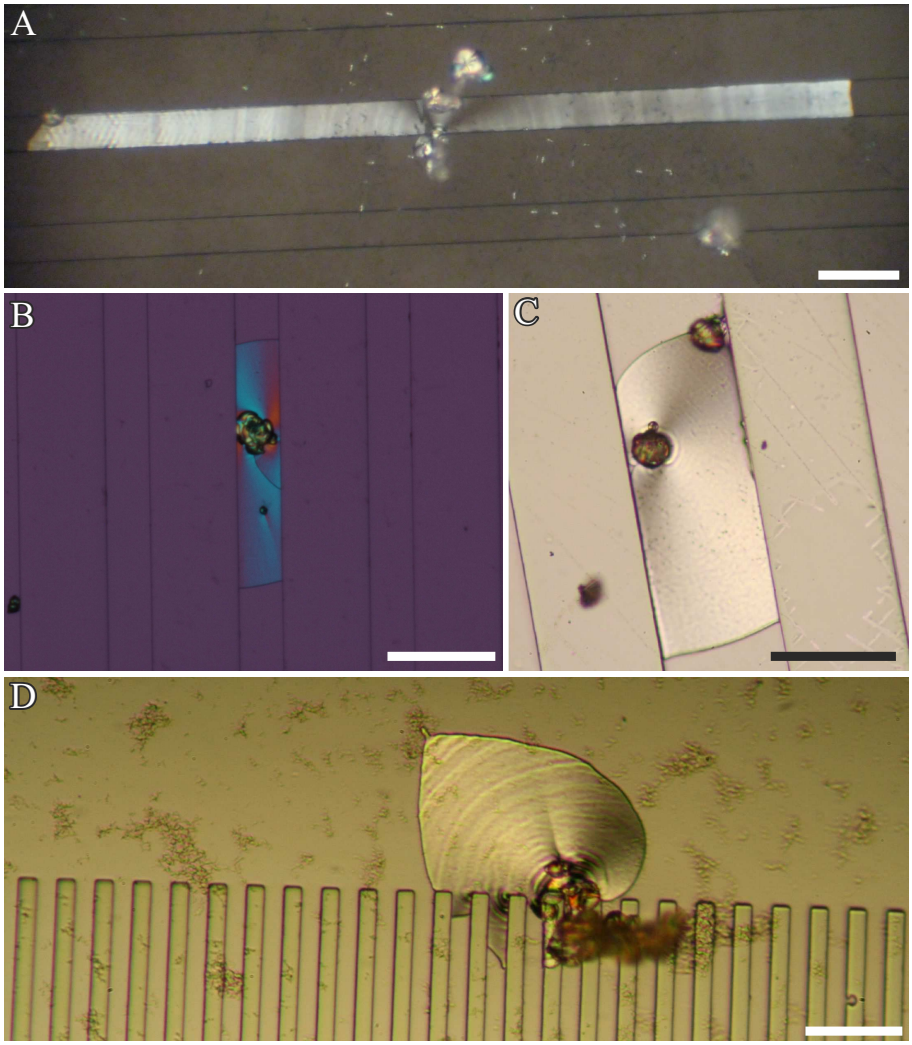

Figure 6.5. Templating silica biomorphs. (A-C) Increasing the bar distances to values $\geq$ 10 μm emerging aggregates become molded into the indents between the bars and exhibit quasi-rectangular stripe-like morphologies. (D) Optical micrograph of a sheet formed right at the border of the patterned area. It is evident that the crystal assembly tends to dodge obstacles and continues growing only along flat pathways, such that it penetrates the channels from the outside and encloses the bar ends. Substrate dimensions: (A) w = 160 μm, d = 80 μm, (B-C) w = 100 μm, d = 40 μm, (D-E) w = 10 μm, d= 10 μmm. Scalebars are 100 μm.

clearly demonstrates that curling does not necessarily occur at the rim of the bar. In addition, it could be shown that sheets are capable of wrapping around sharp corners.

In view of the gained results a growth scenario can be proposed in which the underlying substrate controls the induction of curvature. An emerging sheet that propagates in direct contact with the top face of the bar will start to curl upon arrival at the gap, due to the abrupt vertical change of the topology at this certain point. Obviously, the polycrystalline assembly cannot continue to grow by following the sudden directional change and, consequently,

curved growth back towards the own surface is favored. Obviously, the dimension of the gap is to large to allow bridging the distance between two paralelly oriented bars by a sheet in the absence of an underlying surface. As a result, formation of twisted forms like helicoids or worm-like braids becomes strongly favored over flat extended sheets in the presence of micropatterned surfaces. In this sense, the use of substrates with a structured topology turned out to be a good strategy for directing the resulting morphologies of silica biomorphs towards complex curved aggregates.

A more definite finding supporting this notion is is given in Figure 6.4 (D-E). In these cases, sheets have grown over several bars and indents, being completely in direct contact with the substrate until growth has ceased at the edge on both sides. Resulting crystalline aggregates have adopted the topology of the PDMS substrate. Beyond that, the observed color interference patterns correlate to those of silica biomorphs grown on unstructured surfaces,[61,67] thus indicating that the structured topology of the substrates does not affect the microstructure of the aggregates. Similar results were obtained when the rectangular bar pattern of the substrate was replaced by a wrinkled topology exhibiting height differences with dimensions similar to those used in the preceding experiments. Similar results were yielded when the rectangular bar pattern was replaced by a substrate with a wrinkled topology exhibiting a height difference that is in the dimension as in the preceding experiments. Indeed, sheets were found to expand across several smoothly curved obstacles, being completely adherent to the underlying surface (Figure 6.4F-G). Interestingly, fractions of helical filaments or worms were quite low compared to the results gained with a line-patterned topology of w and d = 5 μm. However factors which decide if a sheets curls or follows the topology of the surface when arriving at an edge are hard to identify. One key parameter could possibly be the actual growth rate of the laminar segment, which has been reported to vary from aggregate to aggregate in one batch.[75] Possibly, sheets that evolve rather slowly are able to change their growth direction in an orthogonal fashion at the rim of a bar, whereas those with higher growth constants prefer folding back on their own surface. On the other side, when the sheet arrives at an edge with low curvature the tendency to follow the topology is higher, independent of the growth velocity.

In summary our results clearly demonstrate that both the shape and topology of silica-

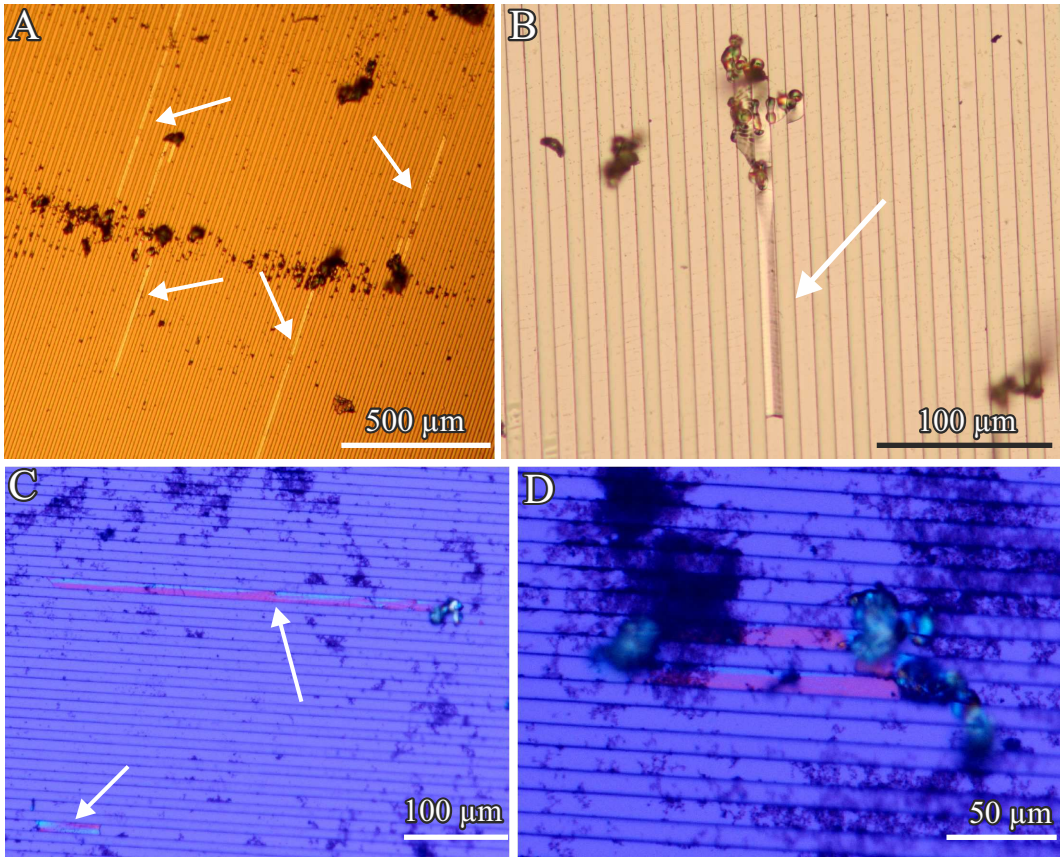

Figure 6.6. (A-D) Further optical micrographs of stripe-like morphologies (indicated by the white arrows) with dimensions of several hundreds of microns, yielded upon growth of silica biomorphs on line-pattern substrates with w = d = 10 µm. The black precipitate in (D) is amorphous silica which has precipitated independent of biomorphs.

carbonate biomorphs can be influenced by using suitable micropatterned growth substrates. Such a strategy can be applied by straightforward means in order to control morphology in a more sophisticated way. By increasing the gap distance to values larger than 10 µm, nucleation of fractal precursors at the indented sites of the substrate becomes possible, and thus the formation of large polycrystalline assemblies. Under these conditions, the evolution of emerging aggregates is now strongly affected by the substrate, as the height of the substrate structures is a multiple higher than the typical thickness of a sheet (cf. Figure 6.1) and acts therefore as an obstacle, provoking in most cases the termination of growth due to an abrupt change of the direction. Therefore sheets were found to grow along the channel paths of the indentations across the surface, forming peculiar elongated, stripe-like morphologies with dimensions of up to several millimeters (see Figure 6.5A-C and Figure 6.6) in a direct molding process. The nanoscale building units of the quasi-rectangular aggregates show fur-

thermore radial orientation starting from the central globular particle outwards in nearly the same manner as observed in experiments with unpatterned substrates, indicated by the typical extinction pattern between crossed polarizers.[67] This further demonstrates that the spatial constraints caused by the substrate structure have no decisive influence on the mesoscaled orientational ordering of the nanocrystallites during growth, whereas, occasionally, the interference patterns slightly differed from the standard case (see Figure 6.6). In comparison to morphologies observed in Figure 6.3, the imprinting of the stripe-like shapes was very frequently observed and the fraction of polycrystalline imprints markedly increases when the distance between the individual bars exceeds 10 μm (see Figure 6.6A).

In cases where aggregate growth starts at unstructured substrate areas in close vicinity to the structured area, propagation of planar sheets occurs at first in a radial manner, until the growing front reaches the structured area at the end of the exposed bars. At this point, the ordinary growth mode becomes disturbed by the presence of structured parts and the sheets start to split in order to dodge the obstacle. Subsequently, growth of the polycrystalline aggregates proceeds along the thin and indented areas of the substrate, leading to a starting infiltration of the indented channels (cf. Figure 6.5).

The reverse scenario also occurred when growth of sheets was initiated inside indented channels. Upon further evolution, the growing front reached the borderline between structured and unstructured surface area. In the absence of a spatial constraint, the laminar aggregates switched to radial growth mode, initiating a leaf-like growth as typically observed in standard experiments (Figure 6.7). Beyond that, this particular sheet formed on top of a larger one which has evolved right at the edge of the structured region, intruding into the neighboring channel, resulting in a stripe-like architecture with a dimension of several hundreds of micrometers (Figure 6.7).

This interesting phenomenon is an impressing indicator for the high flexibility of polycrystalline laminar segments of silica biomorphs when being exposed to certain spatial constraints during morphogenesis. Taken together, the experiments described in this section clearly show that the shape of biomorphs can be directly taylored using microstructured substrates as growth templates.

In view of industrial applications, the presented strategy might be of particular interest for

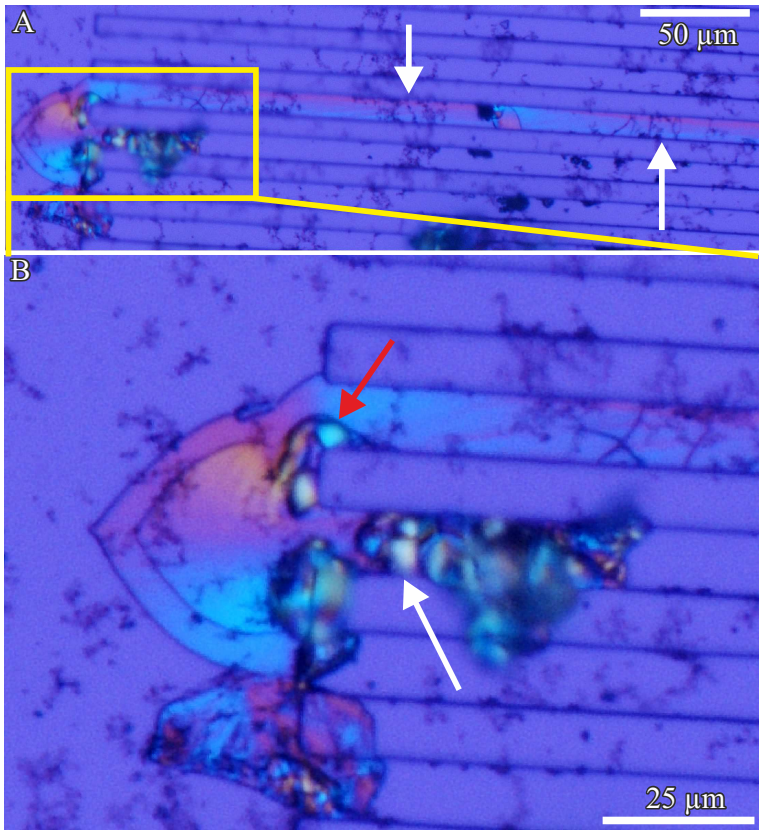

Figure 6.7. Polarized light microscopy images of laminar aggregates that formed near the rim of the patterned region on a substrate with w = d = 10 µm. (A) Overview of the entire assembly, comprising two cardioid shaped sheets grown on top of each other in the unstructured part right at the border, as well as two rectangular segments penetrating neighboring channels of the patterned area. One of these segments extends into the template over a distance on the millimetre scale, whereas the other is only several microns in length. (B) Higher magnification of the border region, showing that the short laminar domain in the left-hand channel emerged from a globular precursor located inside the channel (indicated by the white arrow). Thus, the sheet grew from the patterned area into the unstructured region, where it immediately began to spread radially and finally adopted its common leaf-like shape. By contrast, the long rectangular segment in the upper channel resulted from ingrowth of a sheet, which initially became extruded outside the templated area from a fractal globule formed at the edge of one of the bars (marked by the red arrow).

the synthesis of taylored inorganic hybrid material from simple educts. It is worth to note that the generated architectures presented in this study resemble, at least to some extent, those prepared by Kim et al. who mineralized $CaCO_3$ structures in a square array of cross-linked channels by using polymer induced liquid precursor (PILP) phases. Crystallization was thereby controlled with the help of specially designed substrates which were functional-

ized with self-assembled monolayers (SAMs) prior to use.[157] This special treatment allowed a directed deposition of PILP droplets onto the functionalized areas of the substrate, resulting in extended 2-D calcite crystals with specific patterns after solidification and mineralization. In a second preceding work, Aizenberg et. al. succeeded to prepare millimeter sized calcite single crystals with specific orientations and periodic holes, again using the beneficial influence of SAMs. In this case, functionalization provoked an area-selective mineralization of amorphous calcium carbonate (ACC) precursors which subsequently transform into the mature calcite crystal.[29,158] Similar templating approaches were utilized for instance with the help of polymeric sea urchin plate replicas[159] to create three-dimensional single-crystalline aggregates with complex non-crystallographic shapes and unique microstructural features. The structures obtained in the presented experiments differ from those mentioned above by their polycrystalline nature and follow a specific long-range order on the mesoscale. Thus, the conducted experiments represent a successful combination of top-down approaches by templating laminar segments in confined reaction volumes with bottom-up self-assembly of nanosized carbonates via dynamic interplay of involved components.

Under normal conditions of biomorph growth, the absence of chirality is explained by the morphogenetic scenario on the nano- and micrometerlevel, as the relative sign of curling is an arbitrary phenomenon and therefore results in racemic mixtures of left- and right-handed helical filaments.[81] However, the applied strategies for the tailored generation of laminar segments according to the topology of the underlying substrate presented in this chapter open up a possible new pathway for the creation of surfaces with specially designed obstacles. These surface structurings might potentially allow the preparation of preferentially oriented helical structures composed of carbonate and silica and thus the induction of chirality in the course of biomorph growth. As a first step towards this approach, the findings in this chapter explain the induction of curvature of progressing laminar filaments on the micrometer level. However corresponding mechanisms on the nanoscale are not yet elucidated and therefore deserve further investigation.

6.5 Conclusions

In the present study the influence of microstructured growth substrates on the morphogenesis of silica-carbonate biomorphs was investigated. For this purpose, polymeric silicone stamps with defined periodically arranged line-pattern topologies were used as substrates for growth of silica biomorphs. The substrate structuring was thereby varied by adjusting the width and mutual distance of the division bars, while the height of the structuring remained constant. When the distance between the individual bars was < 5 μm, nucleation could not occur at the indented areas and growth was only observed on the top faces of the bars. In these cases, emerging laminar segments usually started to curl by reaching the edges of the exposed structurings. As a consequence to the enhanced curling of protruding laminar segments, a significant increase in the fractions of helicoidal and worm-like architectures was stated. These findings confirm the hyothesis that foreign extrinsic surfaces play an important role during the morphogenesis of silica biomorphs. Furthermore, this strategy enables a specific tailoring and favoring of distinct morphologies within one batch. Upon alteration of the substrate structuring by increasing the distances between the exposed bars, nucleation and growth of planar sheets occurs in the indented substrate areas, resulting in nearly rectangular stripe-like biomorph aggregates. Lateral growth of the aggregates is thereby prevented by the physical limitation of the substrate pattern. Results of these experiments might possibly serve as a novel strategy for tailoring the design of innovative silica-carbonate hybrid material.

7 Crystallization of mixed alkaline-earth carbonates in alkaline silica solutions

7.1 Abstract

The ability of silica to influence the mineralization of alkaline-earth carbonates at elevated pH has for long been an outstanding example for the formation of biomimetic structures in the absence of any organic matter. Under suitable conditions, silica-stabilized carbonate nanocrystals can spontaneously self-assemble into hierarchical materials with sinuous morphologies, commonly referred to as "silica-carbonate biomorphs". However, at ambient temperature and pressure, growth of these self-organized crystal aggregates has largely been restricted to the higher homologues in the alkaline-earth series, i.e. $SrCO_3$ and $BaCO_3$, which crystallize in orthorhombic lattices. In turn, corresponding architectures of the much more relevant calcium carbonate could up to now only be prepared by laboriously favoring the formation of metastable (and likewise orthorhombic) aragonite. To address this problem in more detail and to investigate differences in the behavior of Ba^{2+}/Sr^{2+} and Ca^{2+} during co-mineralization with silica, we have crystallized metal carbonates in the presence of silica at high pH, using barium and strontium chloride solutions that contained increasing molar fractions of Ca^{2+}. The resulting materials were analyzed with respect to their composition, structure and crystallography. The obtained data demonstrate that the development of complex shapes is strongly affected already by small amounts of Ca^{2+}. Indeed, morphologies typically observed for $SrCO_3$ and $BaCO_3$ remained absent above certain thresholds of added calcium, which were found to vary slightly between barium and strontium. Instead, globular and hemispherical structures were generated, owing to fractal branching of an elongated pseudo-hexagonal core crystal through its basal faces due to poisoning by silica. These

alterations in the growth behavior are mainly ascribed to relatively strong interactions of hard calcium ions with silicate species in solution, shifting their speciation towards higher oligomers and even inducing partial coagulation. Under these circumstances, the dynamic coupling supposed to drive the self-assembly of biomorphs can no longer be initiated, so that curved polycrystalline structures are not formed. This notion is confirmed by additional experiments in the presence of high amounts of sodium chloride, which proved to have similar effects on the chemistry of silica and thus the growth behavior as Ca^{2+} ions. Our results further demonstrate that the observed hemispherical particles exhibit distinct polymorphism depending on the ratios of metal ions in solution, with orthorhombic solid solutions (aragonite-type $(\mathrm{Sr,Ca})\mathrm{CO_3}$ and $(\mathrm{Ba,Ca})\mathrm{CO_3}$) being formed at lower Ca^{2+} contents, whereas Sr^{2+}/Ba^{2+}-substituted calcite prevails at higher Ca^{2+} fractions. In the case of Ba^{2+}/Ca^{2+} mixtures, there is moreover an intermediate range where virtually identical morphologies were confirmed to be Ba^{2+}-doped vaterite. These findings extend the variety of structures and compositions accessible in these simple systems, and may explain difficulties previously encountered in attempts to prepare $CaCO_3$ biomorphs at standard conditions.

7.2 Introduction

In the last decades, the demand for new materials with specific properties has drastically increased. Modern synthetic approaches often follow strategies relying on bottom-up self-assembly of rather simple and cheap educts.[160–163] In this context, so-called "silica biomorphs" have attracted growing attention, as these mesoscopically ordered architectures spontaneously develop from purely inorganic precursors via concerted interactions of the involved components.[59–62,67–69,74–76,80–82,87,125] Biomorphs consist of alkaline-earth carbonate (usually $BaCO_3$) nanorods, which are stabilized and interwoven by amorphous silica, and build up complex crystal aggregates that resemble biogenic minerals and display a broad variety of non-crystallographic morphologies, ranging from flat sheets over helicoids to coral- or worm-like structures.[66–68,84]

Recently, considerable progress has been made towards an understanding of the mechanisms leading to morphogenesis on the micrometer level, as well as the driving forces governing particle-based crystallization at the nanoscale.[61,81,86,87] In essence, a scenario was proposed

that segments the growth process into two principal stages: all characteristic architectures arise from a micron-sized carbonate crystal seed, which nucleates heterogeneously after some delay and soon adopts an elongated pseudo-hexagonal habit typical for orthorhombic carbonates.[61,75,125] Upon further growth, this crystal starts to split at both ends along the c-axis due to non-specific poisoning by oligomeric silicate species, leading to tilted outgrowths at non-crystallographic angles. Branching occurs through the basal {001} faces and, after self-similar (fractal) propagation, yields increasingly bifurcated particles that develop through dumbbell-shaped forms eventually into closed spherulites or spacious cauliflower-like structures.[61,68,81,125] From a morphological point of view, this growth behavior is similar to what has been observed for fluorapatite crystallization in gelatin matrices.[88,90,91] In a subsequent second stage, fractal branching gives way to polycrystalline mineralization, where silica-sheathed carbonate nanoparticles are constantly nucleated and serve as building blocks for the construction of biomorphic aggregates, which then evolve free from symmetry constraints towards complex curved morphologies. The continuous production of nanocrystal units is explained by local variations of pH and supersaturation nearby the front of the aggregates, as a consequence of the inverse trends in solubility of silica and carbonate with pH in alkaline media: growth of carbonate particles causes a decrease of pH in their vicinity (due to bicarbonate dissociation), which leads to local precipitation of silica and stabilization of the crystallites.[92] Ongoing silica condensation then re-increases the pH at the front, so that a novel event of carbonate nucleation is induced and the previous steps are reiterated. Thus, the mineralization of the two components is coupled via the local pH, resulting in alternating precipitation through autocatalytic processes.[81,86,87]

However, this dynamic interplay does only occur within a certain range of conditions, as determined by parameters like the bulk pH[125], and recent studies also demonstrated that the final morphologies displayed by silica biomorphs may strongly depend on subtle factors.[61,69,76,84]

Another mandatory requirement for the formation of true silica biomorphs (i.e. nanocrystalline aggregates exhibiting sinuous shapes) seems to be the use of carbonates that crystallize in an orthorhombic structure, such as strontianite ($SrCO_3$) and witherite ($BaCO_3$); both being isomorphous with the $CaCO_3$ polymorph aragonite). In fact, Ba^{2+} and Sr^{2+} salts can be mixed at arbitrary ratios without any change in the morphologies of the resulting biomorphs

being discernible, which suggests that both metal ions are homogeneously distributed within the mature aggregates.[59] Calcium carbonate - the by far most abundant mineral within the alkaline-earth series and of high relevance for industrial processes - also forms biomimetic structures in silica-rich environments.[99–101,126] However, in line with the above notion, these precipitates consisted of rhombohedral calcite and did not display intricate curved morphologies as those being characteristic for biomorphs (like worms or helicoids). Rather, their structure and formation mechanism could in most cases be explained by selective adsorption of silicate species on specific crystallographic planes, causing changes in relative growth rates of distinct calcite faces. Actual $CaCO_3$ biomorphs were in turn produced by tuning the synthesis conditions in order to shift polymorph selection in the direction of aragonite. This was successfully accomplished by increasing the temperature to $80°C$, thus kinetically favoring the formation of aragonite[84], or by using suitable seed crystals.[82] Clearly, it would be desirable to develop a bottom-up protocol allowing for the preparation of $CaCO_3$ biomorphs at ambient temperature, without the need for external triggers like seeds. Preliminary observations made in very recent work have indicated that silica-aragonite biomorphs might indeed grow spontaneously in silica gels under very particular conditions (i.e. specific concentrations, pH, location in the gel, etc.).[85] However, detailed insight into the role of the different parameters and control over the final structures has not yet been gained.

Another potential way to generate $CaCO_3$ biomorphs at room temperature is to work with mixtures of calcium and barium or strontium, as it is known that both witherite and strontianite can incorporate Ca^{2+} into their crystal lattice (forming solid solutions)[164–166], and that even minor amounts of the larger Ba^{2+} or Sr^{2+} ions can force calcium carbonate into the aragonite modification.[167] Here, we have investigated the possibility to grow silica-aragonite biomorphs by crystallizing carbonates from mixtures of $BaCl_2$ or $SrCl_2$ and $CaCl_2$ under the influence of dissolved silica at high pH. Experiments were performed in which the ratio of Ba^{2+}/Sr^{2+} to Ca^{2+} was systematically varied, at overall constant metal ion concentration. After mixing with dilute silica sols, the alkaline metal chloride solutions were exposed to the atmosphere over periods of up to several days, until crystallization occurred due to progressive ingestion of CO_2. The resulting precipitates were investigated in terms of morphology, composition and structure with different techniques, focusing on the specific influence of the

divalent calcium ions on morphogenetic pathways.

7.3 Experimentals

7.3.1 Materials

Barium chloride dihydrate (Sigma-Aldrich, $\geq$ 99%), strontium chloride hexahydrate (Sigma-Aldrich, ACS reagent, $\geq$ 99%), and calcium chloride dehydrate (Riedel-de Haën, ACS reagent, $\geq$ 99%) were used without any further purification. The silica source and the preparation method for corresponding solutions was the same as described in section 5.3

7.3.2 Crystallization Experiments

Synthesis of silica-carbonate biomorphs was performed applying a similar procedure and using the same concentration of components described in section5.3.[68,75,76,87,125] First, the silica stock was diluted with water by a factor of 1:350 (v/v) and then mixed at a ratio of 20:1 (v/v) with 0.1M sodium hydroxide solution. Crystallization was initiated by combining 5 mL of the resulting silica sol (pH $\sim$11.3) with the same volume of 0.01 M metal chloride solutions containing different molar fractions of $CaCl_2$ (x_{Ca} = 0, 0.02, 0.10, 0.20, 0.50, 0.80, and 1.00) next to either $BaCl_2$ or $SrCl_2$. Experiments were conducted at $20 \pm 1°C$ in sterile 6-well microplates (Nunclon, polystyrene, 10 mL total volume, 9.6 cm^2 bottom area, 1.7 cm in depth), into which glass coverslips (22 x 22 mm) were placed as growth substrates before filling with growth solution. After exposure of the samples to the atmosphere over predefined periods (varying between 18 h and 3 days and depending on the Ca^{2+} content), the substrates were removed with a pair of tweezers and subsequently washed with water and ethanol (Baker, p.a.), followed by drying in air.

7.3.3 Characterization Methods

At first, the time-dependent macroscopic behavior of the samples at distinct barium/strontium to calcium ratios was observed visually. To that end, time-lapsed series of photographs were recorded with a remote-controlled Canon EOS 350D digital camera. The pH of the samples was measured directly after mixing reagents (i.e. the metal salt mixture with the silica sol) and after a period of 24 h hours by means of a polymer-based electrode (Mettler-Toledo, In-

Lab Expert), which was connected to a Schott CG-843 laboratory pH meter. The initial pH was found to be 11.0 $\pm$ 0.1 independent of the $CaCl_2$ content and whether Ba^{2+} or Sr^{2+} was used, which is in good agreement with values reported for pure Ba^{2+} systems in previous work.[75,125] Within one day, the pH decreased to 9.6 $\pm$ 0.1 in all samples due to in-diffusion of CO_2 into the alkaline solutions, forming carbonic acid which rapidly deprotonates to give carbonate and bicarbonate species.

Isolated precipitates were routinely studied by polarized optical microscopy (POM) using a Nikon Eclipse E400 transmission microscope, onto which a Canon EOS 350D camera was mounted for imaging. For scanning electron microscopy (SEM), aggregates were grown directly on a conducting foil, which was placed on the bottom of the wells as a growth substrate. After careful rinsing with water and ethanol, the foil carrying the precipitates was mounted directly on the SEM stub and coated with a thin gold layer. Specimens were investigated with a Zeiss LEO Gemini 1530 or a FEI Quanta 400 T microscope, at acceleration voltages ranging from 3 to 10 kV. Energy-dispersive X-ray (EDX) spectroscopy measurements were carried out with the help of an installed Oxford INCA microanalysis system, while working at an acceleration voltage of at least 10 kV. Spectra were recorded at three different positions on the stub, in order to average results for a given sample. X-ray diffraction (XRD) data were recorded on a STOE STADI P diffractometer using Cu-K_α radiation and a germanium single crystal monochromator (λ = 1.540598 Å). Patterns were recorded over a 2Θ range of $8°$ to $90°$ at a scanning speed of $0.8°$/ min. DLS measurements were performed, applying a similar procedure already described in the experimental section of chapter 3.

7.4 Results

7.4.1 Morphological Analysis

Reference Experiments

First, reference experiments were performed in which witherite and strontianite were crystallized in the absence of Ca^{2+} under conditions commonly applied for the synthesis of silica biomorphs (5 mM Ba^{2+} or Sr^{2+}, 8.4 mM SiO_2, pH ˜11). The resulting aggregates exhibited

morphologies very similar to those reported previously[62,67–69,75,80,82,85,125], without any significant morphological or structural differences between $BaCO_3$ and $SrCO_3$ being discernible. Typical forms include regular helicoids, flat leaf-like sheets, as well as thicker and more tightly wound worms (Figure 7.1A-F), with dimensions of up to several hundreds of microns and size distributions that agree well with data published for silica-witherite biomorphs in earlier work.[75,125] Along with these complex polycrystalline structures, various fractal aggregates - globules, dumbbells, and clusters thereof - with diameters in the range of 10 μm were frequently observed (Figure 7.2), all of which arise from an initial rod-like carbonate seed crystal that splits at both of its ends due to the poisoning influence of oligomeric silicate species, as described above and explained in detail elsewhere.[81] Bottom views re-

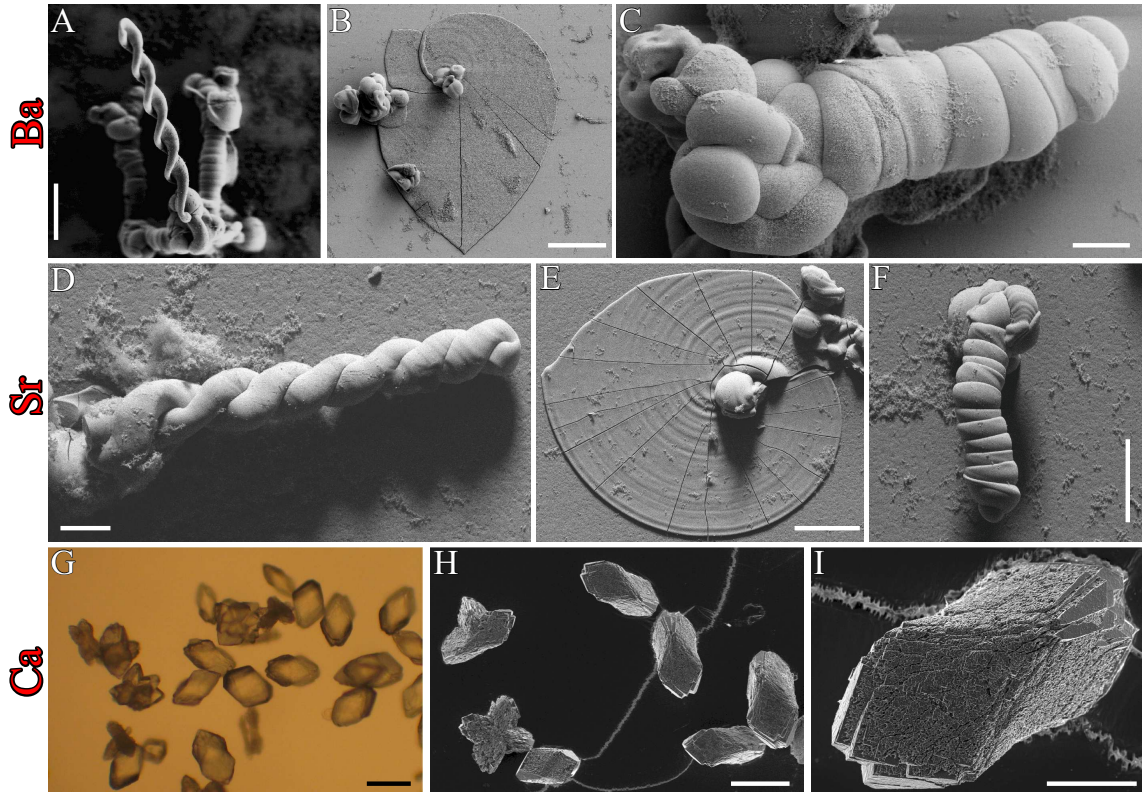

Figure 7.1. FESEM and optical micrographs of $BaCO_3$ (upper panels), $SrCO_3$ (middle panels), and $CaCO_3$ (lower panels) structures formed upon precipitation from silica-containing solutions at high pH. (A-C) Silica-witherite biomorphs, showing helicoidal filaments (A), flat sheets (B), and worms (C) as main morphologies. (D-E) Silica-strontianite biomorphs, virtually indistinguishable from their $BaCO_3$ counterparts. (G-I) Unusual calcite crystals, elongated along their c-axis and exhibiting dome-like outgrowths. Scale bars: (A-B) 50 μm, (C) 10 μm, (D) 20 μm, (E-H) 50 μm, and (I) 20 μm.

veal that bifurcation of the core crystal occurs along the [001] direction (Figure 7.2C), and

that progressive branching does at first yield dumbbell-like particles (Figure 7.2A), which finally become closed to give spherulithic architectures (Figure 7.2B and D). These fractal structures were shown to be precursors of the more characteristic non-crystallographic morphologies displayed by silica biomorphs.[61,68,81] For instance, after some time, laminar domains (composed of silica-stabilized nanocrystals) start to sprout radially from the globular units and subsequently grow flat in a nearly two-dimensional manner into extended sheet-like objects (Figure 7.1F and 7.1H, with the initial fractal clusters being visible in the center of the leaves). The more elaborate, curved ultrastructures (helicoids and worms, cf. Figure 7.1E and 7.1G) in turn emerge when sheets become curled at their rim and distinct segments begin to wind around one another; parameters determining the final shape of these twisted aggregates have been thoroughly discussed in the literature.[75,81]

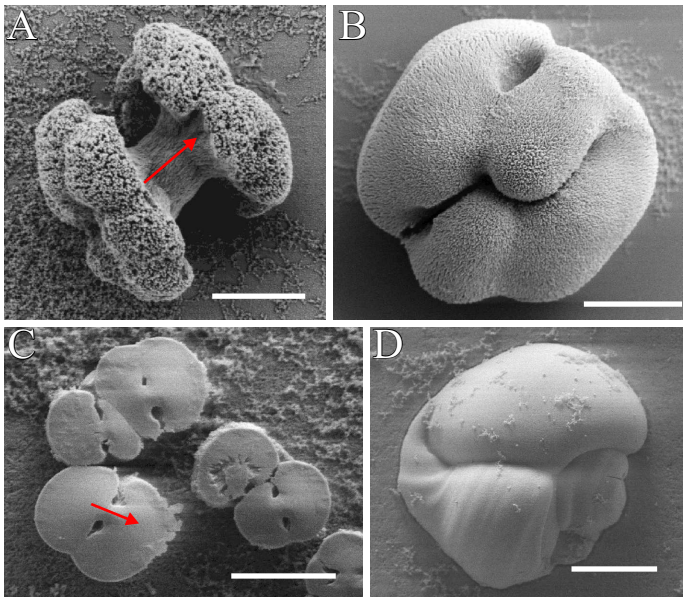

Figure 7.2. Fractal architectures of (A-B) $BaCO_3$ and (B-C) $SrCO_3$, produced by continuous branching of an initial seed crystal along its c-axis (indicated by arrows), at first yielding dumbbell-like morphologies (A and C), which then develop into more or less closed spherulites (B and D). Note that these structures are precursors of the curved forms generated during the second stage of biomorph growth (however, not all of these particles give rise to characteristic polycrystalline aggregates, so some of them remain as "by-product"). Scale bars are A 2 μm, B 5 μm, C 10 μm, D 20 μm

When crystallization was carried out under the same conditions, but using 5 mM $CaCl_2$ instead of $BaCl_2$/$SrCl_2$, the solutions became turbid several minutes after mixing of reagents (see Figure 7.3, in contrast to the previous experiments with Ba^{2+} and Sr^{2+}.

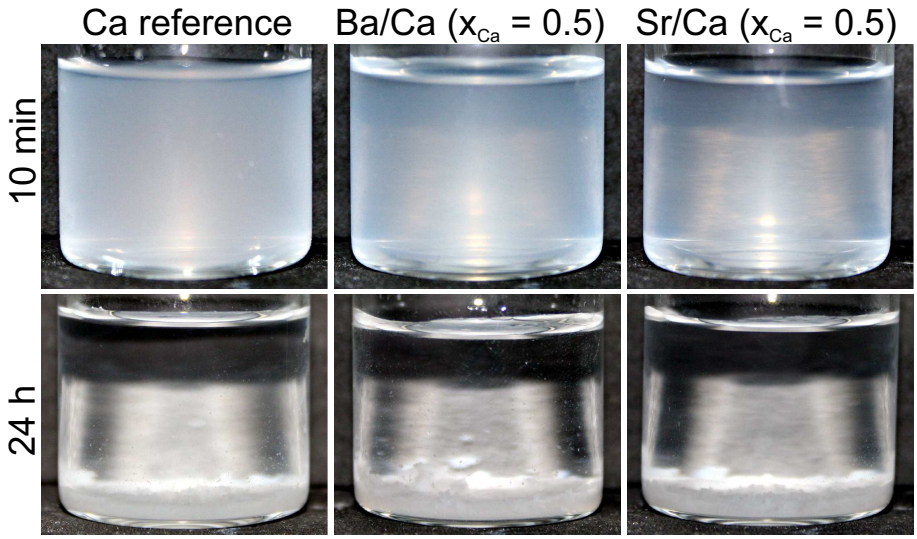

Figure 7.3. Photographs of vials showing the macroscopic behavior of samples containing 5 mM $CaCl_2$ (left) or 2.5 mM each of $CaCl_2$ and $BaCl_2$ (middle) or $SrCl_2$ (right). Pictures were taken 10 min and 24 h after mixing reagents (metal chloride solution and alkaline silica sol). Initially, the solutions have a turbid appearance as a result of reinforced silica condensation and polymerization in the presence of Ca^{2+} ions, which screen the negative charges of individual silicate species. Continued polycondensation ultimately leads to coagulation and the formation of a layer of silica gel on the bottom of the vials (cf. lower panels). Subsequent carbonate crystallization occurs predominantly within this gel medium.

This can most likely be ascribed to stronger interactions of the calcium ion, exhibiting a comparable higher charge density, with the negatively charged colloidal silicate species existing at the given alkaline conditions.[129] Thereby, the divalent cation screens the charges and provokes polymerization of silica, causing coagulation and the deposition of a layer of silica gel on the bottom of the well. Within this layer, crystals with extraordinary shapes and fairly uniform dimensions (ca. 50 μm) grew within a period of about 3 days (Figure 7.1G-I), and were confirmed to be calcite by X-ray diffraction (cf. Figure 5). Closer examination suggests that these crystals are elongated along the crystallographic c-axis and consist of micron-sized, tabular subunits. Moreover, they display large dome-like outgrowths on one of their ends (Figure 7.1J). Similar morphologies and structures have been obtained previously by crystallization of $CaCO_3$ in silica gels upon in-diffusion of $CaCl_2$[85,100], and were also observed during growth from solution at high supersaturation.[101] Thus, elongation of calcite single crystals and subsequent further distortion of the rhombohedral habit in the presence of dissolved silica is well documented in the literature, and has been explained by adsorption and

condensation of silicate ions on specific planes parallel to the c-axis.[126] Taken together, it is obvious that Ba^{2+} and Sr^{2+} readily form biomorphs at ambient conditions, whereas Ca^{2+} "only" gives complex single and/or mesocrystals. We now turn to consider changes in the growth behavior traced when gradually replacing Ba^{2+}/Sr^{2+} by Ca^{2+}.

Effect of added calcium ions on the growth behavior of silica-witherite biomorphs

Introducing Ca^{2+} to the mother solution of $BaCO_3$ biomorphs (at a constant total metal ion concentration of 5 mM) proved to have a strong influence on the morphology of resulting precipitates. Firstly, visual observations show that for calcium molar fractions equal to or higher than 0.20, the samples become turbid soon after mixing (see Figure 7.3), as in the case of the reference experiments with pure $CaCl_2$, thus indicating significant Ca^{2+}-induced silica condensation also at lower cation concentrations. Again, crystallization occurred exclusively within the gel domains formed after some delay due to ongoing silica polymerization. Furthermore, the time required for crystals to be observed (ca. 3 days) was considerably longer than in the absence of Ca^{2+} ($<$ 10 h), and also the absolute number of particles was found to decrease with increasing x_{Ca}. Figure 7.4 illustrates the morphological evolution observed for mixtures of $BaCl_2$ and $CaCl_2$ at different molar fractions of Ca^{2+}. Drastic changes in the distribution of morphologies can be discerned already at calcium molar fractions as low as 0.02 (Figure 7.4A). In fact, there was not a single characteristic biomorph occurring throughout a series of syntheses at these conditions. Instead, fairly large networks (up to 300 μm) composed of multiple fractal spherulites were observed. Individual units closely resemble those formed in Ca^{2+}-free experiments (cf. Figure 7.2), which suggests that the self-similar branching process (i.e. the first stage of morphogenesis) is not noticeably affected by the Ca^{2+} ions. On the other hand, the fact that biomorphic ultrastructures were not at all formed indicates that the second stage of morphogenesis - i.e. coupled co-mineralization of silica and carbonate and their assembly into curved nanocrystalline aggregates - cannot be initiated in the presence of even small amounts of calcium ions.

At a Ca^{2+} fraction of 0.10, we could again only distinguish spherulitic objects, however with quite distinct appearance. Indeed, the observed crystal architectures consisted of rather thick, blocky subunits with widths in the range of 5 μm, which were arranged radially outwards from a common origin (Figure 7.4B-C). Single subunits can clearly be identified as cyclic

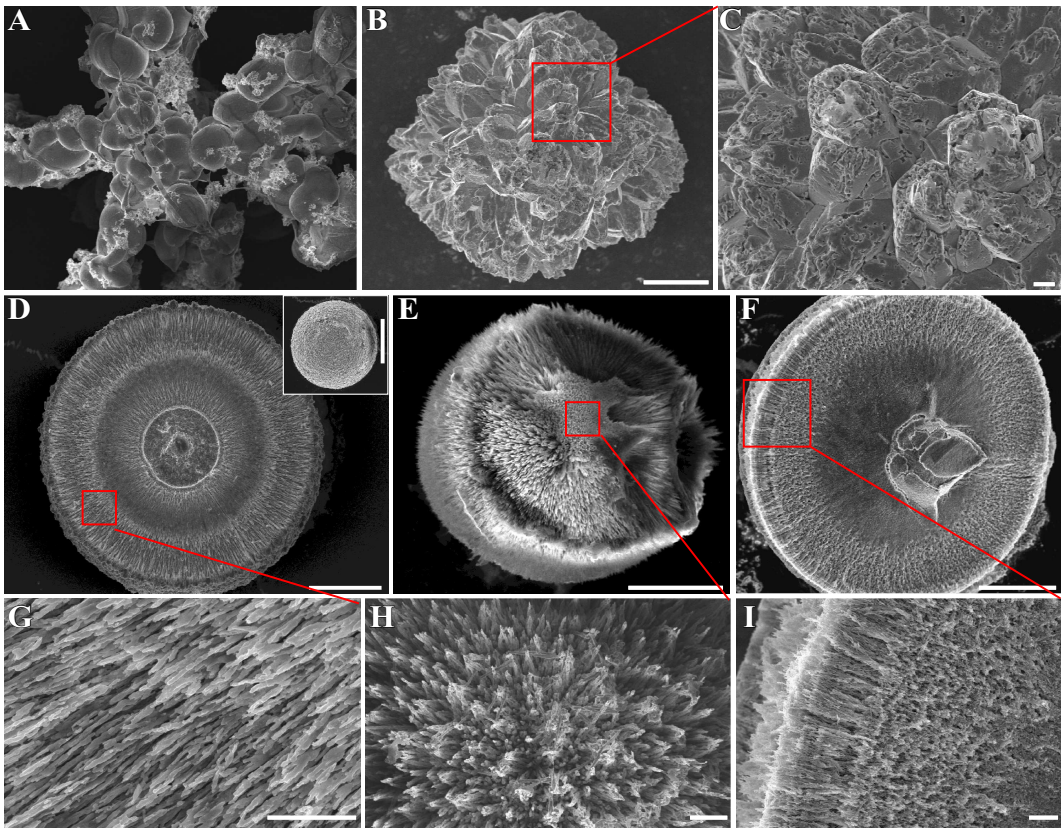

Figure 7.4. FESEM images of fractal crystal aggregates grown from silica-containing mixtures of Ba^{2+} and Ca^{2+} at calcium molar fractions of (A) 0.02, (B-C) 0.10, (D and G) 0.20, (E and H) 0.50, and (F and I) 0.80. (C, G-I) Close-up views of the precipitates formed at distinct Ca^{2+} contents, revealing their microstructure. Increasing the calcium concentration does at first result in fairly large assemblies of blocky subunits (B), before nearly perfect (hemi)spherical structures are obtained at higher Ca^{2+} fractions (D-F). Scale bars are 20 μm, (A-F), 50 μm (inset of D), and 2 μm (C, G-I).

witherite drillings, which are twinned on the {110} planes and thus adopt a bipyramidal pseudo-hexagonal morphology.[166] Evidently, branching is less pronounced here than in the reference experiments without Ca^{2+} (Figure 7.2) and those conducted at lower x_{Ca} (Figure 7.4A), leading to structures with much smaller fractal dimensionality and larger subunits. When the calcium content is further increased to 0.20 and 0.50 (Figure 7.4D-E), almost perfectly spheroidal aggregates with diameters of around 100 μm are obtained. Zooms onto the surface of the precipitates reveal ordered fiber-like subunits (Figure 7.4G-H) that emanate radially from the growth center and are about 1 μm wide, suggesting a high degree of fractal branching. Widely identical morphologies and textures were also observed even when the amount ofCa^{2+} exceeded that of Ba^{2+} in the mixtures (i.e. at x_{Ca} = 0.80, Figure 7.4F and

I). Bottom views of these structures further confirm the radial arrangement of the building units and moreover show that they are in fact hemispheres with an entirely flat bottom side (cf. Figure 7.4D and F). This indicates that the original crystal seed was nucleated heterogeneously at the walls of the vessel and subsequently continued growing in direct contact with the interface, as in the case of the fractal precursors found in the reference experiments without Ca^{2+} (cf. Figure 7.2B and D). However, in contrast to the latter, the core crystal does not seem to have attached to the walls via its lateral faces, but rather through its basal plane (see below). Another main difference is that the hemispheres produced at these Ca/Ba ratios are considerably larger than the globules formed in the absence of calcium ions (100 μm vs. 10 μm).

Effect of added calcium ions on the growth behavior of silica-strontianite biomorphs

Replacing barium by strontium proved to have similar tendencies in terms of visual observations, as perturbation of the reactive volume set in short after mixing of reagents or with a delay of about 1 h, depending on the calcium concentration. Also the formation of a silica gel-like carpet on the bottom of the wells was observed above calcium molar fractions of 0.20, in which crystallization of typical aggregates occurred independently after gel formation. Figure 7.5 shows a gallery of different morphologies observed with increasing concentrations of Ca^{2+}.

Unlike the experiments performed with mixtures of $BaCl_2$ and $CaCl_2$ (Figure 7.4), characteristic biomorphic aggregates like regular helicoids (Figure 7.5A) or worm-like braids (not shown) still occurred in the presence of 2 mol% Ca^{2+}. However, these structures were less frequent and seemed to be less developed as compared to counterparts grown from calcium-free solutions. At a Ca^{2+} molar fraction of 0.10, merely clusters of interpenetrating globular units with sizes of about 200 μm were observed (Figure 7.5B), whereas twisted shapes typical for silica biomorphs remained absent. The raspberry-like form of these architectures is similar to fractal entities found during growth of $BaCO_3$ biomorphs at lower pH[66,125], and furthermore strongly resembles morphologies produced upon addition of sodium chloride (cf. Figure 7.8). Again, the data indicate that crystallization is terminated at the end of the fractal stage beyond a certain threshold in the calcium content (which is somewhat higher than in the $BaCO_3$ case), and that the dynamic interplay leading to non-crystallographic ul-

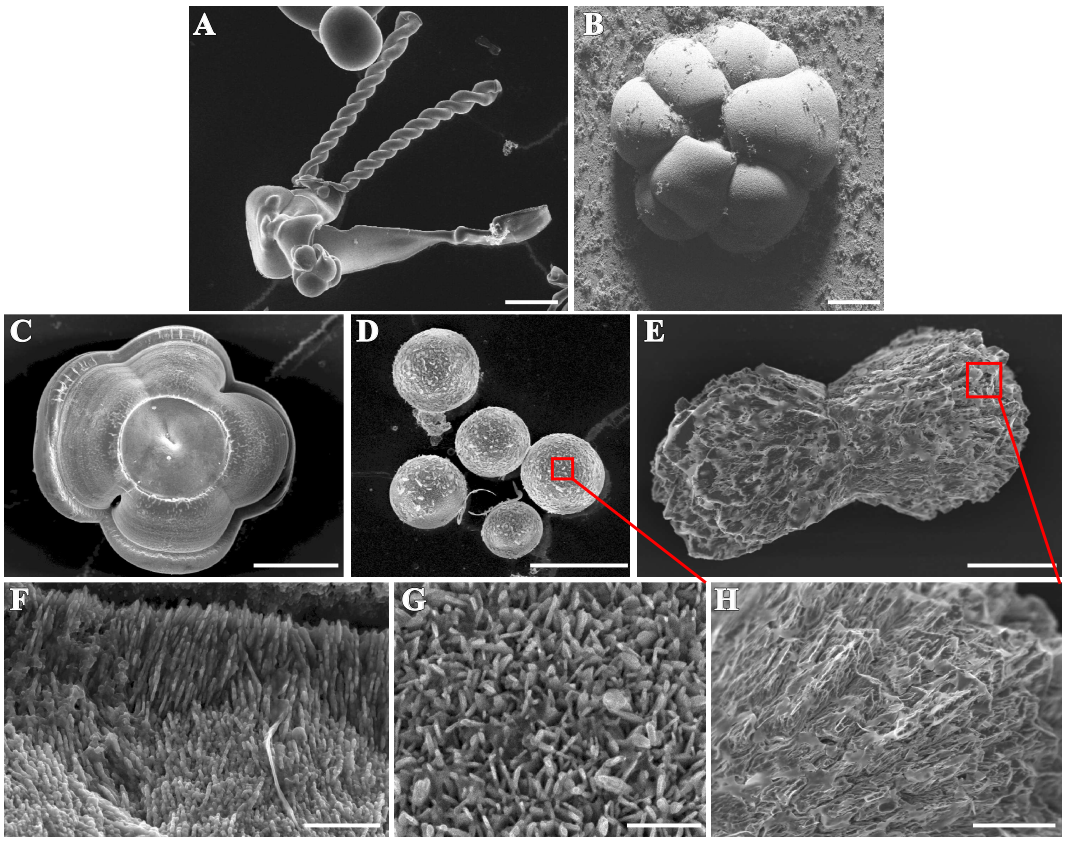

Figure 7.5. FESEM images of aggregates formed upon carbonate crystallization from mixtures of $SrCl_2$ and $CaCl_2$ under the influence of silica at high pH. The respective molar fraction of Ca^{2+} in the mother solutions was varied as follows: (A) 0.02, (B) 0.10, (C) 0.20, (D) 0.50, and (E) 0.80. While biomorphs are still observed at low calcium content (A), solely fractal structures (either spherical or raspberry-shaped) were obtained for $0.10 \leq x_{Ca} \leq 0.50$ (B-D). In the presence of excess Ca^{2+} (x_{Ca} = 0.80), crystals displaying elongated habits and consisting of multiple fibrous projections (E) represent the main morphology. (F-H) Higher magnifications of the precipitates shown in (C-E), providing insight into structural details. Scale bars are 50 μm (A-E), 1 μm (F-G), and 10 μm (H).

trastructures can no longer be excited under these conditions.

Increasing the Ca^{2+} concentration in the mother solution to molar fractions of 0.20 and 0.50 also gave exclusively fractal aggregates, which were smaller (ca. 100 μm, cf. Figure 7.5C-D) than those formed at x_{Ca} = 0.10 and furthermore differed to some extent in terms of their morphology. While precipitates grown at 20 mol% Ca^{2+} were usually reminiscent of four-petalled clover sheets (Figure 7.5C), those obtained from solutions containing equal amounts of Sr^{2+} and Ca^{2+} proved to be perfect spheroids (Figure 7.5D). Both types of structures again evolved in contact with vessel walls, as is evident from their flat bottom sides (cf. Fig-

ure 7.5C). Close-up views of the texture of the aggregates disclose myriads of nanoscale subunits, either fibrous (Figure 7.5F) or platy (Figure 7.5G), thus supporting the notion of extensive fractal branching in mixed Sr^{2+}/Ca^{2+} systems at intermediate molar ratios. Finally, at the highest calcium content investigated in this series (x_{Ca} = 0.80), the observed crystal morphologies (Figure 7.5E and H) were fundamentally distinct from those seen at lower Ca^{2+} concentrations and rather resembled architectures found in the reference experiments with neat $CaCl_2$ solutions (Figure 7.1I-K). That is, the isolated crystals likely originated from calcite rhombohedra that became elongated along their c-axis and developed multiple projections due to specific adsorption of silicate species on the $\{110\}$ faces, as described in detail elsewhere.[101,126]

7.4.2 Crystal polymorphism and composition

EDX analysis

Aggregates obtained from the experiments at different $Ca^{2+}/Sr^{2+}/Ba^{2+}$ contents were further examined with respect to their elemental composition as well as their crystalline modification and corresponding cell parameters. For this purpose, representative architectures at the distinct calcium concentrations (according to Figures 7.4 and 7.5) were first analyzed by means of EDX spectroscopy. Figure 7.6 shows a plot of the measured Ca/Me ratios (where Me is the sum over the atom percentages detected for calcium and barium/strontium, i.e. Me = at% Ca + at% Sr/Ba) as function of analytical fraction of Ca^{2+} in solution. The data show the presence of noticeable amounts of Ca^{2+} in the crystals already at low solution contents, suggesting that added calcium ions are incorporated into the mineralizing carbonate phase, obviously forming solid solutions (as verified by XRD, see below). Interestingly, a linear trend with fairly good correlation can be observed up to x_{Ca} = 0.50, which means that the amount Ca^{2+} included in the lattice of the mixed crystals directly scales with the analytical fraction in the mother liquor, indicating virtually complete miscibility of the distinct cations in the solid solution. Contrarily, at x_{Ca} = 0.80, the Ca/Me atomic fractions diverge from the linear trend towards higher calcium contents, especially in case of Ca^{2+}/Ba^{2+} mixtures, where deviations are already visible at x_{Ca} = 0.50. In fact, hardly any barium seems to be incorporated into the forming crystals at x_{Ca} = 0.80 (Ca/Me = 0.97), whereas strontium and

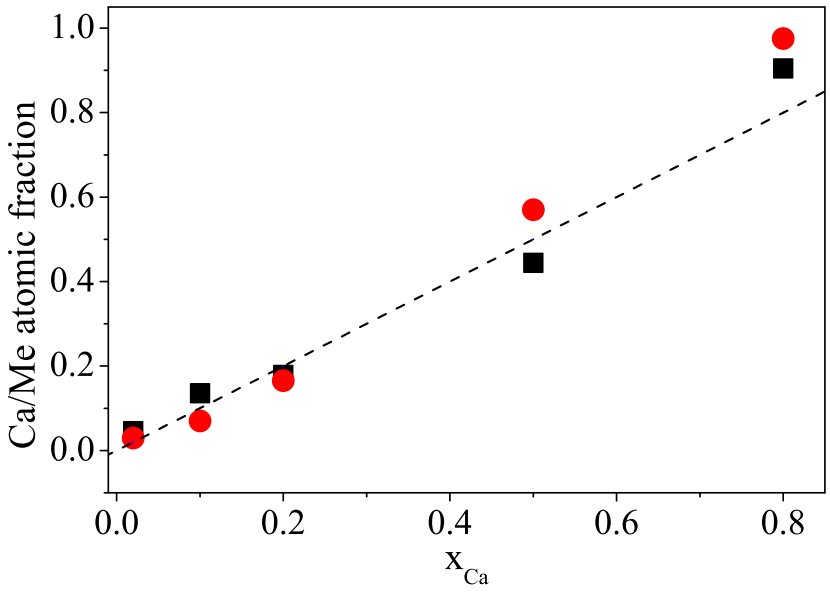

Figure 7.6. Ca/Me atomic ratios determined by EDX spectroscopy for typical aggregates obtained from mixtures of Ca^{2+} and either Ba^{2+} (●) or Sr^{2+} (■) at different solution compositions. The dashed line represents complete miscibility of calcium and strontium/barium in the resulting crystals (i.e. a situation where the fractions of Ca^{2+} in the initial solution and in the final solid state are equal). See text for further explanations.

calcium still exhibit somewhat higher miscibility at these ratios (Ca/Me = 0.90). Most likely, this result can be ascribed to smaller differences in the ionic radius between Sr^{2+} and Ca^{2+} (1.18 vs. 1.00 Å) as compared to Ba^{2+} and Ca^{2+} (1.36 vs. 1.00 Å).[168]

The silica content of the aggregates, given as the Si/Me atomic ratio, was found to be on the same order of magnitude (generally < 0.10, in most cases < 0.05) for all of the various fractal structures produced under the different conditions investigated (see Table 7.1). The obtained values thus are similar to silica levels reported for the globular clusters occurring during the first stage of morphogenesis in silica-witherite biomorphs.[75] Since their formation is based on crystal growth poisoning by a non-absorbable impurity (silica) that is constantly pushed ahead by the growing front and not noticeably incorporated[89], the resulting architectures contain very little silica (as observed). This explains the low count rates for Si in the EDX spectra and furthermore confirms that that the distinct spheroidal forms shown in Figures 7.4 and 7.5 have been generated by fractal branching at non-crystallographic angles.

x_{Ca}	Si / (Ba + Ca)	Si / (Sr + Ca)
0.02	0.247	0.053
0.1	0.022	0.071
0.2	0.019	0.037
0.5	0.058	0.081
0.8	0.028	0.017

Table 7.1. Si/Me atomic ratios measured for crystal aggregates produced in silica-containing mixtures of $CaCl_2$ and $BaCl_2$ or $SrCl_2$ at various calcium contents (Me corresponds to the sum of the alkaline-earth cations). Spectra were recorded from three different positions in the samples, always using representative morphologies. Generally, the amount of silica in the precipitates is rather low ($<$ 10 at%), except for the unexpectedly high Si counts found for x_{Ca} = 0.02 in Ba^{2+}/Ca^{2+} systems. Values in this range (Si/Me $\approx$ 0.2-0.3) have been reported for $BaCO_3$ biomorphs carrying an outer silica skin[69], which formed due to secondary precipitation of amorphous SiO_2 on the as-grown aggregates.[75] In the present case, the high silica content is likely to originate from artifacts during sample isolation and/or washing (secondary precipitation upon rinsing with ethanol or drying), but might also be related to the long growth time (3 days) chosen for this sample. On the other hand, the Si/Me ratio determined for the Sr^{2+}/Ca^{2+} aggregates generated at x_{Ca} = 0.02 (which still displayed characteristic curved morphologies) is relatively low when compared to literature values for mature silica-strontianite biomorphs.[69,82] However, recent studies have shown that the fraction of silica in bare biomorphs (no external skin) typically varies between 0.02 and 0.1,[69] thus being well in line with the present results.

X-ray diffraction

Diffraction patterns recorded from powdered samples (Figure 7.7) demonstrate that the alkaline-earth carbonates crystallize in aragonite-type lattices (virtually phase-pure, no other peaks observed) up to certain molar fractions of Ca^{2+} in the mother solutions, which differ depending on whether Sr^{2+}or Ba^{2+} is used. In the case of strontium, the forming aggregates favor an orthorhombic phase up to 50 mol% Ca^{2+} (Figure 7.7A-E), whereas only up to 20 mol% can be included into the corresponding witherite/aragonite lattice (Figure 7.7H-K). Moreover, with increasing calcium content, reflections are shifted towards higher 2Θ values (illustrated for the $\{111\}$ peak by the red line in Figure 7.7A-E and H-K due to the incorporation of the smaller Ca^{2+} ion into the strontianite/witherite structure (lattice contraction). This confirms the formation of mixed alkaline-earth carbonate lattices, i.e. solid solutions, in line with the EDX data.

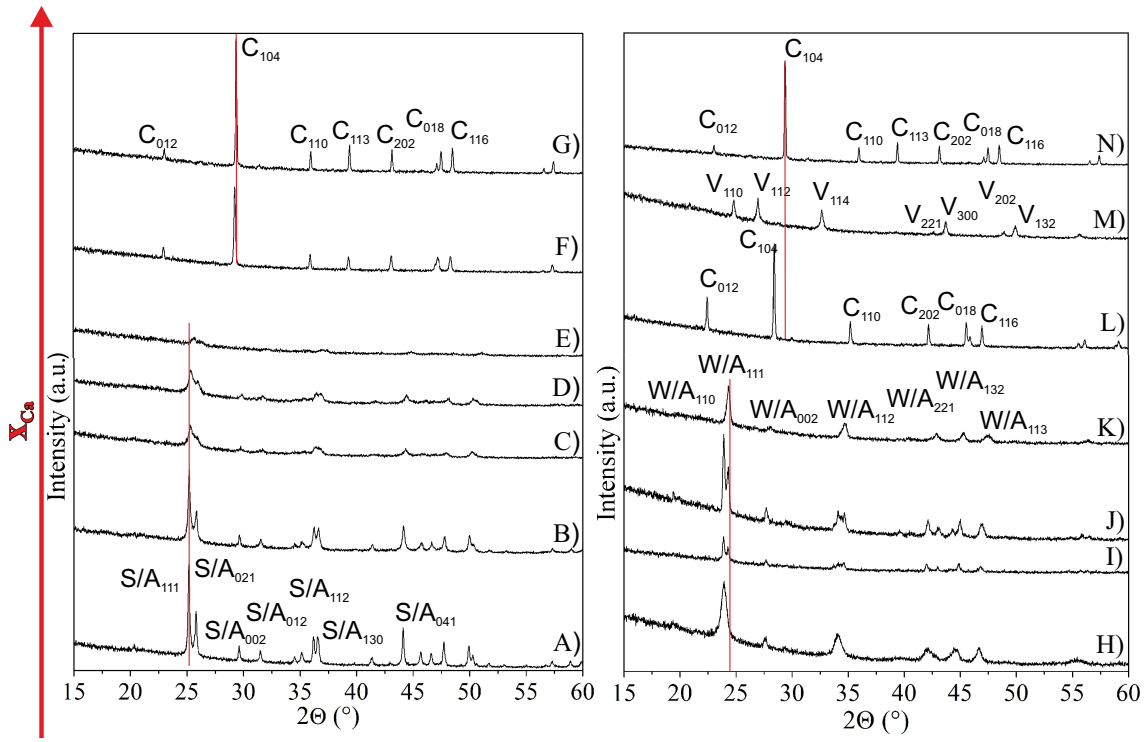

Figure 7.7. Powder XRD patterns of precipitates isolated after crystallization of alkaline-earth carbonates from dilute silica sols containing different amounts of Ca^{2+} and either Sr^{2+} (left) or Ba^{2+} (right). The molar fraction of Ca^{2+} ions in the samples was gradually increased according to: 0 (A and H), 0.02 (B and I), 0.10 (C and J), 0.20 (D and K), 0.50 (E and L), 0.80 (F and M), and 1.00 (G and N). Notation: C, calcite; V, vaterite; A, aragonite; S, strontianite; W, witherite.

To extract the lattice parameters of these mixed crystals, the XRD patterns were further analyzed and fitted employing the least-square minimization method. Cell volumes resulting for the distinct calcium molar fractions are plotted in Figure 7.8. For both strontium and barium carbonate, the volume of the unit cell decreases linearly with increasing x_{Ca}, as a consequence of the integration of the small Ca^{2+} cation into the orthorhombic lattice. Thereby, the decline of the cell volume is obviously much steeper in the case of calcium/barium mixtures, due to the larger difference in the ionic radii of Ba^{2+} and Ca^{2+} as already mentioned above, necessitating a higher degree of contraction. When x_{Ca} is increased to 0.80 in Ca^{2+}/Sr^{2+} systems, calcite is the only polymorph and there are no more reflections of aragonite-type carbonates discernible in the patterns (Figure 7.7F), in line with the traced morphological change at these Ca^{2+} fractions (cf. Figure 7.5D and E). Comparison of peak positions to those of the particles produced in the absence of strontium (Figure 7.7G) suggests a slight

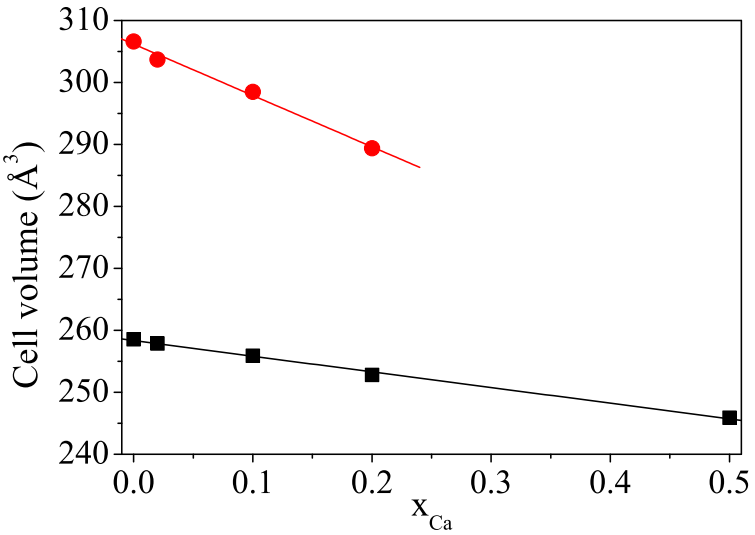

Figure 7.8. Cell volumes of orthorhombic solid solutions formed upon co-precipitation of $CaCO_3$ and $SrCO_3$ (■) or $BaCO_3$ (●) from alkaline solutions in the presence of silica and at distinct Ca^{2+} molar fractions. Values were derived by least-square minimization of the XRD patterns shown in Figure 7.7. In both cases, the cell volume decreases linearly as the smaller calcium ions become incorporated into the orthorhombic crystal system. Fits to the data (full lines) give slopes of -25.25 (Å/x_{Ca}) and -82.83 (Å/x_{Ca}) for $CaCO_3$/$SrCO_3$ and $CaCO_3$/$BaCO_3$ solid solutions, respectively.

shift down to lower 2Θ values (from $29.38°$ to $29.26°$, corresponding to an increase in the cell volume from 367.6 to 370.8 Å^3), presumably owing to the inclusion of the larger Sr^{2+} ions into the rhombohedral lattice, as reflected in the EDX data (ca. 10 at% incorporated Sr) and also reported in previous studies.[166,169–171] Similar behavior is observed at x_{Ca} = 0.50 for mixtures of $CaCO_3$ and $BaCO_3$ (Figure 7.7L). However, due to the higher amount of barium in the mother solution, significantly more Ba^{2+} is incorporated into the calcite structure (up to 45 at% according to EDX). This, together with the size of the barium cations, leads to a much more pronounced shift of the (104) reflection (to about $28.42°$). Most surprisingly, we find that, for a Ca^{2+} molar fraction of 0.80 (Figure 7.7M), vaterite is the exclusive crystalline phase present in the samples. This is clearly unexpected because vaterite is metastable under the given conditions, and calcite was obtained at both lower (Figure 7.7L) and higher (Figure 7.7N) calcium content. In order to rule out subtle kinetic effects and issues of sample preparation, this experiment was repeated multiply, each time yielding vaterite as the predominant polymorph. As the EDX data indicate only traces of barium in the crystals (cf. Figure 7.6), it seems as if Ba^{2+} - in mixtures with Ca^{2+} at these particular ratios - is somehow able to

stabilize vaterite in solution. Furthermore, it is highly intriguing to note that the hemispherical structures shown in Figure 7.4D, 7.4E, and 7.4F all consist of a different polymorph (aragonite, calcite, and vaterite, respectively), despite their close morphological and textural similarity.

7.4.3 Effect of the growth behavior by increasing the ionic strength

The above data illustrate that addition of Ca^{2+} to mother solutions of silica-witherite and -strontianite biomorphs can drastically influence the final morphologies. A possible explanation for this behavior is based on specific ion effects, that is, the harder calcium ions interact much more strongly with silicate ions than their softer higher homologues Sr^{2+} and Ba^{2+}, thereby inducing silica polycondensation via charge screening. In this way, the speciation of silica may be dramatically altered in solution and hence no longer allow for chemically coupled co-precipitation to occur. Consequently, self-assembly does not proceed beyond the initial stage of fractal branching. However, if the main role of added Ca^{2+} is to screen the charges of silicate species and thus facilitate their condensation, then simple electrolytes like sodium chloride should have a similar impact on morphogenesis at sufficiently high concentrations (because the Debye screening length decreases with growing ionic strength). To test this hypothesis additional experiments were performed recently in which attempts were made to grow $BaCO_3$ from solutions containing different amounts of excess salt (NaCl, Figure 7.9).[70] First distinct effects could be noted in this study at a salt concentration of 50 mM, where no more sheets and helicoids were formed. Instead, globular particles and variously shaped, colony-like clusters of interpenetrating spheroids were observed (Figure 7.9A). Frequently, worm-like structures were seen to emerge from these clusters and grow to lengths of often more than 100 μm. Starting from a NaCl content of 100 mM, also worms were absent and none of the polycrystalline morphologies characteristic of biomorphs remained. Instead, exclusively fractal architectures with diameters around 200 μm were found after growth was completed (Figure 7.9B), typically displaying raspberry-like shapes (Figure 7.9C). As already stated above, these structures arise from splitting of an initial $BaCO_3$ single crystal and subsequent self-similar ramification, as is evident from close-up views of their surface (Figure 7.9D), which reveal myriads of nanoscale projections and hence again suggest a large degree of branching. Fractal aggregates with similar raspberry-like morphologies, but

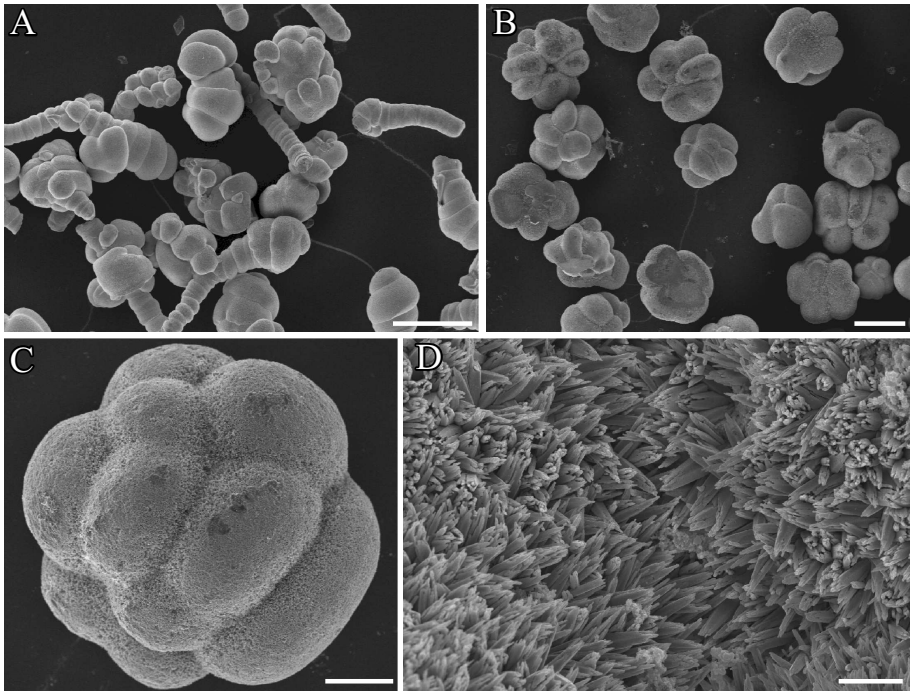

Figure 7.9. $BaCO_3$ crystal aggregates grown from alkaline silica-containing solutions, to which (A) 50 and (B-D) 250 mM of excess NaCl had been added. Scale bars are 100 μm (A-B), 30 μm (C), and 3 μm (D). (adopted from[70])

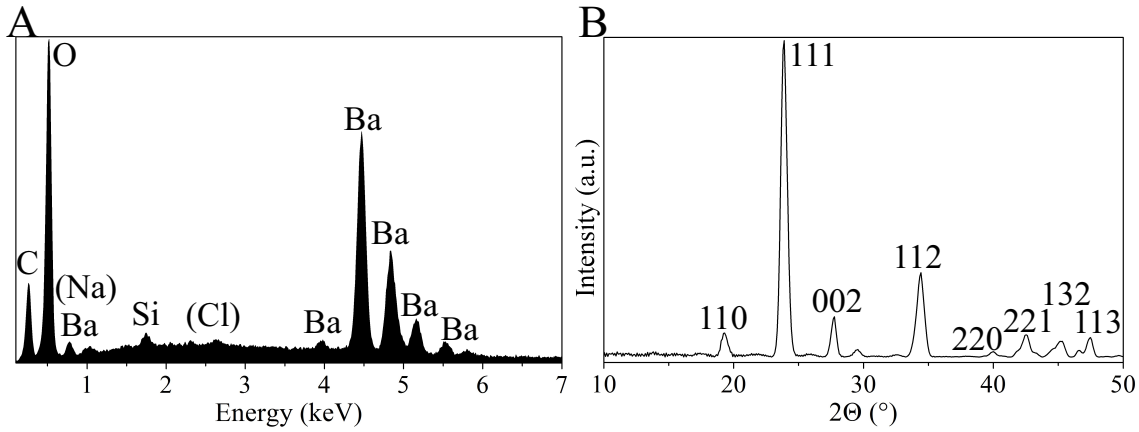

Figure 7.10. (A) EDX spectrum of raspberry-like crystal architectures grown in the presence of 500 mM NaCl. It is evident that the aggregates consist mainly of $BaCO_3$, with certain amounts of occluded silica (Si/Ba ratio: 0.04). Peak positions theoretically expected for Na and Cl are indicated in brackets. Quantitative evaluations assign non- zero fractions to both of these elements, but the calculated values are generally only slightly above or even below the detection limit of the technique (∼0.2 wt%). (B) Corresponding XRD pattern, verifying the presence of phase-pure witherite. (adopted from[70])

smaller dimensions (∼30 μm), were reported to occur in samples at pH 10 where, likewise, no distinct biomorphic shapes could be generated.[66,73,125] Thus, excess salt is obviously ca-

pable of influencing morphogenesis in a way that is comparable to what has been observed in the presence of Ca^{2+} ions (cf. Figure 7.5B), as expected. However, to achieve this, drastically higher concentrations of monovalent ions are required (100 mM NaCl vs. 0.1 mM Ca^{2+}); this behavior is well-known in the literature and can presumably be ascribed to the bridging ability of divalent cations.[172] EDX analyses of the precipitates do not show significantly increased counts of Na or Cl (even at a very high excess of salt), while XRD data confirm the crystalline phase to be pure witherite (see Figure 7.10). These results further corroborate that the added ions do not interact directly with the crystallizing carbonate phase (which is the major component in the final aggregates), but rather affect the growth process indirectly by influencing the silica in solution.

7.5 Discussion

7.5.1 Prevention of biomorph formation in the presence of Ca^{2+} ions

The results obtained from experiments with mother solutions containing mixtures of different alkaline-earth cations have shown that the presence of Ca^{2+} leads to substantial changes during crystallization and prevents the formation of silica biomorphs already at very low concentrations. The most obvious discrepancy between samples with and without added calcium is that the otherwise transparent solutions turn markedly turbid within minutes as soon as Ca^{2+} is present. The colloidal particles (and polymeric solutes) formed at this stage consist of amorphous silica with certain amounts of entrapped or surface bound Ca^{2+}.[132] With time, these silica colloids sediment towards the bottom of the crystallization wells, where they accumulate and eventually cross-link to build up a layer of silica gel (cf. Figure 7.3), in which growth of carbonates occurs after some delay. These observations clearly demonstrate that calcium ions can catalyze silica polycondensation and coagulation processes by screening repulsive charges much more efficiently than the less polar Sr^{2+} and Ba^{2+} ions (lower charge density due to larger cation size), as reported also in previous work.[134,172,173] Naturally, reinforced condensation in solution will cause the distribution of silicate species to shift towards higher oligomers, long before any carbonate mineralization has commenced. Thus, crystallization will occur under conditions where the actual concentration of silicate monomers and dimers - which likely represent active species during growth of biomorphs[87]

- is significantly increased. An apparent consequence of these circumstances is that morphogenesis ceases at the end of the initial fractal route and the system cannot pass into the second stage of chemically coupled co-precipitation and polycrystalline growth. Most probably, this is because considerable amounts of silica were already coagulated independent of carbonate crystallization, so that critical supersaturation levels required for local polymerization and cementation of carbonate nanocrystals are no longer accessible.[87] Therefore, the dynamic pH-based interplay between silica and carbonate - which, as is known, occurs only within a certain window of bulk conditions[72,125] - cannot be maintained, rendering concerted self-assembly of complex morphologies impossible. In this regard, direct interactions between Ca^{2+} and silicate, which can be considered negligible in case of Sr^{2+} and Ba^{2+}, preclude the formation of biomorphs in these systems.

The notion that enhanced silica condensation prevents growth of curved crystal aggregates has been confirmed by further experiments in the presence of sodium chloride, used as background electrolyte to vary the ionic strength and, with it, the Debye screening length in solution. Indeed, similar effects were found in terms of the occurring morphologies (i.e. only fractal structures and no more biomorphic shapes); however, drastically higher concentrations of monovalent ions ($\geq$ 100 mM NaCl) were needed to induce changes comparable to those observed for minor contents of divalent Ca^{2+}. Thus, high ionic strengths progressively shield the negative charges of silicate species, thereby favoring their oligomerization[172] and ultimately resulting in the formation of raspberry-like architectures, instead of biomorphs. A second potential explanation for the distinct growth behavior at elevated salinity refers to the supply of the system with carbonate ions. In fact, large amounts of salt depress the rate of CO_2 uptake by the solutions due to a decrease of its solubility in water (which obviously does not apply for experiments with added Ca^{2+} ions).[174] In order to trigger and maintain coupled co-precipitation, sufficient bulk concentrations of carbonate species are needed over extended periods of time. This criterion may not be met in media of at high ionic strength, and furthermore has proven to be one of the key parameters for the morphological selection at lower pH.[66,125] In this sense, both the silica and (time-dependent) carbonate speciation in solution seem to be inappropriate for self-assembly in reasonably concentrated NaCl solutions.

In mixtures of calcium and barium, Ca^{2+} molar fractions as low as 0.02 were sufficient to hinder the formation of biomorphs, showing that the cations primarily act in a catalytic way. By contrast, biomorphs were still obtained in Ca^{2+}/Sr^{2+} systems at the same composition. In principle, this behavior is counter-intuitive, as Sr^{2+} is harder than Ba^{2+} and thus should more efficiently support Ca^{2+} in provoking silica polycondensation. Although we can only speculate about possible reasons for this finding, one may argue that the competition of the distinct cations for interaction sites at the silica is the decisive factor in this context. In other words, Sr^{2+} is more readily capable of displacing Ca^{2+} at silicate groups thanBa^{2+}, thus decreasing the overall tendency for coagulation. That is, the barium cations leave all interaction potential open to Ca^{2+}, whereas Sr^{2+} behaves as a true competitor (though itself not being able to coagulate silica under the given conditions). This idea is supported by dynamic light scattering measurements, which demonstrate that cation-induced silica condensation is faster in calcium-barium than in calcium-strontium mixtures (see Figure 7.11). An alternative scenario is based on the fact that, at lower calcium fractions ($x_{Ca} \leq 0.2$, cf. Figure 7.6), more Ca^{2+} is incorporated into the lattice of $SrCO_3$ than for $BaCO_3$ (e.g. 1.09 at% Ca in $SrCO_3$ vs. 0.51 at% Ca in $BaCO_3$ at x_{Ca} = 0.02) Consequently, less free calcium ions would then be available in solution for cation-induced silica condensation, allowing biomorphs to grow in Ca^{2+}/Sr^{2+} mixtures up to a calcium molar fraction of 0.02. Another interesting observation is that added Ca^{2+} ions retard carbonate crystallization in the samples, such that the growth period had to be increased to 3 days (instead of about 12 h in case of pure witherite and strontianite biomorphs). As already mentioned, the pH of the solutions and its variations over time did not noticeably change with the calcium content. This implies that the temporal profiles of the actual carbonate concentration should be similar in all systems and, hence, that the free amount of alkaline-earth cations is lower in Ca^{2+}-containing mixtures. These considerations suggest that Ca^{2+} as well as Sr^{2+} or respectively Ba^{2+} ions are temporarily bound to (likely polymeric) silicate species or rather the gel matrix deposited on the bottom of the vials. As a result, the supersaturation of the alkaline-earth carbonates is decreased as compared to the pure systems, leading to longer growth times. We note, however, that the lower bulk supersaturation could as such be an important limiting factor for the ability of biomorphs to form under the particular circumstances, as described in detail in a recent

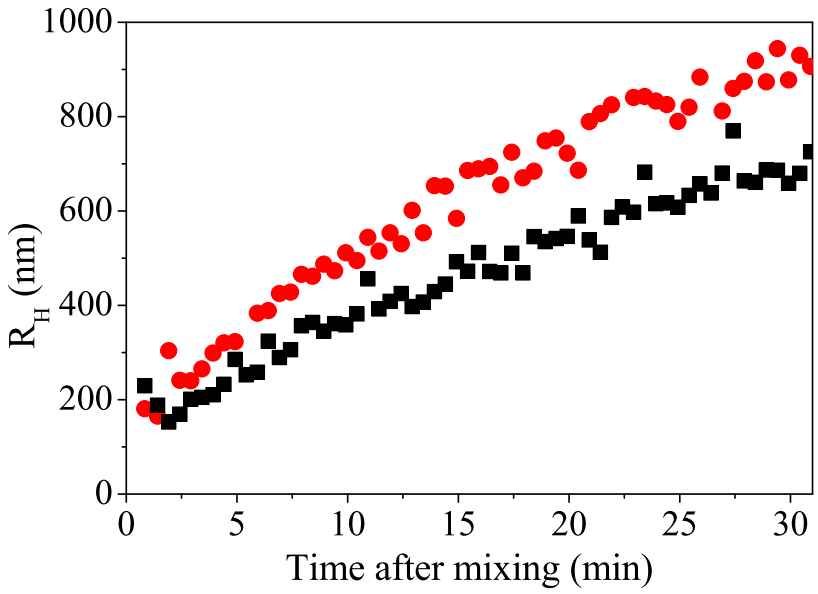

Figure 7.11. Temporal development of the hydrodynamic radius (R_H) of scattering species observed as a function of time after combining alkaline silica sols with mixtures of $CaCl_2$ and $BaCl_2$ (●) or $SrCl_2$ (■) (x_{Ca} = 0.02 at a total metal ion concentration of 5 mM), as monitored by in-situ dynamic light scattering. The increase of the average size is due to progressive cation-induced condensation of silicate species in solution, leading to the formation of silica polymers and colloidal particles. Evidently, polymerization proceeds faster in the presence of Sr^{2+} than with Ba^{2+}. This might be due to the fact that Ba^{2+} is harder than and may therefore more readily compete with Ca^{2+} for interaction with silicate ions, thus reducing the coagulation power of Ca^{2+} under the given conditions. Consequently, biomorphs can still be grown at low calcium contents in mixtures with Sr^{2+}, whereas this is not possible in the case of Ba^{2+}.

study.[125] Decelerated crystallization in the presence of Ca^{2+} could to some extent also be due differences in the solubility of the orthorhombic alkaline-earth carbonates (pK_{SP} = 8.34 for $CaCO_3$, 9.27 for $SrCO_3$, and 8.56 for $BaCO_3$ at 25°C.[175–177] Thus, aragonite is more soluble than strontianite and witherite, and might therefore slow down growth rates for mixed crystals at a given level of supersaturation.

A final aspect that may contribute to the lack of biomorphs already at low Ca^{2+} fractions is related to the surface energies and structures of the mixed alkaline-earth carbonate crystals. Recently, Aquilano and co-workers proposed that adsorption of silica on $BaCO_3$ nanoparticles (and hence their stabilization) is promoted by epitaxial matching of silicate chains on the carbonate surfaces, which was demonstrated for witherite on α-quartz and inferred for the inverse case.[85,178] Silica adsorption was furthermore suggested to reduce the interfacial

tension of the carbonate particles and consequently increase nucleation rates to values enabling the formation of nanocrystalline assemblies. These interactions could possibly be altered upon inclusion of Ca^{2+} into the witherite (and strontianite) lattice, so that carbonate nanocrystals (i.e. the building units of biomorphs) can no longer be stabilized and/or nucleated at sufficiently high frequencies.

7.5.2 Fractal branching at different Ca^{2+}/Sr^{2+} and Ca^{2+}/Ba^{2+} ratios

Apart from the fact that biomorphs cannot grow already in the presence of minor amounts of Ca^{2+}, our data further demonstrate that various fractal structures are generated over a wide range of compositions. At low calcium contents ($x_{Ca} \leq 0.02$ for Ba and ≤ 0.1 for Sr), these branched architectures are widely identical to those produced in the absence of Ca^{2+} and typically adopt either dumbbell-like or spherulitic shapes (cf. Figure 7.2). In many cases, several of these fractal spheroids bundle to build networks (Figure 7.4A), or grow together yielding architectures with raspberry- or cauliflower-like appearance (Figure 7.4B and Figure 7.9). However, a commonality of all these forms is that they arise from a seed crystal, which was nucleated heterogeneously with its long axis parallel to the underlying substrate, as is evident from corresponding bottom views (cf. Figure 7.2). In fact, nucleation appears to occur on the lateral faces of the pseudo-hexagonal rod, that is, on either the$\{011\}$ or the $\{020\}$ planes. Splitting at both ends and subsequent bifurcation then inevitably results in dumbbell-like intermediates, which later may be closed to give (notched) spheres. These circumstances are illustrated schematically in Figure 7.12A-C. Above a certain threshold in the molar fraction of Ca^{2+} ($x_{Ca} \geq 0.1$ for Ba and $x_{Ca} \geq 0.2$ for Sr), the morphological variety of the observed fractal patterns becomes strongly restricted. Essentially, most of the precipitates display (more or less perfect) hemispherical shapes (cf. Figure 7.4B-F and Figure 7.5C-D) and microstructures that are characterized by numerous nanometric projections arranged radially outwards from the center of the hemisphere (cf. Figure 7.4G-I and Figure 7.5F-G). In this context, the crystals produced from Ca^{2+}/Ba^{2+} mixtures at x_{Ca} = 0.10 (Figure 7.4B-C) are an exception, because they are hardly branched and rather consist of partially intergrown micron-sized subunits, for reasons that shall not be further discussed here. The formation of hemispherical structures at higher calcium content can be understood when inspecting the flat bottom sides of the aggregates, which were in contact with

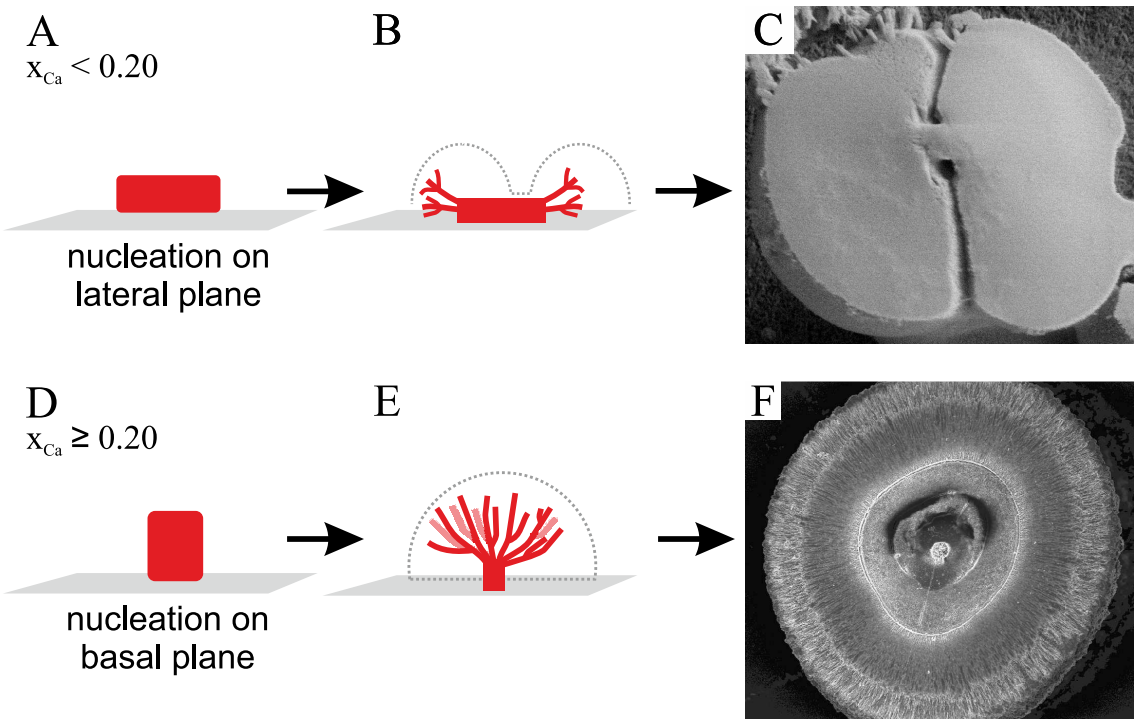

Figure 7.12. Schematic representation of the fractal growth mechanisms envisaged for lower (A-C) and higher (D-F) calcium fractions. Note that structures are not drawn to scale.

an interface during both nucleation and growth. In corresponding images (especially Figure 7.4D), the seed crystal located in the core of the hemispheres is seen in cross- rather than longitudinal section with respect to the c-axis, suggesting that the heterogeneous nucleation behavior differs from that found at lower Ca^{2+} fractions. Particularly, the core crystal seems to have nucleated on the substrate via its basal {001} faces (instead of the lateral planes), as visualized in Figure 7.12D-F. Self-similar ramification during the following stages of growth leads to hemispherical entities as indicated in Figure 7.12E, whereas no dumbbell-like intermediates are observed under these circumstances. A possible reasoning for this change in the nucleation behavior is that incorporation of Ca^{2+} into the mineral phases (as detected by EDX and XRD, cf. Figures 7.6-7.8) alters the relative surface energies of the different crystallographic faces, rendering nucleation through {001} favorable over {011} and {020}. This might also explain why the transition from the distinct fractals found with no or little added Ca^{2+} to the hemispheres occurs at higher calcium contents in Ca^{2+}/Sr^{2+} mixtures than inCa^{2+}/Ba^{2+} systems, since changes in the structure and surface energies (with respect to the pure phases) are expected to be greater when incorporating calcium in the lattice of witherite (Ba^{2+} being larger than Sr^{2+}).[169,171,179–182] In the case of Ca^{2+}/Ba^{2+} mixtures, the

situation is more complicated. First, it can be noted that mixed orthorhombic phases occur only up to 20 mol% Ca^{2+}, presumably because of the larger difference in cation size and greater structural mismatch. At x_{Ca} = 0.50, the forming crystals therefore prefer a calcitic modification (cf. Figure 7.7L), into which Ba^{2+} ions are included in fractions as high as 0.43. This confronts values reported in earlier work, which were considerably lower.[171,180,183,184] Indeed, partition coefficients determined for Sr^{2+} and Ba^{2+} in calcite based on the present experiments (D_{Sr},calcite = 0.48 at x_{Ca} = 0.80 and D_{Ba},calcite = 0.86 at x_{Ca} = 0.50) exceed those obtained previously by factors ranging from 5 to 45 ($D \approx$ 0.03-0.08 and 0.02-0.03 for Sr^{2+} and Ba^{2+}, respectively, in calcite).[185,186] Although this unexpected discrepancy cannot be explained, one may speculate that the presence of silica in the mother solutions could somehow promote incorporation of the larger alkaline-earth cations into calcite. Increasing the Ca^{2+} molar content to 0.80 in calcium-barium systems led to the - likewise unexpected - observation of vaterite being the exclusive crystalline phase detected (Figure 7.7F). EDX analyses of these crystals have shown that they include only traces of barium (ca. 0.5 at%). This complies well with data reported by Brecevic et al. who concluded that absorption of Ba^{2+} into the vaterite lattice causes distortion (due to larger cation radius) and therefore is strongly limited.[187,188] However, these low amounts of foreign ions appear to be effective in stabilizing vaterite against energetically favored transformation to calcite, possibly in co-operation with the silicate species in solution.

Last but not least, it is remarkable that the gradual changes in polymorphism, traced when raising the calcium content in mixtures with barium from 0.2 over 0.5 to 0.8, are not at all reflected in the resulting morphologies and structures, given that hemispheres of similar sizes were formed at all three compositions (Figure 7.4D-F) and also the constituting nanoscale subunits looked widely identical (cf. Figure 7.4G-I). Nonetheless, as outlined above, these architectures can obviously consist of any of the three anhydrous polymorphs of calcium carbonate, i.e. aragonite (x_{Ca} = 0.20), calcite (Ca^{2+} = 0.50), and vaterite (x_{Ca} = 0.80), which contain greater or lesser amounts of incorporated foreign ions. This is of particular interest when considering that these aggregates are supposedly generated by progressive branching of an initial core crystal, and that the habit of this seed crystal should be different for the three polymorphs (rod for aragonite, rhombohedron for calcite, and presumably sphere for

vaterite).

7.6 Conclusions

In this chapter, the crystallization of alkaline-earth metal carbonates from silica-containing solutions at high pH was studied, in which Ba^{2+} or respectively Sr^{2+} was gradually replaced by Ca^{2+} in mixtures of the corresponding chloride salts. The results clearly demonstrate that even minor amounts of calcium ions can strongly interfere with the growth behavior otherwise observed for witherite and strontianite under the influence of silica in the absence of Ca^{2+}. In particular, the formation of complex curved morphologies is fully prevented as soon as a certain threshold in the calcium molar fraction is exceeded ($\geq$ 2 and 10 mol% for mixtures with strontium and barium, respectively). These findings are mainly ascribed to strong interactions between the "hard" Ca^{2+} ions and the primary structuring agent in solution, i.e. dissolved silicate species. Charge screening by the cations catalyzes silica polycondensation, shifting its speciation towards higher oligomers and eventually inducing coagulation. This leads to circumstances where the chemistry and/or concentration of the relevant components in solution are no longer suitable for dynamically coupled co-mineralization to be initiated. In this regard, it seems as if the failure to produce calcium carbonate-based silica biomorphs at ambient conditions is not solely due to crystal polymorphism (i.e. because $CaCO_3$ favors calcite over aragonite), but also - and probably for the most part - originates from specific ion effects related to the different polarity of the alkaline-earth cations. This notion is supported by the observation that mixed $CaCO_3$/$SrCO_3$ and $CaCO_3$/$BaCO_3$ particles, as obtained over a wide range of metal ion ratios, did not assemble into biomorphic ultrastructures (unlike corresponding mixtures of $SrCO_3$ and $BaCO_3$[59]), even when their crystal phase was confirmed to be an orthorhombic aragonite-type solid solution. Thus, the only conceivable way to enable true bottom-up self-organization of $CaCO_3$biomorphs (no seeding or the like) from dilute sols at room temperature - as observed for both $SrCO_3$ and $BaCO_3$ - would be to deliberately avoid or reduce ionic interactions between Ca^{2+} and silicate ions in solution which is up to know practically impossible.

Instead of intricate sinuous morphologies, co-precipitation of the alkaline-earth carbonates and silica afforded a wealth of different fractal structures, all of which contained the distinct

metal cations in ratios corresponding more or less to those prevailing in the mother liquor (complete miscibility for orthorhombic solid solutions, lower partitioning of Sr^{2+} and Ba^{2+} into vaterite and calcite). Further parameters such as the degree of fractal branching, the detailed size and shape of both the subunits and the entire aggregates, or the crystal orientation during heterogeneous nucleation at interfaces were shown to vary in a subtle manner as depending on the amount of Ca^{2+} present. Concerning the polymorphism of the architectures, we found that aragonite-type mixed phases prevail in samples at an excess of the larger strontium or barium ions, whereas Sr^{2+}/Ba^{2+}-substituted calcite was obtained at high Ca^{2+} fractions, both being widely in line with previous literature. An interesting peculiarity is the formation of pure vaterite in the presence of Ba^{2+} under particular conditions (i.e. at a Ca/Ba ratio of 4:1), which may or may not be induced by a cooperative stabilization of this actually metastable polymorph by barium ions and silicate species. In any case, the results in this chapter have illustrated that virtually identical structures (micron-sized hemispheres consisting of uniform fibrous subunits) can be generated on the basis of either of the three anhydrous polymorphs of calcium carbonate, simply by adjusting the Ba^{2+} content in the mother solutions. This, together with the above-mentioned variations in the nucleation and growth behavior of the resulting bifurcated entities, highlights that silica-controlled crystallization of alkaline-earth carbonates is not only capable of yielding complex curved forms like biomorphs (even though they are certainly the most prominent example in this context), but can also lead to fractal aggregates with obviously great diversity in terms of morphology, structure, and composition.

8 Conclusions and Outlook

The present work deals with the mineralization of alkaline-earth carbonates (mainly barium carbonate) from dilute silica solutions at high pH. It has for long been known that the concerted interaction between these purely inorganic components leads to amazing architectures with intricately curved and helical shapes, which were termed silica-carbonate biomorphs. Recently a general concept was proposed by García-Ruiz and co-workers that explains the spontaneous formation of these biomimetic aggregates on basis of pH-mediated interactions of the silica and carbonate speciations at alkaline conditions. In this way, the building units of biomorphs are continuously produced via chemically coupled co-precipitation of components, that is, crystallization of carbonate provokes the precipitation of silicate and vice versa (see chapter 2). Therefore studies conducted in the scope of this work were on the one hand dedicated to reinforce and advance the already existing picture of the formation mechanism and, on the other, to shed light on certain morphogenetic aspects.

In this context the influence of the initial bulk pH on the morphogenesis was studied in detail and re-evaluated in **chapter 5**. Therefore crystallization experiments were conducted in which the initial pH values were varied between 9.8 and 11.9. The collected data unambiguously demonstrated that typical morphologies of silica biomorphs only occur when the starting pH of the mother solutions was adjusted to values within a certain corridor, ranging roughly between 10.2 and 11.1. Outside of this window, merely globular architectures were observed, resulting from continuous branching of an initial carbonate crystal core. In order to explain these findings on basis of the proposed formation mechanism, the concentrations of relevant species for barium carbonate mineralization were determined in-situ during growth. Therefore the temporal progression of the bulk pH in the different mother solutions was recorded continuously and combined with time-dependent Ba^{2+} concentration profiles,

measured with in-situ X-ray fluorescence spectroscopy, in order to calculate the temporal development of the barium carbonate supersaturation for the different start conditions. The resulting curves showed that dynamically coupled co-precipiation of components (and thus the formation of biomorphs) is only triggered when the system maintains certain levels of $BaCO_3$ supersaturation over extended periods of time ($\sim$ 10 h). This parameter is however strongly influenced by the prevailing bulk pH in solution as it controls the flow of atmospheric CO_2 into the system. In contrast, according to Melero-García et al. the pH range for the production of silica biomorphs is in gel experiments slightly lower (9.3-9.8).[72] This discrepancy is explained in chapter 5 by fundamental differences in the setup between growth in silica sols and gels. In the latter case the barium carbonate supersaturation is predominantly controlled by diffusion of acidic Ba^{2+} ions into silica gel that already contains dissolved carbonate species, which explains decreased pH corridor for growth of biomorphs.

In **chapter 3** the influence of silica on the mineralization of barium carbonate was studied at high supersaturation conditions. To that end, precipitation was induced by direct mixing of barium chloride with sodium carbonate solutions containing varying amounts of dissolved silica. At low SiO_2 contents crystallization occurred immediately after combining of reagents. Analysis of the formed precipitate showed the formation of elongated carbonate crystals that were bifurcated due to the poisoning influence of oligomeric silicate species. The extent of ramification was furthermore dependent on the silicate concentration even resulting in highly branched cauliflower-like objects at 750 ppm SiO_2. In turn, fast crystallization was prevented above certain thresholds of silica and, interestingly, amorphous nanoparticles could be isolated from the reactive solutions. Detailed structural studies on the formed particles, performed with HR-TEM and micro-EDX spectroscopy, revealed a silica core that was surrounded by a thin layer ($\sim$ 1-2 nm) of amorphous barium carbonate, which in turn was again sheathed by an external silica skin with a thickness of up to 20 nm. This is in sharp contrast to experiments conducted with calcium carbonate, where the particles had exactly the reverse composition (ACC in the core and silicate in the shell).[92] The formation of the hybrid particles with the observed composition was explained by the presence of local pH gradients, generated locally on the surfaces of either silicate or carbonate, suggesting again the validity of the proposed theory of pH coupled precipitation of silicate and

carbonate. In view of this finding this concept might be exploited to prepare multilayered heterogeneous structures in future work, if conditions are carefully controlled. For instance, it might be possible that continuous addition of reagents ($BaCl_2$ and Na_2CO_3/silica), rather than singular mixing, might lead to the deposition of further carbonate and silica layers on the nanoparticles, potentially giving rise to onion-like structures with domains of alternating composition. Such layer-by-layer (LbL) mineralization has been achieved, among others, for silica-titania hybrids by using surface-adsorbed protamine as condensation catalyst.[189] However, fabrication of these materials requires multiple adsorption, precipitation, and washing steps. By contrast, the methodology described in chapter 3 represents a fast and easy one-pot route for the formation of layered nanoparticles, which appears promising with respect to the development of bottom-up strategies for the synthesis of advanced materials. Furthermore, the core-shell-shell character of the particles and the fact that components can be selectively dissolved might be of interest for fields in which controlled release and/or confinement are important.[190] It would be furthermore interesting if the concept of chemically coupled precipitation of components on the nanoscale is transferable to other minerals. A straightforward substitution for future work in this context could be the use of iron oxides instead of carbonates (i.e. co-precipitation of iron hydroxides at high pH). This can be a very interesting point for material scientists in general as magnetic nanoparticles could possibly be generated via an one step route using simple and cheap precursor.

Additional interesting observations were made in chapter 3 when following the time-dependent behavior of the initially formed hybrid particles. At very high SiO_2 concentrations (1870 ppm) the amorphous state of barium carbonate could be permanently trapped, which was ascribed to impervious external silica skins. In contrast, at intermediate silicate concentrations, the initially formed particles showed pronounced aggregation which ultimately resulted in a segregated silica hydrogel phase that hosted temporarily trapped amorphous barium carbonate. Remarkably the carbonate component was gradually released into the surrounding medium, indicating that the external silica layers are somewhat porous in this case. Recrystallization of the previously dissipated carbonate units yields then interestingly complex biomimetic ultrastructures within this silica-hydrogel matrix as similarly observed for barium carbonate silica systems at comparable low supersaturation in diffusion based systems.

This finding teaches us that the formation of silica biomorphs is not necessarily linked to the diffusion of one of the components (either atmospheric CO_2 into silica solutions containing equally distributed Ba^{2+} ions, or barium into silica gel containing pre-dissolved carbonate) as they are formed also at precipitation conditions via recrystallization of amorphous units. Indeed, such precursor particles were isolated at early stages from diffusion based preparation systems (atmospheric CO_2 into alkaline silica sols).[71] It is conceivable that these particles also exhibit the same composition as those observed in chapter 3. Therefore one can speculate if the formation of biomorphs, i.e. the generation of nanosized $BaCO_3$ rods occurs also via transient amorphous particles as observed in certain biominerals.

The answer to the question if a growing $BaCO_3$ rod can induce silica precipitation locally around its surface and thus prevent further growth is given in **chapter 4**. In order to get detailed insights, a titration based setup was utilized where the precipitation of barium carbonate was achieved by constantly adding $BaCl_2$ to a carbonate buffer containing varying amounts of silicate at constant pH. Certain silica related influences on the nucleation behavior could be detected with the help of an ion selective Ba^{2+} electrode. The provoked effects could be quantified on basis of certain characteristics of the resulting titration curves: i) influence on the slope in the prenucleation stage, ii) retardance of nucleation, and iii) influence on the solubility in the post-nucleation stage. Detailed investigations of the precipitated phase showed furthermore a drastic miniaturization of the barium carbonate crystals in the presence of silicate and corresponding EDX mappings revealed continuous silica skins around individual rods. The findings from this study re-inforce the model pH coupled co-precipitation of carbonate and silica and disclose novel insights into fundamental processes of barium carbonate nucleation in general.

Experiments in **chapter 6** using micropatterned PDMS stamps (periodically arranged bars with constant height of 5 μm) as growth substrate were intended to clarify the actual origin of curvature in the biomimetic architectures on the microscale, i.e. why do flat laminar segments that grow at first in direct contact with the underlying substrate, start to curl at a certain point? The results from these experiments suggest that curvature is induced due to the absence of foreign surfaces which provoked emanating sheets to curl around themselves in order to use their own intrinsic surface as substrate. This hypothesis could be verified as

the morphological selection was strongly linked to the geometries of the substrate topology. This empirical finding explains the induction of curvature on a rather global scale. However the processes on the nanoscale remain still unresolved in this context. This question is truly of central interest since the answer should also shed light on the driving forces for the spontaneous self-assembly of the nanoscale building units of silica biomorphs (i.e. the mutual orientation of rods within the mature architectures). Apart from that, variation of the substrate structuring (i.e. increasing the distance between individual bars) resulted in nearly reactangular stripe-like biomorph aggregates demonstrating that growing sheets can adopt virtually any shape, depending on the physical limitations in the confined volume they grow. This finding is a nice example of the combination of top down templating effects of the prefabricated moulds and bottom-up self-assembly relied on the concerted interactions between silicate and carbonate.

Chapter 7 reports on experiments conducted with barium and strontium chloride solutions containing increasing molar fractions of Ca^{2+} ions. The motivation of this study was based on the fact that growth of silica biomorphs, in form of helices and worm-like structures, is restricted to $SrCO_3$ and $BaCO_3$ minerals at ambient conditions. Related architectures with $CaCO_3$, the mineral of utmost interest within the alkaline-earth carbonate series, could until now, only be prepared when the conditions were adjusted so that the formation of metastable aragonite (orthorhombic lattice as in case of strontianite and witherite) was favored. Unfortunately, typical sinuously shaped aggregates remained absent even when only small amounts of calcium were added to the reactive solutions. Interestingly, the thresholds slightly varied between barium and strontium. Instead of typical biomorphic shapes, globular and hemisperical structure developed, both resulting from fractal branching of an elongated pseudo-hexagonal core crystal through its basal faces due to poisoning by silica. The different growth behavior in the presence of Ca^{2+} ions is mainly ascribed to the relatively strong interactions of hard calcium ions with silicate species in solution, shifting its speciation towards higher oligomers and even inducing partial coagulation. These interactions lead to circumstances where chemically coupled co-precipitaiton of silicate and carbonate cannot occur preventing the formation of polycrystalline material on a global scale. This notion is supported by corresponding experiments in the presence of high amounts of NaCl which

caused similar effects on the chemistry of silica. The results furthermore showed that the observed hemispherical particles were solid solutions of Ba- or $SrCO_3$ and calcium carbonate and exhibited orthorhombic crystal lattices. This matter of fact suggests that the difficulty in the preparation of calcium carbonate biomorphs is not solely based on the different polymorph selection at ambient conditions. Also the interactions between the divalent metal ion have to be rather subtle in order to induce the formation of typical forms displayed by silica-carbonate biomorphs.

All in all, the results deduced from the performed experiments substantiate the proposed concept of chemically coupled co-precipitation of silica and carbonate, however direct experimental evidence is still missing. A potential strategy in this context would be to measure the pH in the close vicinity on the growth front. Noticeable changes or, in the ideal case, temporal oscillation of the pH would be the ultimate proof of the concept of autocatalytic growth. To that end, current investigations are focused on the design of a suitable setup, using fluorescent dyes that are immobilized on a substrate, exhibiting a suitable pH dependent emission intensity. Any possible local pH changes on the front during growth of a flat sheet, could be recorded with the help of a convocal fluorescence microscope. First promising candidates as fluorescent pH sensor are dyes based on boron-dipyrromethene (BODIPY), since their dynamic work range is roughly between pH 7 and 12 (the range where the postulated pH oscillations are expected to occur).[191]

9 Appendices

A Additional Figures for chapter 4

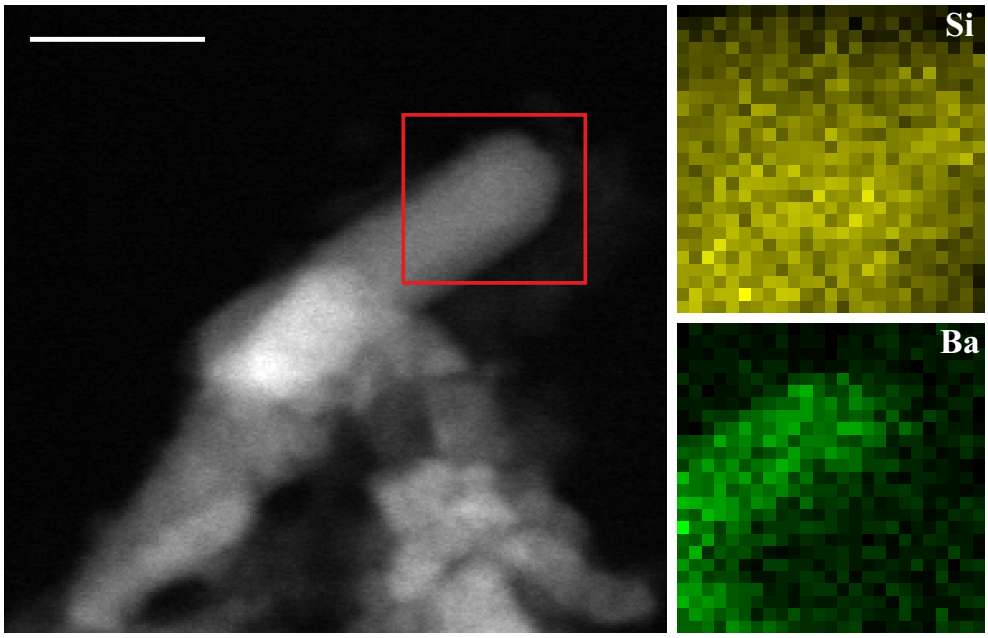

Figure 9.1. EDX mapping analysis of a crystal formed at pH 10.5 from a solution containing 300 ppm SiO_2. The investigated area is highlighted by the red rectangle in the corresponding STEM image (left). The resulting local distributions of Si (yellow) and Ba (green) suggest the presence of a continuous silica skin around the barium carbonate core. Scale bar: 50 nm

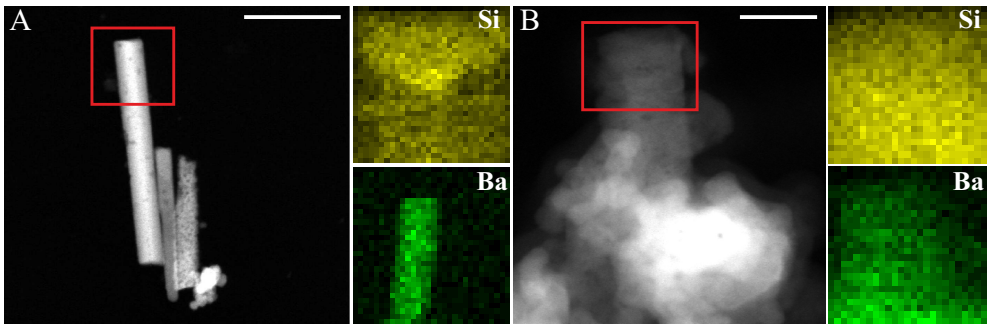

Figure 9.2. STEM images and corresponding EDX maps for relevant elements (Si and Ba), acquired from particles generated in titration experiments at pH 11.0 under the influence of (A) 600 and (B) 1200 ppm SiO_2. Also at this pH level, a continuous matrix of silica can clearly be discerned around the crystalline $BaCO_3$ rods. Scale bars (A) 200 nm and (B) 50 nm.

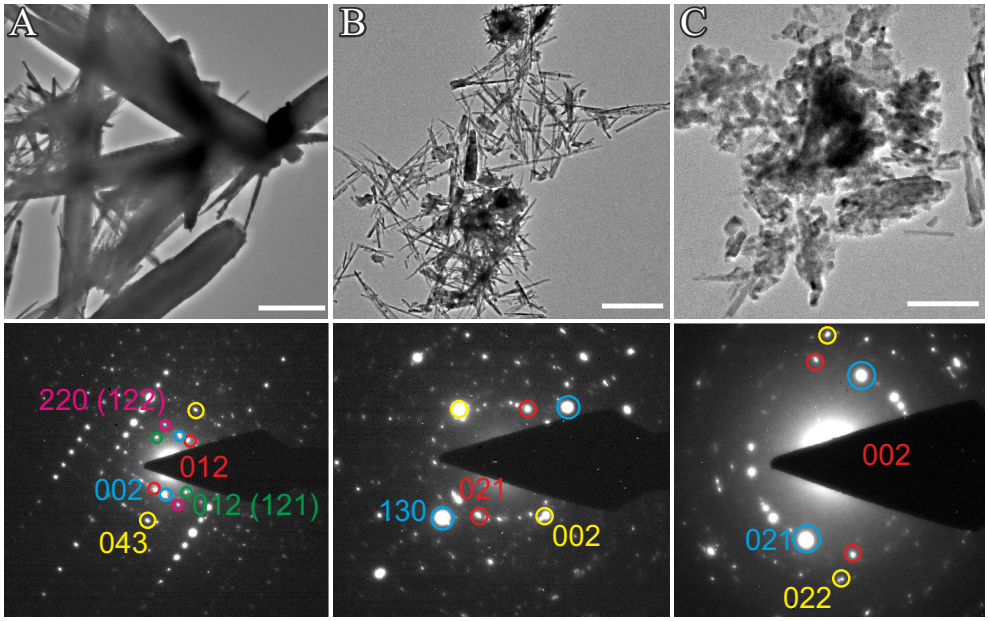

Figure 9.3. Additional TEM micrographs of crystals isolated from titration experiments performed at pH 10.0 in buffers containing (A) 0, (B) 300, and (C) 600 ppm SiO_2. Spots in the corresponding electron diffraction patterns shown below can be indexed to distinct crystallographic planes of the witherite lattice, as indicated. Indexing was achieved by comparing measured d-spacings with database values.[143] Scale bars are (A-B) 1 μm and (C) 200 nm.

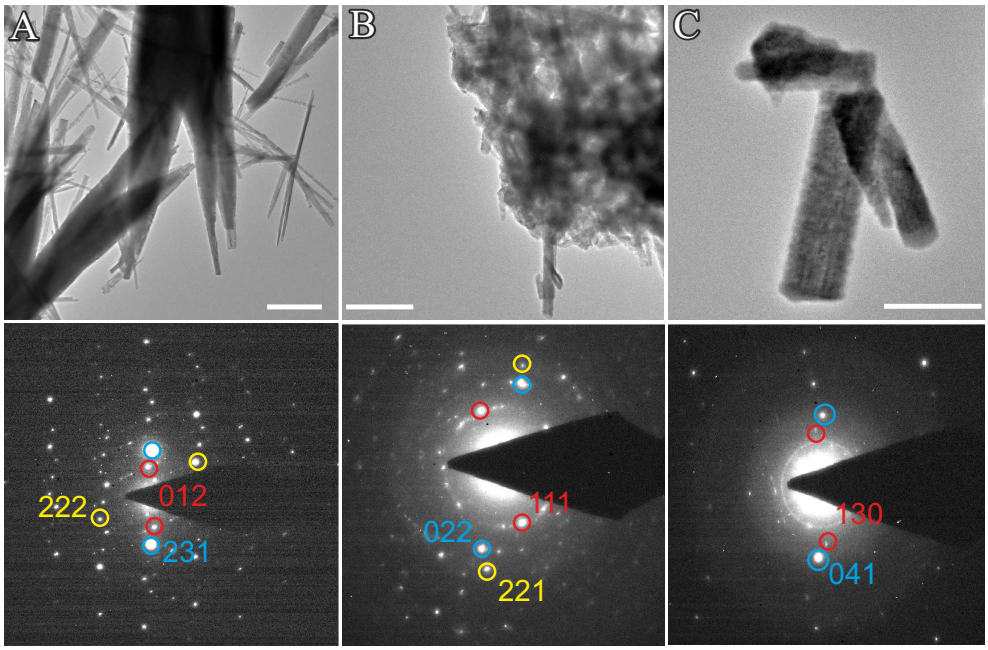

Figure 9.4. TEM images and ED patterns of crystalline products resulting from titration assays at pH 10.5 in the presence (A) 0, (B) 300, and (C) 600 ppm silicate. The highlighted diffraction spots could be indexed to witherite planes as indicated. Scale bars are (A) 1μm, (B) 200 nm, and (C) 100 nm.

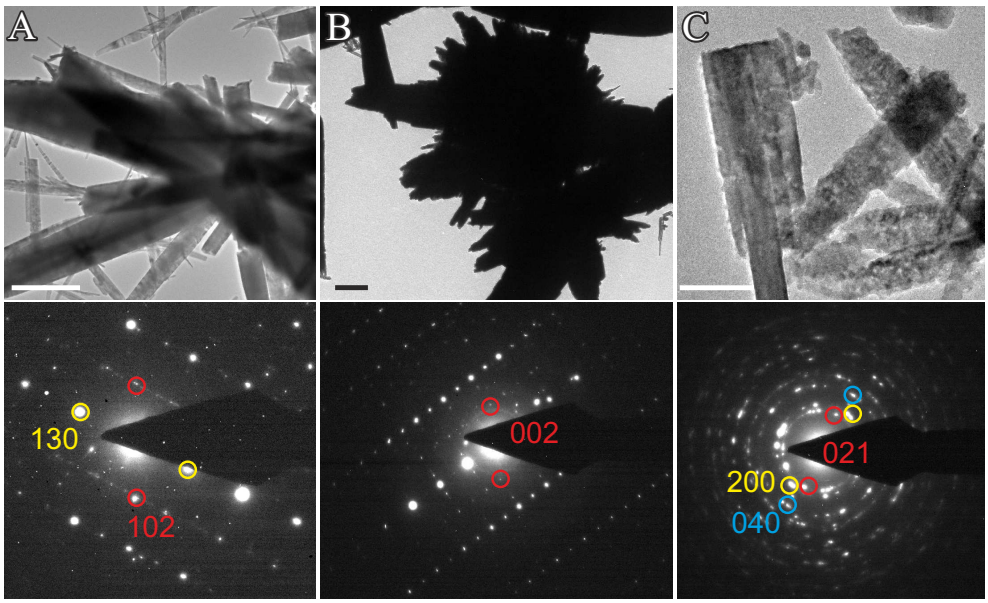

Figure 9.5. Supplementary TEM and electron diffraction data for particles generated in titration measurements at pH 11.0 in the absence of silicate (A) and under the influence of 300 (B) and 600 ppm SiO_2 (C). ED patterns can all be indexed to crystalline witherite. Scale bars are (A-B) 1μm, and (C) 100 nm.

B Additional polarized optical micrographs for chapter 5

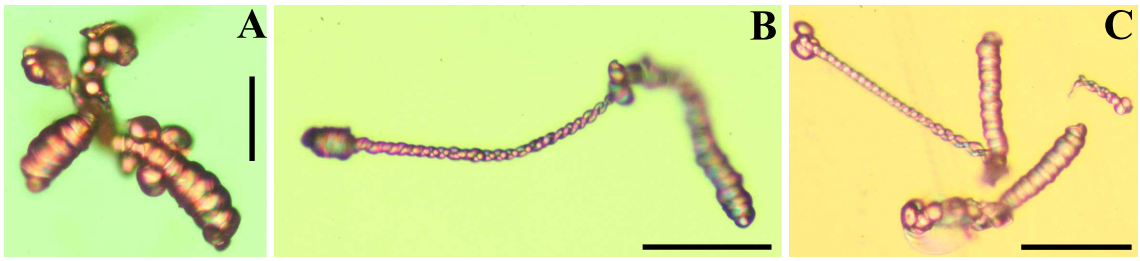

Figure 9.6. Helical filaments and worm-like braids, viewed between crossed polarizers. Aggregates were grown from solutions at starting pH levels of (A) 10.66, (B) 11.02, and (C) 11.14. Scale bars are 25 μm (A), 200 μm (B), and 100 μm (C).

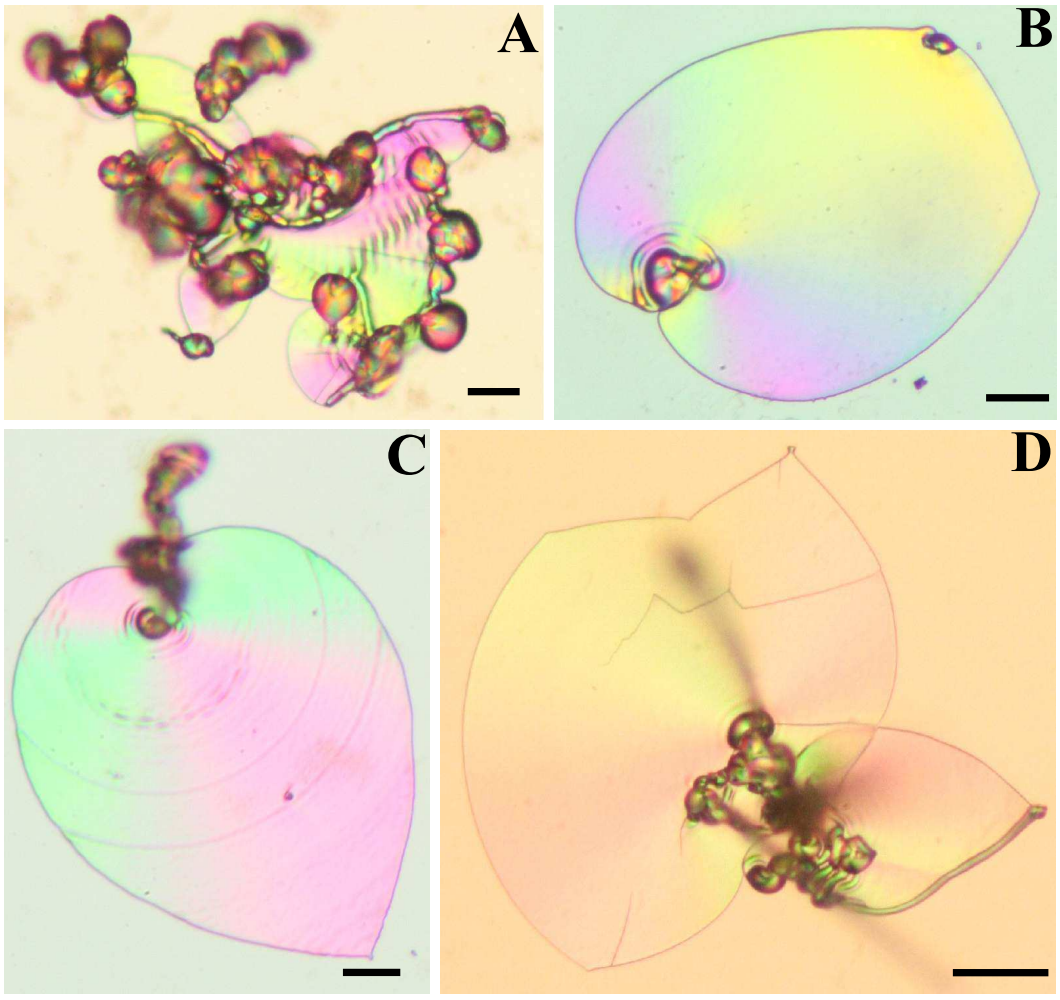

Figure 9.7. Polarized light microscopy images of sheet-like aggregates. The initial pH of the mother solution was (A) 10.22, (B) 10.66, (C) 11.02, and (D) 11.14. Scale bars are 50 μm

10 References

1 E. Haeckel, *Kunstformen der Natur*, Prestel Verlag: Munich/New York, 2005.

2 P. Q. Harting, *J. Microsc. Sci.*, 1872, **12**, 118.

3 S. B. Mukkamala, A. K. Powell, *Chem. Commun.*, 2004, 918.

4 M. Crusack, A. Freer, *Chemical Reviews*, 2008, **108**, 4433.

5 L. Addadi, D. Joester, F. Nudelman, S. Weiner, *Chem. Eur. J.*, 2006, **12**, 980.

6 L. Addadi, S. Weiner, *Angew. Chem. Int. Ed.*, 1992, **31**, 153.

7 Y. Politi, T. Arad, E. Klein, S. Weiner, L. Addadi, *Science*, 2004, **306**, 1161.

8 H. A. Lowenstam, S. Weiner, *On Biomineralization*, Oxford University Press, New York, **1989**.

9 R. Blakemore, *Science*, 1975, **190**, 377.

10 J. Aizenberg, A. Tkachenko, S. Weiner, L. Addadi, G. Hendler, *Nature*, 2001, **412**, 819.

11 J. Aizenberg, G. Hendler, *J. Mater. Chem.*, 2004, **14**, 2066.

12 L. Addadi, S. Raz, S. Weiner, *Adv. Mater.*, 2003, **15**, 959.

13 S. Mann, *Biomineralization: principles and concepts in bioinorganic chemistry*, Oxford University Press, Oxford, **2001**.

14 F. C. Meldrum, S. Ludwigs, *Macromol. Biosci.*, 2007, **7**, 152.

15 R. J. Park, F.C. Meldrum, *Adv. Mater.*, 2002, **14**, 1167.

16 R.Q. Song, H. Cölfen, *Cryst. Eng. Comm.*, 2011, **13**, 1249.

17 B. R. Heywood, S. Mann, *Adv. Funct. Mater.*, 1994, **6**, 9.

18 M. Li, H. Schnablegger, S. Mann, *Nature*, 1999, **402**, 393.

19 Y. Yang, M. Suzuki, S. Owa, H. Shirai, K. Hanabusa, *J. Mater. Chem.*, 2006, **16**, 1644.

20 L. A. Gower, D. A. Tirell, *J. Cryst. Growth*, 1998, **191**, 153.

21 J. H. Zhu, S. H. Yu, A. W. Xu, H. Cölfen, *Chem. Commun.*, 2009, 1106.

22 T. Wang, J. Mitchell, H. Börner, H. Cölfen, M. Antonietti, *Phys. Chem. Chem. Phys*, 2010, **12**, 11984.

23 M. Antonietti, M. Breulmann, C. G. Göltner, H. Cölfen, K. K. W. Wong, D. Walsh, S. Mann, *Chem. Eur. J.*, 1998, **4**, 2493.

24 W. Zhu, C. Cai, J. Lin, L. Wang, L. Chen, Z. Zhuang, *Chem. Commun.*, 2012, DOI: 10.1039/c2cc33197g.

25 F.C. Meldrum, H. Cölfen, *Chemical Reviews*, 2008, **108**, 4332.

26 R. J. Park, F.C. Meldrum, *J. Mater. Chem.*, 2004, **14**, 2291.

27 E. Loste, R. J. Park, J. Warren, F.C. Meldrum, *Adv. Funct. Mater.*, 2004, **14**, 1212.

28 E. Loste, F. C. Meldrum, *Chem. Commun.*, 2001, 901.

29 J. Aizenberg, D. A. Muller, J. L. Grazul, D. R. Hamann, *Science*, 2003, **299**, 1205.

30 W. B. Yue, A. N. Kulak, F.C. Meldrum, *J. Mater. Chem.*, 2006, **16**, 408.

31 W. Yue, R. J. Park, A. N. Kulak, F.C. Meldrum, *J. Cryst. Growth*, 2006, **294**, 69.

32 M. Lai, A. N. Kulak, D. Law, Z. B. Zhang, F.C. Meldrum, D. J. Riley, *Chem. Commun.*, 2007, **34**, 3547.

33 S. D. Sims, J. M. Didymus, S. Mann, *J.. Chem. Soc., Chem. Commun.*, 1995, 1031.

34 S. Raz, S. Weiner, L. Addadi, *Adv. Mater.*, 2000, **12**, 38.

35 N. Gehrke, H. Cölfen, N. Pinna, M. Antonietti, N. Nassif, *Cryst. Growth Des.*, 2005, **5**, 1317.

36 F. C. Meldrum, S. T. Hyde, *J. Cryst. Growth*, 2001, **231**, 544.

37 Z. R. Tian, J. A. Voigt, J. Liu, B. Mckenzie, M. J. Mcdermott, *J. Am. Chem. Soc.*, 2002, **124**, 12954.

38 J. Rieger, T. Frechen, G. Cox, W. Heckmann, C. Schmidt, J. Thieme, *Faraday Discuss.*, 2007, **136**, 265.

39 Y. Oaki, S. Kajiyama, T. Nishimura, H. Imai, T. Kato, *Adv. Mater.*, 2008, **20**, 3633.

40 Y. Oaki, H. Imai, *Langmuir*, 2005, **21**, 863.

41 D. Walsh, B. Lebeau, S. Mann, *Adv. Mater.*, 1999, **11**, 324.

42 Z. Chen, Z. Nan, *J. Colloid Interface Sci.*, 2011, **358**, 416–422.

43 H. Cölfen, L. Qi, *Chem. Eur. J.*, 2001, **7**, 106.

44 S.H. Yu, H. Cölfen, M. Antonietti, *J. Phys. Chem B*, 2003, **107**, 7396.

45 L. Qi, H. Cölfen, M. Antonietti, M. Li, J.D. Hopwood, A.J. Ashley, S. Mann, *Chem. Eur. J.*, 2001, **7**, 3526.

46 T. Wang, A. W. Xu, H. Cölfen, *Angew. Chem. Int. Ed.*, 2006, **45**, 4451.

47 X. H. Guo, F. Meng, X. Qu, M. Wang, C. Mao, J. Zhang, W. Wang, S.H. Yu, *CrystEngComm*, 2012, **14**, 3213–3219.

48 J. W. Mullin, *Crystallization*, Butterworth-Heinemann, Oxford, 4th edition, 2001.

49 M. Niederberger, H. Cölfen, *Phys. Chem. Chem. Phys.*, 2006, **8**, 3271.

50 H. Cölfen, *Top. Curr. Chem.*, 2007, **271**, 1.

51 H. Cölfen, M. Antonietti, *Angew. Chem. Int. Ed.*, 2005, **44**, 5576.

52 H. Cölfen, M. Antonietti, *Mesocrystals and non-classical crystallization*, Wiley, Chichester, 2008.

53 H. Cölfen, S. Mann, *Angew. Chem. Int. Ed.*, 2003, **42**, 2350.

54 R. L. Penn, J. F. Banfield, *Science*, 1998, **281**, 969.

55 S. H. Yu, H. Cölfen, K. Tauer, M. Antonietti, *Nature Materials*, 2005, **4**, 51.

56 F. Lippmann, *Sedimentary carbonate minerals*, Springer Verlag, Berlin, 1973.

57 M. M. Reddy, G. H. Nancollas, *J. Cryst. Growth*, 1976, **35**, 33.

58 J. M. Garcia-Ruiz, Ph.D. Thesis, Universidad Complutense, Madrid, 1980.

59 J. M. Garcia-Ruiz, J.L. Amoros, *J. Cryst. Growth*, 1981, **55**, 379.

60 J. M. Garcia-Ruiz, *J. Cryst. Growth*, 1985, **73**, 251.

61 M. Kellermeier, H. Cölfen, J. M. Garcia-Ruiz, *Eur. J. Inorg. Chem.*, 2012, **32**, 5123.

62 J. M. Garcia-Ruiz, S. T. Hyde, A. M. Carnerup, A. G. Christy, M. J. Van Kranendonk, N. J. Welham, *Science*, 2003, **302**, 1194.

63 J. M. Garcia-Ruiz, A. Carnerup, A. G. Christy, N. J. Welham, S. T. Hyde, *Astrobiology*, 2002, **2**, 353.

64 J. M. Garcia-Ruiz, *Origins Life Evol. Biosphere*, 1994, **24**, 451.

65 Feb. 2013, `http://oceanservice.noaa.gov/gallery/image.php?siteName=nosimages&cat=Brain%20Coral`.

66 J. M. Garcia-Ruiz, *Geology*, 1998, **26**, 843.

67 S. T. Hyde, A. M. Carnerup, A. K. Larsson, A. G. Christy, J. M. Garcia-Ruiz, *Physica A*, 2004, **339**, 24.

68 M. Kellermeier, J. Eiblmeier, E. Melero-Garcia, M. Pretzl, A. Fery, W. Kunz, *Cryst. Growth Des.*, 2012, **12**, 3647.

69 A. E. Voinescu, M. Kellermeier, A. M. Carnerup, A. K. Larsson, D. Touraud, S. T. Hyde, W. Kunz, *J. Cryst. Growth*, 2007, **306**, 152.

70 Matthias Kellermeier, Ph.D. Thesis, University of Regensburg, 2011.

71 A. M. Carnerup, Ph.D. Thesis, Australian National University; Canberra, Australia, 2007.

72 E. Melero-Garcia, R. Santisteban-Bailon, J. M. Garcia-Ruiz, *Cryst. Growth Des.*, 2009, **9**, 4730.

73 T. Baird, P. S. Braterman, P. Chen,J. M. Garcia-Ruiz, R. D. Peacock, A. Reid, *Mater. Res. Bull.*, 1992, **2627**, 1031.

74 E. Bittarello, D. Aquilano, *Eur. J. Mineral.*, 2007, **19**, 345.

75 M. Kellermeier, E. Melero-Garcia, F. Glaab, J. Eiblmeier, L. Kienle, R. Rachel, W. Kunz, J. M. Garcia-Ruiz, *Chem. Eur. J.*, 2012, **18**, 2272.

76 M. Kellermeier, F. Glaab, A. M. Carnerup, M. Drechsler, B. Gossler, S. T. Hyde, W. Kunz, *J. Cryst. Growth*, 2009, **311**, 2530.

77 J. A. Speer, *Rev. Mineral.*, 1983, **11**, 145.

78 R. Oldenbourg, *Nature*, 1996, **381**, 811.

79 Y. Jiang, H. Gong, D. Volkmer, L. Gower, H. Cölfen, *Adv. Mater.*, 2011, **23**, 3548.

80 S. T. Hyde, J. M. Garcia-Ruiz, *Actual. Chim.*, 2004, **275**, 4.

81 J. M. Garcia-Ruiz, E. Melero-Garcia, S. T. Hyde, *Science*, 2009, **323**, 362.

82 T. Terada, S. Yamabi, H. Imai, *J. Cryst. Growth*, 2003, **253**, 435.

83 H. Imai, T. Terada, T. Miura, S. Yamabi, *J. Cryst. Growth*, 2002, **244**, 200.

84 A. E. Voinescu, M. Kellermeier, B. Bartel, A. M. Carnerup, A. K. Larsson, D. Touraud, W. Kunz, L. Kienle, A. Pfitzner, S. T. Hyde, *Cryst. Growth Des.*, 2008, **8**, 1515.

85 E. Bittarello, F. R. Massaro, D. Aquilano, *J. Cryst. Growth*, 2009, **312**, 402.

86 W. Kunz, M. Kellermeier, *Science*, 2009, **323**, 344.

87 M. Kellermeier, E. Melero-Garcia, W. Kunz, J. M. Garcia-Ruiz, *J. Colloid Interface Sci.*, 2012, **380**, 1.

88 S. Busch, H. Dolhaine, A. DuChesne, S. Heinz, O. Hochrein, F. Laeri, O. Podebrad, U. Vietze, T. Weiland, R. Kniep, *Eur. J. Inorg. Chem.*, 1999, 1643.

89 H. D. Keith, F. Padden, *J. Appl. Phys.*, 1963, **34**, 2409–2421.

90 S. Busch, U. Schwarz, R. Kniep, *Adv. Funct. Mater.*, 2003, **13**, 189.

91 P. Simon, E. Rosseeva, J. Buder, W. Carrillo-Cabrera, R. Kniep, *Adv. Funct. Mater.*, 2009, **19**, 3596.

92 M. Kellermeier, E. Melero-Garcia, F. Glaab, R. Klein, M. Drechsler, R. Rachel, J. M. Garcia-Ruiz, W. Kunz, *J. Am. Chem. Soc.*, 2010, **132**, 17859.

93 D. Gebauer, A. Völkel, H. Cölfen, *Science*, 2008, **322**, 1819.

94 D. Gebauer, H. Cölfen, A. Verch, M. Antonietti, *Adv. Mater.*, 2009, **21**, 435.

95 D. Gebauer, A. Verch, H. G. Börner, H. Cölfen, *Cryst. Growth Des.*, 2009, **9**, 2398.

96 A. Verch, D. Gebauer, M. Antonietti, H. Cölfen, *Phys. Chem. Chem. Phys*, 2011, **13**, 16811.

97 A. Picker, M. Kellermeier, J. Seto, D. Gebauer, H. Cölfen, *Z. Krist.*, 2012, **227**, 744.

98 R. Demichelis, P. Raiteri, J. D. Gale, D. Quigley, D. Gebauer, *Nat. Commun.*, 2011, **2**, 590.

99 S. Dominguez Bella, J. M. Garcia-Ruiz, *J. Mat. Sci.*, 1987, **22**, 3095.

100 S. Dominguez Bella, J. M. Garcia-Ruiz, *J. Cryst. Growth*, 1986, **79**, 236.

101 M. Kellermeier, E. Melero-Garcia, W. Kunz, J. M. Garcia-Ruiz, *Adv. Chem. Phys.*, 2012, **151**, 277.

102 A. E. S. Van Driessche, L. G. Benning, J. D. Rodriguez-Blanco, M. Ossorio, P. Bots, J. M. Garcia-Ruiz, *Science*, 2012, **336**, 69.

103 D. Li, M. H. Nielsen, J. R. I. Lee, C. Frandsen, J. F. Banfield, J. J. De Yoreo, *Science*, 2012, **336**, 1014.

104 S. Mann, *Nature Materials*, 2009, **8**, 781.

105 Y. Ma, S. Weiner, L. Addadi, *Adv. Funct. Mater.*, 2007, **17**, 2693.

106 C. E. Killian, R.A. Metzler, Y. U.T. Gong, I.C. Olson, J. Aizenberg, Y. Politi, F. H. Wilt, A. Scholl, A. Young, A. Doran, M. Kunz, N. Tamura, S. N. Coppersmith, P. U. P. A. Gilbert, *J. Am. Chem. Soc.*, 2009, **131**, 18404.

107 S. Raz, P.C. Hamilton, F. H. Wilt, S. Weiner, L. Addadi, *Adv. Mater.*, 2003, **13**, 480.

108 Y. Politi, D. R. Batchelor, P. Zaslansky, B. F. Chmelka, J. C. Weaver, I. Sagi, S. Weiner, L. Addadi, *Chem. Mater.*, 2010, **22**, 161.

109 J. Tao, D. Zhou, Z. Zhang, X. Xu, R. Tang, *Proc. Natl. Acad. Sci. U.S.A.*, 2009, **106**, 22096.

110 C. C. Tester, R. E. Brock, C. H. Wu, M. R. Krejci, S. Weigand, D. Joester, *CrystEng-Comm*, 2011, **13**, 3975.

111 E. Beniash, L. Addadi, S. Weiner, *J. Struct. Biol.*, 1999, **125**, 50.

112 J. J. J. M. Donners, B. R. Heywood, E. W. Meijer, R. J. M. Nolte, N. Sommerdijk, *Chem. Eur. J.*, 2002, **8**, 2561.

113 B. Guillemet, M. Faatz, F. Gröhn, G. Wegner, Y. Ganou, *Langmuir*, 2006, **22**, 1875.

114 J. Rieger, E. Hädicke, I. U. Rau, D. Boeckh, *Tenside Surf. Det.*, 1997, **34**, 430.

115 Y. Liu, Y. Cui, R. Guo, *Langmuir*, 2012, **28**, 6097.

116 K. Sawada, *Pure Appl. Chem.*, 1997, **69**, 921.

117 A. W. Xu, Q. Yu, W. F. Dong, M. Antonietti, H. Cölfen, *Adv. Funct. Mater.*, 2005, **17**, 2217.

118 J. Ihli, Y. Y. Kim, E. H. Noel, F. C. Meldrum, *Adv. Funct. Mater.*, 2012, DOI: 10.1002/adfm.20120180

119 X. R. Xu, A. H. Cai, R. Liu, H. H. Pan, R. K. Tang, K. W. Cho, *J. Cryst. Growth*, 2008, **310**, 3779.

120 L. B. Gower, D. J. Odom, *J. Cryst. Growth*, 2000, **210**, 719.

121 D. C. Basset, B. Marelli, S. N. Nazhat, J. E. Barralet, *Adv. Funct. Mater.*, 2012, **22**, 3460.

122 S. E. Wolf, J. Leiterer, V. Pipich, R. Barrea, F. Emmerling, W. Tremel, *J. Am. Chem. Soc.*, 2011, **133**, 12642.

123 A. Gal, S. Weiner, L. Addadi, *J. Am. Chem. Soc.*, 2010, **132**, 13208.

124 A. Gal, A. Hirsch, S. Siegel, C. Li, B. Aichmayer, Y. Politi, P. Fratzl, S. Weiner, L. Addadi, *Chem. Eur. J.*, 2012, **18**, 10262.

125 J. Eiblmeier, M. Kellermeier, D. Rengstl, J.M. Garcia-Ruiz, W. Kunz, *Cryst. Eng. Comm.*, 2013, **15**, 43.

126 H. Imai, T. Terada, S. Yamabi, *Chem. Commun.*, 2003, 484.

127 J. R. Martinez, F. Ruiz, Y. V. Vorobiev, F. Pérez-Robles, J. Gonzáles-Hernández, *J. Chem. Phys.*, 1998, **109**, 7511.

128 P. Pasierb, S. Komornicki, M. Rokita, M. Rekas, *J. Molol. Struct.*, 2001, **596**, 151.

129 R. K. Iler, *The chemistry of silica. Solubility, Polymerization, Colloid and Surface properties, and Biochemistry*, John Wiley & Sons, Inc, New York, **1979**.

130 L. Svensson, L. O. Öhman, *J. Chem. Soc , Faraday Trans.*, 1986, **82**, 3635.

131 S. Sjöberg, *J. Non-Cryst. Solids*, 1996, **196**, 51.

132 M. Kellermeier, D. Gebauer, E. Melero-Garcia, M. Drechsler, Y. Talmon, L. Kienle, H. Cölfen, J. M. Garcia-Ruiz, W. Kunz, *Adv. Funct. Mater.*, 2012, **22**, 4301.

133 P. M. Dove, C. J. Nix, *Geochim. Cosmochim. Acta*, 1997, **61**, 3329.

134 W. L. Marshall, J. M. Warakomski, *Geochim. Cosmochim. Acta*, 1980, **44**, 915.

135 S. Weiner, J. Mahamid, Y. Politi, Y. Ma, L. Addadi, *Front. Mat. Sci. Cin.*, 2009, **2**, 104.

136 T. Wang, J. Zhuang, J. Lynch, O. Chen, Z. Wang, X. Wang, D. LaMontagne, *Science*, 2012, **338**, 358.

137 C. A. Jones, M. R. Mirkin, *Nature*, 2012, **491**, 42.

138 S. H. Yu, H. Cölfen, *J. Mater. Chem.*, 2004, **14**, 2124.

139 D. Gebauer, H. Cölfen, *Nano Today*, 2011, **6**, 564.

140 D. G. Hall, *J. Phys Chem.*, 1996, **100**, 7230.

141 P. C. Cheng, G. Y. Cheng, M. H. Kou, P. Y. Shia, P. O. Chung, *J. Cryst. Growth*, 2001, **226**, 458.

142 A. Navrotsky, *Proc. Natl. Acad. Sci. U.S.A.*, 2004, **101**, 12096.

143 J. P. R. de Villiers, *Am. Mineral.*, 1971, **56**, 758.

144 E. M. Pouget, P. H. H. Bomans, J. A. C. M. Goos, P. M. Frederik, G. de With, N. A. J. M. Sommerkijk, *Science*, 2009, **323**, 1455.

145 A. R. Finney, P. M. Rodger, *Faraday Discuss.*, 2012, **159**, 47.

146 G. Falini, S. Fermani, M. Gazzano, A. Ripamonti, *Chem. Eur. J.*, 1997, **3**, 1807.

147 A. Sugawara, T. Ishii, T. Kato, *Angew. Chem. Int. Ed.*, 2003, **42**, 5299.

148 T. Wang, H. Cölfen, M. Antonietti, *J. Am. Chem. Soc.*, 2005, **127**, 3246–3247.

149 N. Nassif, N. Gehrke, N. Pinna, N. Shirshova, K. Tauer, M. Antonietti, H. Cölfen, *Angew. Chem. Int. Ed.*, 2005, **44**, 6004.

150 M. Balz, H. A. Therese, J. Li, J. S. Gutmann, M. Kappl, L. Nasdala, W. Hofmeister, H. J. Butt, W. Tremel, *Adv. Funct. Mater.*, 2005, **15**, 683.

151 X.H. Guo, S.H. Yu, *Cryst. Growth Des.*, 2007, **7**, 354.

152 S. Hayashi, K. Ohkawa, Y. Suwa, T. Sugawara, T. Asami, H. Yamamoto, *Macromol. Biosci.*, 2008, **8**, 46.

153 S. Wu, H. Cao, S. Yin, X. Zhang, V. Chernow, *Inorg. Chem.*, 2009, **48**, 10326.

154 G. Falini, S. Albeck, S. Weiner, L. Addadi, *Science*, 1996, **271**, 67.

155 A.G. Checa, A.B. Rodriguez-Navarro, *Biomaterials*, 2005, **26**, 1071.

156 M. Pretzl, A. Schweikart, C. Hanske, A. Chiche, U. Zettl, A. Horn, A. Böker, A. Fery, *Langmuir*, 2008, **24**, 12748.

157 Y. Y. Kim, E. P. Douglas, L. B. Gower, *Langmuir*, 2007, **23**, 4862.

158 J. Aizenberg, *Advanced Materials*, 2004, **16**, 1295.

159 C. Li, L. Qi, *Agew. Chem. Int. Ed.*, 2008, **47**, 2388.

160 K. Prashant, *Nanosc. Res. Letters*, 2010, **5**, 1367.

161 S. Zhang, *Nature Biotechnology*, 2003, **21**, 1172.

162 M. Shimomura, T. Sawadaishi, *Curr. Opin. Colloid Interface Sci.*, 2001, **6**, 11.

163 X. Chen, S. Lenhert, M. Hirtz, N. Lu, H. Fuchs, L. Chi, *Acc. Chem. Res.*, 2007, **40**, 393.

164 D. W. Lea, G. T. Shen, E. A. Boyle, *Nature*, 1989, **340**, 373.

165 J. M. Alia, Y. Diaz de Mera, H. G. M. Edwards, P. Gonzales Martin, S. Lopez Andres, *Spectrochi. Ac., Part A*, 1997, **53**, 2347.

166 L. L. Y. Chang, R. A. Howie, J. Zussman, *Non silicates: sulphates, carbonates, phosphates and halides*, The Geological Society, second edition, 1998.

167 J. L. Wray, F. Daniels, *J. Am. Chem. Soc.*, 1957, **79**, 2031.

168 R. D. Sannon, *Acta Crystallogr. A*, 1976, **32**, 751.

169 M. Raitzsch, A. Duenas-Bohorquez, G. J. Reichart, L. J. de Nooijer, T. Bickert, *Biogeosciences*, 2010, **7**, 869.

170 T. A. Gebrehiwet, G. D. Redden, Y. Fujita, M. S. Beig, R. W. Smith, *Geochem. Trans.*, 2012, **13**, 1.

171 Y. Terakado, M. Taniguchi, *Geochem. J.*, 2006, **40**, 161.

172 R. K. Iler, *J. Colloid Interface Sci.*, 1975, **53**, 476.

173 R. Zerrouk, A. Foissy, R. Mercier, Y. Chevallier, J. C. Morawski, *J. Colloid Interface Sci.*, 1990, **139**, 20.

174 R. E. Zeebe, D. Wolf Gladrow, CO_2 *in seawater: equilibrium, kinetics, isotopes*, Elsevier Oceanography Series, 2001.

175 E. Busenberg, L. N. Plummer, *Geochim. Cosmochim. Acta*, 1986, **50**, 2225.

176 L. N. Plummer, E. Busenberg, *Geochim. Cosmochim. Acta*, 1982, **46**, 1011.

177 E. Busenberg, L. N. Plummer, *Geochim. Cosmochim. Acta*, 1984, **48**, 2021.

178 E. Bittarello, F. R. Massaro, M. Rubbo, E. Costa, D. Aquilano, *Cryst. Growth Des.*, 2009, **9**, 971.

179 N. E. Pingitore, M. P. Eastman, *Geochim. Cosmochim. Acta*, 1986, **50**, 2195.

180 A. J Tesoriero, J. F. Pankow, *Geochim. Cosmochim. Acta*, 1995, **60**, 1053.

181 R. B. Lorens, *Geochim. Cosmochim. Acta*, 1981, **45**, 553.

182 J. Tang, S. J. Köhler, M. Dietzel, *Geochim. Cosmochim. Acta*, 2008, **72**, 3718.

183 N. E. Pingitore, M. P. Eastman, *Chem. Geol.*, 1984, **45**, 113.

184 D. P. Gillikin, F. Dehairs, A. Lorrain, D. Steenmanns, W. Baeyens, L. André, *Geochim. Cosmochim. Acta*, 2006, **70**, 395.

185 Y. Yoshida, H. Yoshikawa, T. Nakanishi, *Geochem. J.*, 2008, **42**, 304.

186 M. J. Malone, P. A. Baker, *J. Sediment. Res.*, 1999, **69**, 216.

187 L. Brecevic, V. Nöthig-Laslo, D. Kralj, S. Popovic, *J. Chem. Soc., Faraday Trans.*, 1996, **92**, 1017.

188 V. Noethig-Laslo, L. Brecevic, *J. Chem. Soc. Faraday Trans.*, 1998, **94**, 2005.

189 N. R. Haase, S. Shian, K. H. Sandhage, N. Kröger, *Adv. Funct. Mater.*, 2011, **21**, 4243.

190 K. T. Kim, S. A. Meeuwissen, R. J. M. Nolte, J. C. M. Van Hest, *Nanoscale*, 2010, **2**, 844.

191 M. Hecht, W. Kraus, K. Rurack, *Analyst*, 2013, **138**, 325.

List of Figures

List of Tables

List of Publications

Parts of this work have already been, or will be published in:

1. Matthias Kellermeier, **Josef Eiblmeier**, Emilio Melero-García, Melanie Pretzl, Andreas Fery, Werner Kunz, "Evolution and Control of Complex Curved Form in Simple Inorganic Precipitation Systems", *Crystal Growth and Design*, 2012, 12, 3647-3655.

2. **Josef Eiblmeier**, Matthias Kellermeier, Doris Rengstl, Juan Manuel García-Ruiz, Werner Kunz, "Effect of Bulk pH and Supersaturation on the Growth Behavior of Silica Biomorphs in Alkaline Solutions", *Cryst. Eng. Comm.*, 2013, 15, 43-53, (cover page)

3. **Josef Eiblmeier**, Matthias Kellermeier, Lorenz Kienle, Mao Deng, Juan Manuel Garcia-Ruiz, Werner Kunz, "Bottom-Up Self-Assembly of Amorphous Core-Shell-Shell Nanoparticles and Biomimetic Crystal Forms in Inorganic Silica-Carbonate Systems", submitted to: *Chemistry of Materials*

4. **Josef Eiblmeier**, Matthias Kellermeier, Lorenz Kienle, Ulrich Schürmann, Werner Kunz, "New Insights into the Early Stages of Silica-Controlled Barium Carbonate Crystallization" *in preparation*

5. **Josef Eiblmeier**, Matthias Kellermeier, Stefan Dankesreiter, Arno Pfitzner, Werner Kunz, "Crystallization of mixed alkaline-earth carbonates in alkaline silica solutions", *in preparation*

Further Publications:

6. Giacomo Pizzorusso, Emiliano Fratini, **Josef Eiblmeier**, Rodorico Giorgi, David Chelazzi, Aurelia Chevalier, Piero Baglioni, "Physicochemical Characterization of Acrylamide/Bisacrylamide Hydrogels and Their Application for the Conservation of Easel Paintings", *Langmuir*, 2012, 28, 3952-3961.

7. Matthias Kellermeier, Emilio Melero-García, Fabian Glaab, **Josef Eiblmeier**, Lorenz Kienle, Reinhard Rachel, Werner Kunz, Juan Manuel García-Ruiz, "Growth Behavior and Kinetics of Self-Assembled Silica-Carbonate Biomorphs", *Chemistry a European Journal*, 2012, 18, 2272-2282.

8. Doris Rengstl, Gordon Tiddy, Ilya Shenderovich, **Josef Eiblmeier**, Werner Kunz, "Influence of chain length and double bond on the thermotropic phase behavior of choline carboxylate soaps". *submitted*

Declaration

Hereby, I declare that I have composed the present dissertation on my own hand, using exclusively the quoted references and resources. Literally or correspondingly adapted material has been marked accordingly.

Erklärung

Hiermit erkläre ich, dass ich die vorliegende Dissertation selbstständig und nur mit den angegebenen Quellen und Hilfsmitteln angefertigt habe. Wörtlich oder sinngemäß übernommenes Gedankengut habe ich als solches kenntlich gemacht.

Regensburg, den 13. Mai 2013 ..... (Josef Eiblmeier)